Title
Exchange of fine sediments with gravel riverbeds

Permalink
https://escholarship.org/uc/item/2w1567vr

Author
Leonardson, Rebecca

Publication Date
2011

Exchange of fine sediments with gravel riverbeds

by

Rebecca Leonardson

A dissertation submitted in partial satisfaction of the
requirements for the degree of
Doctor of Philosophy

in

Environmental Engineering

in the

Graduate Division

of the

University of California, Berkeley

Committee in charge:

Professor James R. Hunt, Co-chair
Professor William E. Dietrich, Co-chair
Professor Mark Stacey
Professor G. Mathias Kondolf

Fall 2010

Exchange of fine sediments with gravel riverbeds

Abstract

Exchange of fine sediments with gravel riverbeds

by

Rebecca Leonardson

Doctor of Philosophy in Environmental Engineering

University of California, Berkeley

Professor James R. Hunt, Co-chair

Professor William E. Dietrich, Co-chair

An excess of fine sediment is the leading cause of impairment of rivers in the United States. Fine sediment poses particular problems for salmon, which bury their eggs within gravel riverbeds. Sand infiltrates the salmon nest and creates a sand seal in the upper pore spaces near the surface. Silt and clay then deposit in the sand seal, reducing bed permeability and cutting off the supply of dissolved oxygen. Large stormflows can mobilize the riverbed and flush out the silt and clay, increasing permeability. Reservoir releases on dammed rivers can simulate this effect; it may also be possible to engineer releases to both increase reservoir flood storage and improve the quality of spawning habitat. Understanding the fraction of fines as a function of depth would allow estimation of bed permeability and ideal flushing depths, which would aid in the design of flushing flows. This dissertation improves understanding of the sand fraction as a function of depth in the sand seal by analyzing infiltration data, testing an existing model, and developing new models. It is found that a simple exponential model performs well at predicting the sand fraction as a function of depth but there is evidence of a more complex structure driven by a change in trapping efficiency as the bed clogs. This study allows for direct calculation of the effect of sand seals on bed permeability and can inform future studies of silt and clay deposition in the sand seal, but it is limited to uniform-flow, plane-bed conditions. The location and structure of salmon nests takes advantage of three-dimensional flow fields to enhance flow over the eggs. These forcing mechanisms should affect infiltration into nests. This relationship is explored in an experiment on sand infiltration into a gravel bed with alternate-bar topography. This study demonstrates that sand seals are created throughout the riverbed, even where sand transport is too small to measure. There is spatial variability in the thickness of a sand seal but not in the mean sand fraction in the sand seal. Local infiltration is increased by bed topography that promotes downwelling and is limited by very high sand transport and by thick sand deposits on the surface. The structure of a sand seal will affect flushing depth, but the duration of a flushing flow depends on the entrainment rate of silt and clay from within the sand seal. The entrainment rate of subsurface fines into suspension is not generally known. A case study on the Russian River in California is performed to estimated the entrainment rate during dam releases large enough to mobilize the riverbed. High-frequency turbidity and discharge data from two USGS gauging stations are used to create a timeseries of cumulative entrainment from the reach. Estimates of bed mobility are used to develop rough estimates of local entrainment. Entrainment decays exponentially at a timescale on the order of days, and this timescale decreases as the discharge event increases. Total estimated entrainment is similar to the supply of suspendable sediment calculated to be in the bed.

To my parents, Nancy and Gene Leonardson

Contents

List of Figures

List of Tables

Acknowledgments

I want to thank my advisors Professors James R. Hunt and William E. Dietrich. It's been an honor to work with both of you. Professor Hunt has provided patient support from finding my field of study through finishing the dissertation. Thanks for continuing to push me towards simplicity and logic. Professor Dietrich has provided inspiration and challenge to be both useful and correct.

Professor Mark Stacey provided much-appreciated feedback and encouragement over many years. Thanks to G. Mathias Kondolf for including me in river restoration activities on campus and in Portugal. Professor John A. Dracup supported my early work in graduate school and imparted much wisdom.

Shelley Okimoto gave final-hour moral and administrative support, making it possible to submit this dissertation.

Thanks to the Berkeley Water Center, the California Climate Change Center, and the National Center for Earth-Surface Dynamics for supporting my research.

My classmates and officemates have made it possible to survive and even enjoy graduate school. Much love and thanks to the environmental fluid mechanics and hydrology group, the geomorphology research group, and John Dracup's research group.

My research collaborators added fun and excitement as well as scientific depth to my projects. Catharine van Ingen provided inspiration and insight on science and graduate school during and after a summer internship at Microsoft Research. Deb Agarwal has provided an amazing computational resource and data structure. Aleksandra Wydzga gave me a great crash-course in flume experimentation at the Saint Anthony Falls Laboratory. Thanks to Wayne Wagner, Brian Yates, and Rusty Holleman for help with field work.

Thanks to Michael Webster and the Ukiah field office of the United States Geological Survey for access to equipment and information on the Russian River. Thanks also to the United States Army Corps of Engineers and to the California Department of Fish and Game.

Eddie Kohler has provided encouragement and love from applying to Berkeley through editing my dissertation conclusions. My parents Nancy and Gene Leonardson have given unending support. Thanks to my friends for listening, being sympathetic, and helping me to see the light at the end of the tunnel: Chris Onufryk, Jason Randolph, Chris Lombardi, Rosey Jencks, Betsey Eagon, my brothers David and Mark Leonardson, and many others. Finally, thanks to the Wednesday Night Crew at the Marine Mammal Center and the 2001-2002 Marin Conservation Corps/Americorps Habitat Restoration Crew.

Chapter 1

Motivation of study

Forty percent of American rivers assessed by the United States Environmental Protection Agency in 1998 were either threatened or impaired by excess fine sediment [80]. Excessive fine sediment supply is the leading cause of impairment of US rivers [80]. The increase in fine sediment supply is driven by an increase in human population and the related urbanization, forestry practices, and agriculture. In addition, fine sediment loading has changed from an episodic to a chronic condition due to logging roads, storm drain systems, reservoir operations, and human and farm animal activity within rivers. Rivers' natural ability to wash these sediments out of the riverbed during large flows has been reduced due to dams and water diversions. Human population continues to grow, and the demand for water and activities that effect waterways rises with it. We cannot expect this resource use to decrease due to improvements in efficiency or voluntary behavioral change [59]. However, water resource management can be altered to either benefit or minimize negative impacts on waterways.

The overabundance of fine sediment has a number of negative impacts on gravel-bedded rivers. Deposited sediment reduces aquatic ecosystem stability, limits hydrologic exchange between groundwater and surface water, and reduces the output of streambank pumping operations [6, 71]. Runs of salmon in California and the Pacific Northwest, over 60% of which are extinct or at risk of extinction [82], experience an additional threat from fine sediment. Infiltration of fine sediment into salmonid redds can smother developing eggs and block pathways for juvenile fish to emerge from the subsurface [5, 10, 43]. Excessive turbidity reduces the availability of food by blocking primary production and limiting visibility needed for hunting.

Spawning salmonids choose nesting sites based on sediment quality and flow conditions. Salmonids prefer areas with coarse gravel and shallow, fast-flowing water; many choose the head or crest of the riffle. Spawning females dig a pit in the riverbed, deposit their eggs inside, and build a pile of gravel on top; this structure is called a redd. In the process, they remove approximately forty percent of fines from the gravel [41]. The local flow conditions, clean gravel, and shape of the redd drive water through the nest, supplying dissolved oxygen and removing metabolic wastes.

After spawning, the adult fish die or abandon the nest. The eggs must survive in the redd for several months before hatching. If the background fine sediment content of the riverbed is high, the redd will start off with reduced permeability. The permeability of the redd decreases as fine sediment is deposited throughout the incubation period. The first time that a stormflow transports sand down the river, the sand can settle into the gravel and clog the pore spaces near the surface. This ”sand seal” traps silt and clay, further reducing the bed permeability.

Loss of habitat due to installation of dams is one of the main causes of the decline in population of Pacific salmon. However, dams can be used to improve spawning habitat in certain conditions. Dams can release large flushing flows to mobilize riverbed gravel and clean the bed of deposited fines. These flows are difficult to engineer and can have unintended consequences. For instance, flushing flows may clear the bed of fines but they can also cause erosion and increase the supply of fines. A flushing flow may be beneficial in November for improving spawning habitat. Once the salmon have laid their eggs, the same flow could result in the scouring or suffocation of salmon eggs [42]. A flushing flow can also waste a lot of effort, money, and water if it is underdesigned or unnecessary.

Researchers and consultants have spent considerable time developing theories, models, and design guidelines for flushing flows [55, 42, 87]. Some flushing releases have been made prior to the spawning season to create and improve spawning habitat by removing fines. Where post-project evaluations have occured, these flows appear to be successful at increasing the number of redds and the local salmonid populations [58, 39]. Flushing flows for habitat improvement have not generally been made during egg development for fear that they may either scour the eggs themselves or mobilize enough fines so that the redds become more clogged [55, 66]. However, fines infiltrate redds and there are scenarios where flushing could increase survival-to-emergence. Moreover, large releases for flood management and other uses are made during the egg development period. These flows could be engineered to benefit or minimize damage to spawning habitat. The purpose of this dissertation is to improve the understanding of fine sediment infiltration in order to make flushing flows during egg development more feasible and effective.

Flushing flows can clean the bed of silt and clay, but they cannot get rid of sand seals. Once the riverbed is mobilized, the sand will be entrained and transported downstream, most likely as bedload. However, this simply makes sand available to infiltrate another portion of the bed. A sand seal is created in 15-20 minutes [5], and will surely be built by the time the flow recedes. Sand seals appear to be pervasive in the field. In Chapter 3 of this dissertation it will be shown that sand seals are built even if sand transport is too small to measure. On the other hand, silt and clay trapped in the sand seal can be entrained and carried out of the river network in suspension.

If the goal of a flushing flow is to improve riverbed permeability, it is important to know the current permeability and estimate how that will change depending on the depth of flushing. These require knowing the mass, depth, and grain size of fine sediment in the sand seal. Current knowledge makes it possible to estimate these values for sand in the sand seal if there is no silt or clay present. Sand seals have been described by their bulk properties and there is one model for predicting how the sand fraction varies with depth in the bed [5, 17, 88]. In Chapter 3, it is demonstrated that the calculated permeability varies up to 63% depending on which sand seal description the calculations are based upon. The model by Wooster would be a natural choice, but it has not been verified in outside studies. In Chapter 2, the performance of the Wooster model is tested, data from sand infiltration experiments are analyzed to better understand development and steady-state sand content in a sand seal, and revised models for the sand fraction as a function of depth are built. This analysis should improve estimates of sand seal permeability and inform design of flushing depths. The depth at which the sand content drops to a negligible amount can be estimated using representative grain diameters of bed gravel and infiltrating sand.

There is no existing model for the depth and mass of silt and clay deposited in a sand seal, which have a much larger impact on permeability than sand. Developing such a model would be an important future study for improving understanding and management of spawning habitat. Insights on particle interactions and trapping mechanisms gained in Chapter 2 will be useful contributions to future study of silt and clay in sand seals.

Salmon spawn in areas of the river with three-dimensional flow patterns that drive flow into the nest; this effect is enhanced by the structure of the redd. Field studies have found significant spatial variability in the depth, mass deposited, and grain size distribution of infiltrated fines; this has been attributed to advection into and out of the streambed, spatial variability in sediment supply, cross-stream flows, and spatial variability in carrying capacity [1, 2, 28, 45]. Quantitative understanding of sand seals is based on uniform-flow, plane-bed experiments. Bed permeability in salmon nests may be very different than predicted from existing infiltration models, and a flushing flow may not have the desired effect on improving redd permeability. The spatial variability of sand infiltration is explored in Chapter 3, which reports on a sand infiltration experiment into a gravel riverbed with alternate bar topography.

The structure of sand seals is important for designing the depth of flushing, but to predict the duration of a flushing flow it's necessary to understand how fast silt and clay will be entrained. There is no model for silt and clay entrainment from the riverbed subsurface as the bed is being mobilized. The reach-averaged removal rate of silt and clay from a riverbed can be estimated for certain rivers with the right set of circumstances. These include the existence of dams that release large flushing flows or flood-control flows, high-frequency suspended sediment transport monitoring at multiple locations downstream of the release point, and a sufficient suspended sediment supply to quantify a downstream difference in sediment transport. An example of this analysis is given for the Russian River in California. This analysis can be used to improve management of flushing flows on the Russian River and the technique can be transferred to other river systems.

This dissertation adds to knowledge that can be used to determine if, when, and how flushing flows should be released for the purpose of spawning habitat maintenance. It can also inform design of flood-control releases to minimize negative impacts on aquatic habitat.

The studies may also have useful insights into management of contaminated sediment, non-flushing regulated flows, streambed pumping, and remote monitoring of fluvial suspended sediment dynamics.

Chapter 2

Modeling sand infiltration into gravel riverbeds

2.1 Overview

This chapter concerns vertical sand infiltration into a stable, plane-bed gravel river bed. A brief overview of earlier studies is given, including field observations, the effects of sand infiltration on salmonids, and a general description of a steady-state sand deposit. A recent model for the sand fraction as a function of depth by Wooster et al. [88] is introduced. The Wooster model is compared against data and improved models for the steady-state sand deposit are developed from an expanded dataset.

The process of infiltration is modeled with a filtration model that includes a trapping coefficient β. By assuming that β is constant until the riverbed is clogged with infiltrated sand, an expression is derived for the steady-state sand fraction as a function of depth. In this steady-state deposit the sand fraction F decays exponentially with depth from a maximum value F_o. Wooster et al. [88] developed empirical expressions for the coefficients F_o and β as functions of the grain size distributions of gravel and sand.

Data from infiltration experiments by Wooster et al. [88] and Gibson et al. [31] are analyzed to determine if infiltration sand deposits can be adequately represented by an exponential model such as the Wooster model. Regression analysis shows that an exponential model performs adequately for most of the experimental conditions studied. Alternate empirical expressions for the coefficients F_o and β as functions of the sediment grain size distributions are developed.

Data from Gibson et al. [31] and results from earlier studies demonstrate that flow conditions affect infiltration. An explicit model for subsurface flow near the sediment-water interface is developed in order to quantify the relationships between flow and infiltration. Further regression analysis is used to relate F_o and β to subsurface velocities.

Close examination of the Wooster et al. [88] and Gibson et al. [31] data suggest that the trapping coefficient β is not constant. The trapping coefficient generally decreases with depth in the bed. This corresponds to the situation in which deposited sand fills the pore throats and increases trapping efficiency. An expression for β that increases linearly with sand fraction is presented and an expression for the steady-state sand fraction $F(z)$ is developed that corresponds to this linearly-varying model.

Deep in the riverbed where the sand fraction is very small, the Gibson et al. [31] data indicate that β decreases as the sand fraction increases. It is proposed that this is due to sand piling on top of gravel grains. These piles are able to capture less and less sand as the piles grow, corresponding to lower trapping efficiency. A theoretical model is proposed to represent this mechanism. This model is implemented numerically with the variable-β throat-trapping model to predict steady-state values of $F(z)$.

The new constant-trapping model generally performs better than the Wooster model. The variable-β models are able to match trends seen in the Gibson et al. [31] data better than the constant-trapping models.

2.2 Background

Sedimentation of gravel riverbeds by sand, silt and clay is one of the most common forms of river pollution in the Western United States [49]. This fine sediment reduces the permeability of the hyporheic zone, reducing survival of salmonid eggs to suffocate [43, 10]. Riverbed fine sediments can also limit the ability of fish fry and macroinvertebrates to find refuge from predators and high flows; reduce the output from streambank pumping operations; and impede important hydrological, chemical, and biological exchange processes between the river and the riverbed [71, 10, 43, 48, 6]. Fine sediment storage can also be problematic if the fines have been contaminated by heavy metals.

Salmonids build nests by stirring up the gravel with their bodies. The exposed fine sediments in the riverbed are entrained by the flow and carried downstream. During the first stormflow large enough to mobilize sand, this sand will infiltrate the bed and be trapped in the upper pore spaces. This creates a sand seal, which stops further sand infiltration but which subsequently traps silt and clay, further reducing the permeability. Sand seals are pervasive in nature; they have been found in almost all of the bed samples collected in field studies of infiltration e.g. [28, 1, 8, 45]. Sand seals have been studied for decades, but there are gaps in knowledge concerning the sand content as a function of depth and the mechanisms that determine this function. This lack of knowledge makes it difficult to predict the permeability of salmon nests. In chapter 3, bed permeability is calculated according to three different descriptions of the sand seal taken from the literature. The calculated bed permeabilities vary by 63%.

The size of fine particles relative to bed particles determines the depth of fines infiltration. Most infiltration studies in river science have used the ratio of the geometric mean or median diameters of gravel and fine sediment to represent this effect e.g. [88, 17, 5]. These ratios are denoted D_g/d_g and D_{50}/d_{50} respectively, where D is the diameter of bed gravel, d is the diameter of fine particles, the subscript g indicates the geometric mean, and D_X (or d_X) is the diameter of a particle larger than the smallest $X\%$ of the grain size distribution. For coarse fines where D_{50}/d_{50} is much less than 10, fines do not infiltrate the bed because they cannot pass through the pores on the bed surface. For moderate sediment where D_{50}/d_{50} is between 10 and 30, fine sediment remains in the upper pore spaces and creates a sand seal [17, 5]. If $30 < D_{50}/d_{50} < 70$, some material is trapped in the upper pore spaces but there is no clearly defined sand seal. When the ratio D_{50}/d_{50} is greater than 70, all fine sediment will settle to the bottom of the gravel column [19]. For most grain size distributions the ratios D_g/d_g and D_{50}/d_{50} are similar; they are often used interchangeably.

Gibson et al. [31, 32] found that the grain ratio D_{15}/d_{85} better represents the behavior of infiltration. This ratio is borrowed from the field of geotechnical engineering, where it is used to determine the effectiveness of geofilters. It reflects the fact that the smallest gravel particles determine the pore throat sizes and the largest fine particles are responsible for blocking the pore throats. Sherard [74] found that performance of gravel filters changes dramatically within a narrow range of D_{15}/d_{85}. If D_{15}/d_{85} is less than 8, the largest sand grains block the uppermost pore throats of the gravel column and most of the sand is unable to enter the filter; if $D_{15}/d_{85} > 10$, some sand particles pass through the gravel column [74].

If a sand seal is created, its physical structure is predictable. Once the sand supply is cut off, fines are winnowed from the bed surface down to a depth of $D_g - 2D_g$ [17, 5]. The sand seal starts at the bottom of the winnowed layer and extends downwards a distance of 2.5 to 5 times the gravel D_{90} [45, 17, 5]. In infiltration studies where the bed was excavated below the sand seal, a small amount of sand was found at moderate depths and a significant mass was found on the flume bottom or the bottom of a sample bucket [31, 45]. In studies where the entire sand seal ($2.5D_{90}$-$5D_{90}$ thick) was collected in a single bulk sample, the mean sand fraction was 5-8% of total bed volume [5, 17].

Cui et al. [14] proposed a theoretical model in which the sand content in a sand seal decreases exponentially with depth in the bed. In two recent sand infiltration studies by Wooster et al. [88] and Gibson et al. [31], the sand seal was sampled in a series of thin horizontal layers, which allows quantification of the sand fraction as a function of depth. Assuming that the sand fraction decreases exponentially, Wooster et al. [88] used their data to build a model for this decay. In this chapter, the general Cui et al. [14] model and the empirical Wooster et al. [88] model are introduced. Data from Wooster et al. [88] and Gibson et al. [31] are used to test the Wooster model and the hypothesis that the sand fraction decays exponentially with depth. The data are then used to develop new models for the sand fraction as a function of depth.

2.2.1 The definition of the sand fraction

There are two definitions of the sand fraction; this dissertation uses a definition given by Cui et al. [14]. the sand fraction F is defined as the volume of sand as a fraction of bed volume

$(F = V_{sand}/(V_{sand} + V_{gravel} + V_{porespace}))$. F is referred to as the specific deposit in the water filtration literature.

Most infiltration studies in river science have used a different definition of the sand fraction. This second definition is denoted with the lowercase f as in Cui et al. [14]. f is defined in other studies as the volume or mass of sand as a fraction of all sediment. In this study it is assumed to be the volumetric fraction $(f = V_{sand}/(V_{sand} + V_{gravel}))$. A transformation between f and F is needed in order to compare results and model predictions from various studies. There is a simple transformation if the porosity of a clean gravel bed ϕ_{gr} is known [14]:

$$F = \frac{f(1-\phi_{gr})}{1-f}, \qquad \text{and} \tag{2.1a}$$

$$f = \frac{F}{(1-\phi_{gr}+F)}. \tag{2.1b}$$

If the grain size distribution (GSD) is known, the porosity can be calculated using an empirical relationship from Wooster et al. [88] between porosity and the geometric standard deviation of the GSD (σ). This relationship was built from unimodal sediment mixtures with σ ranging from 1.2 to 3 and particle diameter ranging from 0.075mm to 22mm:

$$\phi = 0.621\sigma^{-0.659} \tag{2.2}$$

The sediments discussed in this chapter fall within the range of sediments used to develop (3.9) in terms of both σ and diameter. Thus, equation 3.9 is used to determine the porosities for both gravel (ϕ_{gr}) and sand (ϕ_s).

2.2.2 Derivation of the exponential Cui model

Until recently, there was no numerical model to predict how F varies depth in the bed. Cui et al. [14] developed a theoretical model for $F(z)$ by adopting a filtration relationship proposed by Sakthivadivel and Einstein [70] for the settling of sand through a riverbed:

$$\frac{\partial q_s}{\partial z} = -\frac{\beta}{D_g} q_s, \tag{2.3}$$

where q_s is the vertical sand flux (units of l/t), z is distance downwards into the streambed (l), and β is the trapping coefficient (-). The geometric mean gravel diameter D_g is included to normalize depth. Sand deposition is related to transport using a mass balance:

$$\frac{\partial F}{\partial t} = -\frac{\partial q_s}{\partial z}. \tag{2.4}$$

Together, (2.3) and (2.4) imply that:

$$\frac{\partial F}{\partial t} = \frac{\beta}{D_g} q_s. \tag{2.5}$$

Cui et al. [14] proposed the following boundary conditions to be consistent with infiltration of a clean gravel bed with constant influx q_o that stops at a time t_{clog} when the sand fraction reaches a maximum possible value F_o:

$$F(t=0, z>0) = 0 \tag{2.6a}$$

$$q_s(t=0, z>0) = 0 \tag{2.6b}$$

$$q_s(t>0, z=0) = \begin{cases} q_o & F(z=0) < F_o, \\ 0 & F(z=0) = F_o. \end{cases} \tag{2.6c}$$

Cui et al. [14] states that the only analytical solution to equations (2.3)-(2.6) is the case where β is constant, in which case $F(z)$ decreases exponentially with depth. This derivation of is not given in Cui et al. [14]. The following derivation was developed in this study.

If β is constant and the boundary conditions in (2.6) hold, then $F(z,t)$ is determined by integrating (2.5):

$$F(z,t) = \int_0^F dF' = \frac{\beta}{D_g}\int_0^t q_s(z,t')\partial t', \tag{2.7}$$

where the apostrophe on F' (t') indicates the integration variable corresponding to F (t). The total flux past any depth z before time t_{clog} is equal to the total flux into the bed minus the sand deposited between the depths of 0 and z. This is represented by rewriting the right side of (2.7):

$$\frac{\beta}{D_g}\int_0^{t_{clog}} q_s(z,t')\partial t' = \frac{\beta}{D_g}\int_0^{t_{clog}} q_s(z{=}0,t')\partial t' - \frac{\beta}{D_g}\int_0^{z} F(z',t_{clog})\partial z'. \tag{2.8}$$

By definition, the first term on the right size of (2.8) equals F_o. Equating the left side of (2.7) with the right side of (2.8) yields:

$$F(z,t_{clog}) = F_o - \frac{\beta}{D_g}\int_0^{z} F(z',t_{clog})\partial z'. \tag{2.9}$$

Taking the derivative of (2.9) with respect to z:

$$\frac{\partial F(z,t_{clog})}{\partial z} = -\frac{\beta}{D_g}F(z,t_{clog}), \qquad \text{and therefore} \tag{2.10}$$

$$F(z,t_{clog}) = F_o e^{-\beta z/D_g}. \tag{2.11}$$

When looking at an infiltration sand deposit, it is assumed that infiltration has come to completion and so $F(z) = F(z,t_{clog})$. For the remainder of this dissertation $F(z,t_{clog})$ is written as $F(z)$ for simplicity. In derivations where the time variable is required it is included explicity.

2.2.3 The empirical Wooster model

The model in Wooster et al. [88] is based on the theoretical model by Cui et al. [14] and assumes a constant trapping coefficient. There are two minor differences between the Wooster model and equation (4.4). The sand profile is offset a distance of $2D_g$ downwards to account for winnowing. In addition, the model uses the alternate definition of the sand fraction ($f = V_{sand}/(V_{sand} + V_{gravel})$):

$$f(z) = f_{o,w} e^{-\beta_w \left(\frac{z}{D_g} - 2\right)}, \tag{2.12}$$

where the subscript w denotes the Wooster model. (2.12) is only valid at depths greater than $2D_g$.

In order to develop empirical expressions for $f_{o,w}$ and β_w, Wooster et al. [88] performed a set of plane-bed sand infiltration experiments into nine different gravel beds under uniform flow. The gravel mixtures in the beds covered a range of D_{50}/d_{50} from 15 to 50 (D_{15}/d_{85} from 6 to 32) (Table 2.1). Regression analysis was used to develop empirical models of $f_{o,w}$ and β_w as functions of the gravel and sand GSD:

$$f_{o,w} = \frac{(1-\phi_s)\phi_{gr}}{1-\phi_s\phi_{gr}} \left[1 - exp\left(-0.0146\frac{D_g}{d_g} + 0.0117\right)\right] \tag{2.13a}$$

$$\beta_w = 0.0233\sigma_{gr}^{1.95} \left[\ln\left(\frac{D_g\sigma_{gr}}{d_g}\right) - 2.44\right], \tag{2.13b}$$

where ϕ_s is the porosity of sand and σ_{gr} is the geometric standard deviation of the gravel grain size distribution (dimensionless). The subscripts gr and s denote gravel and sand while the subscript g denotes geometric mean. The model uses a five empirical coefficients.

In order to test Wooster model performance against data, predicted values of $f(z)$ are transformed into $F(z)$ using equation (3.1).

The new models must also be comparable to the Wooster model. To do this, I adopt the Wooster assumption that sand is winnowed to a depth of $2D_g$. If β is constant, $F(z)$ decays exponentially with depth, and the following will be used to model $F(z)$:

$$F(z) = F_o e^{-\beta(z/D_g - 2)}. \tag{2.14}$$

2.2.4 The effect of flow on infiltration

The relationship between flow conditions and infiltration is uncertain. In flume experiments, infiltration has been positively correlated to shear stress [5, 17]. In field studies, Frostick et al. [28] found that infiltration was high in areas of high velocity and in contrast Carling and McCahon [8] found high infiltration in areas of slack water. Sear et al. [72] found that infiltration of suspended sediment was negatively correlated to shear stress but that infiltration from bedload was unrelated to shear stress. Gibson et al. [31] performed duplicate sand infiltration experiments with and without water flowing using the same sediment mixtures. Significantly less sand infiltrated in the no-flow experiments than in the experiments with flow using the same sediment.

The Wooster model does not address flow because discharge was held constant for all experiments. By including the Gibson et al. [31] flow and no-flow experiments, a small range of flow conditions is represented in infiltration data. In this chapter, these data are used to incorporate flow into a model for $F(z)$. Because infiltration is a subsurface process, the analysis focuses on subsurface flow. In order to accomplish this, an explicit model for flow in the upper pore spaces is developed.

2.3 Analysis of experimental sand seal data

In this section, the experiments of Wooster et al. [88] and Gibson et al. [31] are reviewed. The results of each experiment are analyzed to determine how well the sand deposit is represented by an exponential model. Assuming that $F(z)$ is represented by (2.14), the coefficients F_o and β are estimated from the data and compared against predictions of the Wooster model. The validity of assuming that β is constant is explored by comparing values of β estimated at different depths.

2.3.1 Summary of experimental conditions

In both the Wooster et al. [88] and Gibson et al. [31] experiments, sand was infiltrated into an immobile gravel bed in a flume. Sand was fed at the entrance and moved along the flume as bedload until it had been transported over the sampling areas. At this point, Gibson et al. [31] immediately cut off the flow. Wooster et al. [88] kept water flowing at the same discharge until all surface fines had been washed away. Afterwards, the flume beds were sampled in a number of locations.

The larger dataset collected by Wooster et al. [88] includes infiltration of one unimodal sand mixture into nine different gravel mixtures at three different feed rates. The bed was sampled in circular pits 12cm in diameter; each pit was excavated in 1-4 horizontal layers. The sand seals built in the low and medium feed rate experiments were similar, while significantly less sand infiltrated at the high feed rate. The Wooster et al. [88] model was built from only the low- and medium-feed data. Similarly, only the low- and medium-feed data are used to develop new models for $F(z)$ in this chapter. Wooster et al. [88] refers to the nine different sediment mixture as Zones 1-9; Zone 10 is a duplicate of Zone 1. In this chapter the notation is changed so that experiment $W1$ corresponds to Zone 1 in Wooster et al. [88], $W2$ to Zone 2, and so on. Experimental conditions are summarized in table 2.1.

The Gibson et al. [31] experiments included infiltration of two different sands into one gravel mixture (G1 and G2 in table 2.1). Gibson et al. [31] performed an additional set of experiments with the same sediments but without water flowing. In the no-flow experiments sand was dropped through the water from above rather than fed through a flume. These experiments are denoted G1nf and G2nf (table 2.1). Samples were collected in 10cm diameter canisters that had been filled with gravel and buried in the bed prior to infiltration. Samples were excavated in 8-10 horizontal layers that extended from the sediment-water interface down to the solid bottom of the canister. The sediment used by Gibson et al. [31] falls within the range of sediment used to develop the Wooster model in terms of D_{50}/d_{50}, D_{15}/d_{85}, and gravel size, and the sands were close in diameter.

The results of the two Gibson et al. [31] medium-sand experiments G1 and G1nf are given in Figure 2.1 as an example of an infiltration experiment. The data represent the four sample pits from G1 (black x's) and the single sample pit from G1nf (green squares). $F(z)$ decreases quickly with depth below the surface, although some sand passes more than 10 gravel diameters and settles onto the flume bottom. There is significantly less sand at depth in the sample pit from the no-flow experiment than in the 4 sample pits from the flow experiment. There are horizontal error bars around the G1nf data. The width of these error bars is the standard deviation of data from the G1 data, which has been binned by depth. The error bars are included to suggest the range of uncertainty in the measurements from G1nf.

The measurements from one of the Wooster et al. [88] experiments, W2, is given in figure 2.2 for comparison. This figure includes data from all three feed rates; it is clear that less sand infiltrates at the highest feed rate. Also notable is the large scatter in $F(z)$ compared to Gibson et al. [31]. One possible reason for this difference is the lack of gravel larger than 13mm in the Gibson et al. [31] riverbed. The random inclusion of a single piece of large gravel in a sample changes the GSD, especially for a small sample like a single layer in a sample pit. Another possibility is due to the Gibson sampling canisters; canister diameter was less than 10 times the gravel D_{85}. The canister could limit the possible packing configurations of gravel particles, essentially limiting the variability of pore shapes and sizes in the sample. Whatever the cause of the reduced scatter, the trend in $F(z)$ is much clearer in the Gibson et al. [31] data.

2.3.2 Does an exponential function represent $F(z)$?

In Figures 2.3 and 2.4, data from all of the Wooster et al. [88] and Gibson et al. [31] experiments are shown. The logarithm of F is plotted against depth, which is normalized by the gravel diameter. If equation (2.14) is representative of an infiltration sand deposit, then there should be a linear relationship between $\ln(F)$ and z/D_g:

$$\ln(F) - \ln(F_o) = -\beta \frac{z}{D_g} + 2. \tag{2.15}$$

Linear regression is performed on the data from each of the experiments to test (2.15). The fitted relationships are shown by solid black lines in Figures 2.3 and 2.4. F_o is the predicted value of F at $2D_g$. If the axes of a plot were rotated, the slope of the black line would be β.

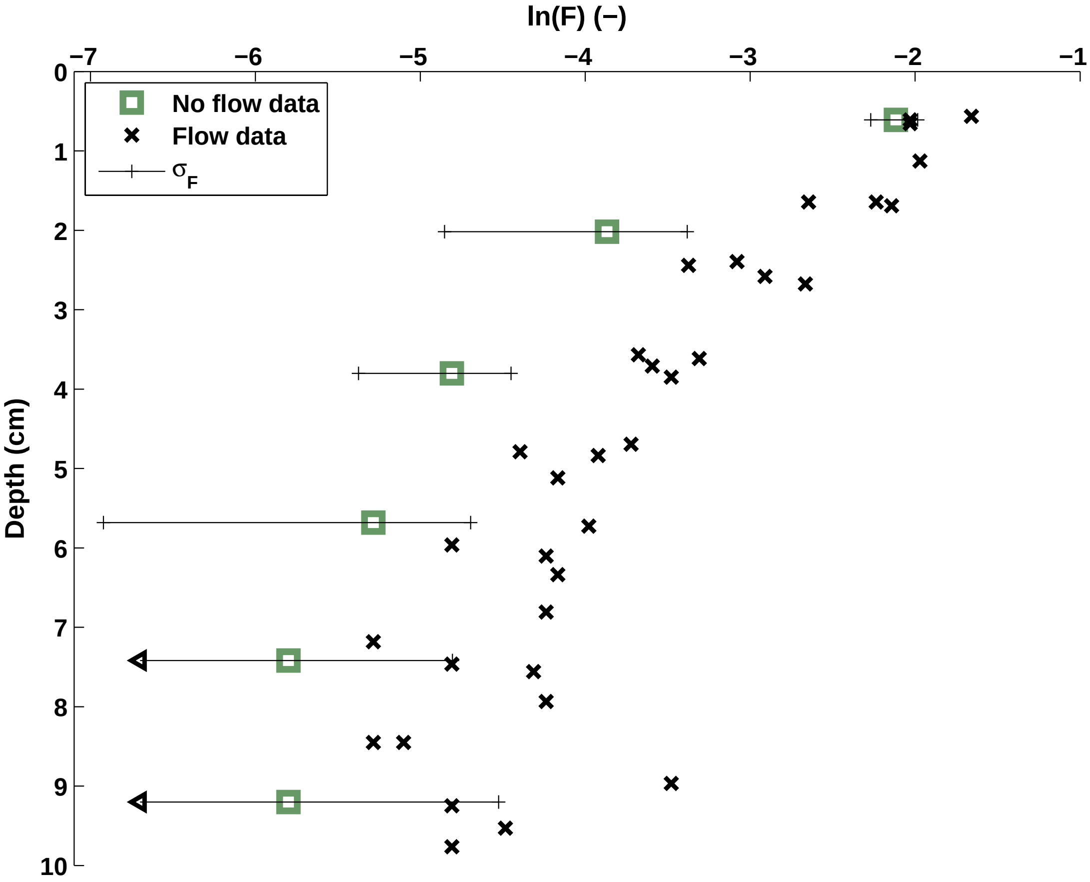

Figure 2.1: Measured subsurface sand fraction in experiments G1 (black x's) and G1nf (green squares). The error bars represent the standard deviation of the flow experiments, but are placed around the no-flow data to represent expected variability. The left arrows near the bottom show where one standard deviation below the measurement is negative. (-) signals that the term is dimensionless.

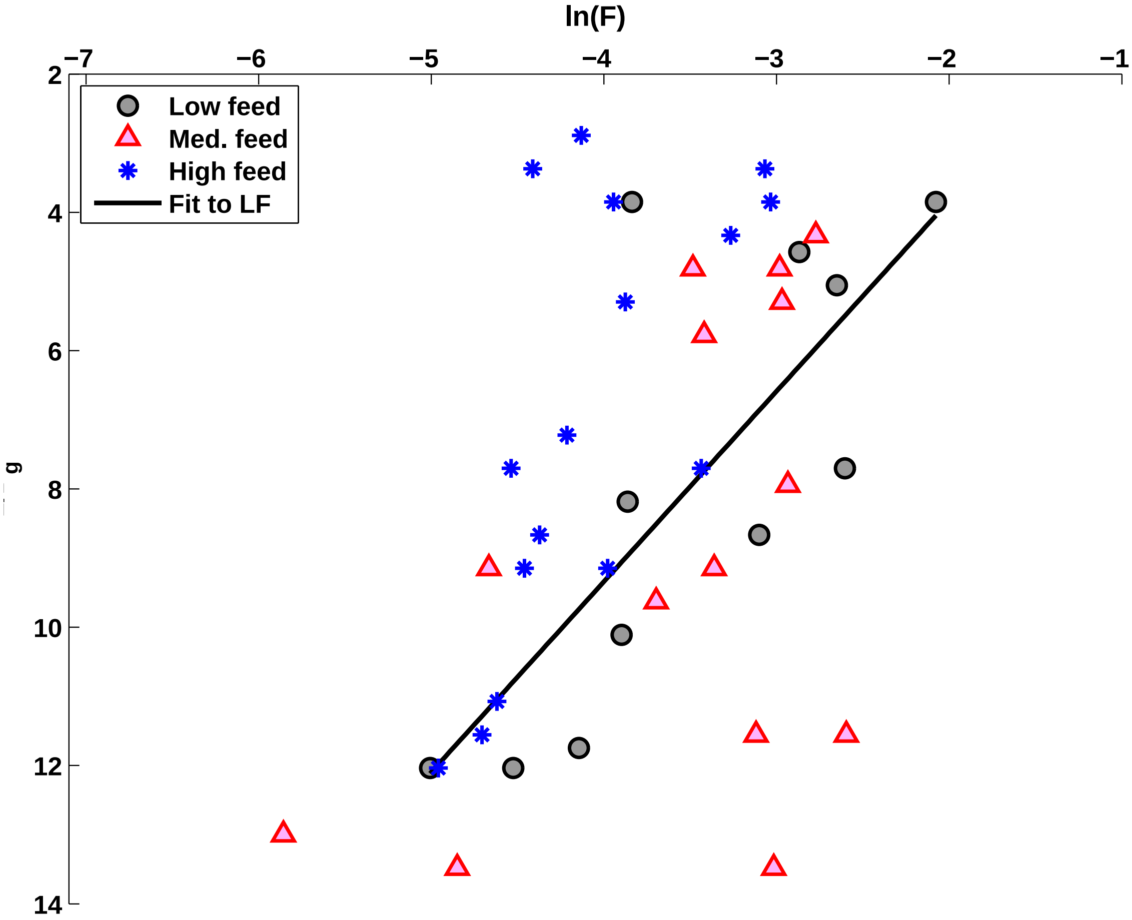

Figure 2.2: The results of experiment W2, with results separated by feed rate. The black line is a fit to the low-feed data.

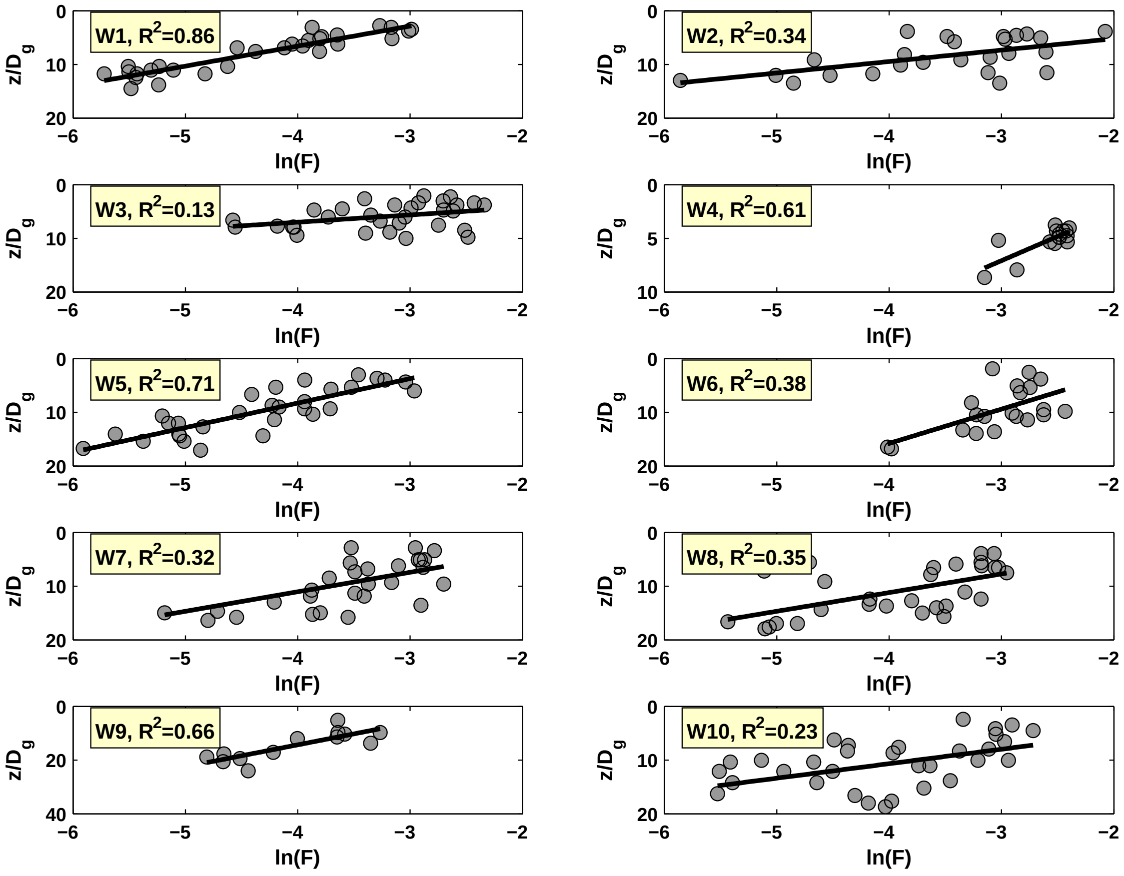

Figure 2.3: Sand fraction as a function of depth for the Wooster experiments. Data shown are from the low-feed and medium-feed experiments. Depth is normalized by the geometric mean gravel grain diameter. The lines shown are the predictions of linear regression for the data.

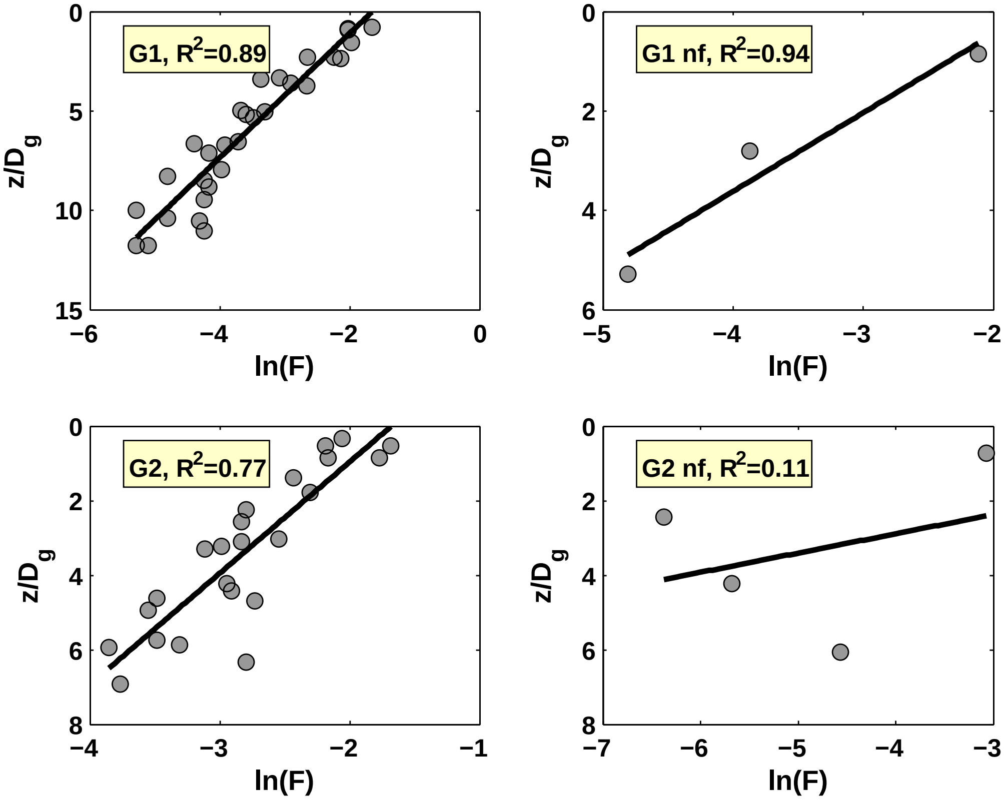

Figure 2.4: Sand fraction as a function of depth for the Gibson experiments. $G1$ is the medium-sand experiment, $G2$ is the fine-sand experiment, and nf indicates the no-flow experiments. Data do not include the bottom layers from the sample pits, as these contained sand collected on the flume bottom. Depth is normalized by the geometric mean gravel grain diameter. The lines shown are the predictions of linear regression for the data.

Study	Expt.	d_{50} (mm)	d_{85} (mm)	D_{50} (mm)	D_{15} (mm)	σ_g (-)	u_* (cm/s)	WSS	Feed rate (kg/min/m)
Wooster	W1 & W10	0.35	0.43	9.2	3.4	1.65	4	0.0014	0.24, 2.4, and 24
	W2			12.9	5.3	1.56			
	W3			15.6	8.1	1.37			
	W4			17.2	13.7	1.17			
	W5			10.6	3.4	1.85			
	W6			7.9	6.1	1.23			
	W7			12.1	4.9	1.62			
	W8			8.4	4.9	1.43			
	W9			5.3	2.5	1.70			
Gibson	G1	0.4	0.78	7.6	5.05	1.42	5	0.002	8.1
Gibson	G1 nf	0.4	0.78	7.6	5.05	1.42	0	0	8.1
Gibson	G2	0.22	0.47	7.6	5.05	1.42	5	0.002	7.7
Gibson	G2, nf	0.22	0.47	7.6	5.05	1.42	0	0	7.7

Table 2.1: Data used in this study. d is the sand diameter, D is the gravel diameter, u_* is the shear velocity, 'nf' indicates no flow, and WSS is the water surface slope.

An exponential model works better for some of the Wooster and Gibson experiments than for others, which is clear from visual analysis of Figures 2.3 and 2.4. The linear regressions fit the data well for W1, W2, W5, W9, G1, G1nf, and G2. In other cases, the fit matches the general trend of the data but the scatter in the data makes it difficult to determine β with certainty (W7, W8, and W10). This uncertainty is seen by comparing W1 and W10, which have the same experimental conditions and very different estimated values of β. Nevertheless, it appears that an exponential model is sufficient for predicting the general shape of $F(z)$ for these experiments.

For the experiments W3, W4, W6, and G2nf, it is not clear that an exponential model works well. The regressions shown are largely due to a few outliers, and they do not represent a pattern in most of the data. It is worth noting that experiments W3, W4, and W6 had the three coarsest riverbeds in terms of the ratio D_{15}/d_{85} for all experiments. Due to the large scatter and limited data of experiment G2nf, it is excluded from further analysis.

2.3.3 Calculating β and F_o from the data

Since an exponential model matches observed patterns in $F(z)$, the data can be used to calculate a constant trapping coefficient β and a maximum sand fraction F_o. There are at least three ways to calculate β and F_o. Each method is prone to different sources of uncertainty. In this section, β and F_o are calculated for each experiment. The median calculated values are taken to be the true values and are used to develop empirical models for β and F_o.

In Figures 2.3 and 2.4, β and F_o were calculated using linear regression through all data for each experiment. The coefficients and the R^2 values from these linear regressions are given in columns (1)-(3) of Table 2.2.

Scatter in the some of the datasets leads to uncertainty in the estimates of F_o and β Table 2.2 (e.g. W2, for which $R^2 = 0.34$.) Some of this scatter is due to variations in the gravel GSD of individual layers of sample pits can affect the estimate of β in column (2) of table 2.2. For instance, if the upper layer of a sample pit has very small pores for the gravel mixture, little sand will pass through and all of the lower layers will appear as outliers in Figure 2.4. Values of β and F_o for this sample pit may be far from the experimental average. The second method for estimating β and F_o avoids these outliers by performing regression on $\ln(F)$ vs. z/D_g for each sample pit separately, discarding the highest and lowest estimates, and taking the average of the remaining values for each experiment. The resulting values are given in columns (4) and (5) of table 2.2. The correlation coefficient between the measured data and the predictions of (2.14) using these values is given in column (6). The values of β are similar to the estimates taken from the first method (column (2)). However, the estimates for Zones 1 and 10 are much closer, suggesting that this is a better method for estimating β.

A third method of calculating β is to compare F between layers in a given sample pit. To do so, (2.14) is evaluated at the depths of z_1 and z_2. These expressions are divided to get rid of F_o:

$$\frac{F(z_1)}{F(z_1)} = \frac{F_o e^{-\beta\left(\frac{z_1}{D_g}-2\right)}}{F_o e^{-\beta\left(\frac{z_2}{D_g}-2\right)}} = e^{\beta(z_2 - z_1)}, \qquad \text{and so} \tag{2.16}$$

$$\beta = \frac{ln(F(z_1)/F(z_2))}{z_2 - z_1}. \tag{2.17}$$

Values of β were calculated using (2.17) data from all of the Wooster and Gibson experiments. Pairs of $F(z)$ values were limited to data taken from individual sample pits and from sample layers at least two centimeters apart. The exclusion of adjacent layers was done to limit the scatter, as small variations in $ln(F(z_1)/F(z_2))$ will lead to large variations in β if $z_1 - z_2$ is small. This excludes all sample pits with only one or two sample layers, including all of experiment W4. The lowest and highest estimates of β for each experiment were discarded and the remaining values were averaged. For experiments W6 and W9 there were only 2 and 1 estimates of β, and so nothing was discarded. The resulting estimates of β are listed in column (8) of table 2.2.

The values of F_o presented in columns (1) and (4) of table 2.2 are calculated by evaluating the functions for $F(z)$ developed by regression analysis at $z = 2D_g$. It is possible to estimate F_o from $F(z)$ in the top layers of the sample pits. Wooster et al. [88] used this approach to develop their model and assumed that F_o was equal to the measured values of F from the top layer in each sample pit. However, some of this data should have been excluded.

Expt.	F_o (1)	β (2)	R^2 (3)	F_o (4)	β (5)	R^2 (6)	F_o (7)	β (8)	F_o (9)	β (10)	$F_{o,w}$ (11)	β_w (12)
W1	5.0	0.23	0.86	5.6	0.25	0.77	3.8	0.24	5.0	0.24	3.8	0.10
W2	8.2	0.16	0.34	7.7	0.14	0.28	8.5	0.18	8.2	0.16	5.6	0.10
W3	5.8	0.09	0.13	8.1	0.16	0.14	6.7	0.28	6.7	0.16	7.0	0.11
W4	11.6	0.13	0.61	13.0	0.17	0.57	-	-	12.3	0.15	10.2	0.05
W5	4.4	0.16	0.71	5.4	0.18	0.62	3.1	0.20	4.4	0.18	3.9	0.11
W6	7.7	0.06	0.38	7.5	0.06	0.22	6.4	0.08	7.5	0.06	4.9	0.03
W7	5.3	0.09	0.32	6.9	0.09	0.29	5.7	0.13	5.7	0.09	4.9	0.09
W8	4.8	0.10	0.35	5.5	0.09	0.36	-	0.15	5.1	0.10	4.5	0.05
W9	4.9	0.08	0.66	7.8	0.11	0.48	-	0.09	6.3	0.09	2.4	0.04
W10	3.8	0.09	0.23	10.2	0.21	0.39	4.5	0.45	4.5	0.21	3.8	0.10
G1	8.8	0.28	0.89	8.4	0.20	0.91	6.5	0.29	8.4	0.28	4.0	0.03
G1 nf	4.9	0.60	0.94	-	-	-	6.7	0.44	4.9	0.52	4.0	0.03
G2	8.6	0.26	0.77	8.5	0.25	0.78	6.7	0.23	8.5	0.25	7.0	0.06
G2, nf	1.0	0.20	0.11	-	-	-	-	-	-	-	7.0	0.06

Table 2.2: Estimated values of F_o and constant β. F_o is given in percentages. '-' indicates insufficient data. Columns (1)-(3) are from regression on data grouped by experiment; (4)-(6) use regression on data grouped by sample pit; (7) is from F in the top layers of sample pits; (8) is calculated using (2.17); (9)-(10) are the best estimates; (11)-(12) are the Wooster model.

Some excavated layers were over $8D_g$ thick; the average value of F within such a layer will be significantly less than F_o if F decays with depth. The top of some sample layers was less than D_g deep; the measured value of F was probably reduced by winnowing.

In this chapter, F_o is assumed to equal the experimental mean of $F(z)$ measured in the upper layers of all sample pits that meet conditions to avoid underestimating F_o. These conditions are that the center of the layer is at a depth between $2D_g$ and $3.5D_g$. If the sand fraction in the upper layer was less than the sand fraction in lower layer of the same pit, this was taken as evidence of winnowing and the sample was excluded. For some of the experiments there were no sample layers matching these conditions. The calculated values of F_o are given in column (7) of table 2.2.

The three sets of estimates for β and F_o given in columns (1)-(2), (4)-(5), and (7)-(8) of table 2.2 are similar. The median values for each coefficient and each experiment are taken as the best estimates. These are given in columns (9) and (10).

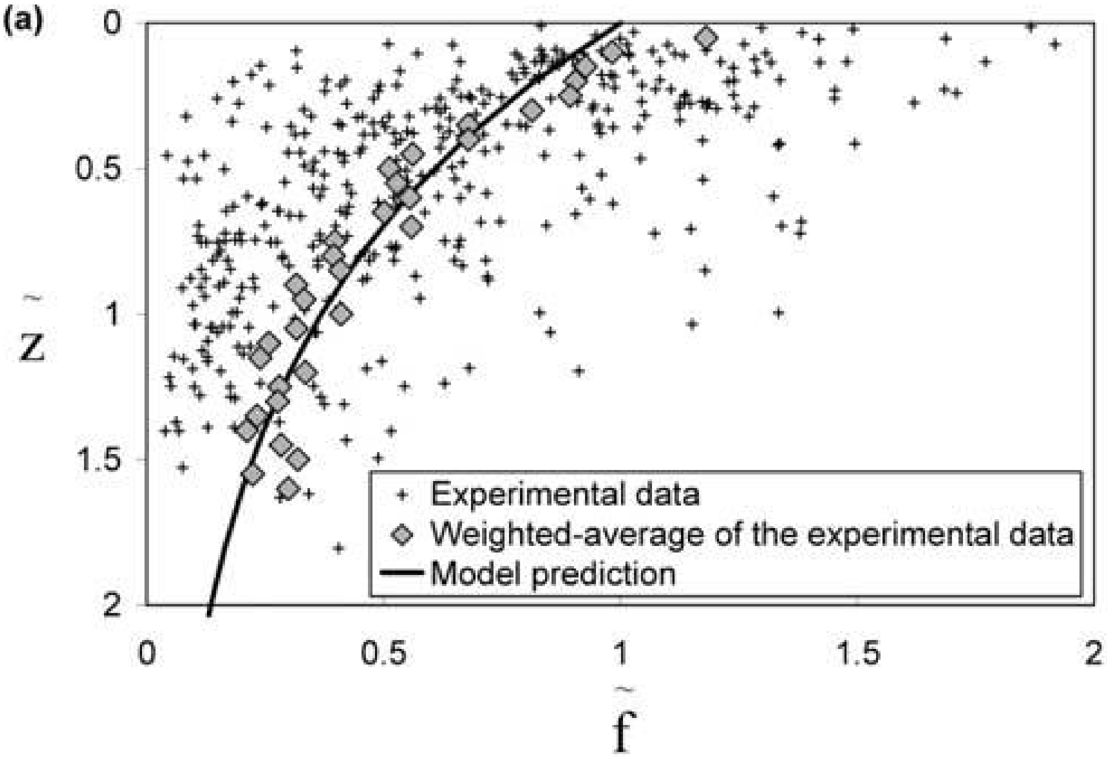

Figure 2.5: Figure 13a from Wooster et al. [88]. This shows the predicted vs. measured values of the sand fraction. Wooster et al. [88] used the tilde to denote nondimensionalization. $\tilde{f} = f/f_o$ and $\tilde{z} = z/D_g$.

2.3.4 Performance of the Wooster model

Some possible problems with the Wooster model are suggested by figures in Wooster et al. [88]. Figure 2.5 is a reproduction of Figure 13(a) from Wooster et al. [88], in which the model is compared against weighted averages of the data. The averages were calculated using an averaging window that moved in z and a weighting factor that favored the closest measurements. The model is close to the weighted averages but underestimates $F(z)$ near the surface. Figure 2.6, which is Figure 7 from Wooster et al. [88], shows the measured and modeled values for $f_{o,w}$ using equation (3.3a). Other than the two coarsest gravel mixtures (W3 and W4) and the finest gravel mixture (W9) are ignored, there is a trend in error between the model and the data. Experiments W3, W4, and W9 probably should have been excluded from the empirical analysis; this will be discussed further during development of the new model. The model overestimates the smallest values of $f_{o,w}$ and underestimates the largest values. Wooster et al. [88] first developed the expression (3.3a) for $f_{o,w}$, and then used it to develop the expression for β_w. Figures 2.5 and 2.6 suggest that (3.3a) does not perform well for typical gravels, which adds error to the expression for β_w (3.3b).

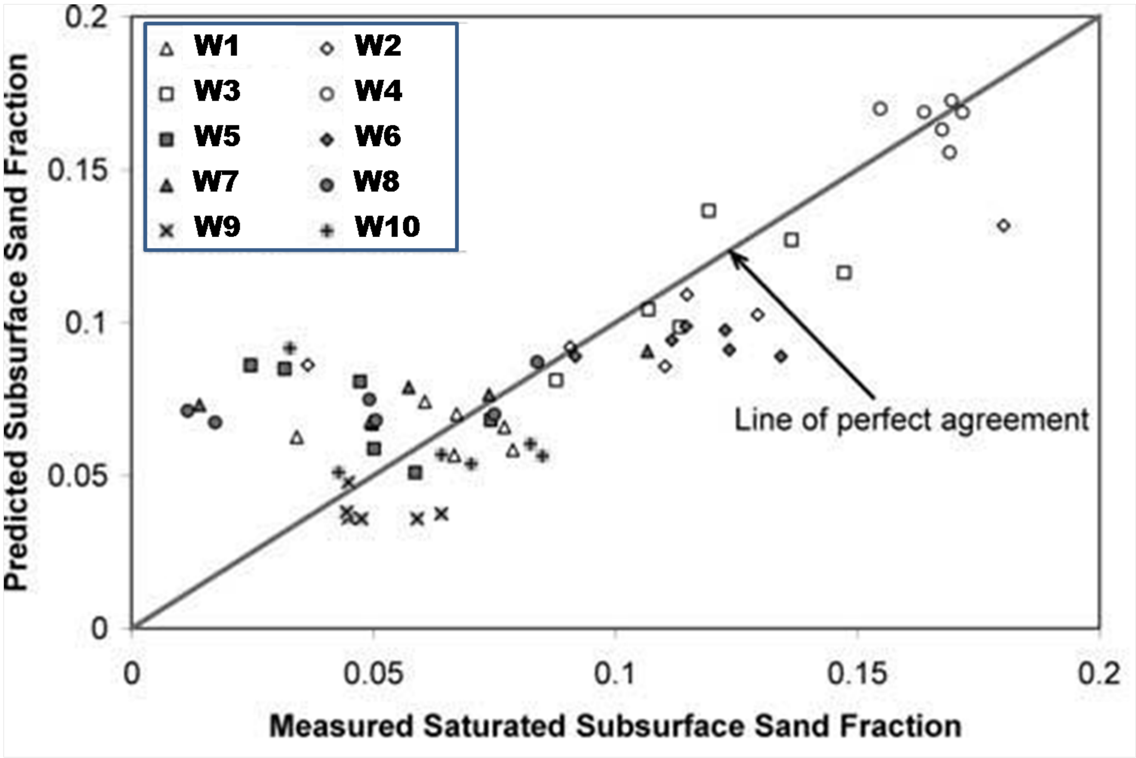

Figure 2.6: Figure 7 from Wooster et al. [88]. The predicted maximum sand fraction vs. the measured value in the top layers of sample pits in the low-feed run. The legend has been altered from the original figure.

Discrepancies between the Wooster model and data can also be seen in Table 2.2. Predicted values of $F_{o,w}$ and β_w are given in columns (11)-(12). The Wooster model tends to underestimate both F_o and β.

In the next section, alternate models will be developed for F_o and β, assuming that β is constant. Before the new models are developed, the data are further analyzed to determine if a constant β is a good assumption.

2.3.5 Evidence that β is not constant

In the previous section it was demonstrated that an exponential model represents the general trend in $F(z)$ for most cases. However, as noted by Cui et al. [14], β should increase as F increases because the trapped sand reduces the pore size and increases trapping efficiency. A close look at the Gibson et al. [31] data suggests that β is not constant. Rather than plotting in a line on the semilog scale in Figure 2.1, the data curve downwards. This behavior suggests that if infiltration is represented by a filtration model with a trapping coefficient β, then β must vary. In this section, the data are analyzed to determine the patterns of this variability.

Earlier, β was estimated by comparing measurements of F at different depths using equation (2.17). These estimates reveal trends in β. However, β was estimated from F and so it is not valid to regress β on F. To make the variables as independent as possible, the estimates of β and measurements of F are binned by depth in increments of D_g. Mean values for each bin are used to develop series of $F(z)$ and $\beta(z)$. These trends are shown in Figure 2.7.

Figure 2.7 shows that β generally increases with F. However, there is significant scatter in the data and so it is difficult to quantify the trend. Furthermore, only a few data points are available at very low F, from experiments G1 and G2. There are no estimates between the deepest two layers in G1 and G2, because the deposited sand on the flume bed would lead to error using equation (2.17).

There is another method to determine β for the Gibson et al. [31] data that includes estimates deeper in the bed and that will smooth over some of the scatter seen in Figure 2.7. The sample pits in the Gibson experiments were excavatd in 8-10 layers. Studying the sand content from the bottom layer upwards in one of these pits is similar to watching the sand seal develop over time in a single layer. Each successive layer upwards can be thought of a filter that has been infiltrated under similar conditions for a longer time. This can be seen by manipulating (2.3) - (2.5).

If β is constant or varies little, it can be estimated by the following equivalence:

$$\beta \approx \frac{\int_0^t \beta q_s \partial t'}{\int_0^t q_s \partial t'}, \tag{2.18}$$

where t' is the dummy variable for time. If the sand fraction is initially 0, the numerator of

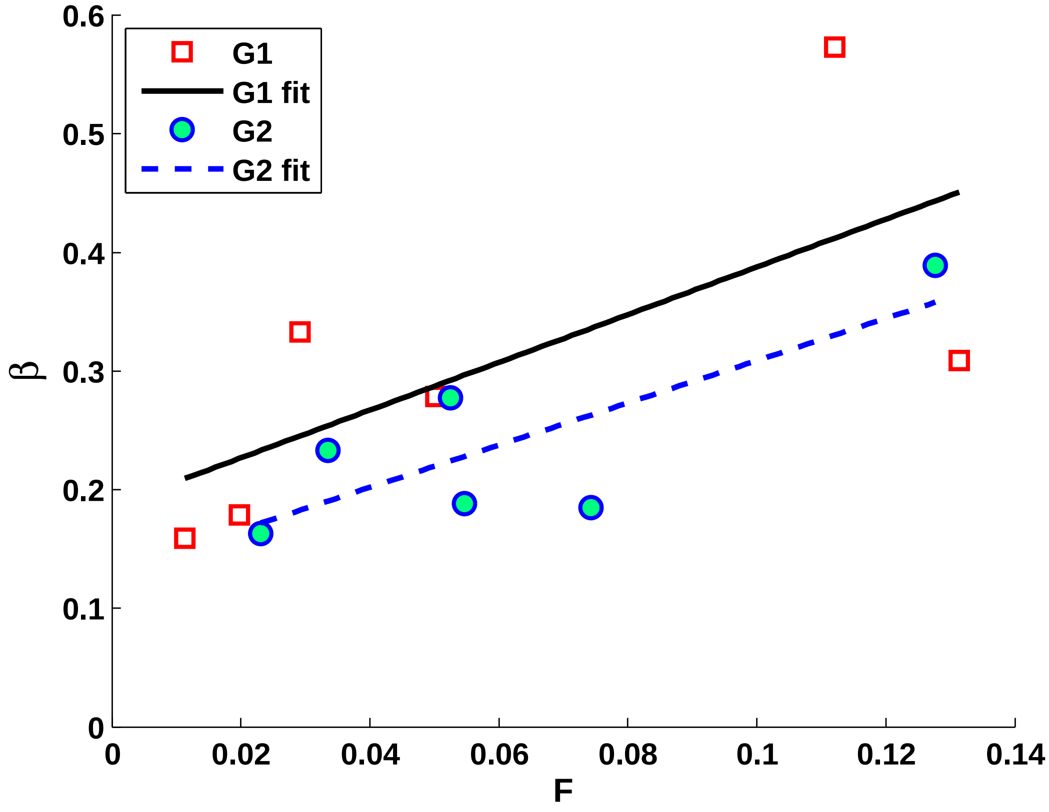

Figure 2.7: Trends in β as a function of F for experiments G1 and G2. β is calculated using equation (2.17). F and β are binned by depth and the median value is taken from each bin, and then the series are equated.

(2.18) is found by integrating (2.5):

$$F(t) = \frac{1}{D_g} \int_0^t \beta q_s \partial t' \tag{2.19}$$

The denominator in (2.18) is the sum of all sand that has passed through a given layer, which has units of depth. By mass conservation, this must equal the integrated volume of sand at or below that layer, $\int_z^\infty F \partial z'$. Thus, (2.18) can be rewritten to estimate $\beta(z)$ from the sand below (z):

$$\beta \approx \frac{\int_0^t \beta q_s \partial t'}{\int_0^t q_s \partial t'} = \frac{D_g F}{\int_z^\infty F \partial z'}. \tag{2.20}$$

It should be noted that if there is a trend in β, that trend will be systematically damped near the surface where F is greatest. This occurs because equation (2.20) integrates over all of the deeper layers and means that the slope of the trend will be underestimated.

β calculated from equation (2.20) is plotted against F for G1 and G2 in Figures 2.8 and 2.9. The figures do not include points for the deepest layer in each pit, where material sits on the flume bottom. All of the sample pits display a variable trend in trapping that looks like a hockey-stick, with β decreasing quickly at low F and then increasing slowly as F increases. An example of this pattern is given in each figure; data points from one sample pit are connected with a solid black line. Data from G1nf are presented alongside G1 in Figure 2.8. This demonstrates that both the average β and the slopes of the trends in β are larger for G1nf than for G1.

The hockey-stick patterns in Figures 2.8 and 2.9 correspond to a high trapping efficiency at low F, a sharp drop at moderate values, and then a slow rise with increasing F. The decrease in β with depth means that trapping is more efficient near the surface. It is clear that the increasing trend between β and F dominates throughout most of the sand seal. The decreasing trend is evident only where F is very small, and it is probably important in the initial stages of infiltration into a clean riverbed.

It is difficult to quantify a trend $\beta(z)$ for the Wooster et al. [88] data. This can be seen by examining Figure 2.2. There are 3 layers from each sample pit and these measurements are clustered at certain depths. The large scatter in $F(z)$ leads to large scatter in estimated $\beta(z)$. This scatter combined with the small range of z represented makes is impossible to find a trend.

2.4 Development of new models

Analyses of the Wooster et al. [88] and Gibson et al. [31] data suggest that the Wooster model underestimates both F_o and β (table 2.2). Although the data are noisy, the Wooster and Gibson data suggest that a constant β model may not fully characterize the sand profile with depth. In the following sections, new models for the steady-state sand fraction as a

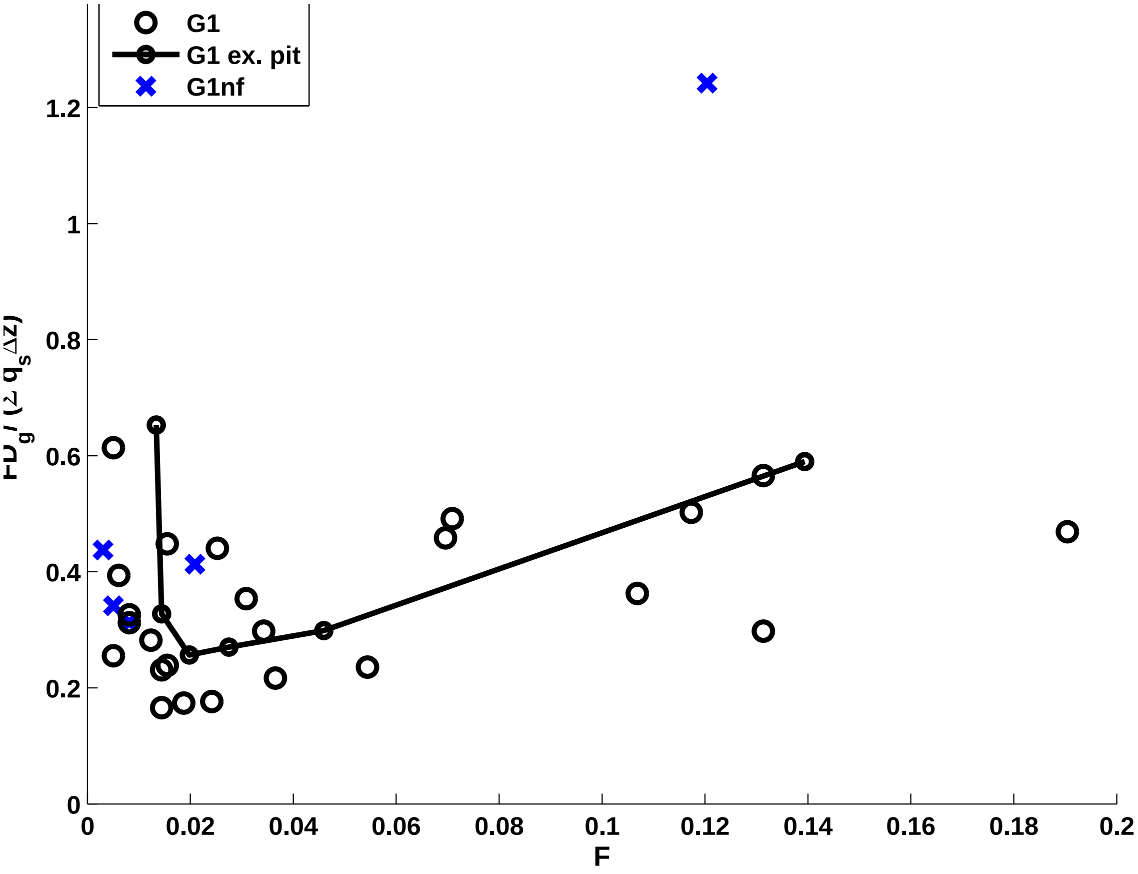

Figure 2.8: The ratio of sand trapped in a given layer to the total amount of sand passing through that layer, from experiments G1 and G1nf. The dashed black line connects the data points from a G1 sample pit to show the hockey-stick pattern; a similar pattern is seen for each sample pit.

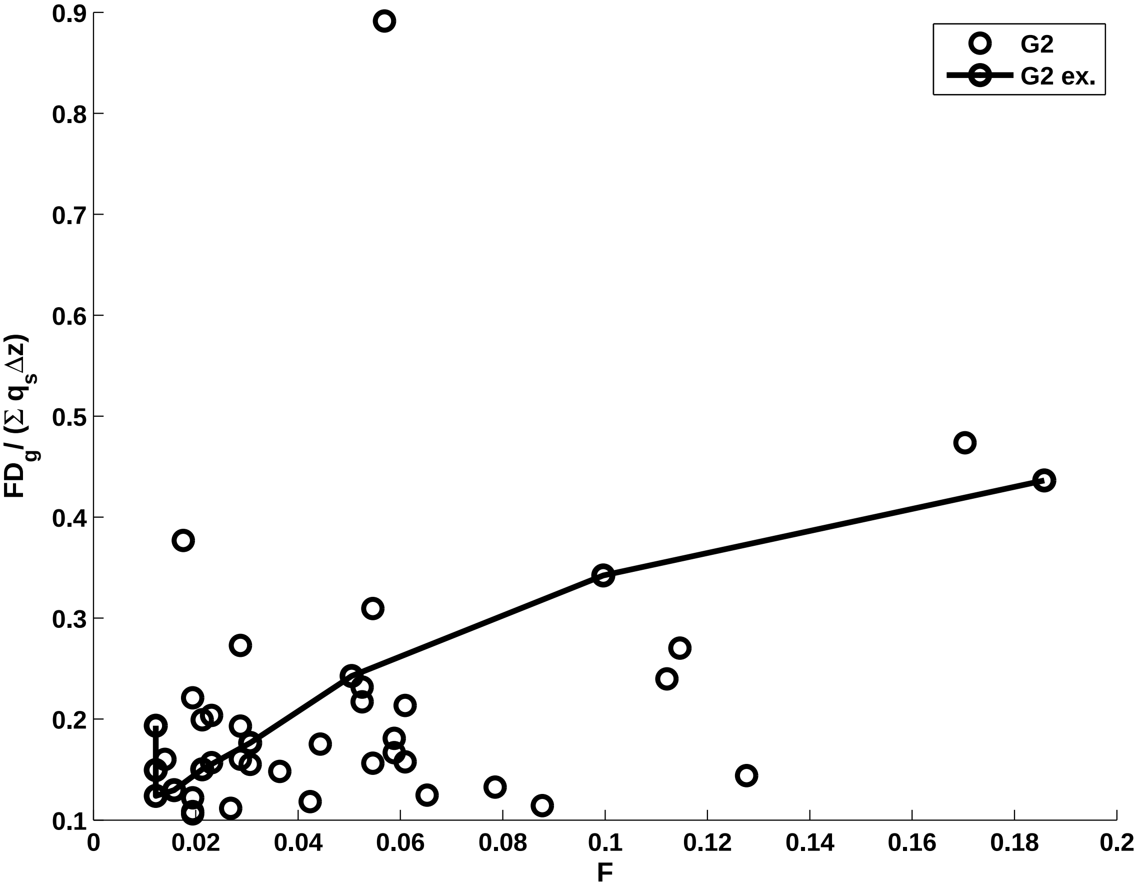

Figure 2.9: The ratio of sand trapped in a given layer to the total amount of sand passing through that layer, from experiment G2. The dashed black line connects the data points from one sample pit to show the hockey-stick pattern; a similar pattern is seen for each sample pit.

function of depth are developed. These models assume that sand infiltration is represented by the basic filtration model (2.3) and that infiltration continues until the sand fraction reaches some maximum value F_o near the surface. It is clear from the Gibson et al. [31] data that flow affects infiltration, and so a flow model is developed to quantify this effect. The predictions of the flow model are used in the models for F_o and β, so the flow model is presented first.

2.4.1 Model for flow through a gravel riverbed

Flow in the upper pore spaces of a gravel riverbed is affected by turbulent momentum exchange across the sediment-water interface. Momentum equations have been derived to describe the flow in the subsurface e.g. [69], but there is no explicit model for estimating the velocity in the upper pores. In this section, such a model is developed by linking results of several fluid mechanics studies. These studies involve a large number of coefficients that are not used in the remainder of this paper. These variables are summarized at the end of this section in table 2.3, while all other variables are summarized at the end of the chapter in table 4.8.

Flow deep in the riverbed is not affected by momentum exchange across the sediment-water interface and so velocity can be calculated directly. Darcys Law applies to flow through porous media only if the bed Reynolds number uD/ν is less than 1-10, where u is the water velocity in the pores [4] and ν is the kinematic viscosity. Flow through clean gravel falls above this range of Reynolds number [4]. Flow through gravel can be described by adding a non-linear velocity term representing advection of momentum to Darcy's Law. This yields Forchheimers Equation:

$$-\frac{1}{\rho}\frac{\partial p}{\partial x} = au_d + bu_d^2, \tag{2.21}$$

where u_d is the seepage Darcy velocity (water discharge per unit area perpendicular to the flow) and a and b are coefficients. The pressure gradient can be taken from the water surface slope, but these were not given in Gibson et al. [31] or Wooster et al. [88]. For Gibson et al. [31], slope was estimated from the given shear velocity by assuming the hydrostatic relationship for bed shear stress $\tau_b = \rho g H S$ and the equality $\tau_b = \rho u_*^2$, where H is water depth, S is water surface slope, and u_* is the shear velocity. For Wooster et al. [88], the water surface slope was assumed to equal to bed slope. To estimate the pressure gradient Typical expressions for a and b are [69]:

$$a = \frac{\nu}{k}, \tag{2.22a}$$

$$b = \frac{1}{c\sqrt{k}}, \tag{2.22b}$$

where k is the intrinsic permeability of the bed and c is a coefficient set to 1.8 for sediment beds. Bed permeability can be estimated using the Kozeny-Carmen relationship

($k = \frac{\phi^3}{180(1-\phi^2)}D^2$). Many alternate expressions for a and b have been proposed. Sidiropoulou et al. [76] compared several theoretical models for a and b against real data and determined that the best models were the following, taken from Ergun [21] and Kadlec and Knight (1996), respectively.

$$a = \frac{150\nu(1-\phi)^2}{\phi^2 d_g^2}, \tag{2.23a}$$

$$b = \frac{2(1-\phi)}{\phi^2 d_g}, \tag{2.23b}$$

The expressions on the left side of (2.21) and for a and b in (2.22) and (2.23)) are sometimes written with a factor of $1/g$, which comes from the derivation of momentum balance. Equations (2.21)-(2.23) are simplified by removing it from all terms. The subsurface flow model is tested using both sets of coefficients (2.22) and (2.23).

In the upper pore spaces, momentum transfer increases the average velocity and creates pressure fluctuations e.g. [52, 69, 85]. Ruff and Gelhar [69] derived a governing equation for mean flow in the upper subsurface. This expression adds a diffusive term representing exchange of momentum to (2.21):

$$-\frac{1}{\rho}\frac{\partial p}{\partial x} + \frac{\partial}{\partial z}\left(\nu_b \frac{\partial u}{\partial z}\right) = au + bu^2 \tag{2.24}$$

where ν_b is the interfacial diffusion coefficient (or eddy viscosity). Ruff and Gelhar [69] use (2.22a) and (2.22b) for a and b.

The solution to (2.24) is a velocity profile that decays exponentially with depth from a slip velocity u_s at the surface to the seepage velocity u_d deep in the bed [69, 52]:

$$u(z) = u_d + (u_s - u_d)e^{-\alpha z}, \tag{2.25}$$

where u_d is calculated using (2.21) and the slip velocity u_s and the decay coefficient α are calculated as follows.

Ruff and Gelhar [69] analytically derived relationships between u_s and ν_b by assuming that ν_b is either constant or varies linearly with depth below the sediment-water interface. These relationships are (2.26a) and (2.26b) in the following, respectively:

$$(u_s - u_d)^3 + \frac{3}{2}\left(\frac{a}{b} + 2u_d\right)(u_s - u_d)^2 = \frac{3}{2}\frac{u_*^4}{b\nu_b} \tag{2.26a}$$

$$(u_s - u_d)^3 + \frac{4}{3}\left(\frac{a}{b} + 2u_d\right)(u_s - u_d)^2 = 2\frac{u_*^4}{b\nu_b}. \tag{2.26b}$$

Water velocity and turbulence decrease with depth below the sediment-water interface and so it is logical to presume that ν_b should vary with depth. However, the limited data available on porous boundary flow has not definitively shown any depth variation and ν_b is generally assumed to be constant e.g. [27, 69, 60]. Both expressions in (2.26) are tested against data in this section.

Until recently, it was not possible to calculate u_s or ν_b without knowing the other. Using data from tracer-based and slip-velocity experiments, Fries (2007) developed an empirical relationship between ν_b and the interfacial Reynolds number $R_* = u_* \sqrt{k}/\nu$. This relationship is valid for values of R_* ranging from 0.01 to 50:

$$\nu_b = \nu A_F R_*^{B_F} \tag{2.27}$$

$$A_F = \begin{cases} 1.49 + 0.52/ - 0.39 & \text{if} \quad 0.01 < R_* < 1 \\ 1.65 + 0.58/ - 0.43 & \text{if} \quad 1 < R_* < 50, \end{cases} \tag{2.28a}$$

$$B_F = \begin{cases} 2.7 \pm 0.1 & \text{if} \quad 0.01 < R_* < 1 \\ 1.6 \pm 0.1 & \text{if} \quad 1 < R_* < 50) \end{cases} \tag{2.28b}$$

The models for u_s and u_d are tested against data from two laboratory studies of turbulent water flow over sediment beds [52, 75] (Equations 2.21-2.28). Assuming a constant diffusion coefficient in the subsurface (2.26a) leads to underestimates of the slip velocity by a factor of 3 (Figure 2.10) . The model that assumes that ν_b varies with depth (2.26b) performs better. Of the two sets of expressions for the coefficients a and b (Equations 2.22 and 2.23), the Ergun and Kadlec and Knight models (2.23) generally perform better (Figure 2.11). Based on these results, (2.23a), (2.23b), and (2.26b) are used to calculate u_s and u_d.

As reported by Nagaoka and Ohgaki [52], Yamada and Kawabata [90] derived an expression for the exponential decay coefficient α in (2.25). This relationship is a function of the bed porosity ϕ, the slip velocity, a void scale b_ϕ, friction factors f_D and C_ϕ, a bed Reynolds number $R_{*,2}$, and the ratio of mixing length to void scale K_l:

$$\alpha = \frac{1}{b_\phi} \left(\frac{f_D}{4K_l} \right)^{1/3} \tag{2.29a}$$

$$b_\phi = \frac{2\phi^2}{3(1-\phi)} D_g \tag{2.29b}$$

$$f_D = \frac{80}{R_{*,2}} + C_\phi \tag{2.29c}$$

$$R_{*,2} = \frac{u_s b_\phi}{\nu} \tag{2.29d}$$

$$C_\phi = \frac{2}{3(1-\phi)} \left(3.22(1-\phi)\sqrt{\phi} \right)^2 \tag{2.29e}$$

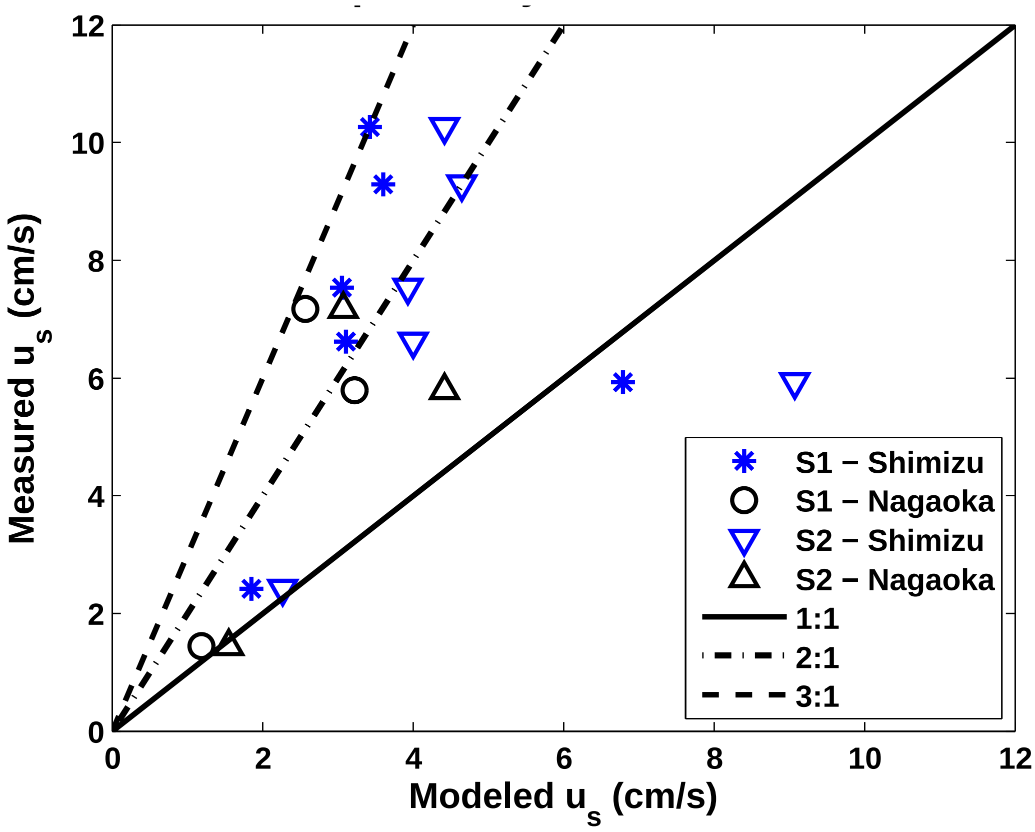

Figure 2.10: The effects of the two sets of coefficients on the slip velocity model. The EKK coefficients are from equation (2.23) and the RG coefficients from (2.22).

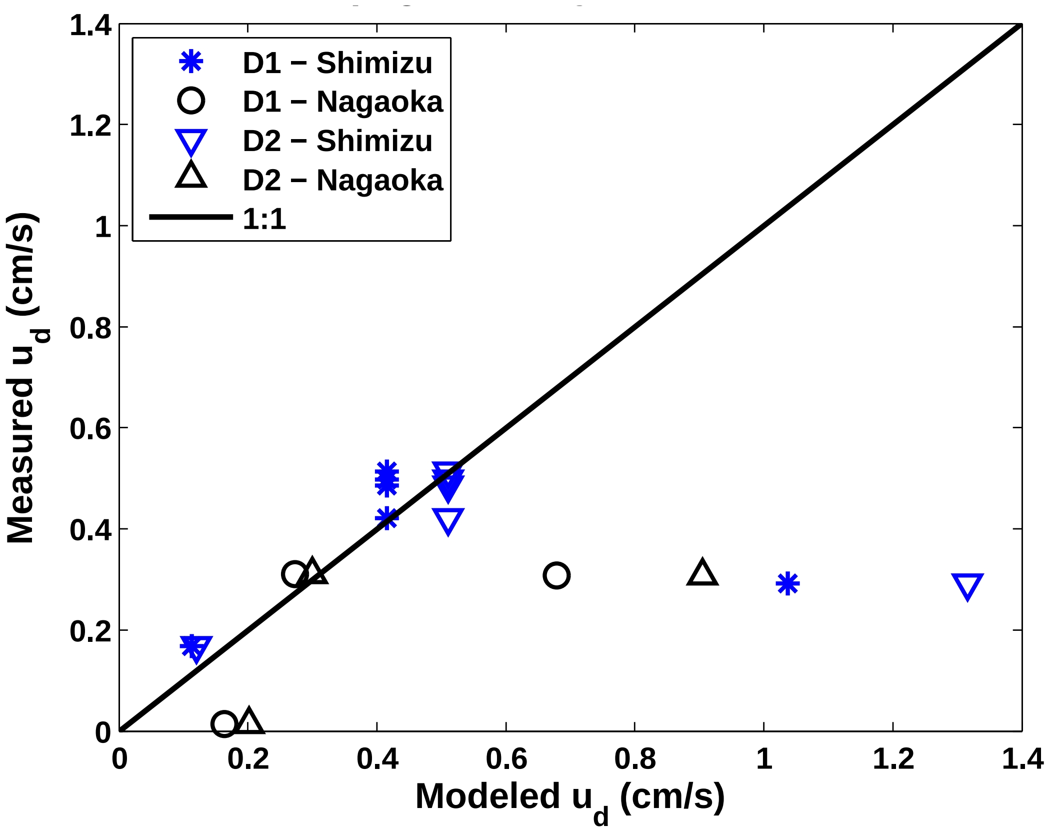

Figure 2.11: The effects of the two sets of coefficients on the seepage velocity model. The EKK coefficients are from equation (2.23) and the RG coefficients from (2.22).

Variable	Description	Units
a, b	Coefficient for the Forchheimer equation	$1/t(1/l^2)$
A_F, B_F	Coefficients for relationship between R_* and ν_b	-
b_θ	Void scale in riverbed	l
C_θ	Porosity coefficient	-
D	Gravel diameter	l
f_D	Drag term in water velocity calculation	-
g	Gravitational acceleration	l/t^2
H	Water depth	l
k	Permeability	l^2
K_l	Ratio of mixing length to b_θ	-
R_*	Interfacial Reynolds number	-
$R_{*,2}$	Bed Reynolds number	-
S	Water surface slope	-
$u(u_s, u_d)$	Water Darcy velocity (slip, seepage)	l/t
α	Decay coefficient for water velocity profile	$1/l$
ν	Water viscosity (kinematic)	l^2/t
ν_b	Interfacial diffusion constant	l^2/t
ϕ	Porosity of riverbed	-
ρ	Density of water	$mass/l^3$

Table 2.3: Variables for subsurface velocity model

Nagaoka and Ohgaki [52] found that the Yamada-Kawabata model for α matched the measured subsurface velocity, if the measured slip velocity is used in (2.29d) and K_l is set to 2.

The velocity profiles for the experiments of Nagaoka and Ohgaki [52] and Shimizu et al. [75] are calculated using (2.21), (2.23), (2.25), (2.26b), (2.27), (2.28), and (2.29), and assuming that $K_l = 2$. The final unknown in the model is the location of $z = 0$. Shimizu et al. [75] and Nagaoka and Ohgaki [52] set the sediment-water interface ($z = 0$) at the plane sitting on top of the upper layer of particles. The proposed velocity profile matches the measured velocity profile if $z = 0$ is set somewhere between $0.25D$ and $0.5D$ below this plane (Figure 2.12). Presuming that Wooster et al. [88] and Gibson et al. [31] defined $z = 0$ in the same way as Shimizu et al. [75] and Nagaoka and Ohgaki [52], the velocity profile in this study has been offset downwards a distance of $0.5D$.

Momentum transfer across the sediment-water interface is likely to change as the sand seal develops and permeability decreases. However, calculating the change in subsurface flow as the sand seal is created is beyond the scope of this study. Therefore, this infiltration model assumes that subsurface flow remains constant.

Clogging occurs at depth $z = 2D_g$, and so velocity at this depth is assumed to drive

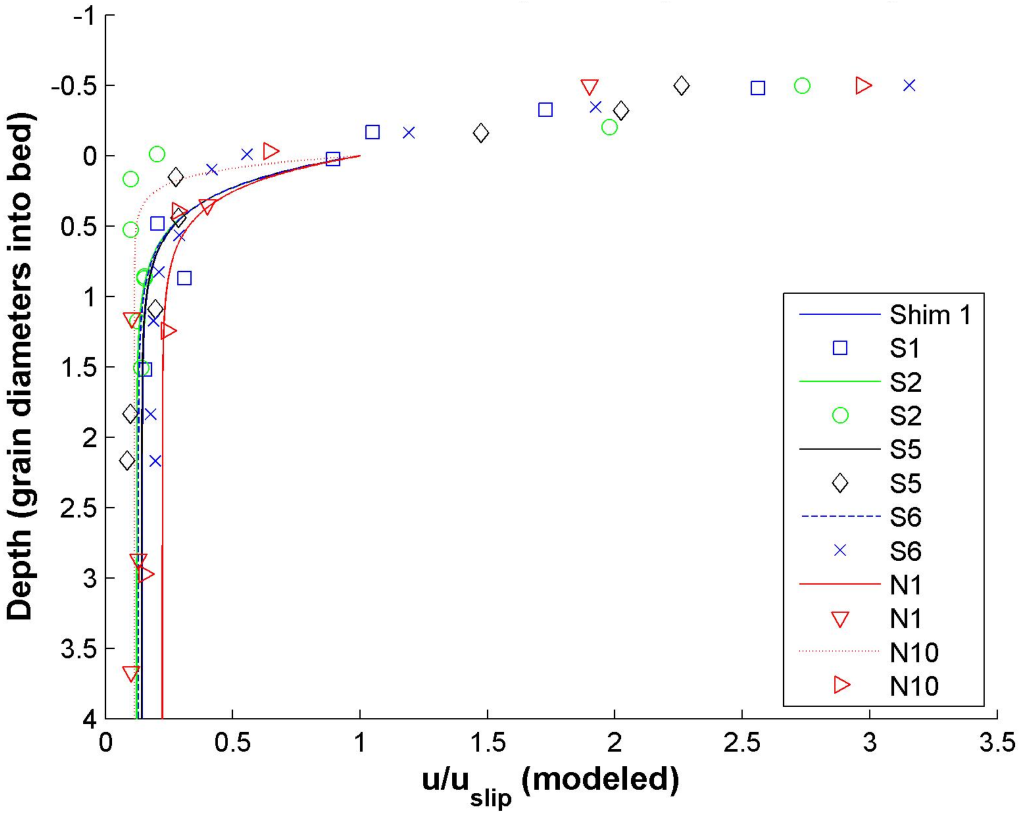

Figure 2.12: Subsurface velocity model. The lines are model predictions and the markers are data points for various experiments from Shimizu et al. [75] (S) and Nagaoka and Ohgaki [52] (N). Velocities and depths are normalized by the modeled slip velocity and grain diameter, respectively. The original studies defined the boundary as the plane sitting on top of the upper particles [75, 52]. In this Figure the profile is offset downwards by $0.5D$ to be closer to the average boundary plane.

clogging. $u(2D_g)$ is incorporated into the model for F_o and tested against calculated values of β.

2.4.2 Revised model for a constant β as a function of grain size

Although the data suggest that trapping is variable, a constant β appears to be sufficient to represent the overall shape of $F(z)$ in the sand seal. In this section an empirical relationship is developed for a constant trapping coefficient β_{rev}, where the subscript *rev* indicates the revised constant-trapping model. The model focuses on the relative sizes of sand and gravel, which is the most important factor affecting infiltration depth [5, 17]. The grain size ratio D_{15}/d_{85} is a good predictor of the behavior of sand trapping in gravel [74, 32], so it is the basis for the empirical β model. Later, the relationship between flow and β is explored.

Values of β in column (10) of table 2.2 are used as the true values β. Results from W3, W4, W9, and G1nf are excluded. As seen in the data analysis section, the patterns in $F(z)$ from W3 and W4 do not correspond to an exponential model. The values of D_{15}/d_{85} for these experiments are so large that a sand seal probably did not form [74, 32]. For experiment W9, D_{15}/d_{85} is so small that it is likely that the coarsest sand was unable to infiltrate the bed and so the correct d_{85} is not known. Experiment G1nf is excluded at this stage because the regression does not include flow variables.

There is a strong linear relationship between D_{15}/d_{85} and β (Figure 2.13). This relationship is used as the new model for β_{rev}:

$$\beta_{rev} = -0.02\frac{D_{15}}{d_{85}} + 0.41. \tag{2.30}$$

Also shown in Figure 2.13 are the calculated values of β for experiments W3, W4, and W9. These fall far from the regression line, indicating that (2.30) is only valid when $7 \lessapprox D_{15}/d_{85} \lessapprox 14$.

Figure 2.8 suggests that flow reduces β, as the estimates for G1nf are higher than those for G1. This relationship is explored in Figure 2.14, where the slip velocity is plotted against residuals between the calculated β in column (10) of table 2.2 and the predicted value β_{rev}. There are decreasing trends between $\beta - \beta_{rev}$ and u_{slip} for both datasets, but the two trends are unrelated to each other. This is not due to choice of velocity; there are similar patterns between $\beta - \beta_{rev}$ and the seepage velocity, the velocity at $2D_g$, and the shear velocity of the overlying open-channel flow. Given the discrepancy, it is not possible to include flow in a model for β_{rev} using the existing datasets.

The new model for β_{rev} is coupled with the model for F_o developed in the next section to predict $F(z)$. These predictions are directly compared with predictions of the Wooster model in the Results section.

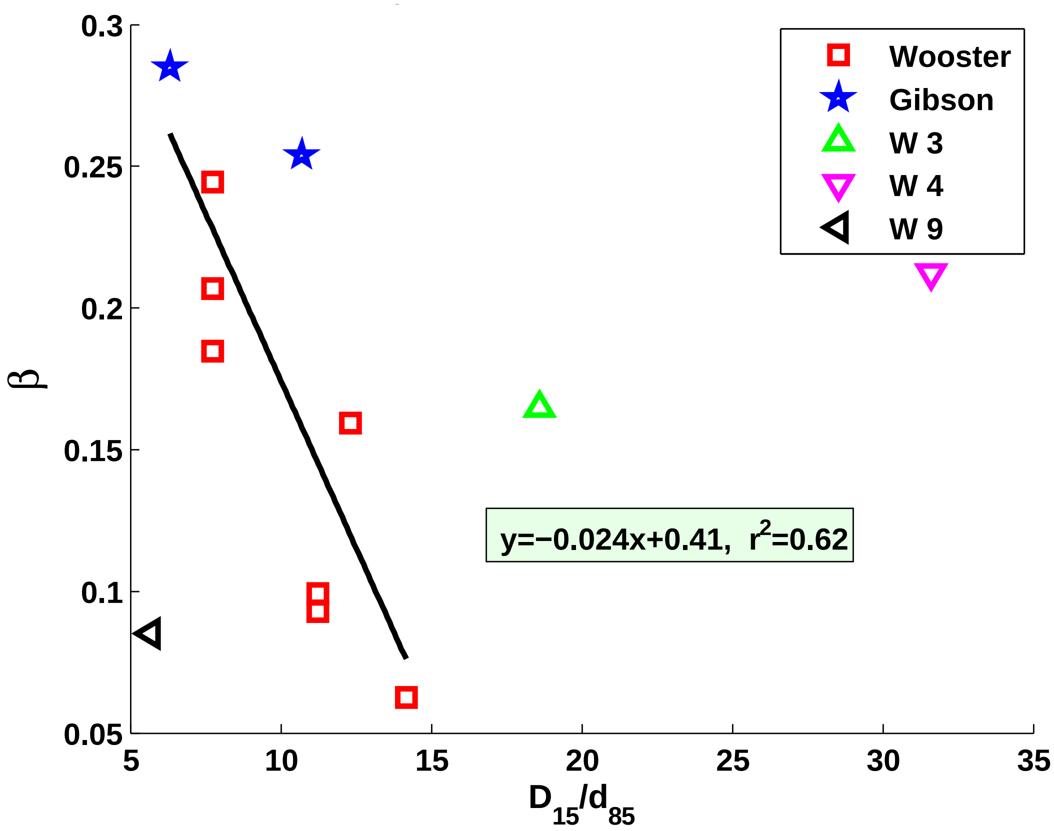

Figure 2.13: The relationship between trapping and the relative grain size of sand and gravel. The average values of β for each experiment are compared with the grain size ratio D_{15}/d_{85}. β is calculated using equation (2.17) on layers at least 2cm apart. The regression line excludes Wooster Zones 3, 4, and 9 and the Gibson no-flow experiments.

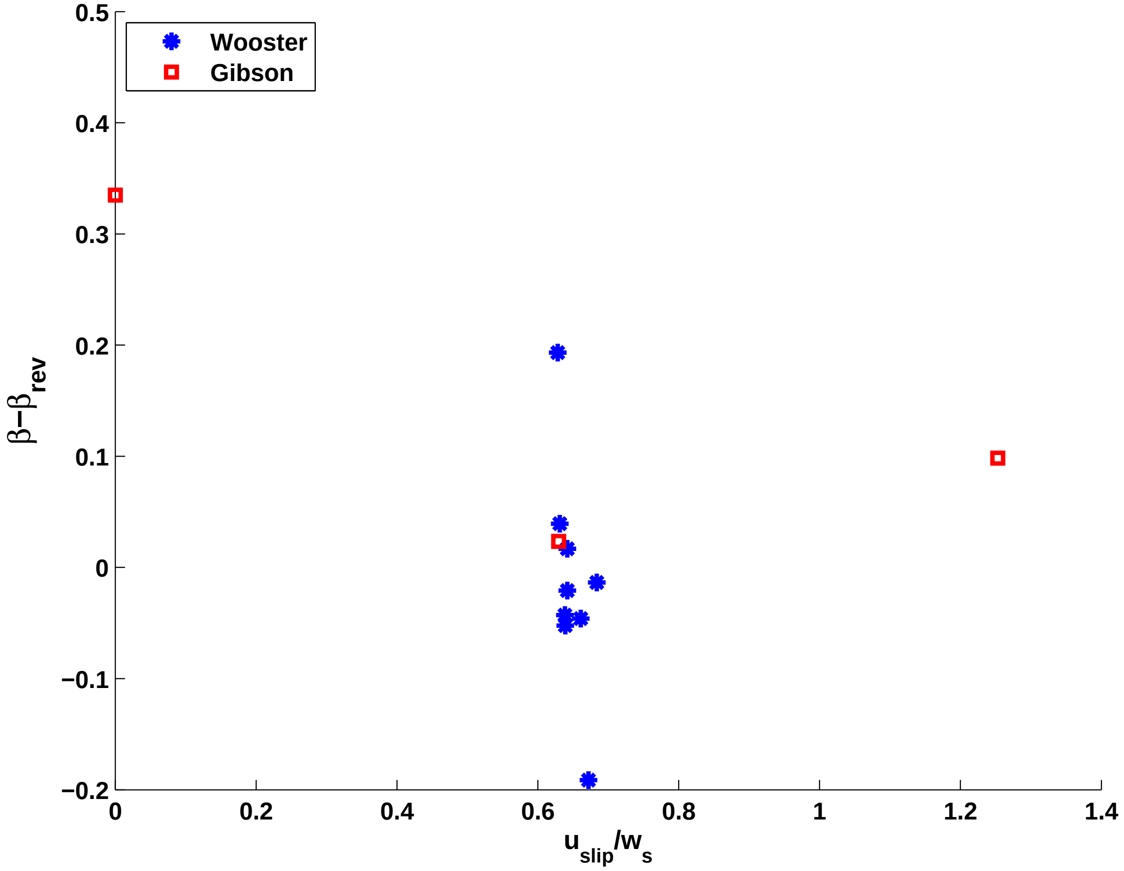

Figure 2.14: The relationship between slip velocity and the residual of the measured and predicted values of β (assuming constant).

2.4.3 Maximum sand fraction F_o

The Wooster model consistently underestimates F_o (Table 2.2). A new model is developed in this section. The maximum fraction of sand that can be deposited in the pore spaces of a gravel-framework bed is limited by particle packing properties. Particle packing is a function of the relative sizes of sand and gravel. Ridgway and Tarbuck [65] developed a commonly used, empirical relationship for the maximum sand fraction:

$$F_{max} = \phi_{gr}(1 - \phi_s)\left[1 - 2.35\frac{d}{D} + 1.35\left(\frac{d}{D}\right)^2\right]. \tag{2.31}$$

The porosity term $\phi_{gr}(1 - \phi_s)$ is the upper limit of volume that sand can occupy in the bed; it is also used in the Wooster model for F_o.

There are several choices for the representative grain diameters D and d in (2.31). The pore size is largely determined by the smallest particles, and so D_{15} is used for the representative gravel diameter. As for the representative sand diameter, d_{85} may be appropriate because the largest particles block smaller particles from entering pore throats depositing there. On the other hand, d_g is representative of the average particle that will fill the pore space. In Figure 2.15, the ratios d_{85}/D_{15} and d_g/D_{15} are plotted against F_o from column (9) of table 2.2 divided by $\phi_{gr}(1 - \phi_s)$. Also shown is the predicted value of the quadratic term on the right side of (2.31). The data follow the trend predicted by (2.31) for both grain ratios. However, the scatter is slightly lower using d_{85}/D_{15}, so this ratio will be used as the basis for modeling F_o.

Equation (2.31) overestimates F_o in an infiltration sand seal (Figure 2.15). One cause of the difference is the inefficiency of infiltration as a particle packing mechanism. This inefficiency can be modeled as a function of the relative strengths of advection and gravitational settling. If the settling velocity of sand is much greater than the horizontal water velocity, the path of a particle of sand will be mostly downwards. If water is not flowing then sand can only access pore space that lies directly under overlying pores, which is a fraction of the gravel pore space equal to ϕ_{gr}. If water is flowing, it will advect sand horizontally into more of the available pore space. A model for the fraction of accessible pore space is taken from the overflow rate of a reservoir [53]. In this model, it takes particles a time of $t = l_z/w_s$ to settle through a pore, where l_z is the pore height and w_s is the particle settling velocity. During this time, a particle advected at the water velocity u will travel a horizontal distance ut. If the width of the pore is l_x, the sand will have access to a fraction of the pore space equal to ut/l_x. Assuming that the pore width and height are equal ($l_x = l_z$), this fraction is simply the velocity ratio u/w_s. If the water velocity is greater than the particle settling velocity, it is assumed that sand can access the full pore space, so (2.31) determines F_o. This can be expressed as velocity correction term K_u:

$$K_u = \begin{cases} \phi_{gr} + \frac{u}{w_s}(1 - \phi_{gr}) & \frac{u}{w_s} < 1 \\ 1 & \frac{u}{w_s} \geq 1. \end{cases} \tag{2.32}$$

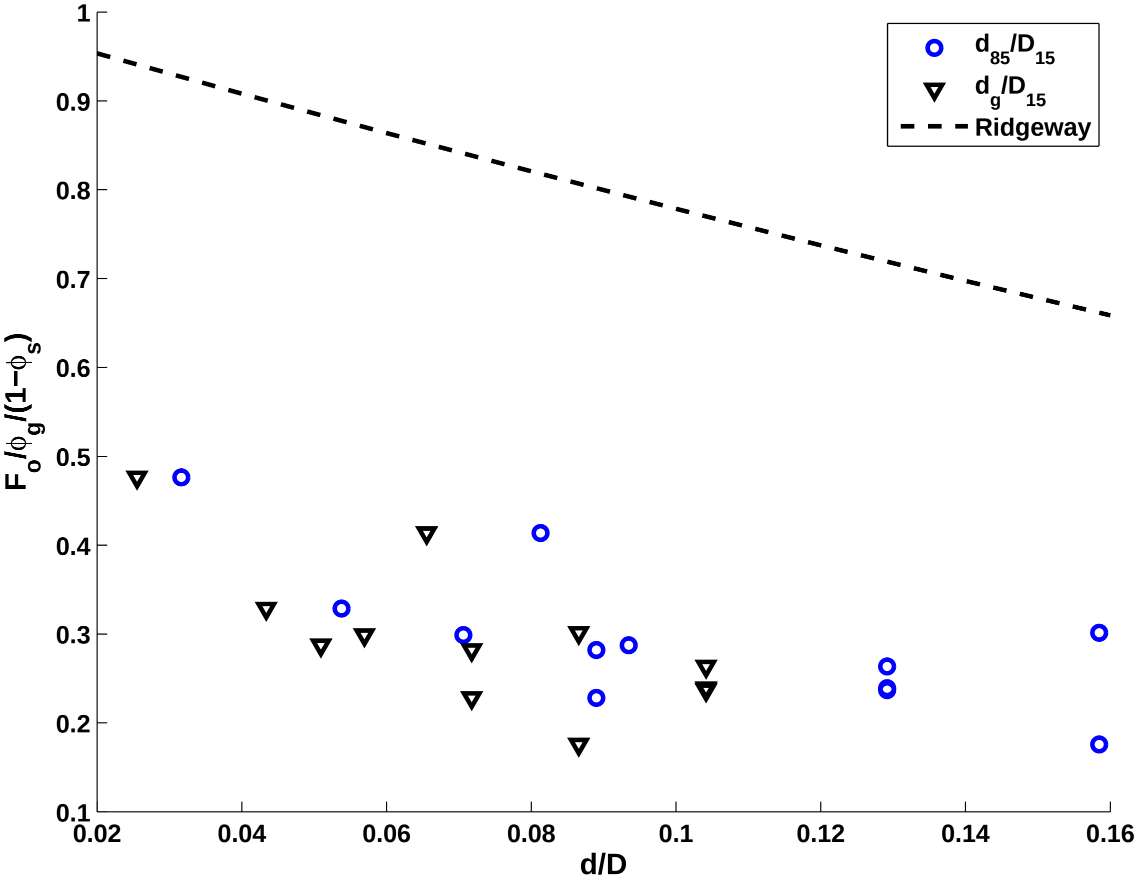

Figure 2.15: The measured sand fraction, divided by the maximum possible bed volume plotted against two grain size ratios. The dashed line is an empirical relationship for the maximum possible sand fraction from Ridgway and Tarbuck [65].

The water velocity is taken as $u(z = 2D_g)$ from the subsurface flow model. The settling velocity w_s is calculated using an empirical relationship for natural particles developed by Dietrich [16]. This relationship is presented using a non-dimensional settling velocity W_* as a function of a non-dimensional particle size D_*:

$$W_* = \frac{\rho w_s^3}{(\rho_s - \rho) g \nu} \tag{2.33a}$$

$$D_* = \frac{(\rho_s - \rho) g D^3}{\rho \nu^2} \tag{2.33b}$$

$$\log W_* = -3.77 + 1.93(\log D_*) - 0.098(\log D_*)^2 - 0.00575(\log D_*)^3 + 0.00056(\log D_*)^4 \tag{2.33c}$$

In Figure 2.16, F_o is plotted against $F_{max} K_u$. The two values are moderately correlated ($R^2 = 0.68$) but the measured values are on average four-fifths of the predicted values. Therefore, I propose the following model for F_o in the sand seal:

$$F_o = 0.8 K_u \phi_{gr} (1 - \phi_s) \left[1 - 2.35 \frac{d_{85}}{D_{15}} + 1.35 \left(\frac{d_{85}}{D_{15}} \right)^2 \right]. \tag{2.34}$$

In Figure 2.17, F_o is plotted against predictions of the Wooster model and equation (2.34). The Gibson et al. [31] data are denoted by filled markers and open markers indicate Wooster et al. [88] data. The new model predictions are close to the 1:1 line while the Wooster model generally underestimates F_o.

2.4.4 A variable trapping coefficient

β increases with F throughout most of the sand seal. At very low values of F, which are seen deep in the bed, β drops quickly as F increases (Figures 2.8 and 2.9). These two trends must correspond to two trapping mechanisms. I propose that these mechanisms are the clogging of pore throats between gravel grains and the building of sand piles on top of gravel grains. These two processes can be represented by separating β into two trapping coefficients β_{th} and β_p and breaking F into sand in piles and sand in pore throats ($F = F_{th} + F_p$).

There is no analytic solution to the governing equations (2.3)-(2.5) if $\beta = \beta_{th} + \beta_p$ and β_{th} and β_p vary in different manners. However, there is an analytic solution using only one variable β if it varies linearly with F. The throat-trapping mechanism dominates in most of the sand seal. Since this chapter focuses on the sand seal, an analytic model is built for $F(z)$ using a linearly-varying β_{th}.

The pile-trapping mechanism is only active deep in the bed where F is very small. These deposits have relatively little impact on bed permeability but can affect the storage of tracers and contaminated material at moderate depths. A theoretical model is built for β_p. The two variable-trapping models are then implemented together in a numerical model.

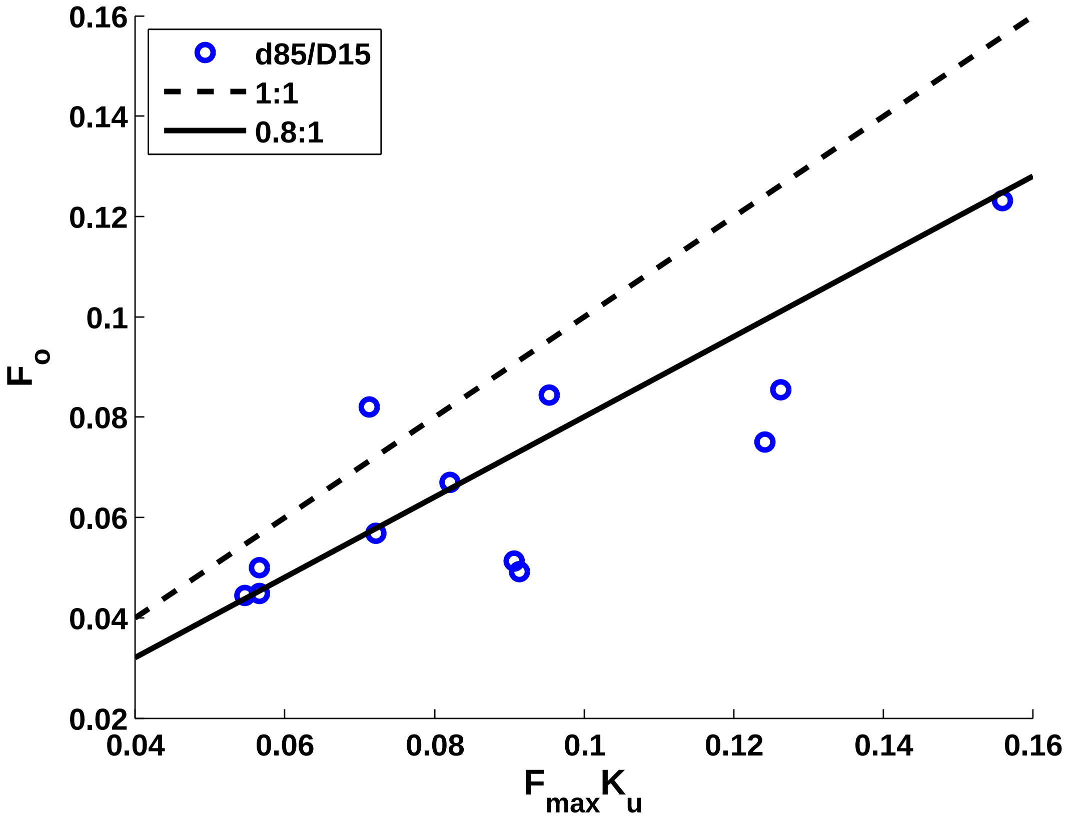

Figure 2.16: The measured sand fraction plotted against the product of the maximum possible sand fraction predicted by Ridgway and Tarbuck [65] and a velocity correction factor K_u. The dashed line is a 1:1 fit and the solid line is 0.8:1.

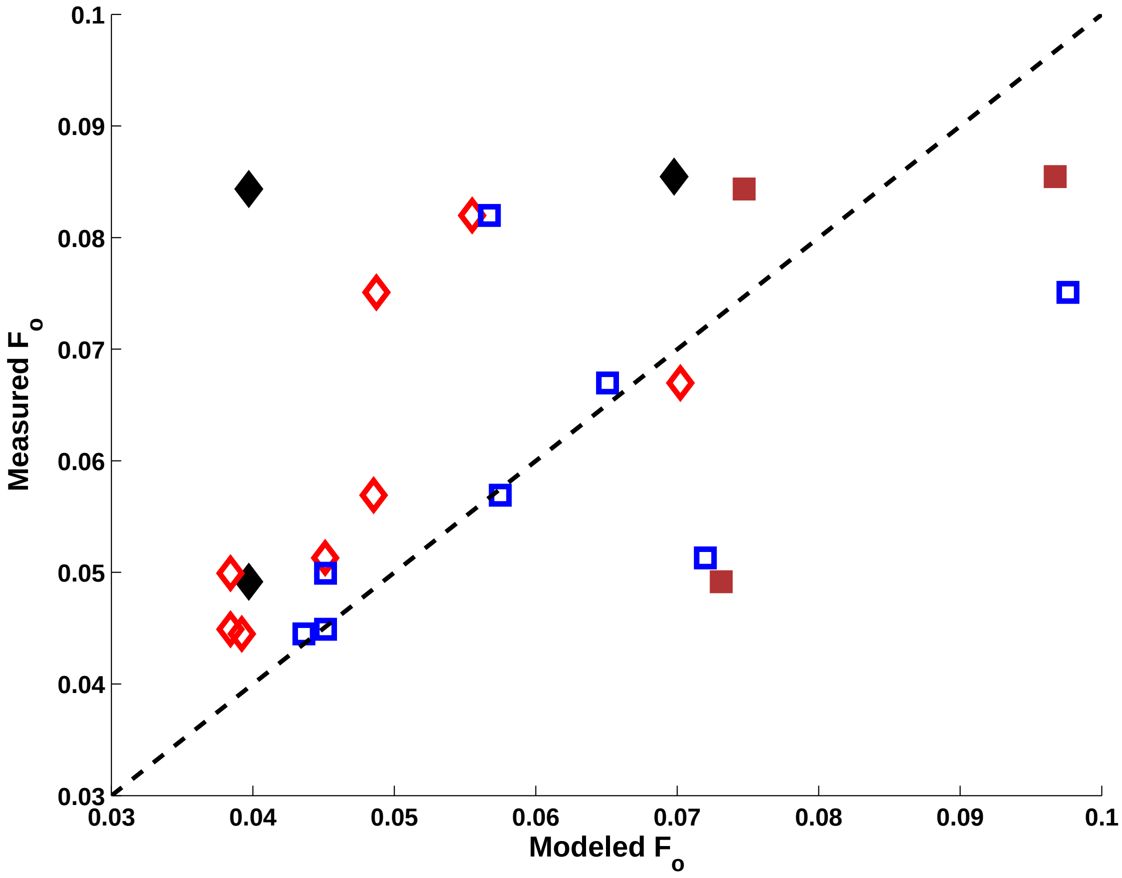

Figure 2.17: Model performance at predicting F_o. Open markers signifay Wooster data and solid marker Gibson data. Diamonds signify predictions by the Wooster model and squares show the performance of equation (2.34).

Analytic solution for $F(z)$ with a linearly-varying β

There is an analytic solution to the governing equations for $F(z)$ in the upper sand seal using a variable trapping coefficient β_{th}. This solution is possible by assuming that $F = F_{th}$ and β_{th} varies linearly with F:

$$\beta_{th} = C_1 + C_2 F \tag{2.35}$$

These conditions are substituted into (2.5), which is rearranged to yield a new mass conservation equation:

$$\frac{\partial F}{(C_1 + C_2 F)} = \frac{q_s}{D_g}\partial t. \tag{2.36}$$

Integrating both sides leads to:

$$\frac{1}{C_2}\ln\left(C_1 + C_2 F\right) = \frac{1}{D_g}\int_0^t q_s dt' + K_1, \tag{2.37}$$

where the integration constant $K_1 = \ln(C_1)/C_2$. Assuming a constant sand flux of $q_{s,o}$ at $z = 0$, then a mass balance on sediment leads to:

$$\int_0^t q_s \partial t' = t q_{s,o} - \int_0^z F \partial z', \qquad \text{so} \tag{2.38}$$

$$\frac{1}{C_2}\ln\left(C_1 + C_2 F\right) = \frac{t}{D_g} q_{s,o} - \frac{1}{D_g}\int_0^z F\partial z' + K_1. \tag{2.39}$$

At this step a decision must be made. If the coefficients C_1 and C_2 are functions of the local water velocity $u(z)$, then C_1 and C_2 will vary with depth. This seems reasonable, but it makes the model complicated to implement because there is no analytic solution. For now, it will be assumed that if they vary, $\partial C_1/\partial z$ and $\partial C_2/\partial z$ are small enough to ignore. Taking the derivative of both sides of (2.39) with respect to z yields:

$$\frac{1}{C_1 + C_2 F}\frac{\partial F}{\partial z'} = -\frac{F}{D_g}, \qquad \text{or} \tag{2.40}$$

$$\frac{\partial F}{C_1 F + C_2 F^2} = -\frac{\partial z}{D_g}. \tag{2.41}$$

Integrating both sides of (2.41) leads to the analytic solution for $F(z)$:

$$\ln\left(\frac{F}{C_1 + C_2 F}\right) = -C_1\left(\frac{z}{D_g} + K_2\right), \qquad \text{or} \tag{2.42}$$

$$F(z) = \frac{C_1 K_2' e^{-C_1 z/D_g}}{1 - C_2 K_2' e^{-C_1 z/D_g}}. \tag{2.43}$$

The integration constant $K_2'(\equiv e^{-K_2 C_1})$ is determined by evaluating (2.42) at $z = 2D_g$, where $F = F_o$.

$$K_2' = F_o / \left(e^{-2C_1}(C_1 + C_2(F_o))\right). \tag{2.44}$$

Expt.	C_1	C_2
G1*	0.223	1.75
G1nf†	0.188	5.93
G2*	0.118	1.92

Table 2.4: Estimates of the coefficients to equation (2.35).

* C_1 and C_2 are the intercept and slope of the trends in Figure 2.7.

† Intercept and slope of trend through G1nf data in Figure 2.8

Estimating C_1 and C_2 from the Gibson data

C_1 and C_2 are the intercept and slope, respectively, of the increasing trends in $\beta(F)$ in figure 2.7. These values are given for experiments G1 and G2 in Table 2.4. For G1nf, C_1 and C_2 are taken from the intercept and slope of the increasing trend seen in Figure 2.8. This slope is an underestimate since at high F, the estimate of $\beta(F)$ is an integral of trapping over all smaller values of F. However, there is no better estimate available.

The analytic solution (2.43) is analyzed using the new model for F_o and the coefficients C_1 and C_2 from table 2.4. The predictions are reported in the Results section.

2.4.5 Development of the pile-building model

β_p represents the fraction of sand passing through a layer of gravel that lands on a sand pile and stays there. Figures 2.8 and 2.9 suggest that this is the dominant trapping mechanism when F is very low and thus it dominates when sand first infiltrates a bed. This mechanism affects the amount of sand trapped at moderate depths and the mass that settles all the way to an impermeable barrier. Modeling this process correctly can help to determine where sediment contaminated by heavy metals may be found, in addition to expanding understanding of subsurface processes.

A theoretical model is developed for the pile-building mechanism based on particle geometry. The trapping coefficient is a function of the area on top of gravel where sand can sit and the vertical distance between encounters with gravel particles, Δ_z. Pile-trapping continues until the sand pile is a cone with sides at the angle of repose. A numerical model is built to solve the governing equations (2.3)-(2.5) for $F(z)$ with the two simultaneous trapping mechanisms with variable trapping coefficients.

Particle shape and the pile-building length scale

D_g is used as a length scale to non-dimensionalize z in the governing equations. The length scale is inherently tied to β, which equals the probability that a sand particle will be trapped as it travels a vertical distance equal to the length scale. While D_g is simple to use, the natural length scale for pile-building Δ_z is slightly different. In this section the expression for Δ_z is developed. A conversion factor between the length scales is incorporated into the expression for β_p so that the non-dimensionalization z/D_g is correct for the pile-building process.

The natural length scale Δ_z is the average distance between the tops of particles on a given vertical line through the bed. This corresponds to the frequency with which an infiltrating sand particle has the opportunity to deposit in a sand pile. Δ_z is the vertical thickness of a gravel particle plus pore space. The average vertical thickness through gravel is the particle volume V_g divided by the projected area, $\pi(D/2)^2$. The proportion of pore space on an average vertical line through a clean gravel bed equals ϕ_{gr} [4]. For each unit distance through gravel on a given line, there is a distance of $(1 - \phi_{gr})^{-1}$ through sediment plus pore space, so:

$$\Delta_z = \frac{V_g}{\pi(D/2)^2(1-\phi_{gr})} \tag{2.45}$$

The volume of a sand pile is a function of the gravel particle shape [3]. Particle shape can be described using the Corey Shape Factor K_{csf}. K_{csf} is equal to the ratio $S/(ML)^{1/2}$, where S, M, and L are the short, medium, and long dimensions of the gravel, respectively. In this study, a gravel particle is modeled as a disc of diameter $D_g(= M = L)$ and semicircular edges with radius of curvature $S/2 = D_g K_{csf}/2$ (Figure 2.18). The volume of the model gravel particle is:

$$V_g = \frac{\pi}{4}\left((D_g - S)^2 S + \frac{2S^3}{3} + \frac{\pi}{2}(D_g - S)S^2\right), \qquad \text{or equivalently} \tag{2.46}$$

$$V_g = \frac{D_g^3 \pi}{4}\left((1-K_{csf})^2 K_{csf} + \frac{2K_{csf}^3}{3} + \frac{\pi}{2}(1-K_{csf})K_{csf}^2\right). \tag{2.47}$$

The length scale is thus:

$$\Delta_z = \frac{D_g}{1-\phi_{gr}}\left((1-K_{csf})^2 K_{csf} + \frac{2K_{csf}^3}{3} + \frac{\pi}{2}(1-K_{csf})K_{csf}^2\right). \tag{2.48}$$

The conversion factor between the length scales D_g and Δ_z is just their ratio, Δ_z/D_g. For typical gravel with $K_{csf} = 0.7$ [37] and $\phi_{gr} = 0.35$, this ratio is 0.8. This implies that the downward path of a sand particle crosses 10 gravel particles in a vertical distance of $8D_g$. If the particle is a sphere, $K_{csf} = 1$ and so $\Delta_z = 2D_g/3(1-\phi_{gr})$, which is close to D_g for typical gravel porosities.

The definition of Δ_z assumes that gravel particles lie flat, but gravel in riverbeds tends to lie at an angle. From the point of view of infiltrating sand, tilted gravel will appear more rounded and the distance between the tops of gravel particles on a given vertical line will increase. This tilt can be represented by varying K_{csf} between 0.7 (natural river gravel) and 1.0 (a sphere) [37]. This change affects $F(z)$, which will be demonstrated in the Results section.

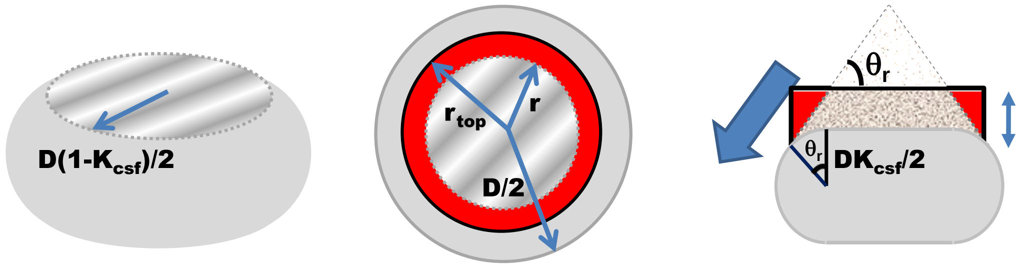

Figure 2.18: A model particle viewed from an angle, from above, and from the side. A pile of sand sits atop the particle in side view. The red area represents the portion of the pile that will capture no more sand when the pile has height h because the edge is at the angle of repose.

Defining β_p

Figures 2.8 -2.9 suggest that pile-building decreases from a moderate value when F is very small to an insignificant value at moderate F. β_p is modeled as a function that equals a finite value when $F_p = 0$ and decreases to $\beta_p = 0$ at a rate set by the growth of sand piles.

When the bed is clean, β_p is defined as the probability of a sand grain landing on top of a gravel particle and remaining there as it travels a vertical distance of D_g. If a sand grain lands where the slope is less than the angle of repose θ_r, it will remain in place rather than bounce off, as these collisions are inelastic [91]. Thus $\beta_p(F_p = 0)$ is the areal fraction of the top of the gravel particle with slope less than θ_r. This area is a circle with radius $r_{top} = D(1 - K_{csf}(1 - \sin\theta_r)/2$, while the total projected area is $\pi(D/2)^2$ (Figure 2.18). Incorporating the length scale conversion,

$$\beta_p(F_p = 0) = \frac{D_g}{\Delta_z}\frac{\pi r_{top}^2}{\pi(D/2)^2} \tag{2.49}$$

As the sand pile grows, the edges of the pile reach the angle of repose θ_r (the area shown in red in Figure 2.18). Any further sand landing on these edges will roll off, and β_p is reduced to the area of the top with slope below the angle of repose:

$$\beta_p(F_p > 0) = \frac{D_g}{\Delta_z}\frac{\pi r^2}{\pi(D/2)^2}, \tag{2.50}$$

where r is the radius of this flat area. r can be calculated from the the thickness of the sand pile ($h = \int_0^t q_s dt/\phi_s$) and the distance that the gravel extends into the bottom of the pile,

$DK_{csf}(1-\cos\theta_r)/2$ (Figure 2.18):

$$r = r_{top} - \frac{\tan\theta_r}{h + \frac{DK_{csf}}{2}(1-\cos\theta_r)} \tag{2.51}$$

The two variable-β models are implemented together using a numerical model. There are a few minor changes in assumptions. The sand fraction is separated into two deposits $F = F_p + F_{th}$. F_p is calculated as the volume of a cone of sand with the top cut off, accounting for sand porosity ϕ_s. β_{th} is altered to account for sand depositing in piles before it has a chance to reach the pore throat. This reduces the flux q_s by a factor of $(1-\beta_p)$, so:

$$\beta_{th} = (1-\beta_p)\left(C_1 + C_2 F_{th}\right) \tag{2.52}$$

Because sand travels downward, the natural implementation for modeling clogging is a one-dimensional finite-differencing scheme which steps downward through the bed at each time step. The flux into a layer equals the flux into the layer above it minus the volume of sand trapped there. The grid spacing is Δ_z, as this represents sand passing the top of a single gravel grain and through a single pore throat. Sand is supplied into the upper boundary at a constant rate until $F = F_o$ in an upper layer. The riverbed is assigned a thickness matching the experimental conditions, to demonstrate the collecting of sand on the flume bottom. The pile-building mechanism continues until $r = 0$, after which $\beta_p = 0$. Infiltration continues until $F = F_o$ somewhere in the bed. F_o varies with depth in the bed because is it is a function of velocity, and $u(z)$ varies with depth. The clogging depth is the depth at which $F = F_o$, rather than $2D_g$.

2.5 Results

2.5.1 Performance of the constant-trapping models

The performance of the new constant-trapping model and the Wooster model on the Wooster et al. [88] and Gibson et al. [31] data is summarized in table 2.5. The better fit for a given experiment will have a slope closer to one and an intercept closer to zero. A higher r^2 value generally corresponds to the better fit but is limited by scatter in the data. The new model performs better than the Wooster model in general. Excluding the experiments with very coarse gravels (W3 and W4) and very fine gravel (W9), the average slope is 31% for the Wooster model and 56% for the new model. Individual experiments are discussed below.

Model performance for individual Wooster et al. [88] experiments is shown in Figures 2.19-2.28. Data for the low and medium-feed experiments is shown by open circles. The Wooster predictions for $F(z)$ are shown by dash-dot black lines. The predictions of the new constant-trapping model are shown by the solid red lines. These figures can be initially hard to decipher. To judge the performance of the model for F_o, compare the predicted value of F near the surface with the maximum measured value. To judge the performance of the β model, compare the slope of the line with the trend in the data.

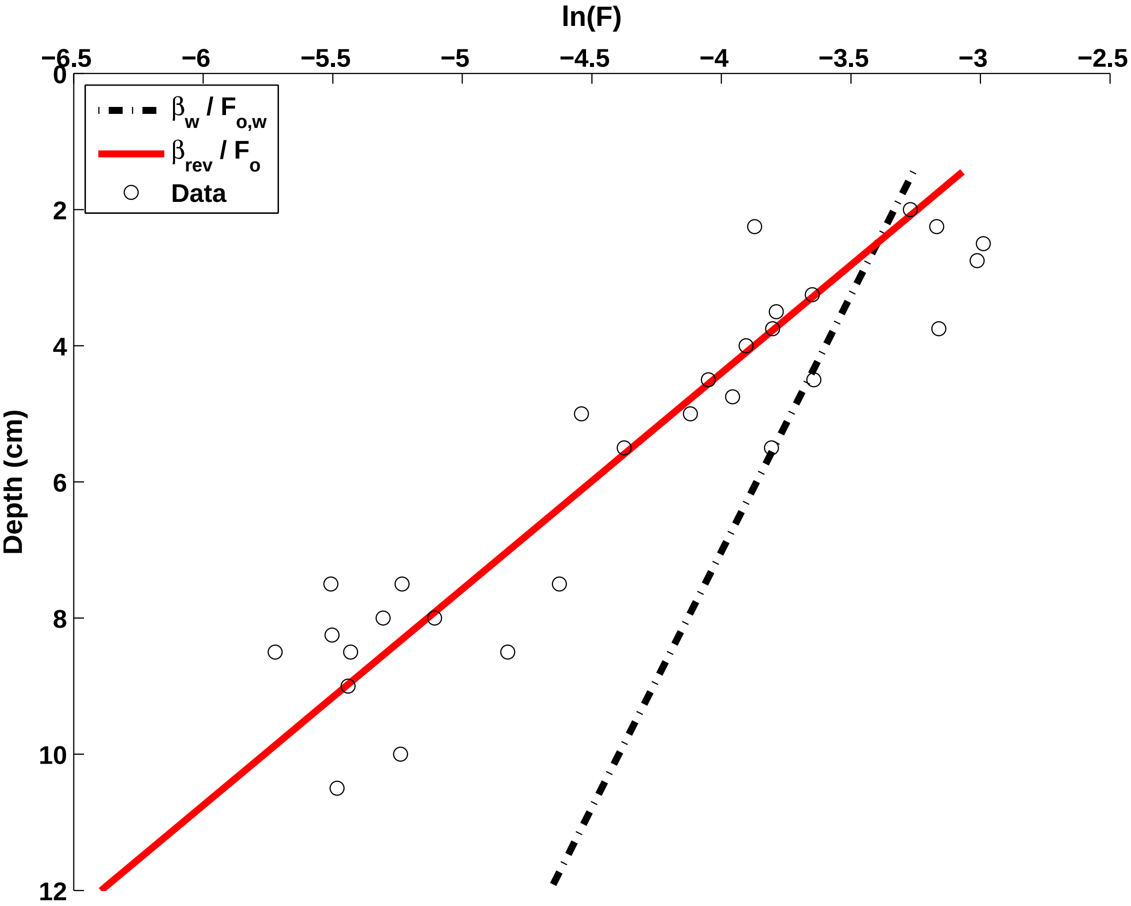

Figure 2.19: Model results for Wooster experiment W1 (medium fine gravel). The lines show the results of the Wooster model (dash-dot black) and the new constant-β model (solid red line). The data are from the Wooster et al. [88] low-feed and medium-feed experiments. The legend entries refer to the two coefficients of the exponential fit.

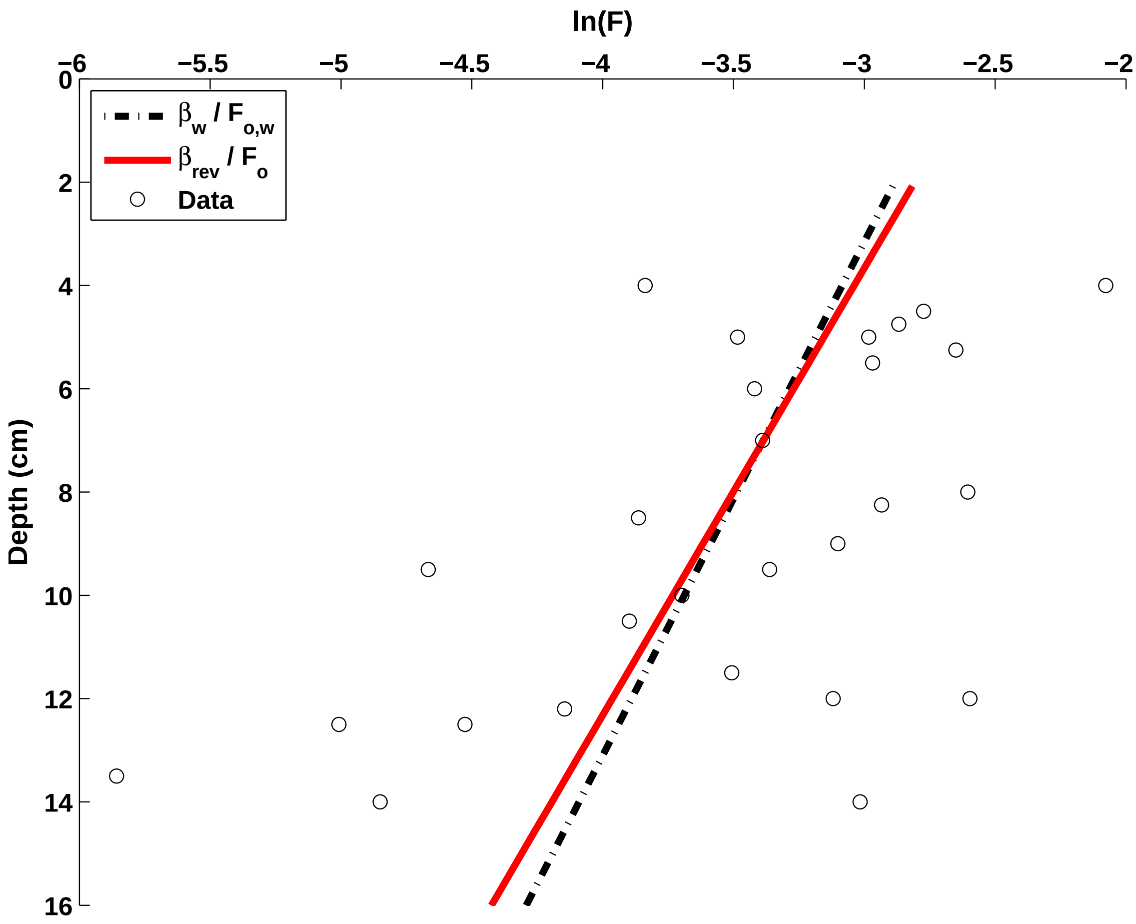

Figure 2.20: Model results for Wooster W2 (coarse medium gravel)

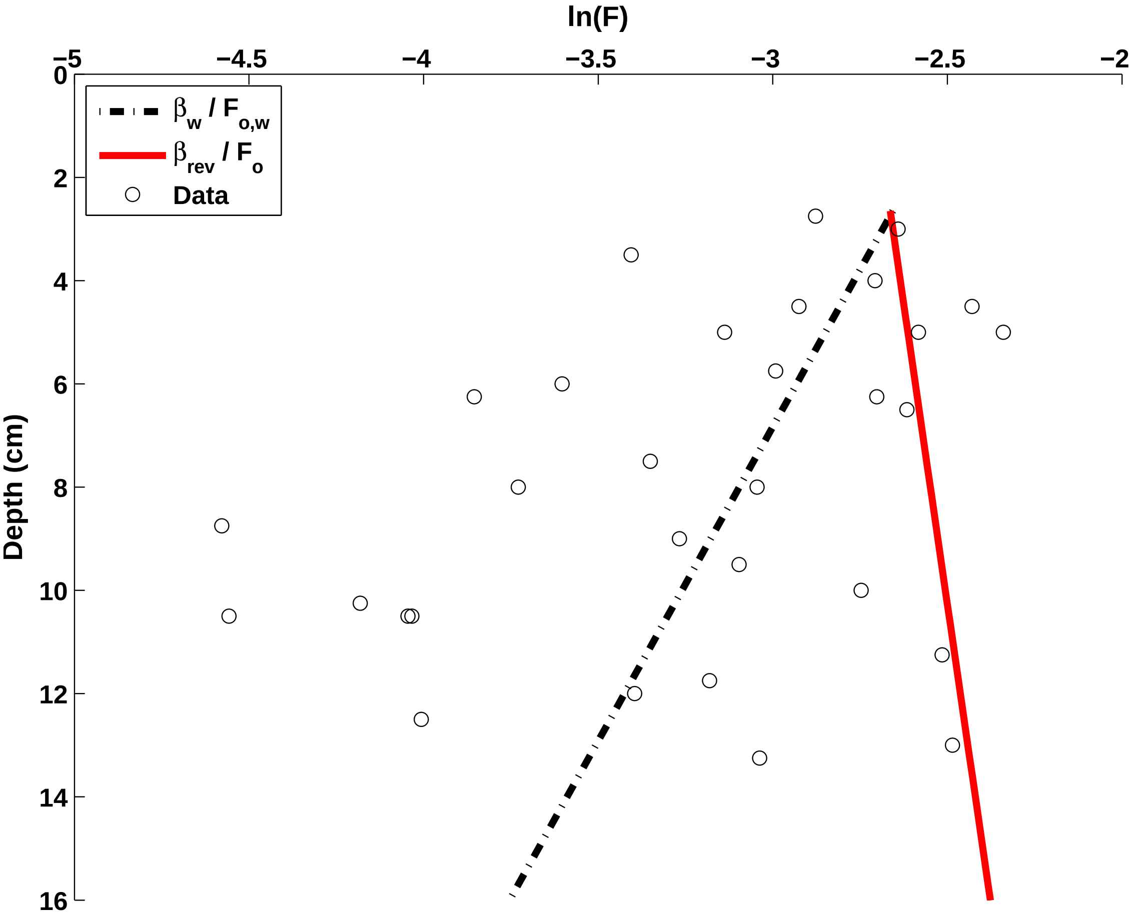

Figure 2.21: Model results for Wooster W3 (coarse gravel).

The new constant-β model performs as well or better than the Wooster model at passing through the high values of $F(z)$ near the surface. This suggests that the model for F_o (equation (2.34)) improves on the Wooster model, $F_{o,w}$.

The two models for β have different strengths and weaknesses. The predicted value of β_{rev} was negative for coarse gravels experiments W3 ($D_{15}/d_{85} = 19$, Figure 2.21) and W4 ($D_{15}/d_{85} = 32$, Figure 2.22). The new2 modelalso performed poorly for the finest gravel experiment, W9 ($D_{15}/d_{85} = 5.8$, Figure 2.27). At moderate grain ratios, the model for β_{rev} matched the slope of the data better than (W1, W5, W6, W7, and W8) or as well as (W2 and W10) the Wooster model. This suggests that the model for β_{rev} is good for $7 < D_{15}/d_{85} < 14$ but not outside this range.

Figures 2.29 - 2.31 show predictions for the the constant-β and the variable β models for the Gibson no-flow experiments. The Wooster models for β_w and $F_{o,w}$ are underestimates for all three experiments. The new model for F_o is better at predicting the sand fraction near the

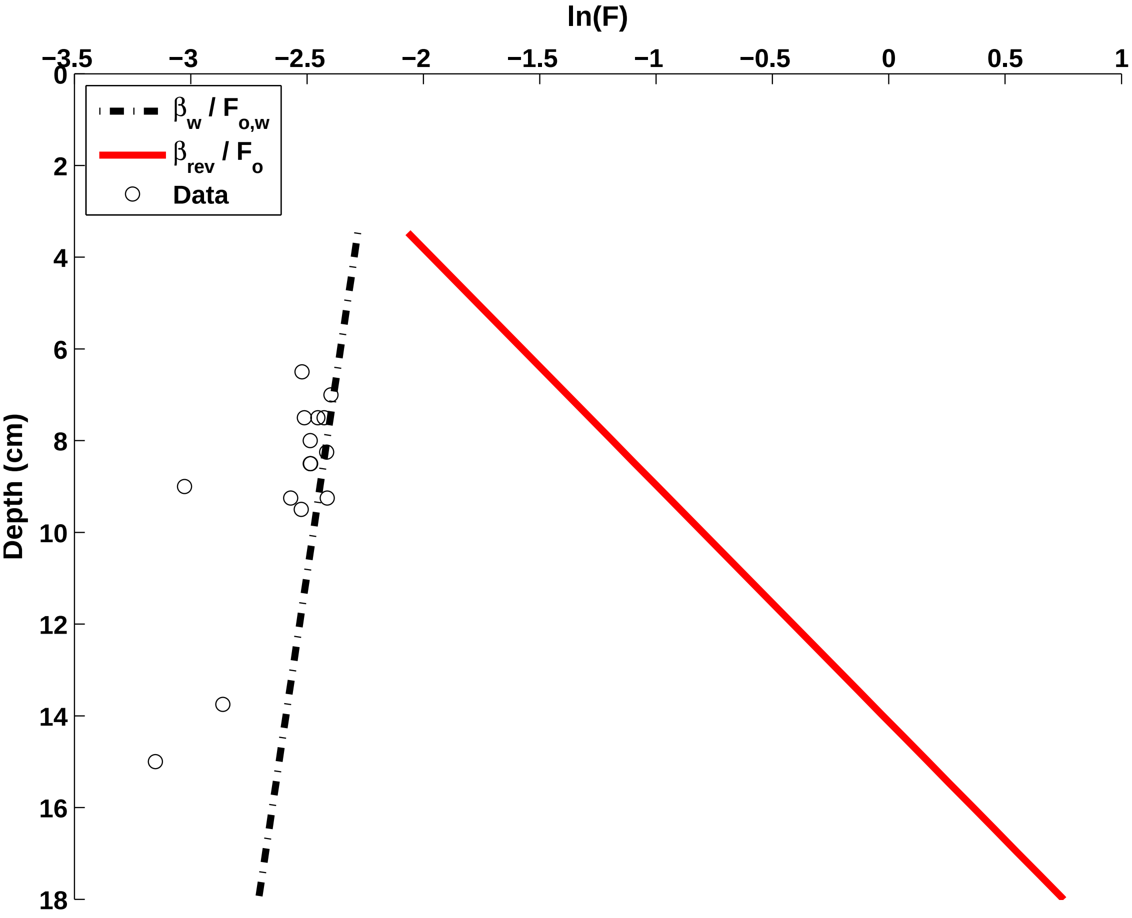

Figure 2.22: Model results for Wooster W4 (very coarse gravel), with the analytic solution.

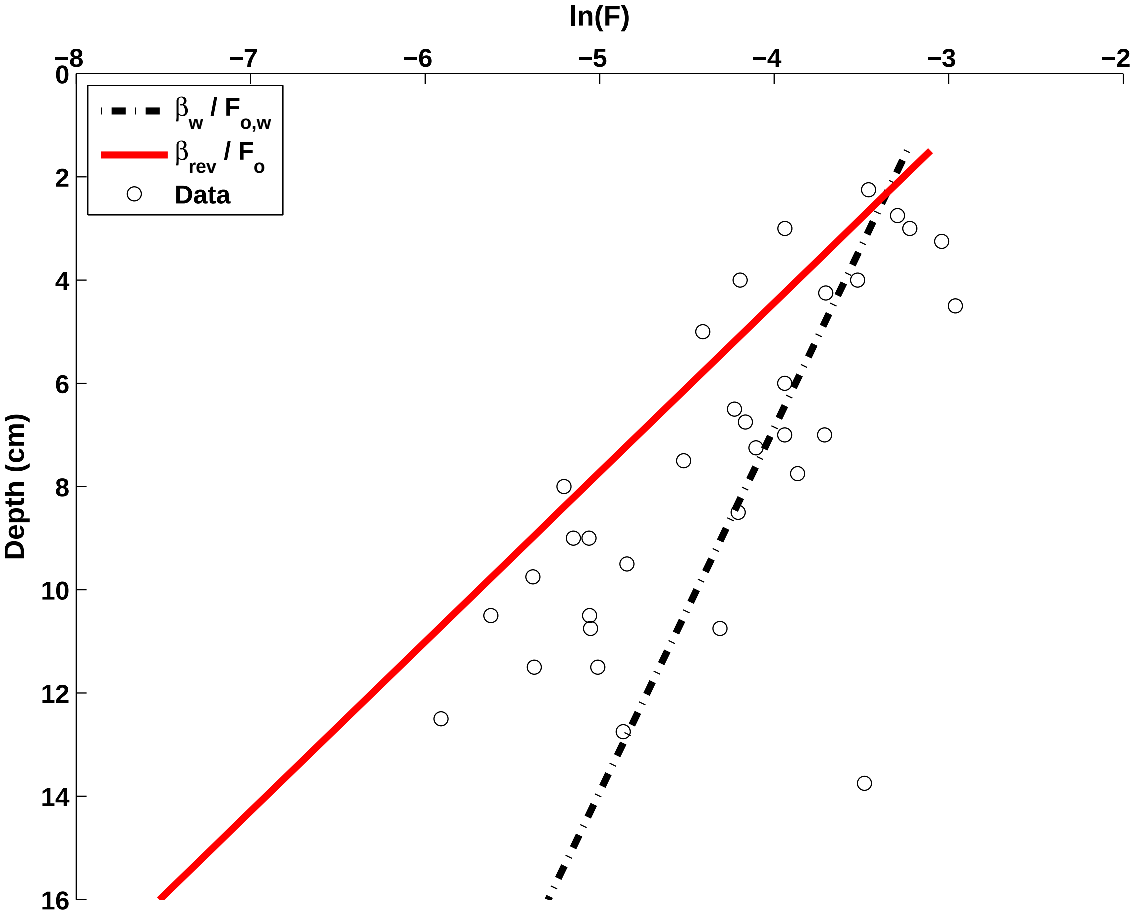

Figure 2.23: Model results for Wooster W5 (medium fine gravel)

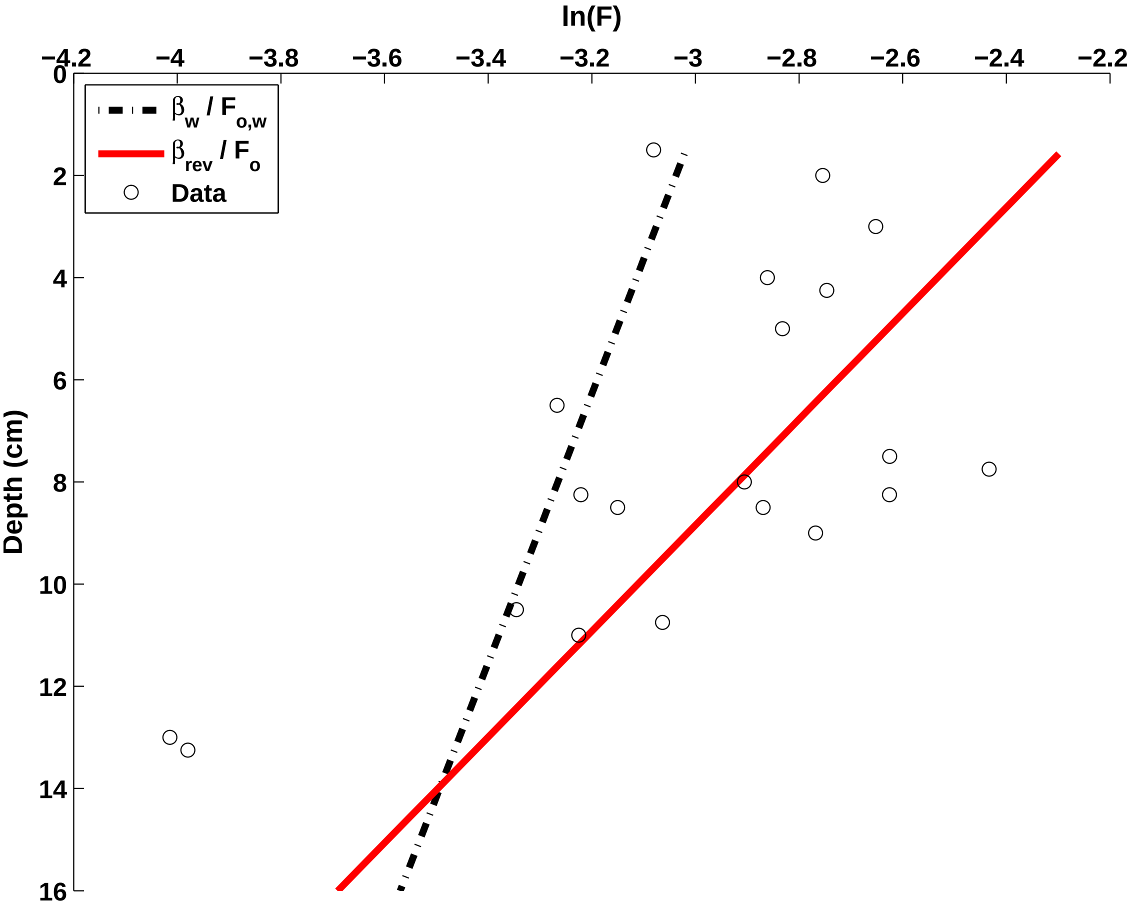

Figure 2.24: Model results for Wooster W6 (very narrowly graded gravel)

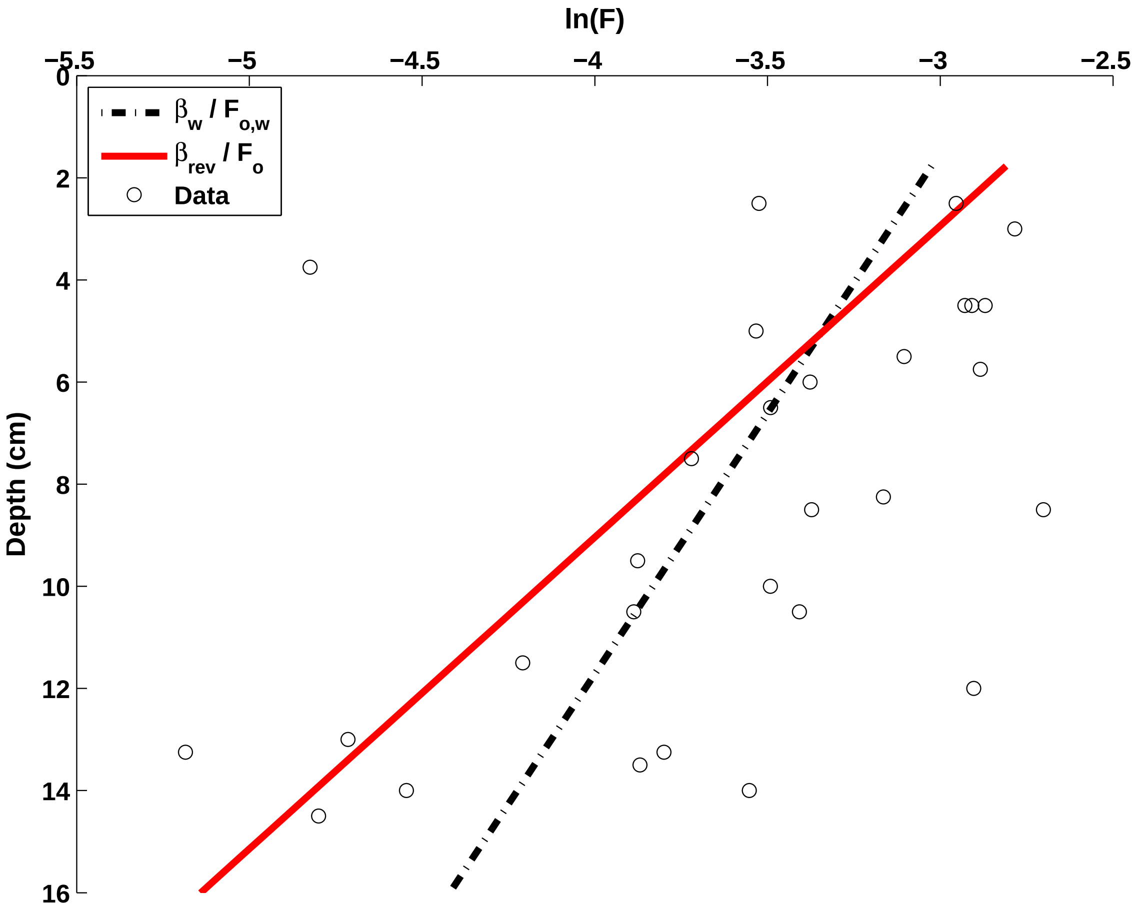

Figure 2.25: Model results for Wooster W7 (medium gravel)

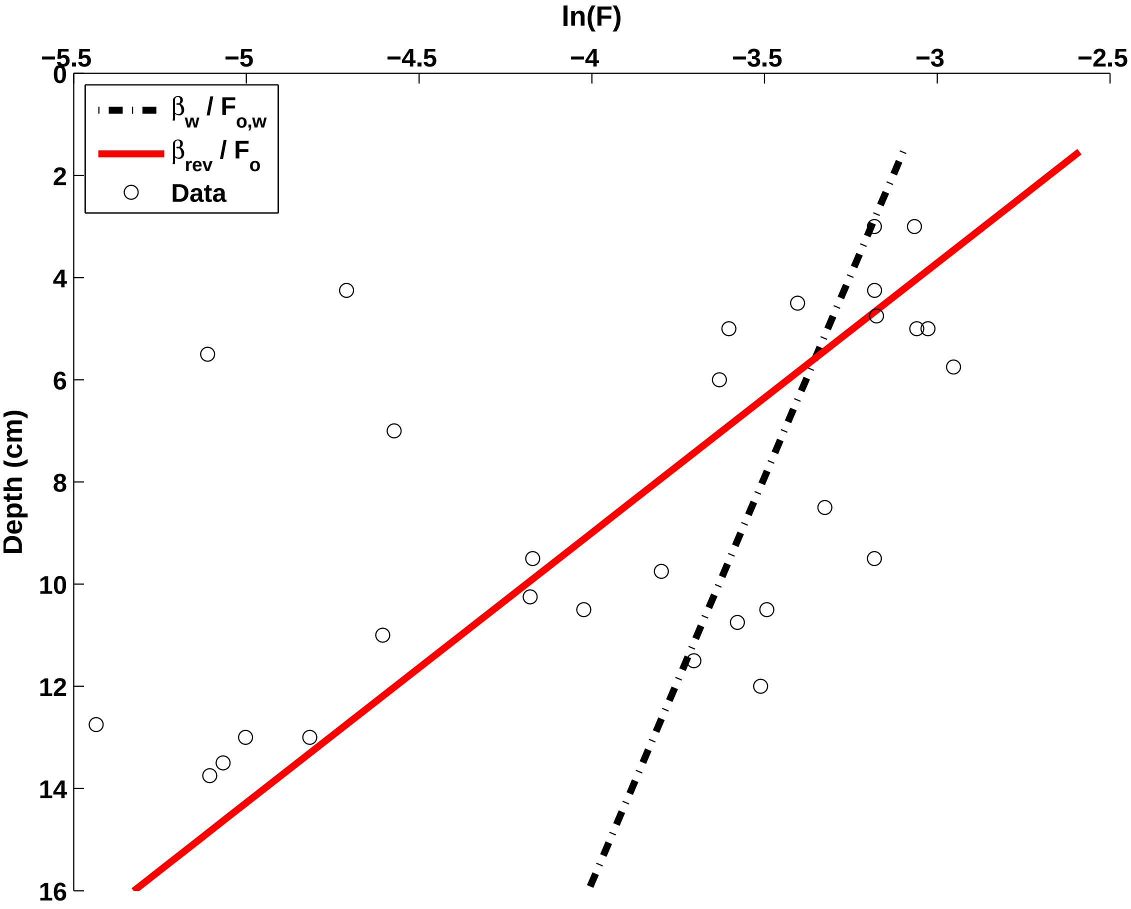

Figure 2.26: Model results for Wooster W8 (narrowly graded medium gravel)

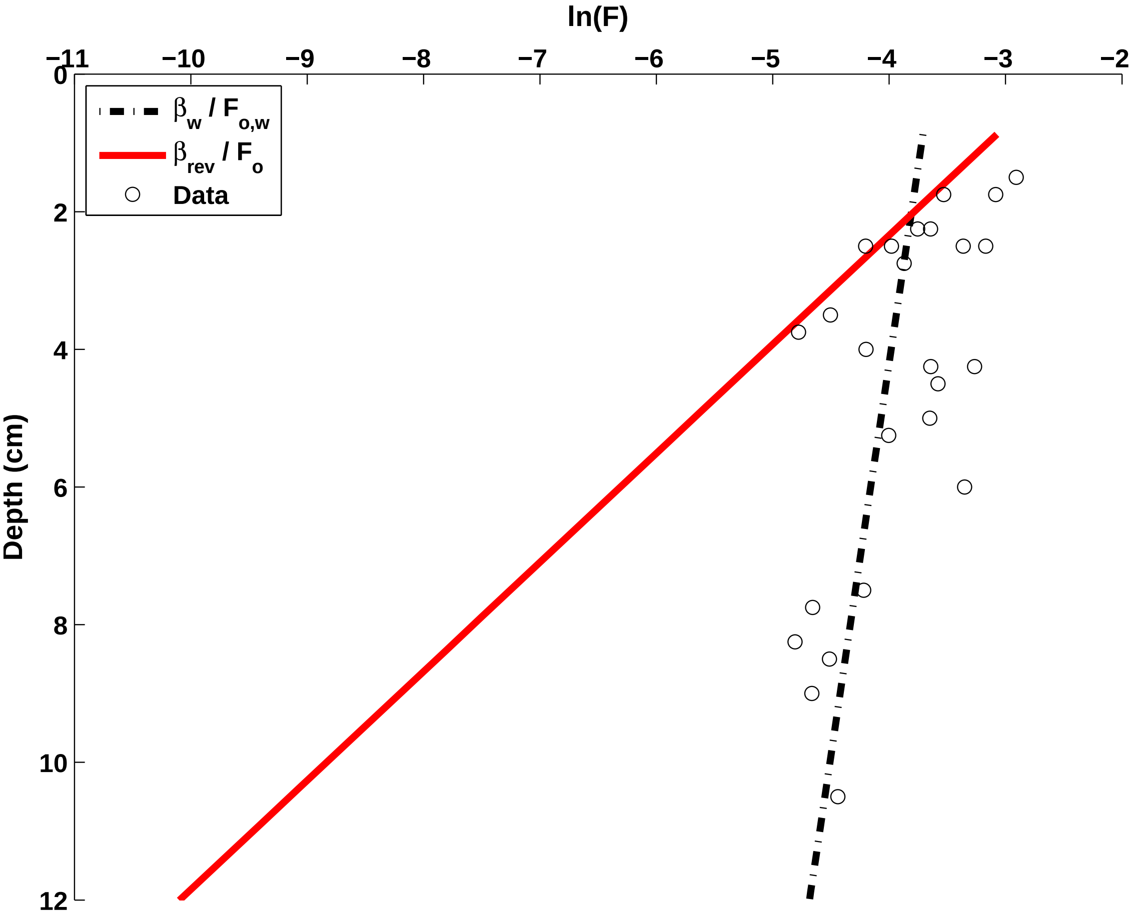

Figure 2.27: Model results for Wooster W9 (very fine gravel). The medium-feed experiment did not work for W9 so the data are excluded.

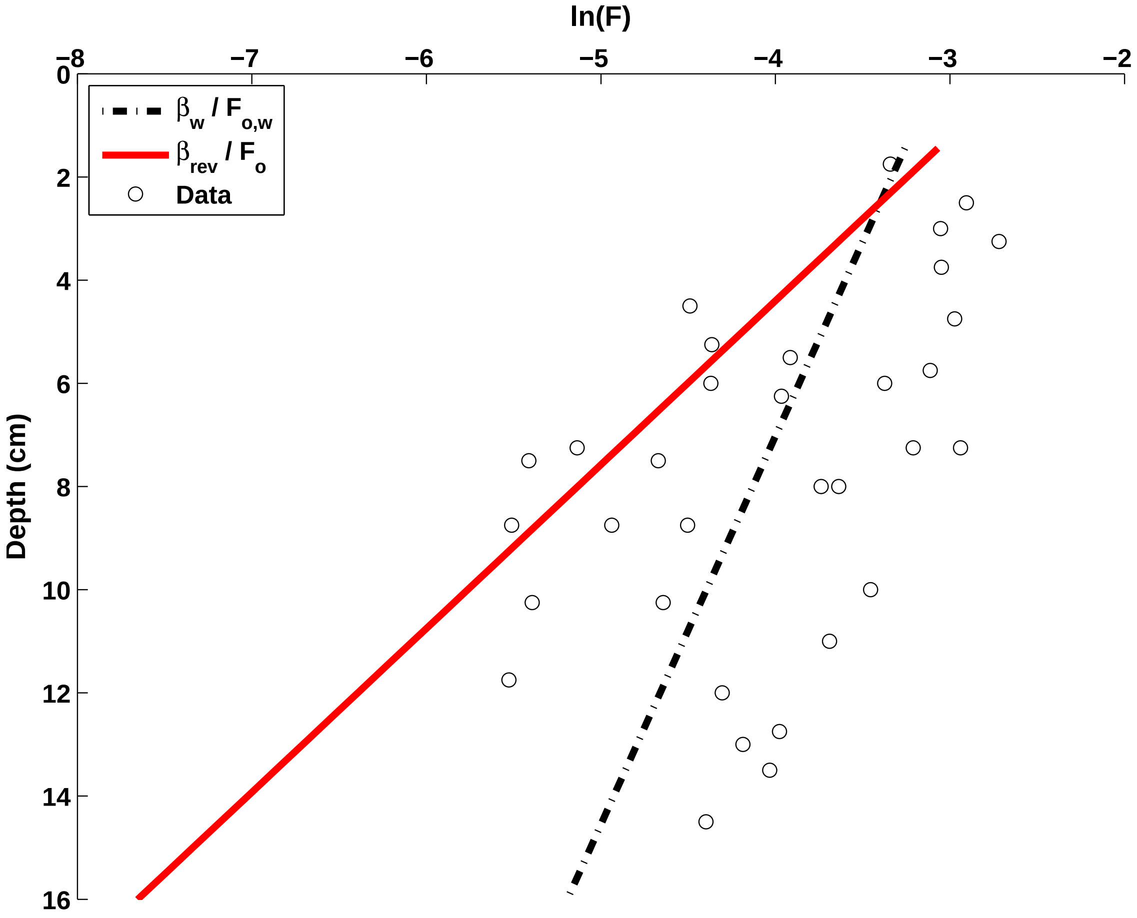

Figure 2.28: Model results for Wooster W10 (medium fine gravel)

	Wooster			New model		
Expt.	Slope	Intercept	r^2	Slope	Intercept	r^2
G1	0.08	0.03	0.67	0.61	0.01	0.89
G2	0.16	0.05	0.29	0.52	0.03	0.41
G1nf	0.08	0.03	0.56	0.71	0.01	0.97
W1	1.68	-0.02	0.76	1.15	0.00	0.77
W2	1.44	-0.00	0.27	1.33	0.00	0.27
W3	0.74	0.01	0.27	-1.58	0.16	0.11
W4	2.05	-0.10	0.59	-0.05	0.10	0.27
W5	1.13	-0.00	0.52	0.97	0.01	0.52
W6	1.81	-0.02	0.26	0.43	0.03	0.21
W7	0.97	0.01	0.29	0.66	0.02	0.26
W8	1.43	-0.02	0.38	0.60	0.01	0.35
W9	2.05	-0.01	0.37	0.88	0.01	0.42
W10	1.40	-0.00	0.39	1.10	0.01	0.39

Table 2.5: Comparison of the performance of the Wooster model and the new constant-trapping model. The slopes, intercepts, and r^2 values are taken using linear regression through the modeled and measured values of $F(z)$ for all experiments.

bed surface thatn $F_{o,w}$. In addition, the new constant-trapping model β_{rev} is much better at matching the average trend of $F(z)$ in the experimental data. However, a constant-β model is not able to recreate the curvature seen in the data on a semilog scale (e.g. Figure 2.31).

The variable-β models were able to recreate the curvature seen in $F(z)$ data (Figures 2.29 - 2.31). Within the sand seal, there is little difference between the two variable-trapping models. The $F(z)$ functions predicted by the numerical model using both β_p and β_{th} (solid blue line) are slightly more concave downwards than the analytic solution with just β_{th} (dashed purple lines). The numerical model was able to recreate the build-up of sand on the bottom of the flume using a mass balance, which can be seen by the sharp increase in $F(z)$ around $z = 8.5cm$. The numerical model predictions for $F(z)$ close to the surface are slightly smaller than the other models because clogging occured at a depth less than $2D_g$.

The numerical model was run under several different conditions to test the effect of the pile-building model. Model predictions from these runs for experiment G2 are given in Figure 2.32. The dash-dot red curve shows model predictions without the pile-building mechanism ($\beta_p = 0$). The other three curves show model predictions with different values of K_{csf} to the effects of particle shape. More sand infiltrates the bed in the model runs with spherical particles and no pile-trapping than with the flatter particles. This indicates that the pile-trapping mechanism can have a significant impact on fines deposited deep in riverbeds. Gravel particle shape has a significant impact on the initial value of β_p, so that notably less sand infiltrates a bed of particles with $K_{csf} = 0.7$ than with rounder particles.

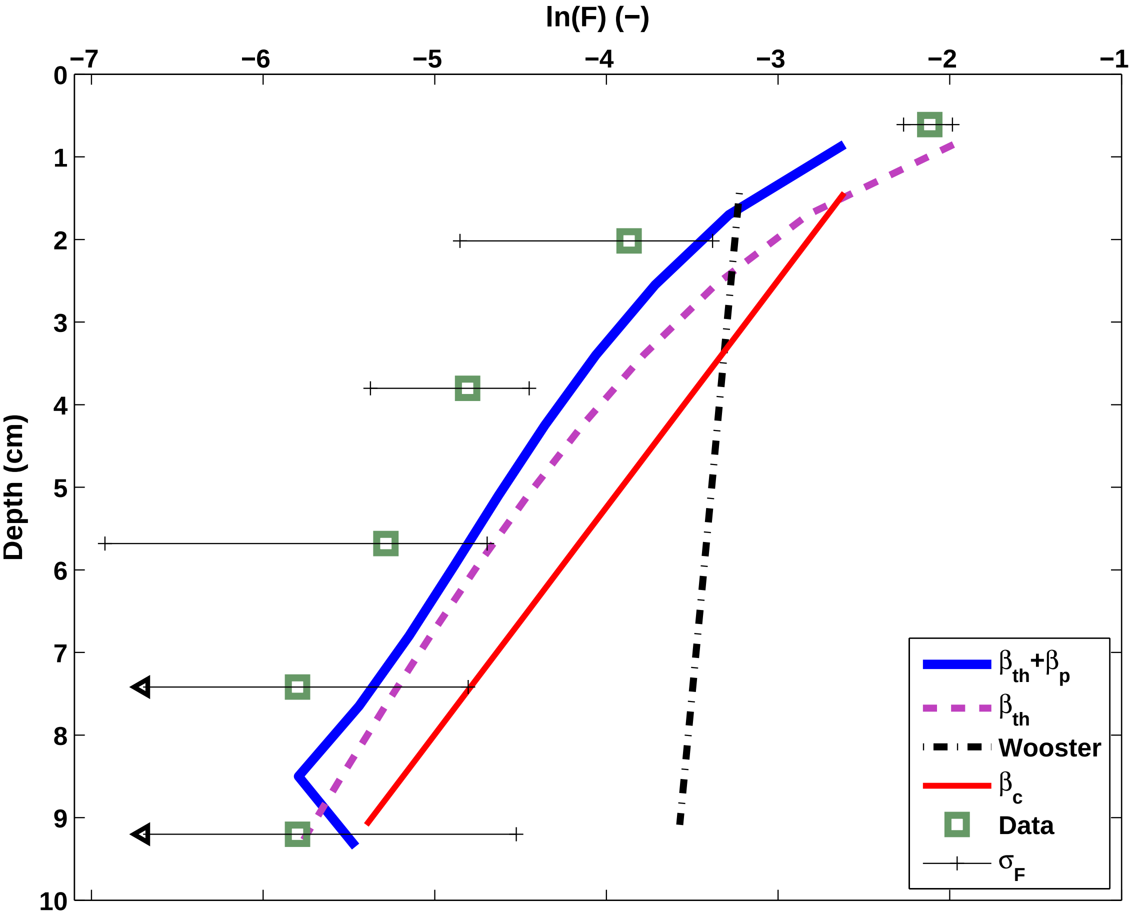

Figure 2.29: Model results on the Gibson no-flow, medium-sand experiment, for the numerical (thick solid blue), analytic (dashed pink), Wooster (dash-dot black), and new exponential fit (solid red). The green squares are data from the no-flow sample pit and the error bars denote the standard deviation of the data from the Gibson medium-sand experiment with flow.

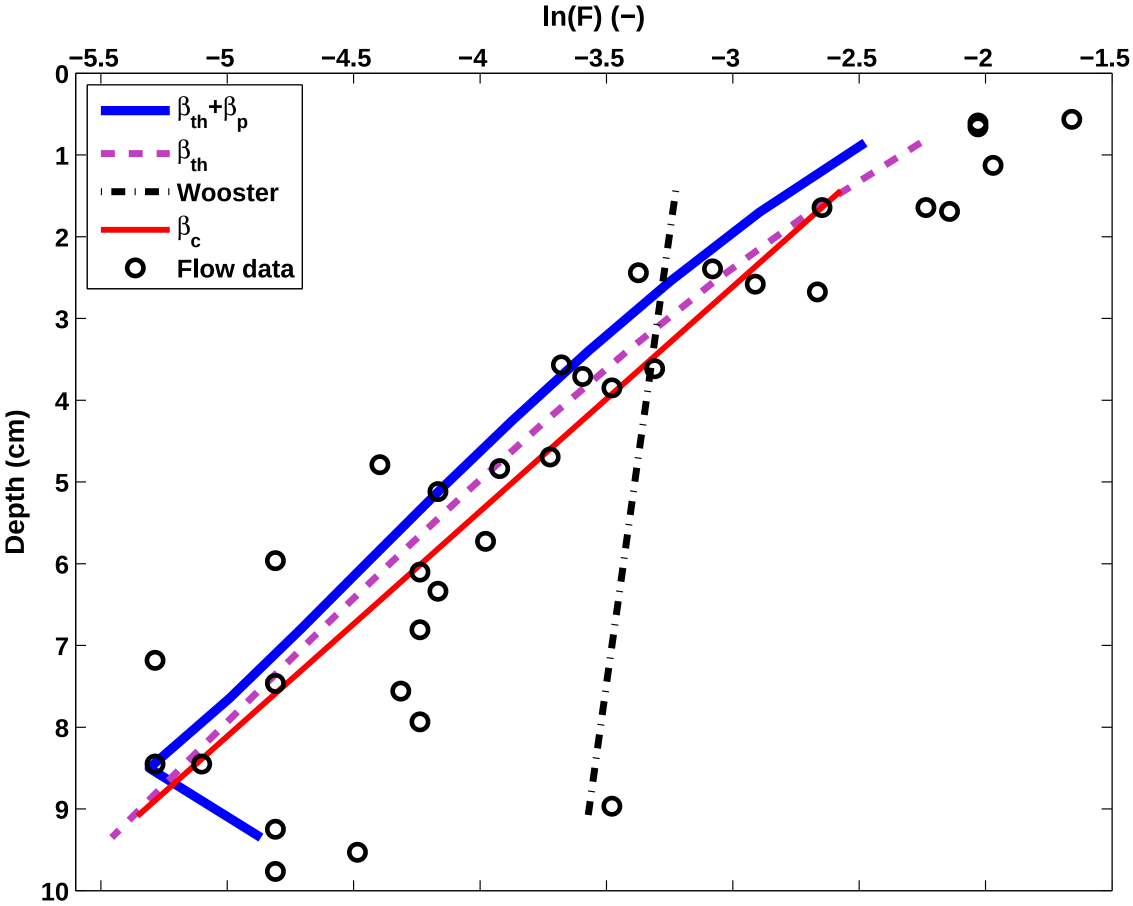

Figure 2.30: Model results for the Gibson medium-sand experiment with flow, showing the numerical (thick solid blue), analytical (dashed purple), and Wooster (dash-dot black), and revised constant-beta (solid red) predictions for $F(z)$.

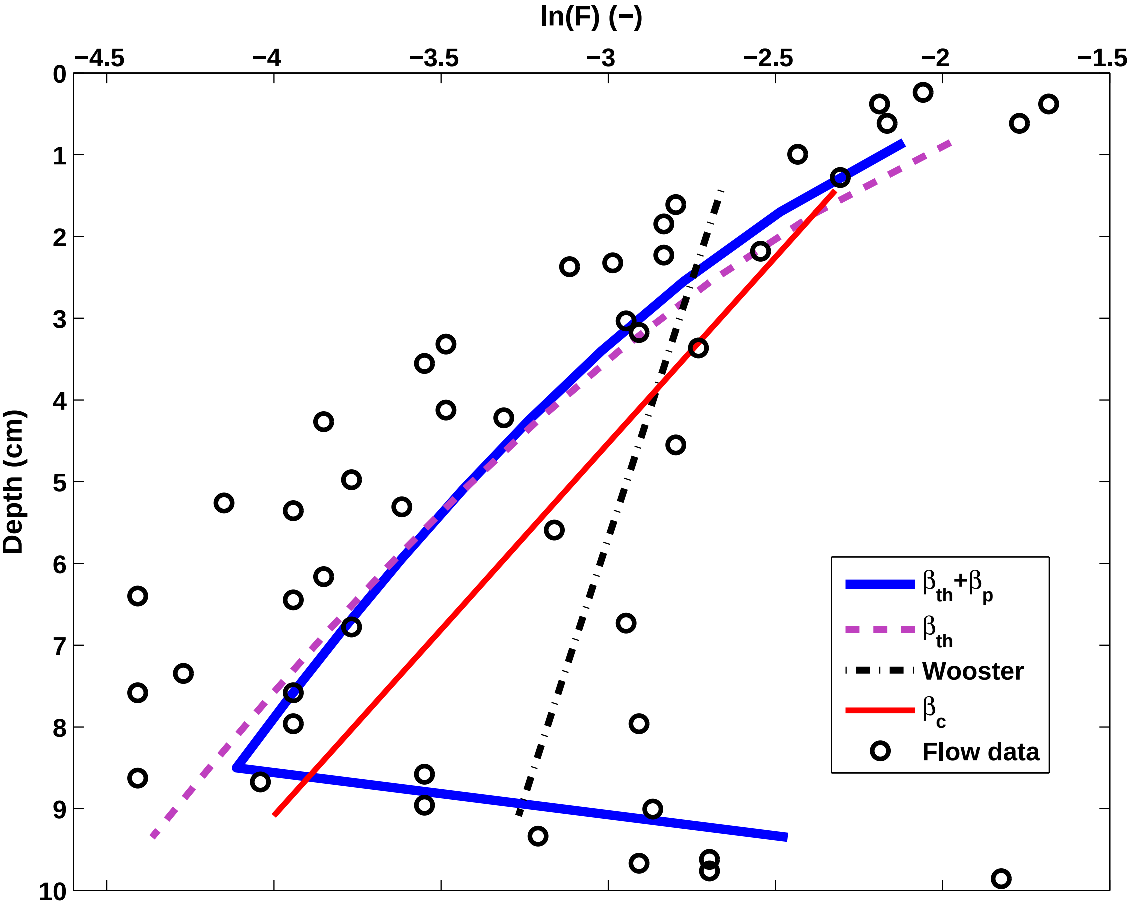

Figure 2.31: Model results for the Gibson fine-sand experiment G2, showing the numerical (thick solid blue), analytical (dashed purple), and Wooster (dash-dot black), and revised constant-beta (solid red) predictions for $F(z)$.

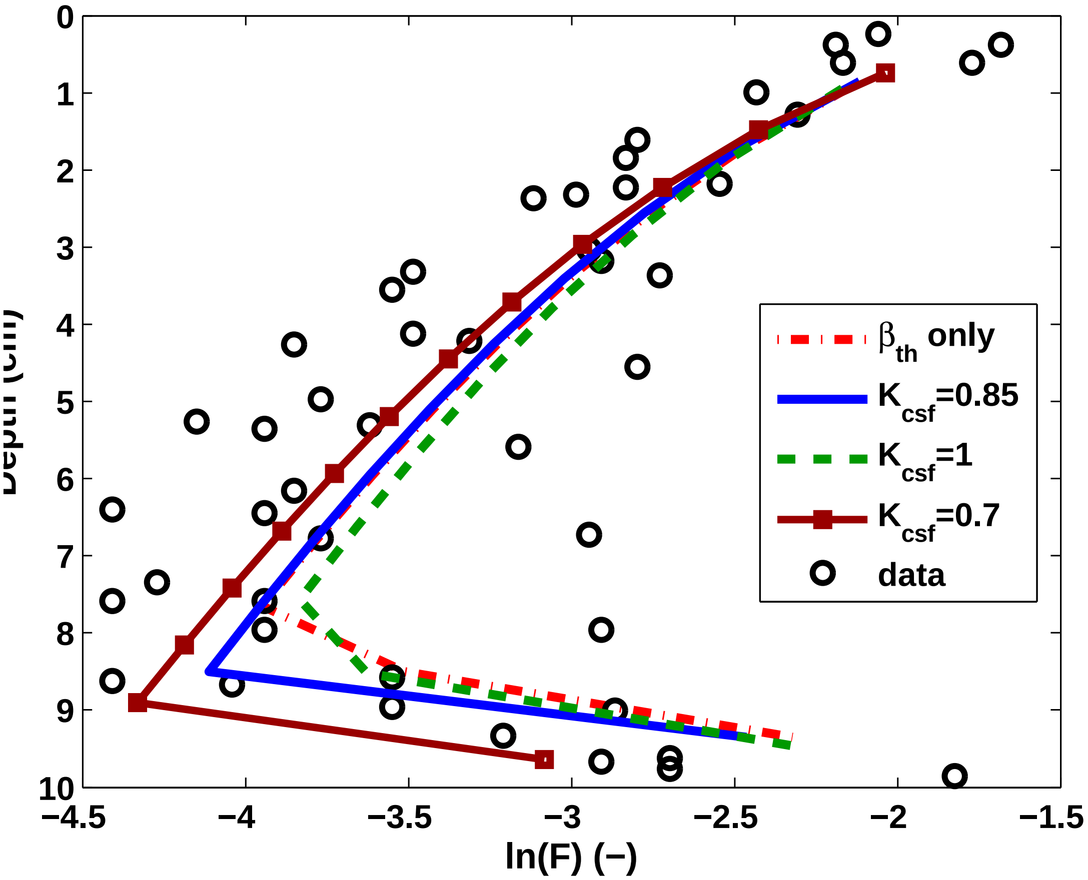

Figure 2.32: Effect of the pile-building mechanism and the choice of Corey Shape Factor on the output of the numerical model. Experiment G2 is used as an example. The dash-dot red curve is the model prediction with no pile-trapping function. The other curves represent model results using different gravel particle shapes.

The mass of sand collected on the flume bed is better predicted by the model runs with $K_{csf} = 0.7$ and $K_{csf} = 0.85$ than with spherical particles or no sand piles.

The theoretical pile-building model corresponded to the data in two ways. Using $K_{csf} = 0.85$, the initial value of $\beta_p = 0.58$ for experiments G1nf and G1. This is close to the value near $F = 0$ in Figure 2.8. The numerical model predicted that pile-building was completed at $F = 0.012$ for G1nf, around the local minimum in Figure 2.8.

2.5.2 Model results on other data

There is little specific data for $F(z)$ in a sand seal that has not been presented in this paper. Earlier studies generally did not report all of the necessary information (GSD, porosity, F, depth of sand infiltration) in order to evaluate the models for F_o and β. The new models are tested on the results of the infiltration experiment in Chapter 3.

2.6 Discussion

The Wooster et al. [88] model was the first attempt to model the sand fraction as a function of depth $F(z)$ within an infiltration sand deposit. The model is comprised of empirical expressions for β_w and $F_{o,w}$ that are functions of the porosities and grain size distributions of gravel and sand. The model is simple to use and is valid for a wide range of gravel and sand GSDs. Its predictions overlap all of the datasets used in this paper except for the Gibson et al. [31] experiments without flow, and it performs well at predicting F at moderate depths. For medium-sized gravel, the model tends to underestimate the sand fraction near the surface and overestimate it at depth. Furthermore, it does not include the effects of flow and so it overpredicts infiltration for the Gibson no-flow experiments.

There are two reasons that the Wooster model for $F_{o,w}$ underestimates the maximum sand fraction. The first is the inclusion of very coarse gravel in the analysis, which heavily swayed the empirical regressions. It may be that infiltration was not completed in W3 and W4 when the experiments were terminated, and so the maximum values of F were significantly less than F_o. The second source of error is that F_o was assumed to equal the value of F measured in the upper layers of all sample pits. If F decreases with depth, then the average value in any given layer is necessarily smaller than F at the top of that layer. The measured sand fraction should serve as a lower bound for the maximum sand fraction rather than a representative value. This is supported by the fact that in some sample pits the sand fraction is larger in a lower layer than in the top layer.

This chapter takes another approach to estimating and modeling F_o. F_o was estimated from the data both by linear regression of F vs. z and from measured values of F in sample layers that met criteria to avoid underestimation. The revised model for F_o uses a well-known particle-packing relationship from Ridgway and Tarbuck [65] and a velocity correction term to account for inefficient particle packing. The new model outperforms the Wooster model at predicting F_o. Both the new model and the Wooster model for F_o have three empirical coefficients. However, two of the coefficients in the new model are taken directly from the particle-packing relationship of Ridgway and Tarbuck [65], which has been used reliably in a different setting for decades. Therefore, the new model only has one uncertain coefficients compared to three uncertain coefficients in the Wooster model. The main drawback to the new model for F_o is that it is more complex to use because the water velocity at $z = 2D_g$ and the particle settling velocity need to be calculated. This can be simplified by replacing $u(z = 2D_g)$ with the seepage velocity in the velocity-correction term. This substitution is valid in most cases because the subsurface velocity decays quickly to the seepage velocity except for riverbeds made of coarse, narrowly-graded gravel.

The Wooster model tends to underestimate β. One cause of this is the inclusion of the (underestimated) expression for $f_{o,w}$ in the regression analysis to model β_w. The combination of these coefficients leads to good estimates of $F(z)$ at moderate depths but causes the model to underestimate F near the surface and overestimate it at depth. Another source of error is the inclusion of the coarse gravel experiments W3 and W4 and the fine gravel experiment W9 in the regression analysis. As seen in Figure 2.13, the relationships between grain size and β are very different for the coarsest and finest gravels than for sediments that fall in the range $7 < D_{15}/d_{85} < 14$. Both models have two empirical coefficients. The Wooster model performs better for the coarsest and finest gravels than it does for moderately-sized gravels because of the inclusion of these outliers in the regression analysis. However, data analysis suggests that an exponential model may not even be appropriate for the coarsest gravel.

The revised constant trapping coefficient β_{rev} avoids these two sources of error. The model is based on estimates of β from the data that did not rely on estimates of F_o. Furthermore, the coarsest and finest gravels were excluded from analysis. There was a strong linear relationship between β_{rev} and D_{15}/d_{85} for most of the gravel mixtures. Combining the model for β_{rev} with the new model for F_o leads to similar or better predictions of $F(z)$ than the Wooster model in almost all cases. However, it is only valid for $7 < D_{15}/d_{85} < 14$. The models for β_{rev} and β_w both have two coefficients.

The reason β_{rev} doesn't work if $D_{15}/d_{85} < 7$ is probably because the coarsest sand does not enter the bed and so the d_{85} of the feed sand is not equal to d_{85} in the bed. In cases where $D_{15}/d_{85} > 14$ the data suggest that an exponential model may not represent $F(z)$. A sand seal may not be forming as a significant mass of sand passes through the pore throats, yet some sand is trapped in the upper pore spaces. It may be that a different representative grain size such as d_{95} causes the throats to clog in these cases. It is also possible that pile-building rather than throat-trapping is the dominant trapping mechanism in the sand seal for these large gravels. The Gibson et al. [31] data ($D_{15}/d_{85} < 11$) suggests that throat-trapping dominates in the sand seal, and so the empirical relationship between β_{rev} and (D_{15}/d_{85}) is probably related to throat trapping. Until another infiltration model for $F(z)$ is developed that covers a wider range of D_{15}/d_{85}, the Wooster model should be used for very coarse and very fine gravels.

There is a curvature in the Gibson data for $F(z)$ when plotted on a log scale, which indicates that a constant β does not fully represent the trapping mechanism during infiltration. The Gibson data suggest that there are two trapping mechanisms, both of which cause β to vary with F. At moderate and high values of F, β increases with F. This is taken to represent the clogging of pore throats with deposited sand, which prevents further sand from passing through. At very low F, there is a sharp drop in trapping efficiency as sand deposits, which is assumed to the building of small sand piles on top of gravel particles.

The throat-trapping mechanism dominates trapping in the sand seal, and so it is more important to model this process than pile-building. An analytic solution was developed for $F(z)$ using a throat-trapping coefficient β_{th} that varies linearly with F. A linear model for $\beta_{th}(F)$ appears to be reasonable based on the Gibson data. Unfortunately, there are not enough data to develop expressions for the coefficients to this linear relationship. Using coefficients estimated from the Gibson et al. [31] data, the analytic solution using β_{th} is able to match the curvature in $F(z)$ data.

A theoretical model is developed for trapping in sand piles using geometric arguments. This model matches patterns seen in the data. Pile-building has a measurable impact on infiltration, and is governed by the gravel particle shape. In the numerical model results, the main impact of the pile-building model was to limit the sand that passed through the bed and deposited on the flume bottom. The pile-building model had little effect if the model particles were spheres because the sand piles were so small. Although pile-building affects $F(z)$, it is not the dominant trapping mechanism in the sand seal. Moreover, there is no analytic solution for $F(z)$ if the two trapping mechanisms are modeled simultanenously. Therefore, this model is not immediately useful in designing flushing flows for salmon habitat management. However, it may be useful in predicting the mass of tracers or contaminated sediment trapped below the sand seal in the riverbed.

In the process of developing an infiltration model that included the effects of flow, an explicit model for calculating subsurface flow was developed. To my knowledge this is the first explicit model to estimate flow in the upper pore spaces. The model is based on flow through the initially clean bed and cannot predict flow patterns as they are altered by sand infiltration.

2.7 Conclusions

This chapter develops and evaluates models for sand infiltration into gravel riverbeds.

The state-of-the-art model by Wooster et al. [88] for trapping efficiency and the maximum possible sand fraction is used to predict the sand fraction as a function of subsurface depth. The Wooster model poorly matches available data in three important ways. First, it does not match the sand fraction near the surface nor its overall trend with depth in conditions where a sand seal is expected. Second, it does not consider flow, which affects both maximum sand fraction and trapping efficiency. Finally, it assumes constant trapping efficiency, but variable trapping efficiency can be observed on the scale of individual pieces of gravel.

In this chapter I address these problems with one new model for the maximum sand fraction and three new models for the trapping coefficient. The maximum sand fraction model incorporates particle-packing and subsurface flow. A revised constant-trapping model is built based on gravel-sand interactions. Next, a fine-structure trapping model with an analytic solution is presented that represents variable trapping efficiency due to the clogging of pore throats. Lastly, a fine-structure model is presented with two interacting equations, one representing the piling of sand on gravel particles and other using the clogging of pore throats. These models match observations better than the Wooster model except when the ratio of gravel to sand size is very large or very small. The new constant-trapping model is simple to use and outperforms the Wooster model at predicting the sand fraction as a function of depth. The fine-structure model can additionally reproduce observations of variable trapping efficiency at different depths, although coefficients for the throat-clogging equation cannot be precisely calculated given currently available data.

The contributions of this chapter are:

- Analysis showing the Wooster model does not match observations, both in broad terms (maximum sand trapping fraction and trapping efficiency) and at finer scales (trapping efficiency).
- An analysis arguing that inclusion of outlying data, use of the wrong sediment size ratio, and the exclusion of subsurface flow and fine structure effects in their analysis cause these failures in the Wooster model.
- Data analysis showing that a constant-trapping model represents the overall trend in most infiltration data but does not capture fine-scale variability and may not work for very coarse gravel.
- Three new models for trapping coefficients based on a more appropriate grain size ratio, two of which reproduce fine structure effects.
- A new model for the maximum sand fraction that includes subsurface flow and particle packing.
- Demonstration that the new constant-trapping model matches observations better than the Wooster model.

Variable	Description	Units
C_i	Coefficient for fitting β	-
$d, (d_{15}, d_{50})$	Sand diameter (percentile diameter)	l
$D, (D_{15}, D_{50})$	Gravel diameter (percentile diameter)	l
f	Sand fraction (of total sediment)	-
F	Sand fraction (of sediment and pore space)	-
F_{max}	Maximum possible sand fraction	-
$F_{o(p,o)}$	Maximum sand fraction corrected for velocity	-
$F_p, (F_{th})$	Sand fraction in piles (pore throats)	-
h_p	The height of a sand pile	l
K	Integration constant	various
K_{csf}	Corey Shape Factor (a.k.a. K_{csf})	-
K_u	Correction factor for velocity	-
L, M, S	Particle length, width, and depth	l
q_s	Sand flux (positive downwards)	l/t
$q_{s,o}$	Sand flux into bed at $z = 0$	l/t
r_{top}	Radius of top of gravel where slope$< \theta_r$	l
t	Time	t
u	Darcy velocity of water	l/t
$V(V_{pile})$	Volume	l^3
w_s	Particle settling velocity	l/t
z	Depth into the streambed	l
$\beta(\beta_p, \beta_{th})$	Trapping coefficient (for piles or throats)	-
Δ_z	Length scale for the pile-trapping model	l
$\phi_{gr}(\phi_s)$	Porosity of gravel (sand)	-
σ	Geometric standard deviation of a grain size distribution	-
θ_r	Angle of repose of sand	-

Subscripts		
g	Geometric mean size	
gr	Attribute of gravel particles	
p	Attribute of sand pile building	
s	Attribute of sand particles	
th	Attribute of pore throat clogging	
w	Related to the Wooster model	

Table 2.6: Variables

Chapter 3

Sand infiltration into a bed with alternate bars

3.1 Abstract

Spawning salmon build nests in gravel riverbeds and deposit their eggs in them. The location and topography of these redds induce advection into the riverbed. This enhanced flow supplies dissolved oxygen and removes waste from the egg packets. The same conditions may maximize sand infiltration, reducing subsurface flow and causing the salmon eggs to suffocate. Laboratory studies and models of sand infiltration into gravel have been one-dimensional, leaving a gap in knowledge about the spatial variability of infiltration due to topographically-induced flows or sediment transport patterns.

This chapter reports on a laboratory infiltration experiment. Sand moving as bedload was infiltrated into a gravel riverbed with alternate bar topography under conditions of minimal gravel transport. Bed samples were collected to quantify spatial variability of sand infiltration. The sand fraction, thickness of the sand seal, and total mass of infiltrated sand are related to hydraulic variables, morphologic units, sediment transport, surface deposition, and grain size distribution of sand. The measured mass of sand and thickness of the sand seal are compared with predicted values from the one-dimensional models presented in chapter 2. A report is given of the unexpected discovery of subsurface, lateral sand transport through a gravel bar.

3.2 Introduction

Salmonids choose redd sites based on substrate quality, bed morphology, and flow conditions. The ideal substrate is coarse gravel with little sand, silt, and clay [40]. Redd sites are clustered in shallow, fast-moving water where bed morphology induces significant hyporheic flow or downwelling, such as in riffle crests (Figure 3.1) e.g. [30, 51]. The redd-building process removes about 40% of the fine sediment from the bed substrate [41]. A completed redd has a sinusoidal shape that directs flow into its upstream face (Figure 3.2). [20]. Together, the cleaner gravel and the advection induced by redd morphology increase subsurface velocities [92]. This flow may also increase sand infiltration into the face of the redd. Infiltrated sand will subsequently trap silt and clay, reducing hyporheic exchange and decreasing the survival-to-emergence of the salmon eggs [10, 6]. Currently, there is limited understanding of the effects of three-dimensional topography and flowfields on sand infiltration into gravel riverbeds. This lack of knowledge makes it difficult to estimate spatial variability in bed permeability, particularly in the redd, and to make management decisions to limit negative impacts of fines.

There are two definitions of the sand fraction used in this chapter. Earlier studies define the sand fraction f as the volume of sand as a fraction of the total volume of sediment. In this chapter, F is defined as the volume of sand as a fraction of bed volume (sediment plus pore space). There is a simple transformation between f and F involving the porosity of clean gravel, ϕ_g:

$$F = \frac{f(1-\phi_g)}{1-f}. \tag{3.1}$$

Sand infiltration deposits in a riverbed with topography are likely to be similar to infiltration deposits seen in one-dimensional experiments, and have been frequently studied e.g. [45, 5, 17, 18, 88]. If the ratio of mean diameters of gravel and sand size is in the range of 10-30, sand particles will be caught in the upper pores rather than settle through the bed. This creates a sand seal, which prevents further deposition of sand into the riverbed. Several laboratory studies have found that the bottom of the sand seal is at a depth of $2.5D_{90} - 5D_{90}$, where D_X is a length larger than the diameter of X percent of the gravel grains [17, 5]. Beschta and Jackson [5] found that the mean fine sediment content in a sand seal is $\bar{f} = 2-8\% (\bar{F} = 1.5-5.5\%)$ of total sediment by volume, where the overbar indicates mean value.

Recent studies have found small amounts of sand deep in the riverbed and suggested that the volumetric sand fraction F decays exponentially with depth in the riverbed [31, 88]. Wooster et al. [88] modeled the sand fraction as a function of depth z as:

$$F(z) = F_o e^{-\beta\left(\frac{z}{D_g}-2\right)}, \tag{3.2}$$

where F_o is the maximum sand fraction, β is a dimensionless decay coefficient, D_g is the geometric mean gravel diameter, and the profile is offset a distance of $z = 2D_g$ into the riverbed to account for winnowing. This exponential model conflicts with the earlier description of the sand seal, which had a defined bottom e.g. [5]. In this study, it is assumed that the defined bottom of the sand seal is related to a visual threshold, where the sand fraction appears to be negligible below a certain F. This value will be assigned later in the chapter and equated with the bottom of the sand seal.

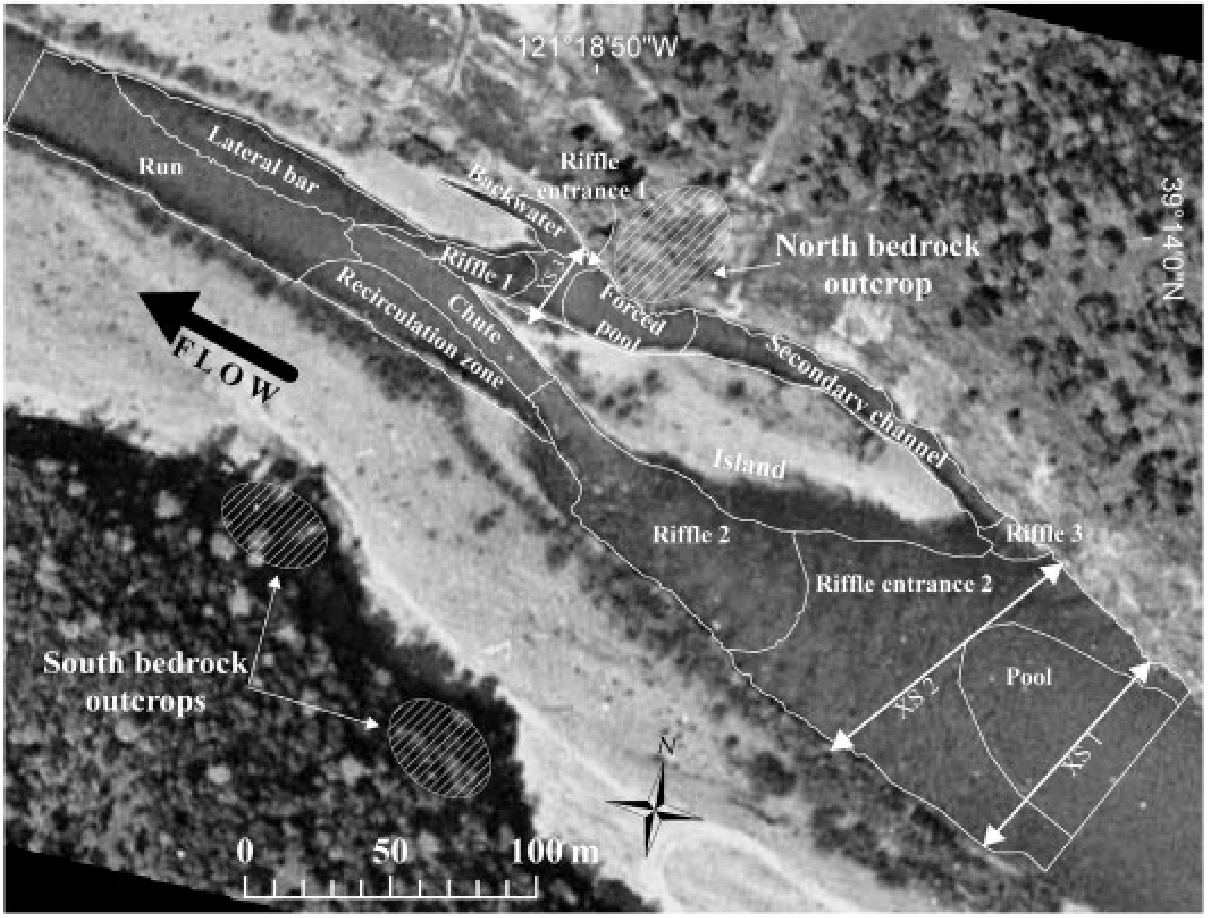

(a) Morphological Units

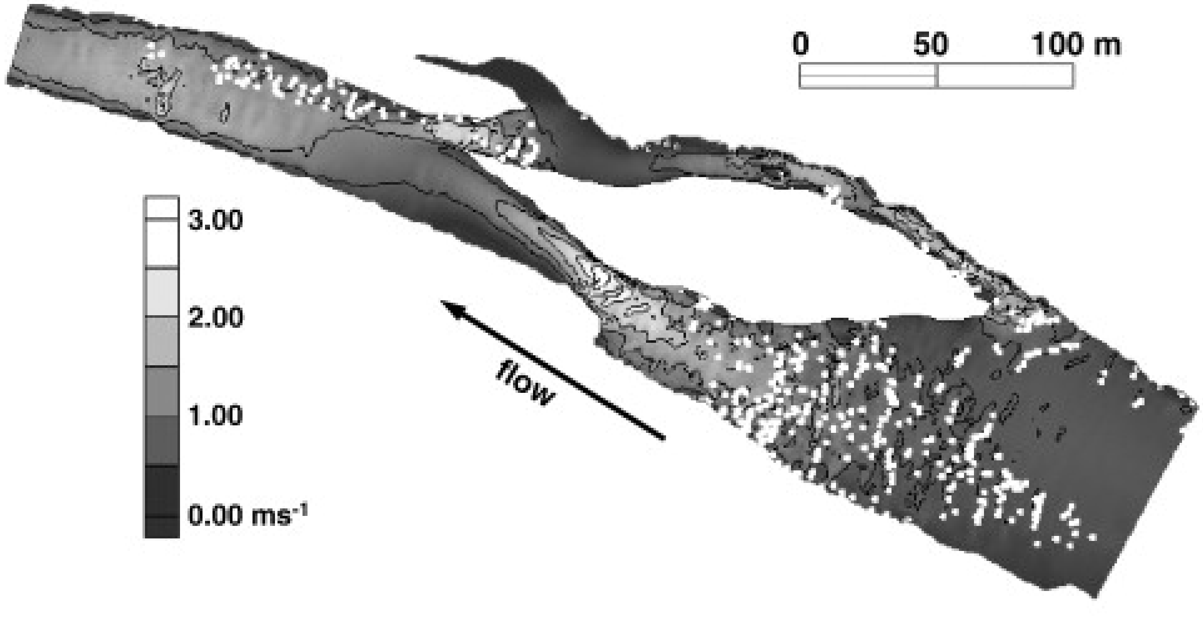

.

(b) Spawning sites and water velocity

Figure 3.1: Spawning sites (white dots) in a stretch on the Yuba River, California from [51]

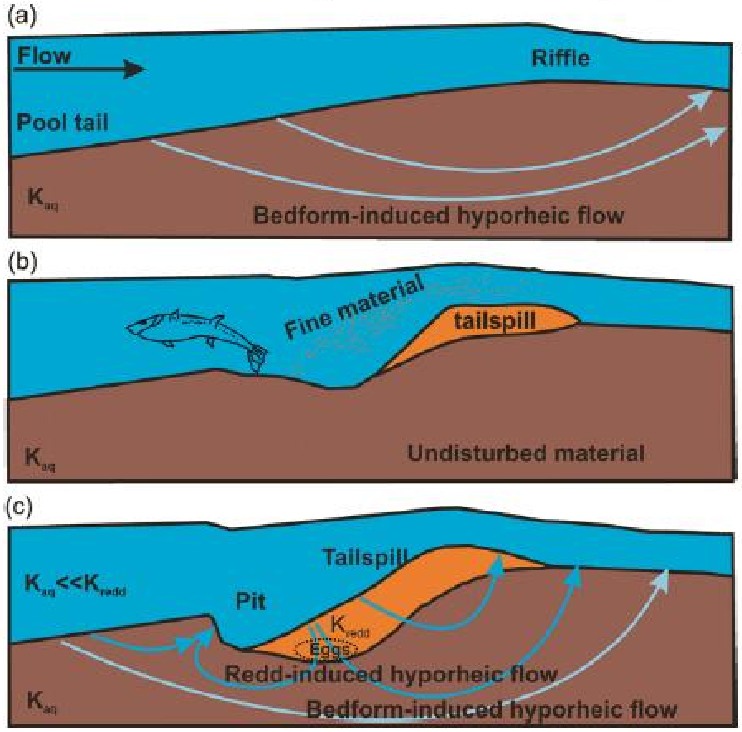

Figure 3.2: An idealized map of downwelling and upwelling patterns around a salmon redd. Figure taken from Tonina and Buffington [79].

Wooster et al. [88] infiltrated sand into nine different gravel mixtures and developed empirical expressions for the coefficients in equation 3.2 as functions of the grain size distribution. Wooster et al. [88] used the alternate definition of the sand fraction, f, and presented their model as:

$$f_{o,w} = (1-\phi_g)\frac{(1-\phi_s)\phi_g}{1-\phi_s\phi_g}\left[1 - exp\left(-0.0146\frac{D_g}{d_g} + 0.0117\right)\right] \tag{3.3a}$$

$$\beta_w = -0.0233\sigma_g^{1.95}\left[\ln\left(\frac{D_g\sigma_g}{d_g}\right) - 2.44\right], \tag{3.3b}$$

where the subscript w denotes the Wooster model, ϕ_s is the porosity of sand, D_g and d_g are the geometric mean gravel and sand diameters, and σ_g is the geometric standard deviation of the gravel grain size distribution. The Wooster coefficient $f_{o,w}$ for the maximum sand fraction can be translated into F_o using equation equation 3.1. Wooster built these relationships using sediment that spanned the ranges of $12 < D_g/d_g < 50$, $1.17 < \sigma_g < 1.9$, and $0.40 < \phi_g < 0.56$.

In chapter 2, revised models were developed for F_o and β as functions of the subsurface velocity and the grain ratio D_{15}/d_{85}:

$$\beta_r = -0.02\frac{D_{15}}{d_{85}} + 0.41 \tag{3.4}$$

$$F_{o,r} = 0.8\phi_g(1-\phi_s)\left(1 - 2.35\frac{d_{85}}{D_{15}} + 1.35\left(\frac{d_{85}}{D_{15}}\right)^2\right)K_u \tag{3.5}$$

where K_u is a velocity-correction factor that equals the fraction of the pore space that sand is able to access when the horizontal subsurface water velocity is equal to u. The subscript r indicates the revised model. The procedure for calculating K_u is given in chapter 2, or it can be approximated as $K_u = \phi_g$. The new exponential model was developed from data that spanned the ranges $6.5 < D_{15}/d_{85} < 14$ and $19 < D_g/d_g < 34$.

It is important to determine whether these models work because the profile of $F(z)$ affects hydraulic conductivity through the bed. A rough estimate of the effect of the sand seal on bed permeability can be made using sand seal descriptions from Beschta and Jackson [5] and from chapter 2. For a given well-mixed layer of sediment, the permeability can be estimated using the Kozeny-Carmen relationship:

$$k = \frac{\phi^3}{180(1-\phi)^2}D_e^2, \tag{3.6}$$

where ϕ is the porosity and D_e is the effective grain size of the sediment. The effective grain size is similar to the geometric mean but it gives greater weight to smaller particles. Smaller particles increase the total particle surface area and thus decrease bed permeability. D_e is calculated from the geometric mean diameters D_i and volumetric fractions f_i of each size fraction i in the GSD [71]:

$$D_e = \frac{\Sigma f_i}{\Sigma(f_i/D_i)}. \tag{3.7}$$

f_i for the sand fraction is equal to the earlier definition of f.

The average permeability through a series of layers with different grain size distributions, such as through the sand seal and the clean gravel below it, can be calculated by summing over all layers:

$$k_{ave} = \frac{\Sigma l_i}{\Sigma(l_i/k_i)}, \tag{3.8}$$

where l_i is the thickness of layer i and k_i is the permeability of layer i.

In a typical redd the egg pocket is 30cm below the bed surface. Based on the description by Beschta and Jackson [5], the sand seal extends from the bed surface to a depth of $2.5D_{90}$ to $5D_{90}$. Permeabilities are calculated using the gravel and sand grain size distributions used in the experiment from this chapter (figure 3.3). If the sand fraction $\bar{F}$ is 1.5% and the sand seal is $2.5D_{90} = 5.5cm$ deep, $D_e = 5.4$mm within the sand seal, $D_e = 6.4$mm in the layer of clean gravel, and the average vertical bed permeability is $3.2x10^{-2}mm^2$. If the sand seal is $5D_{90}$ thick and $\bar{F} = 5.5\%$, $D_e = 3.6$mm and the average permeability is 63% lower. If $F(z)$ decreases exponentially with depth as in equation 3.2 and F_o and β match the predictions in equation 3.4 and equation 3.5, the average bed permeability will be 40 percent lower.

There have been several studies of infiltration of suspended silt and clay into laboratory riverbeds with topography. Diplas and Parker [17] studied infiltration of suspended fine silt into a gravel bed with completely submerged alternate-bar (3-D) topography. They found that infiltration was greatest at the bar tail and where flow was most tranquil. Bedforms with 2-D topography like dunes induce flow into and out of the bed (advective pumping) [20]. This flow drives suspended fines into the faces of dunes, significantly reducing interfacial exchange with values of D_g/d_g up to 70 [64, 62]. To the extent of my knowledge, there has been no previous 2-D or 3-D laboratory study of sand infiltration into gravel.

Field studies have revealed significant spatial variability in riverbed fines. On a morphological unit scale, fine sediments accumulate preferentially in low-velocity areas such as pools and flats [28, 72, 77]. Infiltration of fine sediment from suspension is highest in areas of low velocity like channel margins, whereas fine sediment infiltrated in areas of high velocity is predominantly in the size ranges of bedload [1, 2, 28, 45, 72, 8]. In conditions under which infiltration occurs, silt and clay generally travel in suspension and sand travels as bedload. Infiltration decreases near banks where cross-channel flow is deflected away, and increases in areas that cross-channel flow is deflected towards [45, 28].

In this laboratory study, sand traveling in bedload was infiltrated into a static gravel bed with 3-D, alternate bar topography. Bed samples were collected to determine the depth and sand fraction of infiltrated sand. The main objectives of this research were to: 1) determine the spatial pattern (if any) of significant differences between measured and predicted infiltration; 2) compare spatial patterns of infiltration of sand from bedload and infiltration of silt from suspension into alternate bar topography; 3) determine if spatial patterns in infiltration can be attributed to sediment supply or pressure-induced advection pumping; and 4) test how the one-dimensional models from chapter 2 perform in a three-dimensional infiltration study.

3.3 Methods

3.3.1 The flume experiment

The sand infiltration experiment was performed on the Main Channel at St. Anthony Falls Laboratory in Minneapolis. The flume is 2.7 meters wide and 55 meters long. The bed material was a widely-graded gravel with $D_{50} = 9.2mm$ and geometric standard deviation $\sigma_{gr} = 2.0$, where the subscript gr refers to gravel (figure 3.3). The infiltrating fine material was narrowly-graded sand with $d_{50} = 0.35mm$ and geometric standard deviation $\sigma_s = 1.6$. The sand was selected so that the ratio D_{50}/d_{50} was between 20 and 30, which is necessary for building a sand seal [17].

The initial bed surface topography was built for an experiment on gravel augmentation [84, 54]. The gravel bed had 3 alternating gravel bars, starting upstream with a forced bar on the right bank (Figures 3.4-3.6). Figure 3.4 is a photograph of the bed from the bottom of the flume looking upstream. Figure 3.5 is a map-view of the bed with the average bed slope removed to show relief. The width to length ratio is strongly distorted to fit it on the page. Figure 3.6 is a view of the same bed from an angle with the depth and width scales strongly distorted. The experiment was performed at low flow and the gravel bars were emergent. The edge of water is shown by the dashed white line in figures 3.5 and 3.6. Adjacent to each bar is a narrow channel. These were connected to each other by shallow riffles that crossed the flume bed. There was a narrow backwater along the flume wall at the downstream end of the central bar. The average bed slope was 0.014.

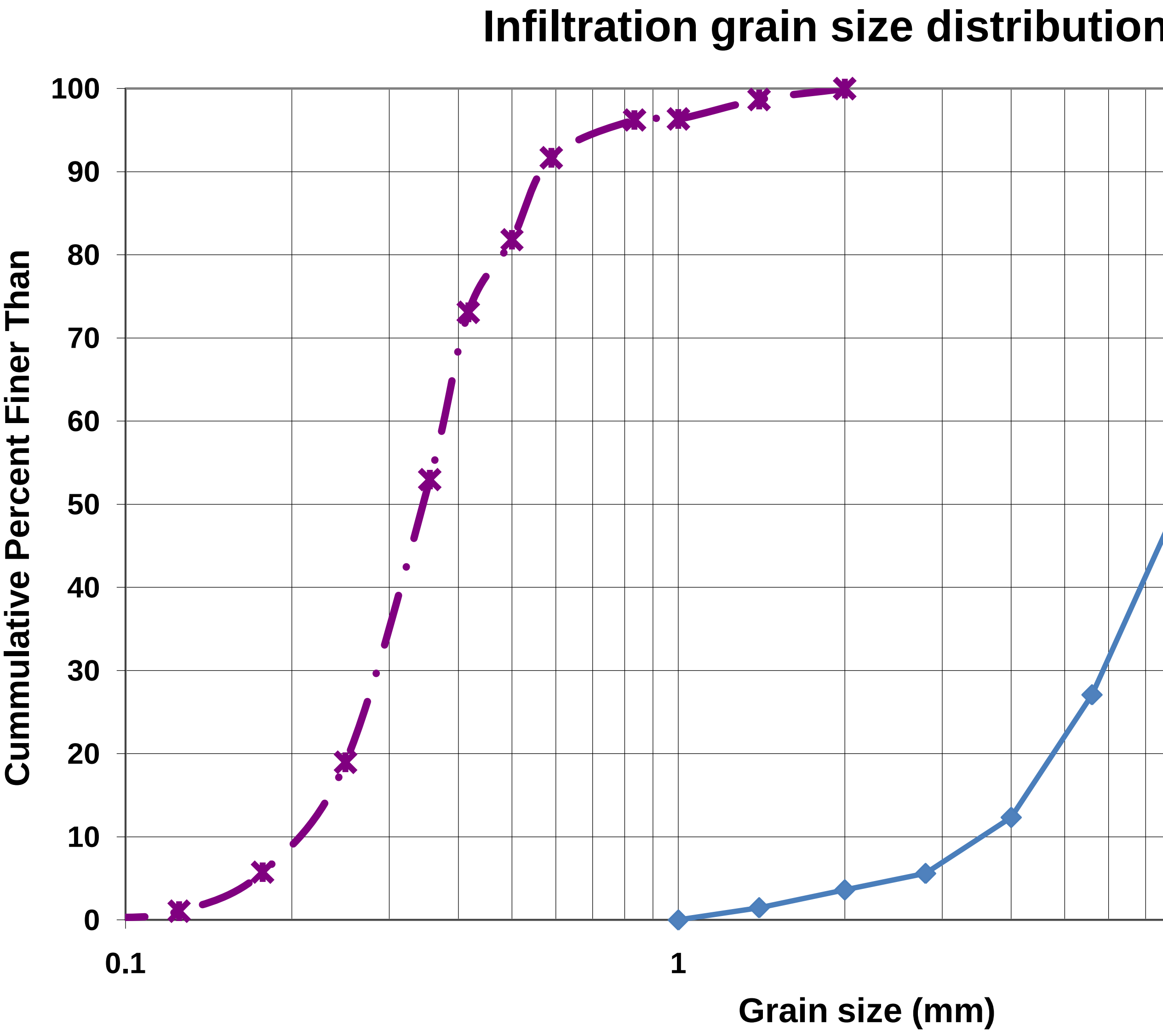

Figure 3.3: Grain size distributions of bed material and infiltrating sand.

Figure 3.4: The flume bed seen from downstream. The angled piece of wood near the bottom end is a bridge.

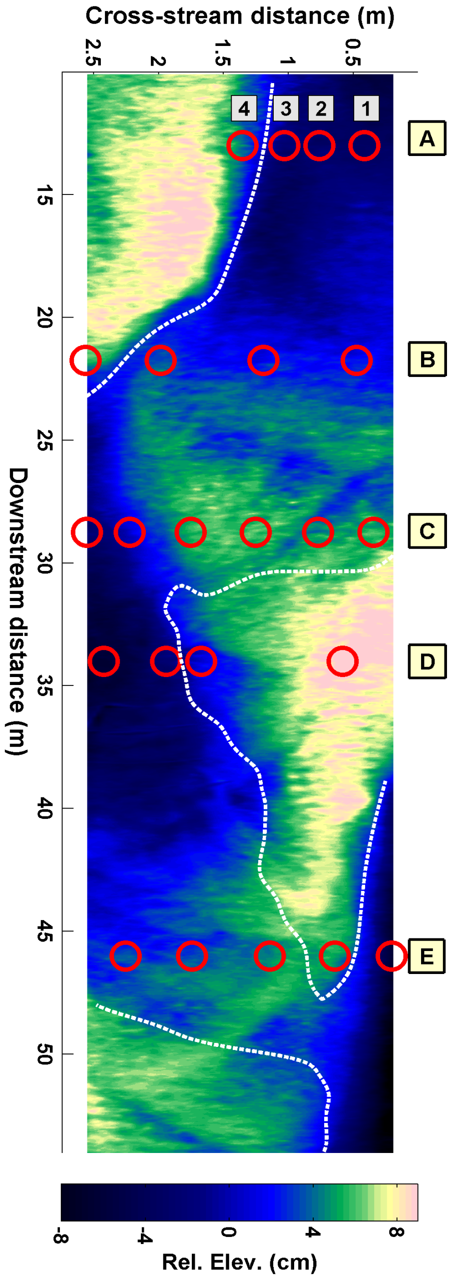

Figure 3.5: The flumebed in map view with average slope subtracted; width and length are not to scale. The dashed white line is the edge of water and red circles are sample sites. Map does not extend to the flume walls (at 0 and 274cm). Cross-sections are lettered (A-E) on the right-hand side. Sample pits are numbered as with pits A1-A4.

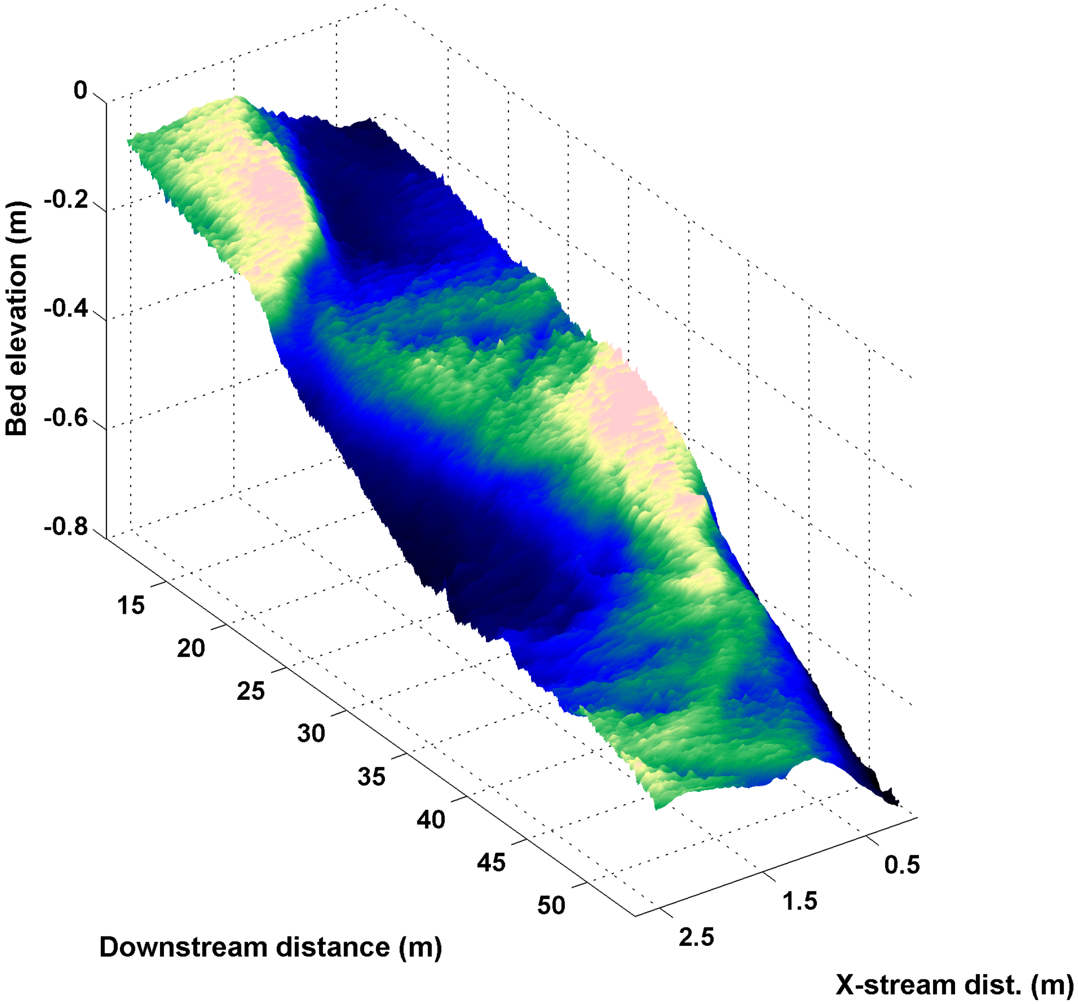

Figure 3.6: Flumebed topography; height, width, and length are not to scale. The color shows relative elevation. Map does not extend to the flume walls (at 0 and 274cm).

Pre-infiltration sampling revealed that the initial bed subsurface contained a high and spatially variable fine sediment content. These subsurface fines ranged in diameter from <0.064 millimeter up to sand in the size range of the experimental sand that was later infiltrated into the bed. Because it would have been impossible to distinguish between the sand in the background fine sediment and introduced sand, the gravel in five study cross-sections was cleaned of all fines less than 2mm in diameter. This was performed by manually removing, sieving, and replacing the gravel to match the original topography. During this process all of the gravel was mixed so that any variability in grain size between the cross-section was lost. The cross-sections were chosen to represent a variety of flow and topographic conditions (Figure 3.5). The area of gravel removed from each cross-section was 1 meter along the channel axis and the entire 2.74 meters across the channel. The gravel was cleaned to a depth of 15cm. This process had a small impact on local topography (<2cm) and may have increased bed porosity. These cross-sections were later used for sampling. They are denoted A-E, with A at the upstream end (Figure 3.5).

The water discharge was set to 35 liters per second. There was no feed of coarse material; gravel transport was minimal and limited to pea-size gravel in the deepest channels. Approximately 2000kg of sand was fed at the top of the flume over a period of 5.5 hours at a rate of 6kg/min. Sand moved downstream as bedload; there was negligible suspended sediment in samples collected at the downstream end of the flume. After the sand feed was stopped, water was left running for 24 hours in order to flush the surface of sand storage. Even after this flushing period, some patches of sand remained on the surface at the end of the experiment. In figure 3.9, these deposits can be seen on top of cross-section C. The maximum thickness of the sand deposits in this photograph was 2.5cm.

After infiltration, the bed was excavated at 4 to 6 sites in each of the 5 cross-sections. The 23 sample pits are numbered starting from the left bank facing downstream to the right (Figure 3.5). At each site, triplicate samples were collected for each of 2 to 3 layers (surface, sand seal, and below the sand seal). The division between the subsamples for the surface layer is shown in figure 3.7. Excavation was performed inside a plastic ring with diameter 25-30cm. During excavation, this ring was pushed progressively to the bottom of the excavated depth to prevent collapse of the pit wall. The bed samples were collected by scraping the bed material out with a small shovel held horizontally. This method limited loss of sand downwards due to disturbance. Excavation was stopped at the level where the sand content was visually determined to drop to a negligible fraction. If the bottom of the sand seal was not found above a depth of 15cm, excavation was stopped to avoid sampling fine sediment that had been in the bed before the experiment. At sample sites where this occured, the sand seal sample included only part of the deposit. The average sand content of the surface layer, sand seal, and the bed below the sand seal was determined by drying and sieving the sediment samples. GSD's are prone to error when sample sizes are too small, as the random inclusion or exclusion of a very large particle will alter the entire distribution. This error was limited by collecting samples greater than 1.5kg; the mass of the largest gravel particle in the samples was 3% or less of the total sample mass [7].

Figure 3.7: A sample pit with the surface layer removed from the upper right subsample. The other sections show the surface armor layer. The zip ties in the middle mark the borders between the three subsamples. The ring (made from a 5-gallon bucket) is pressed into the bed while excavating to prevent the walls from collapsing.

Bed topography was measured before and after the infiltration experiment with 10mm x 10mm topographic scans. These scans were made using a commercially-made range-finding laser that had been mounted on a cart which moved up and down the length of the flume. The laser scanner could be moved laterally across the channel to within 20cm of the flume walls. There was minor topographic change due to scour of gravel within the deepest channel (up to 3cm) and deposition of sand in patches (up to 5cm). Topographic scans (10mm x 1mm) were also performed during excavation to record the thickness of the excavated layers. Negligible scour occured within the sample cross-sections but there was sand deposition over 1cm thick at several sites. Water surface elevation was measured at three times during the experiment using a commercial ultrasonic sensor that was mounted on the moving cart. There was minimal difference in water surface elevation between these scans.

3.3.2 Numerical hydraulic modeling

Flow variabiles were estimated in order to examine the local effects of flow on infiltration and to implement the one-dimensional infiltration model for $F(z)$. Because the water was too shallow to measure velocity, flow was modeled using the Multi-Dimensional Surface-Water Modeling System (MD-SWMS) developed by the U.S. Geological Survey [47]. Bed topography and water discharge were used as model inputs. The roughness coefficient was allowed to vary within a range that was reasonable for the bed gravel GSD; roughness varied based on water depth in order to conserve mass and momentum. The output included maps of bed shear stress, water surface elevation, water depth, and downstream and cross-stream water velocity. The model was verified by comparing the predicted water surface elevation with measurements taken during the run. The average root mean square error of the difference between measured and modeled water surface elevation was less than 1%. Water depth error was very small at the site of most sample pits. The exceptions to this were in cross-section C, where the water depth was overestimated by 20-40% at all of the pits, and at pit E1 in the backwater. The error at pit E1 is irrelevent because there was no possible infiltration at that location. The mean error on discharge (difference from 35 liters per second) throughout the flume was less than 0.05%. The sample pits are listed with descriptions of the morphologic unit and the hydraulic variables in table 3.1. The site locations describe the local morphology. Channel tail is defined as the transitional area between the downstream end of the channel and a riffle, channel head is between a riffle and the upstream end of the channel, bar head is in the riffle upstream of the head of a bar, and bar is on dry gravel.

3.3.3 Estimation of variables

Porosities were calculated using a relationship developed by Wooster et al. [88], based on the standard deviation of the GSD, σ. It was built with data spanning values of σ from 1.2

Pit	Location	η (cm)	u_* (cm/s)	u (cm/s)	q_s g/cm/min	Surface deposition
A1	Channel	5.9	6.8	65	3.8	none
2	Channel	5.4	6.4	61	10.4	none
3	Channel edge	3.7	4.7	45	*BM*	patchy & thin
4	Bar	-	-	-	-	-
B1	Channel tail	3.6	4.4	42	1.1	patchy & thin
2	Channel tail	3.9	5.0	47	2.6	thick
3	Channel tail	2.4	3.7	36	3.0	none
4	Bar	-	-	-	-	-
C1	Bar head	1.9	1.8	17	*BM*	thick
2	Bar head	3.5	4.1	39	*BM*	patchy & thick
3	Riffle	1.6	4.5	46	*BM*	patchy & thin
4	Riffle	0.8	3.7	29	*BM*	patchy & thin
5	Riffle	3.5	5.5	51	*BM*	patchy & thick
6	Channel head	7.1	7.2	68	93	none, erosion
D1	Bar	-	-	-	-	-
2	Dry bank	-	-	-	-	-
3	Channel edge	3.5	5.6	53	*BM*	patchy & thin
4	Channel	7.5	8.1	77	18.8	none
E1	Backwater	*	*	*	-	-
2	Bar**	-	-	-	-	-
3	Riffle	1.3	3.0	28	0.3	thick
4	Riffle	3.1	4.7	45	0.3	patchy & thin
5	Riffle	2.7	5.5	52	3.5	none

Table 3.1: Experimental conditions at sample locations. η is water depth, u_* is shear velocity, and u is average water velocity, all predicted by MD-SWMS. q_s is the mean bedload transport rate at that location; *BM* indicates that the q_s was below a measureable level. Surface deposition is the description from the lab notebook of the surface sand deposit at the site location.

* MD-SWMS had significant error at E1.

** E2 was on the spit of a gravel bar under exposed (dry) gravel.

to 3:

$$\phi = 0.621\sigma^{-0.659} \tag{3.9}$$

Spatial variability in the GSD of riverbed gravel was eliminated in the study areas in the process of cleaning them of fines. Therefore, D_g and ϕ_g were calculated from the average grain size distribution (GSD) for gravel in the flumebed. The sand variables d and ϕ_s were calculated from the feed sand GSD. Bed permeability was calculated using the Kozeny-Carmen equation equation 3.6.

The particle settling velocity was calculated using an empirical relationship for natural particles by Dietrich [16] (equations 35a-35c in chapter 2).

3.4 Results

3.4.1 General results of flume experiment

Sand was found in all sample pits below the water line except E1, the pit in the backwater at the downstream end. The bulk average sand fraction in the sand seal $\bar{F}$ was calculated by sieving the three subsamples and taking the mean value. The mean and standard error of $\bar{F}$ from these subsamples is given in table 3.2 for each sample pit. Figure 3.8 is a map of the measured value of $\bar{F}$ in the sample pits. The marker size denotes the value of $\bar{F}$. The sample pit B2 must be excluded from analysis of measured sand fraction, because the sand seal sample was contaminated with sand from the surface deposit. The sample pit in the backwater (E1) had no contact with sand transport and so no sand infiltrated; it is also excluded from analysis. For the remaining sample pits below the water line, the flume average of $\bar{F}$ is 4.5% ($\bar{f} = 7.4\%$) with a standard deviation of 0.8% and standard error of 0.2%. In general the variability between the subsamples is similar than the intersite variability. Thus, it appears that there is little spatial variability in $\bar{F}$.

Although the variability is small, the average value of $\bar{F}$ increased progressively downstream (Table 3.2, figure 3.8). If there were progressive downstream fining as seen in large systems e.g. [63], infiltration would be expected to increase because the maximum possible sand fraction F_o would increase and the trapping coefficient β would decrease (equations equation 3.5 and equation 3.4). However, there was no consistent downstream pattern in the GSD of infiltrated sand and a bedload sample collected at cross-section E matched the feed sand GSD. The downstream sites may have been infiltrated by sand traveling at very low concentrations ahead of the sheet of bedload sand, but there was no measurable suspended or bedload transport ahead of the main bedload sheet.

The top and bottom of the sand seal layer are listed as z_{top} and z_{bot} in table 3.2. Where there was no deposition, there was a surface layer of gravel from which sand had been winnowed away (see the left and bottom in figure 3.7 for an example). For these pits, z_{top} is the depth at which sand becomes abundant. Where there was surface deposition, such as in cross-section C (figure 3.9), the surface layer included the surficial sand and the top layer of

Pit	$\bar{F}/s.e.$ (%)	z_{top} (mm)	z_{bot} (mm)	$l_{meas}/s.e.$ (mm)
A1	4.3/0.1	7.5	72.5	2.8/0.1
2	3.7/0.1	7.6	69.1	2.3/0.0
3	2.8/0.6	13.5	77.7	1.8/0.4
4	0	-	-	-
B1	4.8/0.6	13.1	69.6	2.7/0.4
2	*	6.0	51.7	*
3	4.2/0.5	18.9	82.4	2.6/0.3
4	0	-	-	-
C1	3.9/0.5	12.7	73.1	2.3/0.3
2	4.1/0.9	10.4	52.0	1.7/0.4
3	5.1/0.3	10.2	86/120**	4.6/0.2
4	3.7/0.5	12.1	90.4	2.9/0.4
5	4.1/0.8	8.3	54.7	1.9/0.4
6	4.8/0.4	9.2	47.4	1.8/0.1
D1	0	-	-	-
2	0	-	-	-
3	5.1/0.3	10.6	79.1/100**	3.5/0.2
4	5.6/0.7	3.1	51.1	2.7/0.3
E1	0	-	-	-
2†	4.7/1.2	55.4	127†	/0.9
3	4.2/0.3	24.5	85.9	2.6/0.2
4	5.6/0.2	10.8	123/123**	6.3/0.2
5	5.9/0.2	8.71	85.8	4.5/0.1

Table 3.2: Results of infiltration experiment. $\bar{F}$ is the mean volumetric sand fraction in the bed (sand, gravel, and pore space), given with its standard error. z_{top} and z_{bot} are the top and bottom of the excavated sand seal. $l_{meas} = (z_{bot} - z_{top})\bar{F}$ is the volume/bed area of sand deposited; the mean and the standard deviation are given.

*B2 Sand seal sample included sand from the surface deposit.

**At C3, D3, and E3, sand seals extended below $z = 10cm$; z_{bot} is listed with average sample depth/maximum depth excavated.

† Sample from gravel bar spit. Very little sand found above $z = 5.5cm$.

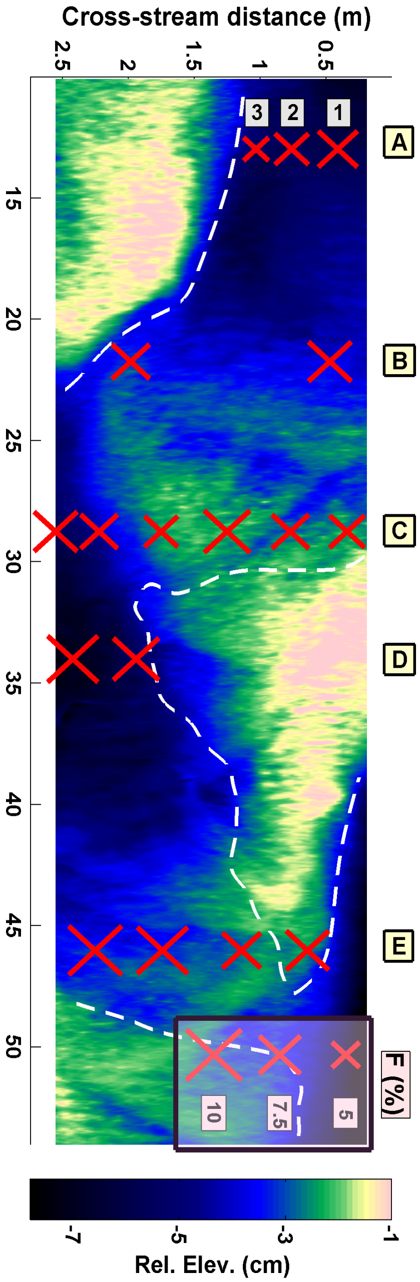

Figure 3.8: Measured sand fraction in the sand seal, shown by the relative size of the markers. The cross-sections are labeled in yellow boxes along the right side. Sample pits are numbered from the left bank as with A1-A3. The legend in the right-hand corner shows the scale of the symbol sizes.

Figure 3.9: Surface sand deposition at cross-section C at the end of the experiment. Photo is taken from the right wall (at 2.74m). The shiny material is confetti used to test velocity.

gravel. For these pits, z_{top} was the elevation of the plane below the first layer of gravel. This depth was chosen to minimize the effects of surface sand deposits and any surface armoring on the sand seal sample. Both methods yielded similar values of z_{top} excluding pits B2 and E2 (table 3.2). Excavation of the surface layer was too shallow in pit B2, so that some of the surface sand was incorporated into the sand seal sample. Pit E2 was under a gravel bar and will be discussed separately. In general z_{top} was in the range of D_g to $2D_g$ or $0.5D_{90}$ to D_{90}, smaller than winnowing depths found by other researchers [17, 88, 5].

There is much more variability in the thickness of the sand seal than in the sand fraction. z_{bot} is the depth at which the sand content became negligible based on visual inspection. Samples collected below z_{bot} had an average sand content of $\bar{F} = 0.8\%$ and so the bottom of the sand seal is assumed to be where $F(z) = 0.008$. In sample pits C3, D3, and E4 excavation was terminated before the bottom of the sand seal was found to avoid sampling below the pre-cleaned gravel. However, excavation continued at pits C3 and D3 in an unsuccessful search for the bottom of the sand seal. Both the depth of the bottom of the sample and the maximum excavated depth are given in table 3.2. A map of the maximum excavated depth is given in figure 3.10. The thickness of the sand seal appears to be highly correlated to the morphological unit; z_{bot} is greatest in the riffles and channel edges and shallowest at the head of channel.

Spatial patterns in the thickness of the sand seal lead to spatial variability in total infiltration, $l_{meas} = (z_{bot} - z_{top})\bar{F}$ (units of depth). l_{meas} is the volume per bed area of infiltrated sand; $l_{meas} * \rho_s$ is the mass per bed area. Values of l_{meas} are given in table 3.2 and figure 3.11. The greatest sand infiltration and the greatest variability in infiltration occured in the riffles (cross-sections C and E). There was moderate infiltration in the channels, edges of channels, and channel tails. The least infiltration occured at the entrance to the channel and at the areas just upstream of bar heads (which are denoted channel head and bar head, respectively, in table 3.1).

The variability of l_{meas} can be compared to variability in the total infiltrated sand found by Wooster et al. [88] in uniform-flow, 1-D infiltration experiments. The mean and standard deviation of $l_{meas} = \bar{F}(z_{bot} - z_{top})$ for each pit are given in table 3.2. On average, the standard deviation σ_l for the pit is 16% of the mean. Figure 3.12 shows σ_l divided by the mean value of l_{meas} for all sample pits (blue circles). For comparison, a similar measure is shown for the experiment in Wooster et al. [88] with the most similar grain size distribution, Zone 5. These are shown with black asterisks, and the values represent the standard deviation between the six sample pits divided by the experimental mean. The values for the Wooster data were obtained by summing over sand in all layers for each pit; these data were obtained through personal communication with John Wooster. Sample volumes in both studies were similar ($\approx 1,000 cm^3$) and so sample size should not affect the relative variabilities. The fact that the variability in the sample pits is similar or smaller than that found by Wooster et al. [88] indicates that the measurements in table 3.2 are representative of local conditions.

There was no downstream fining of sand either in bedload or in sample pits. However, there were variations in the infiltrated sand GSD related to morphological unit. This can be seen in figure 3.13, which compares the GSD of feed sand and that found in three sample pits. In most of the sample pits, the infiltrated sand is slightly coarser than the feed sand. The sand seal GSD at the edge of channels is significantly finer than feed sand and sand infiltrated in the channel. The GDS shown in figure 3.13 is from sample pit D3; it is very close to the GSD found at the other edge of channel site A3. Infiltration at both channel edge sites was quite deep, which is expected for finer sand.

There is a complex relationship between sediment transport and infiltration. Figure 3.14 is a plot of bedload transport rate q_s against the thickness of the sand seal (red circles). The values of q_s are the mean value from measurements taken during periods of significant transport at that cross-section. Sample sites with sediment transport that was below a measurable level are all plotted with $q_s = 0.01 g/cm/min$ so that they appear on this semilog plot. For sample sites with measurable bedload transport, there is a possible negative relationship between q_s and z_{bot}. However, there is significant infiltration at many sites without measurable transport.

At sites without measurable bedload transport, surface deposits indicate that the sediment supply was not negligible. The size of the surface deposit is shown for all sites with negligible sediment transport; these are plotted in filled black triangles and correspond to the

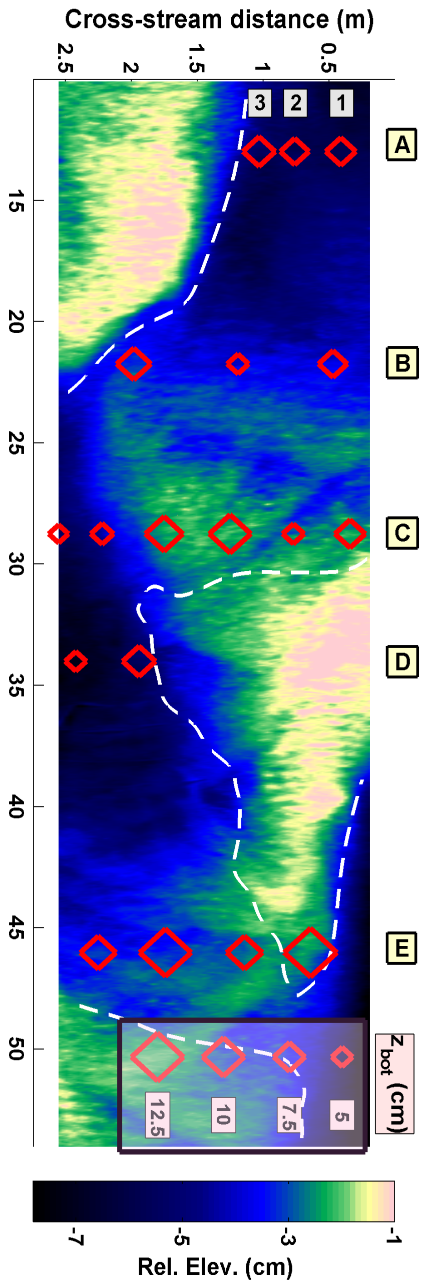

Figure 3.10: Thickness of the sand seal, shown by the relative size of the markers. The cross-sections are labeled in yellow boxes along the right side. Sample pits are numbered from the left bank as with A1-A3. The legend in the right-hand corner shows the scale of the symbol sizes.

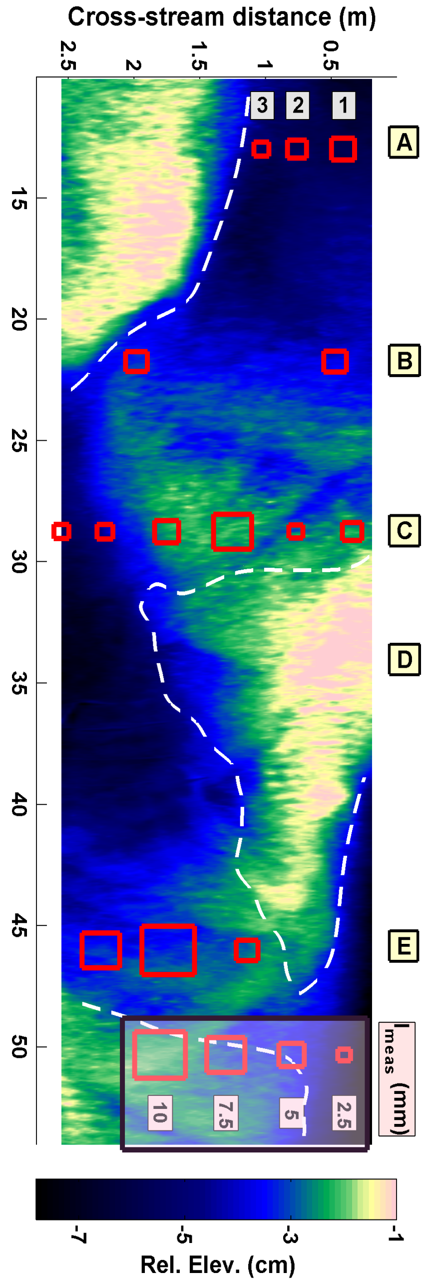

Figure 3.11: Total infiltration (volume per bed area), shown by the relative size of the markers. The cross-sections are labeled in yellow boxes along the right side. Sample pits are numbered from the left bank as with A1-A3. The legend in the right-hand corner shows the value of the symbol sizes.

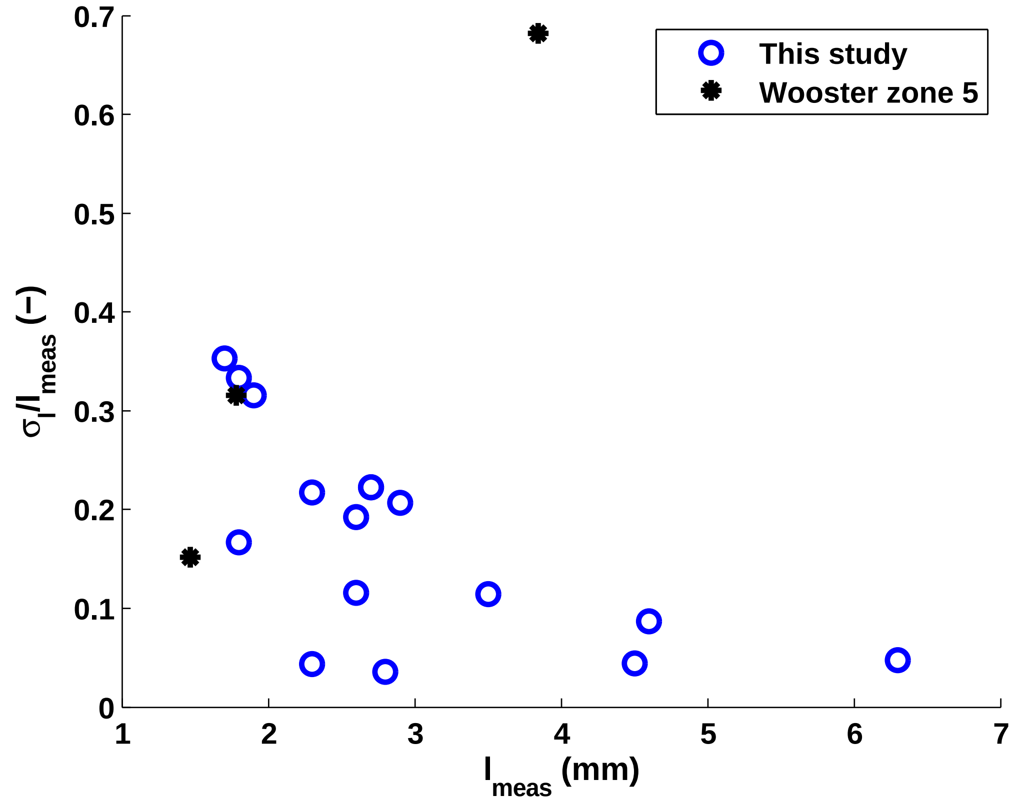

Figure 3.12: The variability of total infiltration l_{meas} for this experiment (blue circles) and a 1-D experiment (black stars) with similar grain size distributions. This 1-D experiment is Zone 5 in Wooster et al. [88]. The three marks denote the three runs. The data were obtained through personal communication with John Wooster.

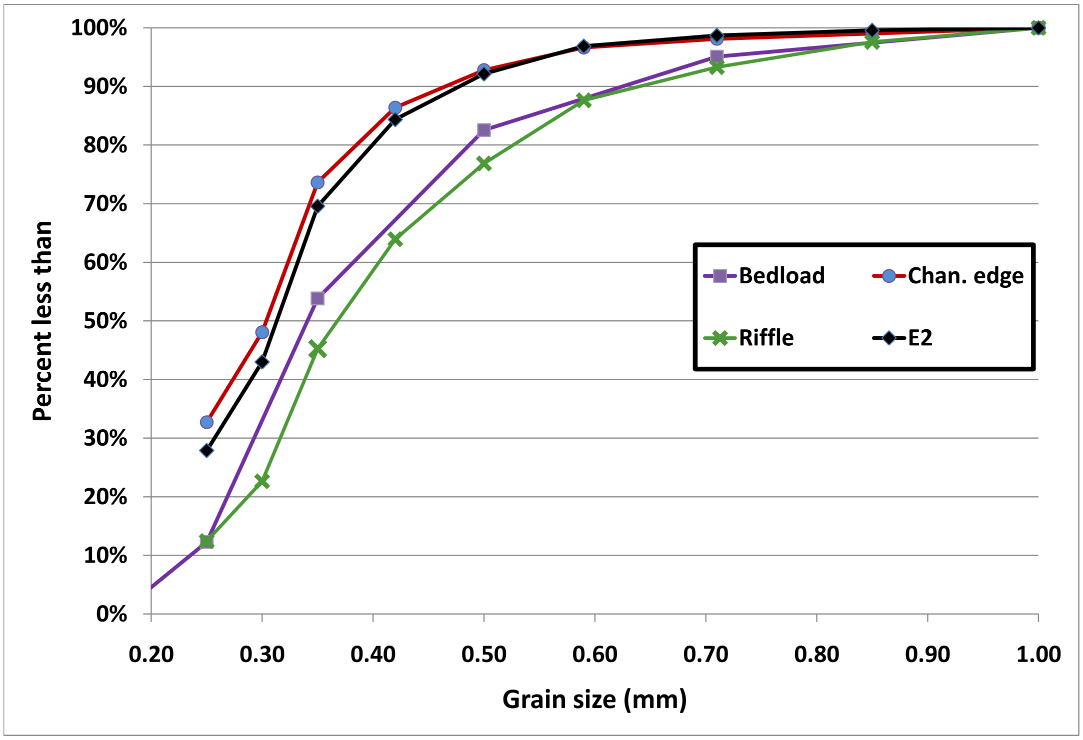

Figure 3.13: Grain size distributions of infiltrated sand. The bedload sample was collected at cross-section E (solid purple line). The sand infiltrated into a riffle (dash-dot green) is typical for all of the morphological units except the channel edge (dashed red with blue circles). The sand transported through the subsurface to E2 is shown in the dotted black line.

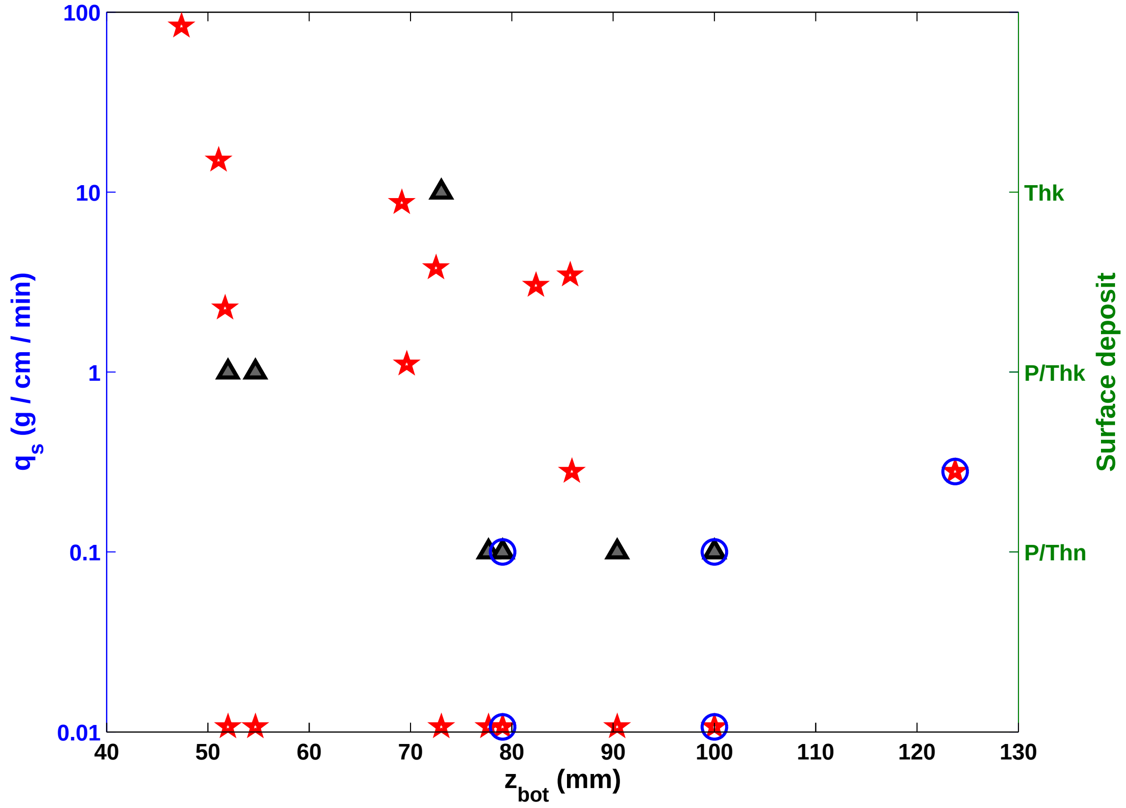

Figure 3.14: The relationship between bedload transport and infiltration depth (red stars). Values of q_s plotted at 0.01 are from sample sites with no measurable bedload transport. For these sites, the surface deposition is given (black triangles and right y-axis). Surface deposition is binned, with thick deposits ('Thk') being thicker than 2cm and thin ('Thn') thinner than 2cm. Patchy deposition is denoted with 'P' as in 'P/Thn'.

right y-axis (figure 3.14). Surface deposit thickness was within the error of the topographic scan and so measured quantities cannot be given. Instead, the values are binned based on their descriptions in the laboratory notes taken during the experiment. Thick deposits are greater than 2cm in thickness, while thin deposits are less than 2cm thick. Patchy deposits indicate that sand did not cover the entire surface. Examples of thick and patchy, thin deposits can be seen, respectively, near the wall at meter 29 and in the middle of the flume in (figure 3.9). There were surface deposits at all sites where q_s was very small. All of the sites with $z_{bot} > 7.5cm$ were covered with thin patchy deposits, whereas shallow infiltration was associated with thick deposits. There is no apparent relationship between surface deposition and z_{bot} at sites where there was measurable sediment transport. There were no apparent relationships between any combination of l_{meas} or $\bar{F}$ and q_s or surface deposition.

There was approximately one centimeter of erosion at the head of the channel at pit C1. Infiltration was relatively small at this site, which may be related to the erosion, the high sediment transport, or local hydraulic conditions.

3.4.2 Correlations with flow variables

In laboratory experiments with two-dimensional bedforms, infiltration of suspended clay and passive tracers is greatest in areas of downwelling such as dune faces [61]. Topographically-induced advective exchange has not been calculated for this experiment but some information can be inferred from outer flow variables. Figures 3.15-3.17 show the relationship between infiltration and several flow variables; the data do not include samples taken on emergent gravel bars or in the backwater. The circled data points are from sample pits C3, D3, and E4, where the sand seal depth exceeded 10cm and the actual values for z_{bot} and l_{meas} are greater than indicated.

There appears to be a negative relationship between shear stress and l_{meas} (Figure 3.15). This is opposite to the results in the infiltration study of Diplas and Parker [17], who found that infiltration increases with shear stress. Shear velocity ($u_* = \sqrt{\tau/\rho}$) is positively tied to turbulent exchange across a 1-D plane bed [27]. However, if bedforms are present then exchange due to advective pumping is likely to dominate turbulent moment exchange [60].

Advective exchange is driven by bed pressure gradients rather than shear stress. Bed pressure increases with water depth, and so a gradient in water depth could trigger advective pumping. Figure 3.16 shows that the local gradient of water depth in the downstream direction is negatively tied to total sand deposition l_{meas}. In other words, infiltration increases where the water becomes shallower and decreases where water depth is increasing. Average water depth η also has an effect on bed pressure gradients and advective pumping. Pressure gradients across submerged 2D bedforms increase when the water depth η decreases because the water has to accelerate more over the top of the bedform [20]. In figure 3.17, there is a clear negative relationship between local water depth and thickness of the sand seal.

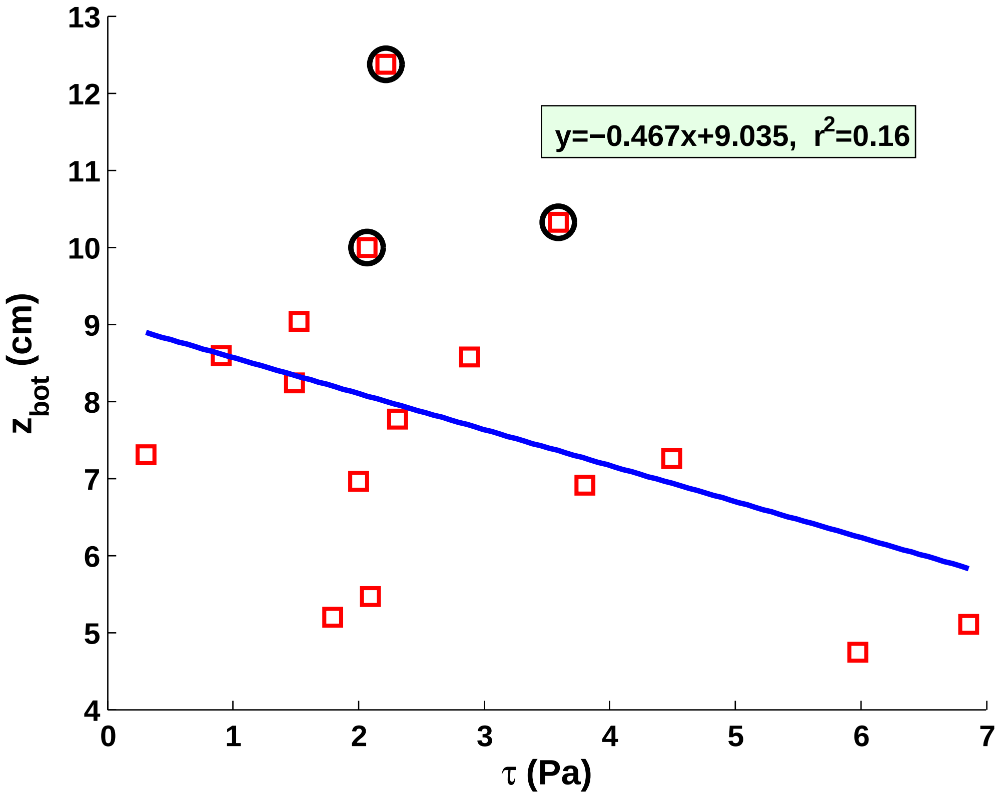

Figure 3.15: The relationship between shear stress and depth of the bottom of the sand seal. The red squares are sample pits, the circled squares indicate where sand infiltration extended below the sample, and the blue line is the linear fit.

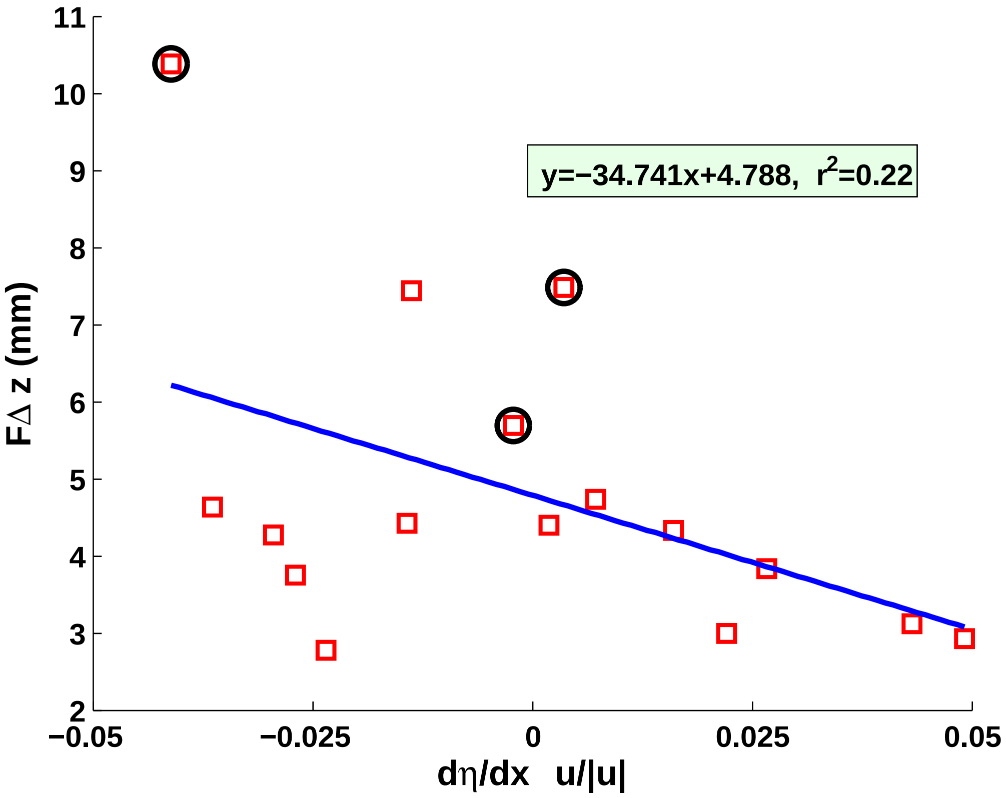

Figure 3.16: Relationship between water depth gradient and total deposited sand. The gradient is projected along the velocity vector. The red squares are sample pits, the circled squares indicate where sand infiltration extended below the sample, and the blue line is the linear fit.

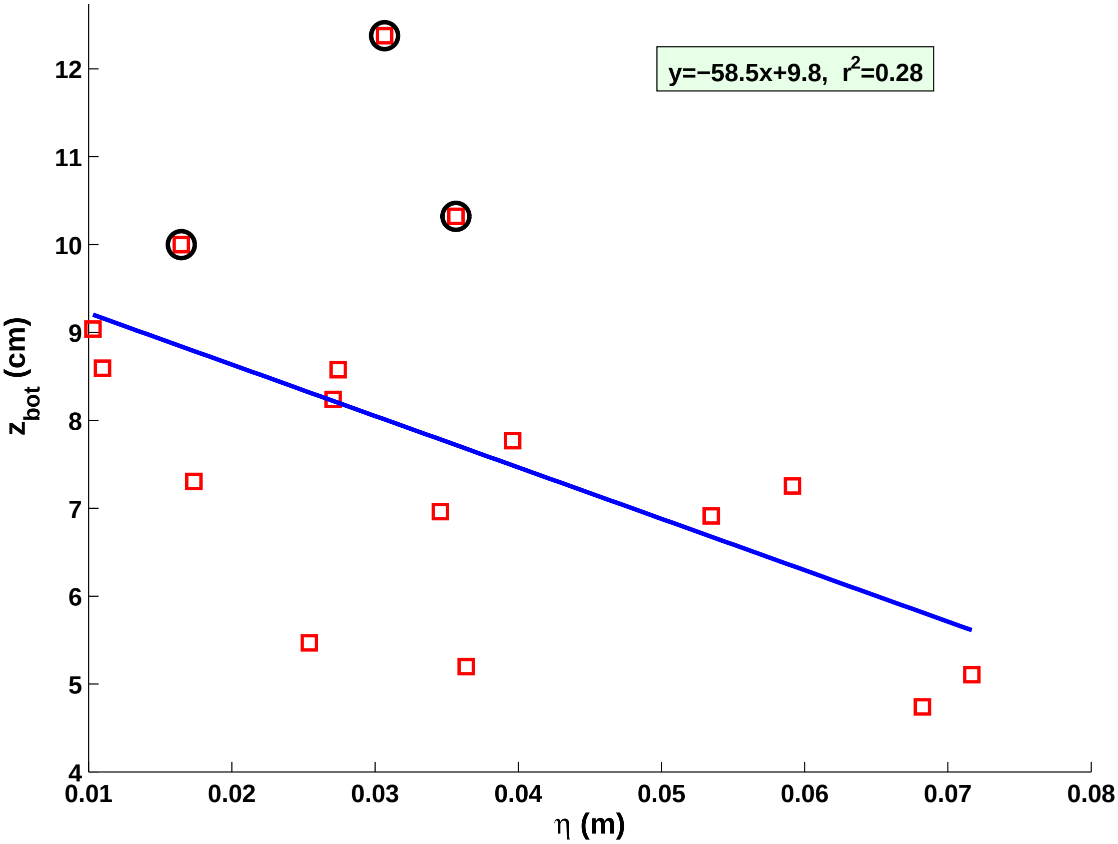

Figure 3.17: The relationship between infiltration depth and the depth of overlying water. The red squares are sample pits, the circled squares indicate where sand infiltration extended below the sample, and the blue line is the linear fit.

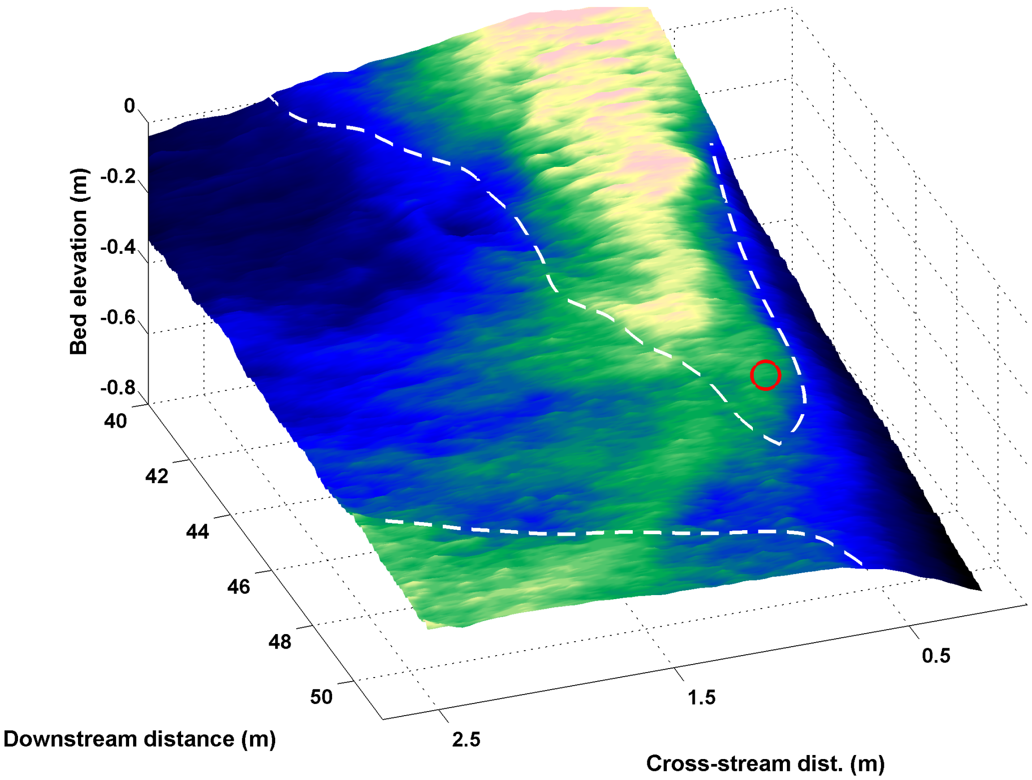

Figure 3.18: The location of sample pit E2 seen from an angle. The dashed white line is the edge of water.

Lateral subsurface sand transport through the bar tail

One sample pit yielded surprising results. Sand was found in the subsurface of pit E2 which was on a gravel bar that had remained above water throughout the experiment. This pit was on a narrow spit between the riffle and a backwater at the downstream end (figures 3.5 and 3.18). In this pit, there was a small fraction of sand ($\bar{F} = 2\%$) near the surface. Deeper, the sand fraction increased to a value was typical of a sand seal ($\bar{F} = 5\%$). There was a strong head gradient across this spit (4cm/30cm) that apparently drove the sand laterally through the subsurface. The head gradient was across the channel, and so the fines arriving at this location must have traveled there through the trench of clean gravel. The data in table 3.2 refer to the lower layer. The GSD of sand in this pit was finer than the feed GSD or that found in riffle samples (figure 3.13). This suggests that the finer material is selectively transported through the subsurface.

Some basic fluid mechanics shows that this lateral sand transport is reasonable. The permeability of the clean bed gravel is $0.03mm^2$, according to the Kozeny-Carmen relationship equation 3.6. The Darcy equation predicts that the discharge is $3cm/s$, and so the pore velocity is $u = 7cm/s$. The form and surface drag from this flow on a sand particle will be close to predictions of Stokes Law: $6\pi\mu ud/2 = 3 * 10^{-7}$Newtons (N), where μ is the dynamic viscosity of water [37]. This is approximately equal to the force of gravity on the same particle $(4/3g(\rho_s - \rho_f)\pi(D/2)^3 = 3.6 * 10^{-7}$N, where ρ_s and ρ_f are the densities of solid and water.)

3.4.3 Comparison of 1-D infiltration models

Because the sand seal layer was collected in one bulk sample, it is not possible to determine how the sand fraction varied with depth below the surface and directly test the 1-D models for $F(z)$ (equations equation 3.2- equation 3.5). Instead, the total volume per area of sand in the bulk sand seal sample $l_{meas} = (z_{bot} - z_{top})\bar{F}$ was compared against the total depth estimated by the models. This was done by integrating the two models for $F(z)$ between the depths of z_{top} and z_{bot}. Both models assume that sand in the armor layer has been winnowed away to a depth of $z = 2D_g$. For samples where z_{top} is smaller than $2D_g$, it was assumed that the sand fraction $F(z)$ was equal to the maximum sand fraction F_o above $z = 2D_g$. The estimates for the Wooster and revised models are denoted l_w and l_{rev} in table 3.3. Measured and modeled estimates of l_{meas} are also given in figure 3.19. The solid and dashed line in figure 3.19 have slopes 1:1 and 1:2. They are included to demonstrate that most of the estimates were between 50% and 100% of the measured values. The Wooster model estimates were slightly higher than the revised model.

The two models were also tested for their ability to predict the depth of the bottom of the sand seal (where $F(z) = 0.008$). This was done by evaluating equation equation 3.2 with the two sets of coefficients. Calculated and modeled values of z_{bot} are given in table 3.3. The Wooster model overestimate z_{bot} while the revised model predictions overlap measured values. However, neither model is able to predict the variability of infiltration depth. The dashed lines show the range of infiltration depths reported in earlier studies $(3D_{90} - 5D_{90})$ [17, 5]. This range captures the central cluster of data points but not the deepest or shallowest pits.

3.5 Discussion

The objectives of this study are to determine spatial patterns of sand infiltration, relate these patterns to those found in in flume studies with suspended sediment, relate the variability in infiltration to flow variables or other forcing factors, and evaluate the performance of the one-dimensional infiltration models on three-dimensional infiltration.

The infiltrated fraction of sand in the sand seal ($\bar{F} = 3.5 - 6\%$, or $\bar{f} = 6 - 10\%$) was in the range of earlier studies [17, 45, 5]. There was little variability in $\bar{F}$. Most researchers who have studied fine sediment infiltration have concluded that grain size distribution is

Pit	z_{bot} (mm)	$z_{b,rev}$ (mm)	$z_{b,W}$ (mm)	l_{meas} (mm)	l_{rev} (mm)	l_W (mm)
A1	73	88	131	3.0	2.0	2.6
2	69	89	131	2.4	2.0	2.5
3	78	87	131	1.9	1.7	2.4
B1	70	86	131	2.9	1.6	2.3
2	52	86	131	*	-	-
3	82	87	131	2.8	1.5	1.9
C1	73	86	131	2.5	1.7	2.4
2	52	86	131	1.8	1.5	1.9
3	100**	90	131	4.2	2.1	2.8
4	90	95	131	3.0	2.4	2.8
5	55	88	131	2.0	1.7	2.1
6	47	89	131	2.0	1.6	1.8
D3	100**	88	131	3.8	1.9	2.6
4	51	88	131	2.9	1.9	2.2
E3	86	87	131	2.8	1.3	1.7
4	123**	88	131	7.0	2.2	3.3
5	86	88	131	5.0	2.1	2.8

Table 3.3: Measured and modeled infiltration results, excluding gravel bar pits. z_{bot} ($z_{b,X}$) is bottom of the sand seal layer. (l_X) is the sand fraction integrated through the sand seal layer.

B2 only analyzed for infiltration depth.

*z_{bot} is the maximum depth excavated where the sand seal bottom was not reached.

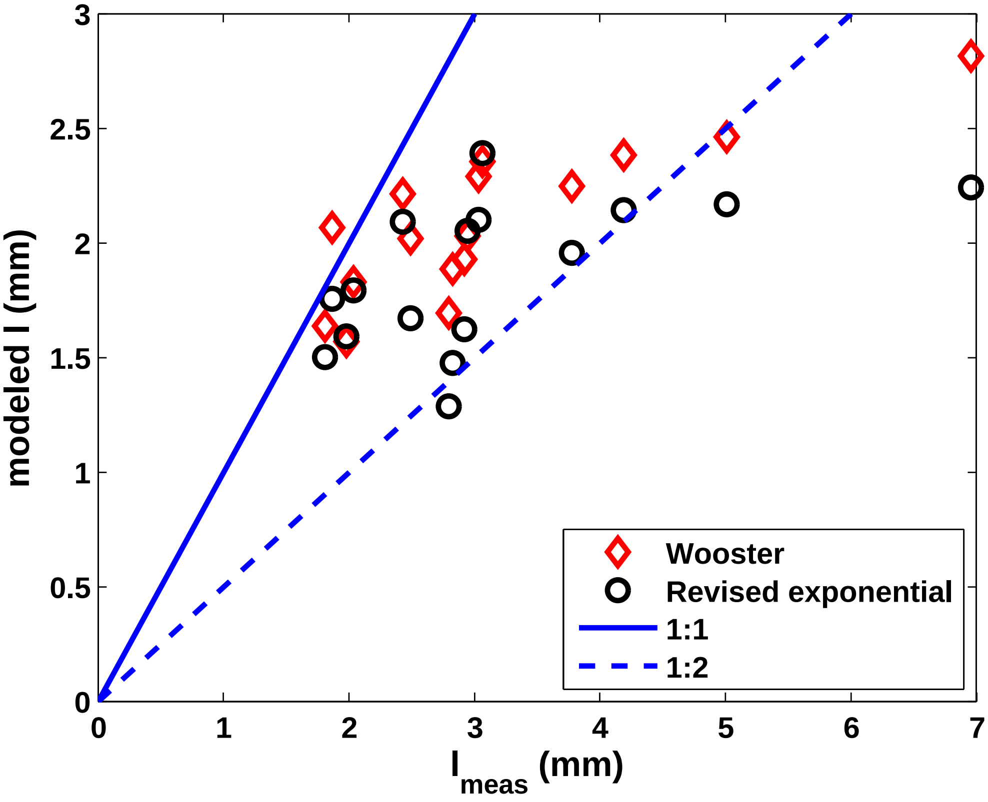

Figure 3.19: Measured and modeled values of l_{meas}, the volume per area of sand deposited in the sample pits. The solid blue line has slope 1:1 and the dashed blue line has slope 1:2.

the largest factor in determining the sand fraction in a sand seal. The uniformity in $\bar{F}$ throughout the sample sites supports this hypothesis, as the gravel grain size distribution was the same in all sample sites, whereas sediment supply, surface deposition, and hydraulic conditions varied.

Spatial variability becomes pronounced when looking at the thickness of the sand seal and the total mass of sand infiltrated. This variability appears to be related to morphological units. In sample pits near the tail end of bars (B3 and E3), infiltration was deep but the total sand deposited l_{meas} was low. Where water was shallow and slow (B3, C1, C4, and E3), total infiltration was low. Total infiltration was greatest in riffles and lowest in the channels and transition areas between channels and riffles.

This pattern of infiltration was different than that found by Diplas and Parker [17] in an experiment infiltrating suspended silt into a bed with alternate bars. They found that infiltration is greatest at the tail end of bars and where flow was most tranquil. The difference in spatial patterns is due to sediment supply and mode of transport. In the experiments of Diplas and Parker [17], the suspended sediment concentration was high, so there was no shortage of supply anywhere. In such conditions, the relative rate of deposition will be greatest in low-velocity areas and at stagnation points from eddies, such as behind bars. Thus, infiltration of silt from suspension is largely driven by the balance between gravitational settling and turbulent resuspension. In contrast, infiltration of sand from bedload appears to be driven by more complex factors, including spatial variability in sand transport. The bedload transport rate at three of the sites in very slow-moving areas (C1, C4, and E3) was very low; this low supply may have reduced total infiltration. The low velocity may also have reduced infiltration by increasing the trapping efficiency, as seen in Chapter 2. However, infiltration is also affected by surface deposition, which occured at all three sites. Diplas and Parker [17] report that there was silt found in the pavement layer but it does not appear that the bed was buried in silt. There was low total infiltration at sample site B3 which was located near a bar tail, was under shallow, slow-moving water, and had moderate sediment supply. This limitation in infiltration is likely caused by local hydraulic conditions. The relationships between infiltration, surface deposition, and hydraulic conditions are discussed in the next several paragraphs.

There is a complex relationship between sediment transport and sand infiltration. Where there was measurable sand in bedload transport, there was a negative relationship between the thickness of the sand seal and the maximum measured bedload transport rate. This corresponds with the conclusions of Wooster et al. [88], who found significanty less sand infiltration at the highest feed rate in their one-dimensional experiments. At sites where sand transport was too small to be measured, there was a relationship between surface deposition and the thickness of the sand seal. There was some surface deposition at all such sites in the channel. Of these sites, the thickest sand seals were found at sites with thin, patchy, surface deposits, while sample pits with shallow infiltration all had thick surface deposits. It appears that either high bedload transport rates or thick surface deposits can block infiltration. This may be due to simple blocking as proposed by Cui et al. [14], whereby sand in transport cannot access pores on the bed in order to reach the subsurface. Surface deposits are also likely to block momentum transfer into the subsurface; this would increase the trapping efficiency and decrease infiltration as seen in chapter 2.

Some of the variability in infiltration appears to be related to flow variables. There is a negative trend between shear stress and infiltration, which is opposite to the results of Diplas and Parker [17]. Shear stress is probably not the best measure for determining sand infiltration into a three-dimensional riverbed. Shear stress is correlated to greater sediment transport, which can block infiltration. In addition, shear stress increases with both velocity and water depth. Given a constant water depth, turbulent momentum exchange across the sediment-water interface should increase with velocity [27]. However, this effect is probably masked by the reduction in advective exchange with increasing depth, which also increases with τ_b.

Analysis of hydraulic variables suggests that advective exchange has an impact on infiltration depth, although there were no strong correlating relationships. Advective exchange with the subsurface is driven by pressure gradients along the bed surface, which are generally caused by bed morphology. The deepest infiltration occured in areas where the water depth was decreasing, indicating downwelling. Infiltration was also negatively tied with water depth; advective exchange is negatively tied with water depth. Verification that subsurface advection causes subsurface sand transport was seen in the sand found underneath a narrow spit of emergent gravel.

The sand transport that occurred through the spit of a gravel bar suggests several possibilities. The water surface gradient across the spit was high enough so that the drag force of water on the sand particles nearly matched gravity. In rivers, similar conditions can between channels and backwaters on the rising limbs of storms or between multiple channels. This sand transport through the subsurface has the potential to fill the pore spaces throughout a gravel bar, thereby reducing exchange and harming the water quality in the backwater.

There was deep infiltration at the edge of the two channels (sample pits A3 and D3). There was no measureable or visible bedload transport at either but by the end of the experiment there was a thin, patchy deposit along the edges of water. The sand found in these pits was significantly finer than the feed sand and all other sample pits except E2, which will be discussed shortly. The measured suspended sediment concentration was zero, yet this fine sand managed to reach the edge of water. The presence of the sand seals in these locations suggests that sand seals can be found in parts of rivers with no apparent sand transport. It also suggests that sand seals will appear even with a very small sand supply.

If sand seals are inevitable, then preventing sand seals isn't a reasonable management goal. A main problems with sand seals themselves is that they trap finer sediment, which further reduces the permeability. The solution to this problem is to focus on management of very fine sediments. This may entail flushing the entire sand seal from the bed, which will release the trapped silt and clay but which will not prevent formation of a new sand seal.

The sample pits most likely to correspond to salmon spawning areas are in riffles. Infiltration was greatest in these areas, and so spawning grounds are particularly prone to sand seal building. However, the sand seal may be protecting the eggs underneath it [48]. The pore velocity estimated for flow through the gravel spit in this experiment ($7cm/s$) is an order of magnitude faster than typical flow through salmon redds e.g. [92]. This suggests that the advection through redds will not transport sand deep into the redd. However, the drag force would be sufficient to transport silt through the subsurface if no sand seal were in place (using the same force balance discussed above). The sand seal can protect salmon eggs by straining out the silt and clay that might otherwise abraid the egg surfaces.

There is a downstream increase in the infiltrated sand fraction $\bar{F}$. Sediment samples suggest that this is not due to downstream fining. A similar pattern was seen by Wooster et al. [88], who found greater infiltration at a downstream site than at an upstream site with the same grain size distribution and hydraulic conditions. Some of the increased infiltration can be attributed to sediment traveling ahead of the bedload wave at a low concentration. Evidence of this pattern of infiltration was seen at the two sample sites on the edge of the channel. This infiltration should occur slowly enough that each sand particle would be exposed to subsurface fluctuations in energy for a long time before being buried in other sand. This would increase the probability of each grain being dislodged and settling further into the bed, effectively lowering the trapping coefficient.

The performance of the 1-D infiltration models at predicting total infiltration was varied. Both the Wooster model and the revised exponential model underestimated total infiltration for all pits, although the modeled values were close to the smallest measured values. Overall, the Wooster model estimates for total infiltration were slightly closer. The revised model predicted a thickness of the sand seal that fell within the range seen, while the Wooster model overpredicted the infiltration depth for all pits. The depths were in the range $2.5D_{90}$ to $5D_{90}$ comparable to earlier studies [17]. The fact that the two models underestimated total infiltration suggests that possibility that greater infiltration occurs under 3-D conditions because there is greater hydraulic exchange with the bed. It may also be that the models need improvement. The fact that the revised model is better at predicting infiltration depth suggests that the new model for β is an improvement on the Wooster model.

3.6 Conclusions

Sand seals can probably be found throughout every gravel-bedded river in the world. They have been found in almost every sample site in every field and infiltration study. In this study, sand seals were found in every sample pit below the water line except an inaccessible backwater. There was no measurable sand transport at many of these sites. This suggests that sand seals will be built even if the sand supply is minimal. There was little variation in the mean sand fraction in the sand seal, supporting earlier findings that the sand fraction is only a function of the grain size distribution.

Although sand seals were prevalent throughout the flume, it is clear that infiltration is not a uniform, one-dimensional process. The thickness of the sand seal, which is determined by the depth of the bottom of the sand seal, varied by a factor of three. Infiltration appears to be limited when access to the subsurface is blocked by either high bedload transport rates or thick surface sand deposits. Downwelling increased the thickness of the sand seal and was able to advect sand laterally through the subsurface of a narrow gravel bar. Infiltration is greatest in riffles. The new infiltration model from chapter two predicted a range of 1cm variability in sand seal thickness, due to variations in mean water velocity. Actual sand seal thickness varied over 8cm, indicating that mean velocity is not the main forcing mechanism.

Variable	Description	Units
d	Particle diameter of fine sediment	l
g	Gravitational acceleration	l/t^2
l	Total infiltrated sand (volume per area)	l
t_{ex}	Timescale of entrainment (exchange timescale)	t
u_*	Shear velocity	l/t
w_s	Particle settling velocity	l/t
x	Downstream distance	l
z	Depth in the bed	l
A	Bed area from which entrainment occurs	l^2
D	Gravel diameter	l
$E(E_1, E_2, E_3)$	Entrainment rate	l/t
E_o	Peak entrainment rate	l/t
H	Water depth	l
K_x	Longitudinal dispersion coefficient	l^2/t
M	Mass per bed area of suspendable sediment	m/l^2
M_o	Initial mass per bed area of suspendable sediment	m/l^2
$Q(Q_G, Q_H)$	Water discharge (at Guerneville and Hopland)	l^3/t
$Q_{sG}(Q_{sH})$	Suspended sediment discharge at Guerneville (Hopland)	m/t
$Q_{sGo}(Q_{sHo})$	Initial SS discharge	m/t
$Q_{sG,bk}(Q_{sH,bk})$	Background SS discharge	m/t
Re_p	Particle Reynolds number	-
S	Slope	-
SSC	Suspended sediment concentration	m/l^3
T	Turbidity	NTU/FNU
W	Channel width	l
Z	Term in the Garcia-Parker entrainment relation	-
ν	Water viscosity (kinematic)	l^2/t
ρ_w	Density of water	m/l^3
ρ_s	Density of sediment	m/l^3
σ_{dp}	Standard deviation of a dispersed distribution in space	l
σ_{dpt}	Standard deviation of a dispersed distribution in time	l

Table 3.4: Variables for sand infiltration into a gravel, laboratory riverbed with alternate bar topography.

Chapter 4

Entrainment and suspended sediment dynamics

4.1 Overview

An overabundance of silt and clay in the riverbed can cause problems for salmon and water extraction activities. Silt and clay can be flushed from the riverbed using large releases from reservoirs. Unlike sand, which will re-infiltrate the riverbed as soon as stormflow recedes, silt and clay can be carried out of the river system in a single flushing flow. Use of flushing flows requires knowing if and when they would be useful, as well as the rate of entrainment of fine sediment from the riverbed. Entrainment of fines into suspension from the subsurface is not well quantified. A significant amount of information about overall sediment supply, timing of sediment supply, and entrainment rates can be learned from high-resolution turbidity data collected on rivers by the U.S. Geological Survey (USGS).

In this chapter, suspended sediment dynamics are studied on the Russian River in California using data from the USGS and other government agencies. The chapter begins with an overview of fluvial suspended sediment dynamics, including a model for entrainment. The Russian River is introduced, including a brief summary of sediment issues, reservoir management, and available data. Entrainment of suspended sediment is studied using turbidity and discharge data collected during four flood-control releases from Coyote Dam in the upper watershed. Cumulative entrainment from a reach is calculated by taking the difference in sediment flux at two gauging stations downstream of the dam, Hopland and Guerneville.

Supporting analyses used to calculate entrainment include sediment and hydrograph travel times and longitudinal dispersion between the sites. Local entrainment is calculated from cumulative entrainment by estimating the mobile fraction of the riverbed during each dam release. Local entrainment is modeled as an exponentially decaying function of time. The timescale and maximum entrainment rates are then related to forcing factors.

Additional sediment analyses were performed for the Russian River. The annual suspended sediment load is calculated over 22 years; this is compared with annual water discharge. The grain size distributions of suspended sediment samples collected during a short dam release are summarized. Suspended sediment samples are used to develop a new relationship between turbidity and suspended sediment concentration at Hopland.

4.2 Background

Excessive fine sediment has a negative impact on many rivers in the United States. It is particularly problematic for salmonids, whose population have declined significantly in California over the past 150 years. Deposition of fines on the streambed limits spawning habitat, suffocates developing salmon eggs, reduces access to refugia from predators and high flows, and appears to reduce prey availability for salmonids [6, 13]. Chronically elevated suspended sediment loads reduce primary production, raise water temperature, abraid fish gills, and decrease the dissolved oxygen concentration [15].

Flushing flows may be used to clean a riverbed of suspended fines. However, flushing flows are expensive, affect water supply, and can have negative and unintended impacts on a river [87]. Possible negative impacts include erosion of gravel, scouring of salmon eggs, and mobilization of fine sediment that will infiltrate and reduce the permeability of salmon nests [42, 92, 44]. Analysis of suspended sediment dynamics in a basin should be performed in order to determine if, when, and how flushing flows should be implemented.

On average, the mass of fines on riverbed surfaces and in pools is linked to the average annual supply of fine sediment e.g. [13]. Land use, dam installation, and other human actions tend to increase the total suspended sediment load or increase the relative proportion of suspended sediment to coarser bed sediment. The annual sediment load can be analyzed to determine the impact of development or erosion-control activities and can give an indication of whether flushing flows would be appropriate in a watershed. However, conditions vary on many timescales and sediment management actions like flushing flows will only be beneficial occasionally. Individual rainstorms can trigger landslides and other processes that increase the fine sediment supply to the river for several years. In this chapter, patterns in sediment yield are studied for relationships to time, water discharge, and large flood events.

A common method of estimating the suspended load is to monitor turbidity and discharge on a river. This estimate is affected by the calibration of turbidity measurements as a proxy for suspended sediment concentration measurements. The relationship between turbidity (T) and suspended sediment concentration (SSC) varies between stations and over time at a given station. In this study, three T-SSC relationships are developed to estimate suspended flux, and to demonstrate error caused by inappropriate transfer of a T-SSC relationship from one site onto another site, and demonstrate how flow conditions affect the relationships.

Calculated suspended load is affected by the time discretization of measurements. Suspended sediment flux is the product of discharge and SSC. These are positively correlated, and a disproportionate fraction of suspended flux occurs at peak discharge e.g. [22]. This leads to error in the cumulative flux calculation if the turbidity monitoring interval is large compared to the time spent at peak flow. This effect is demonstrated by comparing annual sediment flux calculated using 15-minute and daily data.

Reservoirs cause many of the sediment problems on rivers but they may be usable to improve spawning habitat. Dam releases (DR's) are regularly made for hydropower, to supply water users downstream, and to create flood storage space in the reservoirs. Some of these releases are large enough to mobilize the bed and are essentially flushing flows. It may be possible to engineer these releases to either minimize bed scour in order to protect salmon habitat or to mobilize the bed to flush fine sediment from the subsurface. In order to design a flushing flows, it is necessary to understand how fast silt and clay is entrained. There is no general method of estimating subsurface entrainment of suspended sediment from a riverbed. On rivers with 15-minute turbidity monitoring, previous large dam releases can be studied as experimental flushing flows.

4.2.1 Entrainment model

Entrainment of suspended sediment is generally modeled as a one-dimensional, steady-state process in which turbulent entrainmend is balanced by particle settling [83, 34, 29]. Garcia and Parker [29] proposed the following empirical model for entrainment from a bed made of fines of a uniform size:

$$E_{GP} = w_s \frac{1.3x10^{-7} Z^5}{1 + 1.3x10^{-7} Z^5 / 0.3} \tag{4.1a}$$

$$Z = \frac{u_*}{w_s} Re_p^{0.6} \tag{4.1b}$$

$$Re_p = \frac{d_{50}^{3/2} \sqrt{g(\rho_s - \rho_w)/\rho_w}}{\nu} \tag{4.1c}$$

where E_{GP} is the entrainment rate ($length/time$), the subscript GP indicates the Garcia-Parker model, w_s is the particle settling velocity (l/t), u_* is the shear velocity (l/t), Re_p is the grain Reynolds number (-), d_{50} is the median particle diameter, ρ_s and ρ_w are the densities of the sediment and water, and ν is the kinematic viscosity of water.

If fines are being entrained from the surface of a bed made of coarser sediment, the entrainment rate is within a factor of 4 of the rate predicted by (4.1) multiplied by the fractional volume of fines, f [34]. For the purposes of this study, if measured entrainment is close to $E_{GP} f$, then I will assume that entrainment is occurring from the riverbed surface.

There is no commonly-used entrainment model for the flushing of suspendable fines from the riverbed subsurface. Entrainment from the subsurface depends on mobilization of the bed sediment [18, 28]. Wu and Chou [89] modeled the flushing of sand into bedload from the subsurface of a sand-gravel bed. The entrainment of sand is fast compared to the mobilization of gravel, and so the gravel transport rate is considered to be the control the sand entrainment rate [89]. Their model tested well against measurements in a laboratory flushing experiment. While the Wu and Chou [89] model is not directly applicable to entrainment of silt and clay from riverbeds, two of their assumptions will be used in this chapter. These assumptions are that the entrainment rate is a function of the mass fraction of fines in the subsurface and a time scale, t_{ex}, that is a function of discharge. These assumptions are expressed as:

$$E = \frac{1}{\rho_s}\frac{M}{t_{ex}}, \tag{4.2}$$

where M is the mass per bed surface area of suspendable sediment (m/l^2).

Assuming that deposition is negligible compared to entrainment, then by mass balance:

$$E = -\frac{1}{\rho_s}\frac{\partial M}{\partial t}. \tag{4.3}$$

Equating (4.2) to (4.3) leads to an exponential model for M and E:

$$M = M_o e^{-t/t_{ex}} \tag{4.4a}$$

$$E = E_o e^{-t/t_{ex}}, \tag{4.4b}$$

where the initial entrainment rate E_o is defined as $M_o/(\rho_s/t_{ex})$.

The entrainment analysis of this chapter will demonstrate that sediment flux data are consistent with an entrainment rate that decays exponentially with time. E_o, t_{ex}, and M_o will be estimated.

4.2.2 The Russian River

In this chapter, the Russian River in Northern California is used as a case study on suspended sediment dynamics. The Russian River faces many of the issues common to California rivers, including excessive sedimentation, reservoir operations, and threatened salmonid runs. There has been intensive monitoring of the streamflow and discharge in the watershed for almost a decade. This dataset is an opportunity to study many unexplored questions about watershed dynamics, including entrainment rates, annual sediment patterns, and the effects of reservoir operations.

Californias Russian River basin is situated in Mendocino and Sonoma counties north of San Francisco (Figure 4.1). The river is listed as impaired for sedimentation/siltation on the U.S. Environmental Protection Agencys 303(d) list [81]. Development in the basin has expanded rapidly, which is correlated to increased fine sediment content in the riverbed [57, 13]. The population of the largest city, Santa Rosa, was 18,000 in 1950; it has grown an average of 47% every decade since. Agricultural land use in the basin is also significant. The Russian River watershed produced approximately 20% of the wine grapes grown in California in 2009 [9]. Sonoma Countys wine and wine-related industries are estimated to

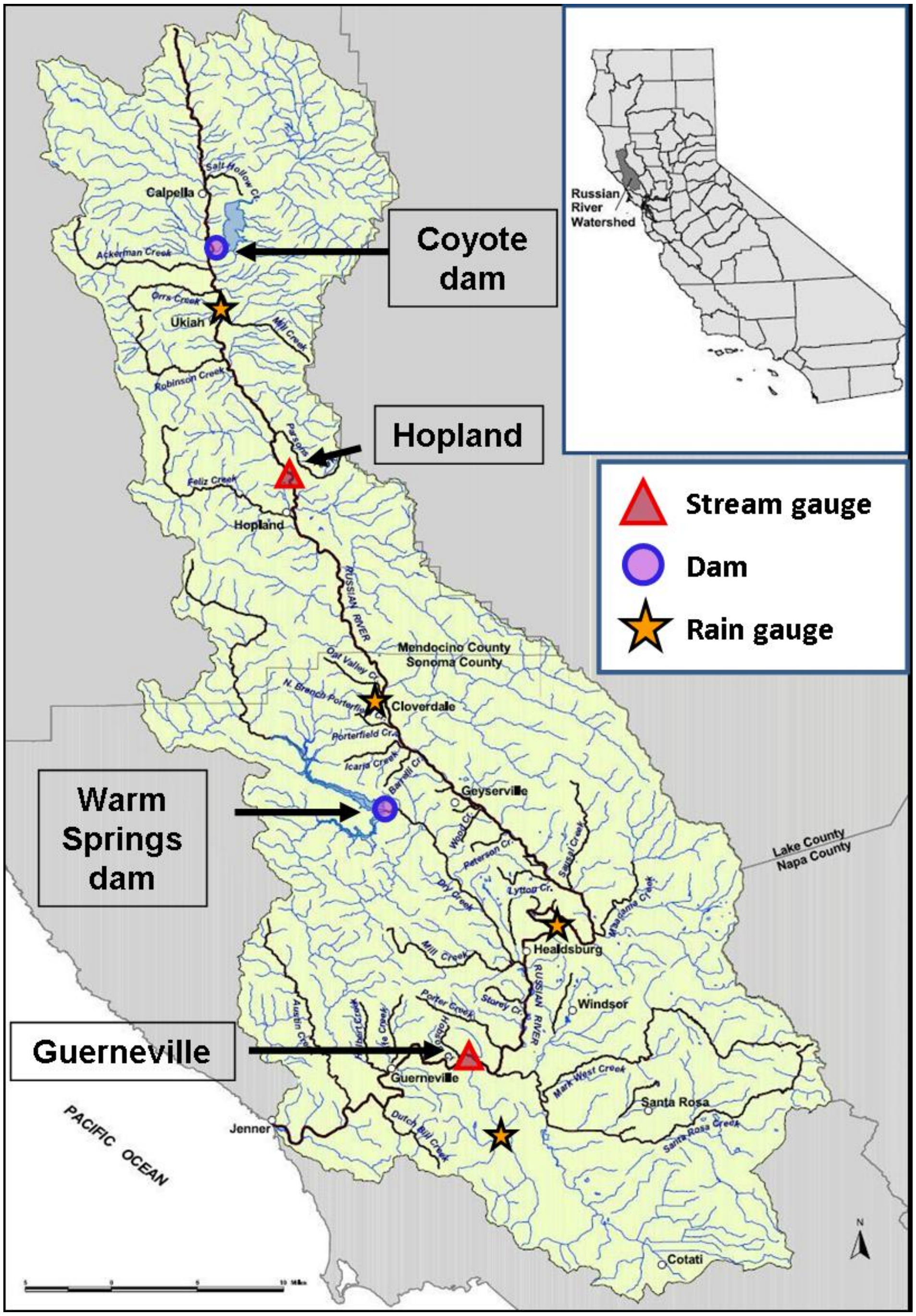

Figure 4.1: Map of the Russian River watershed with USGS gauging stations and NOAA precipitation gauges. The red triangles are the Hopland and Guerneville monitoring stations. The blue circles and orange stars indicate one or more monitoring stations. Background from Circuit Rider Productions.

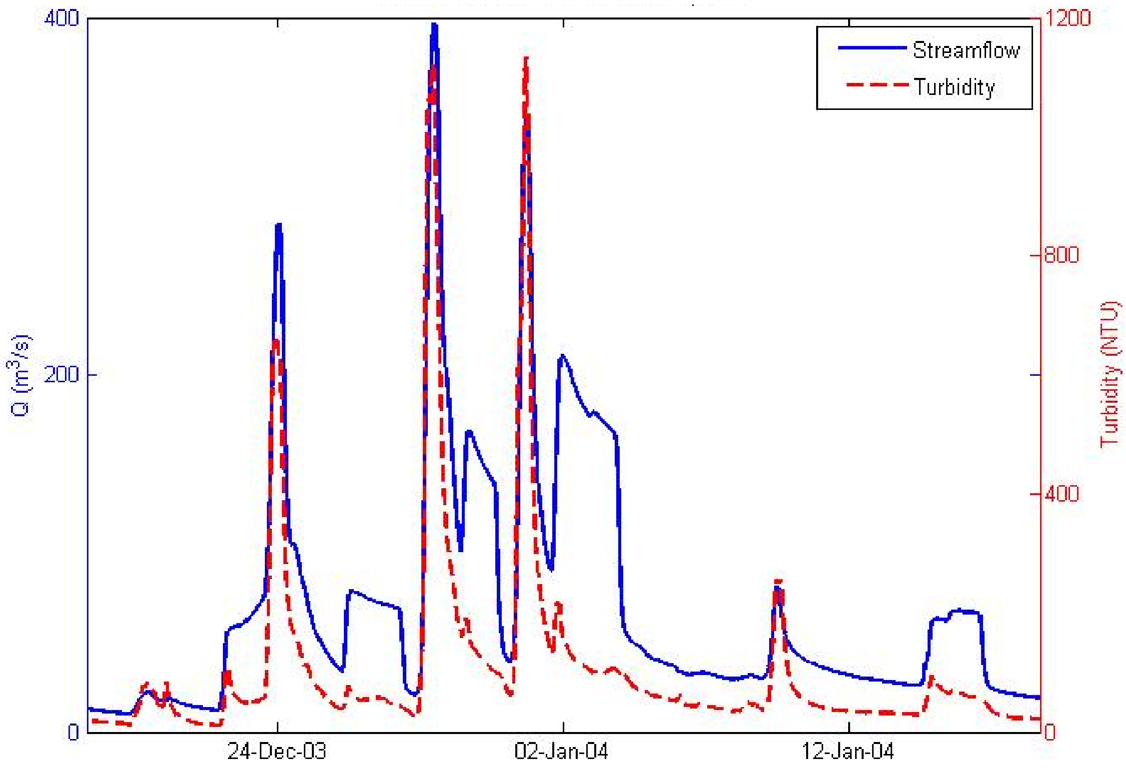

Figure 4.2: Streamflow (solid blue) and turbidity (dashed red) over several storms and dam releases at Hopland. The square hydrographs are the dam releases.

be worth $8 billion annually [50]. This economic benefit relies on practices that affect the river, including farming up to the edge of the riverbank and pumping water from below the riverbed.

The Russian River hosts at least 49 different fish species including threatened populations of anadromous steelhead trout, Chinook salmon, and Coho salmon [12]. Steiner [78] estimates that annual salmon escapement decreased from 20,000 in the late 19th century to 1000 in the late twentieth century. The Chinook salmon spawn on the mainstem and so the population is affected by the cumulative sediment issues throughout the watershed.

Reservoir operations affect both the hydrograph and sediment dynamics in the basin. Coyote Dam was built on the East Fork Russian River in 1958 (Figure 4.1), creating Lake Mendocino. In 1984, Warm Springs Dam was built on Dry Creek, creating Lake Sonoma. When the reservoirs are full and heavy precipitation is expected, one or both dams release large amounts of water to create flood storage. This creates distinctive hydrographs that appear as square waves in the discharge record (Figure 4.2). Discharge and turbidity data collected during releases from Coyote Dam are analyzed to estimate entrainment.

S	L	W	
Bed slope	Length km	Ave. width m	Width range m
0.002	97	45	30-75

Table 4.1: Hydraulic variables for the Russian River between Hopland and Guerneville. The current width is relatively constant due to channel straightening and bank reinforcement. The width range was determined in a boat survey of the reach between Hopland and Cloverdale. Sources of other data: USGS, [68, 25]

Shortly after the construction of Coyote dam, fishermen and river managers noted that periods of high turbidity associated with stormflows were extended in reservoir outflow long after the storm had passed. The USGS performed a detailed analysis of the effect of the reservoir on turbidity, sampling turbidity and suspended sediment concentration almost daily from 1965-1968 at eight stations [67]. The USGS has continued to sample river sediment at 25 sites in the basin. Some of these data are used in this study.

The suspended sediment yield in the basin is quite variable. The USGS reported mean suspended sediment discharge at Guerneville between 1967 and 1986. The mean annual sediment yield from this record is 0.13 mm. The 1964 storm appears to have increased sediment yield for several years, but there was large spatial variability. Sediment yield was lowest in the in the basin upstream of Cloverdale (0.39 mm/yr) during 1965-68, while the yield of the watershed above Guerneville averaged 0.63 mm/yr [67]. The highest sediment yield in the basin was 0.83mm in the Dry Creek watershed [67]. The sediment yield is high, but lower than the nearby Eel River basin, which is estimated at 0.6mm/yr or above e.g. [36, 56].

Hydraulic parameters for the Russian River are given in Table 4.1.

The entrainment estimates in this chapter will be tested by comparing them with the mass of suspendable sediment in the riverbed. The d_{95} of suspended sediment in USGS samples collected at Guerneville is 0.125mm, so this can be taken as the upper bound of suspended sediment (Figure 4.3). Taking the average of the fraction of sediment finer than 0.125mm from USGS bed samples at Hopland, $f = 0.05$. Suspended sediment can be entrained from the active layer. Wilcock et al. [86] found that the active layer is $1.7D_{90}$ thick for plane-bed transport on the Trinity River, where D is the diameter of bed gravel. The mean D_{90} in all USGS bed samples collected from Hopland at Guerneville is 25mm (Figure 4.3). Assuming the porosity of the bed is 30% and a sediment density of 2,650kg/m^3, there is 1.5mm (4.0kg/m^2) of suspendable sediment in bed.

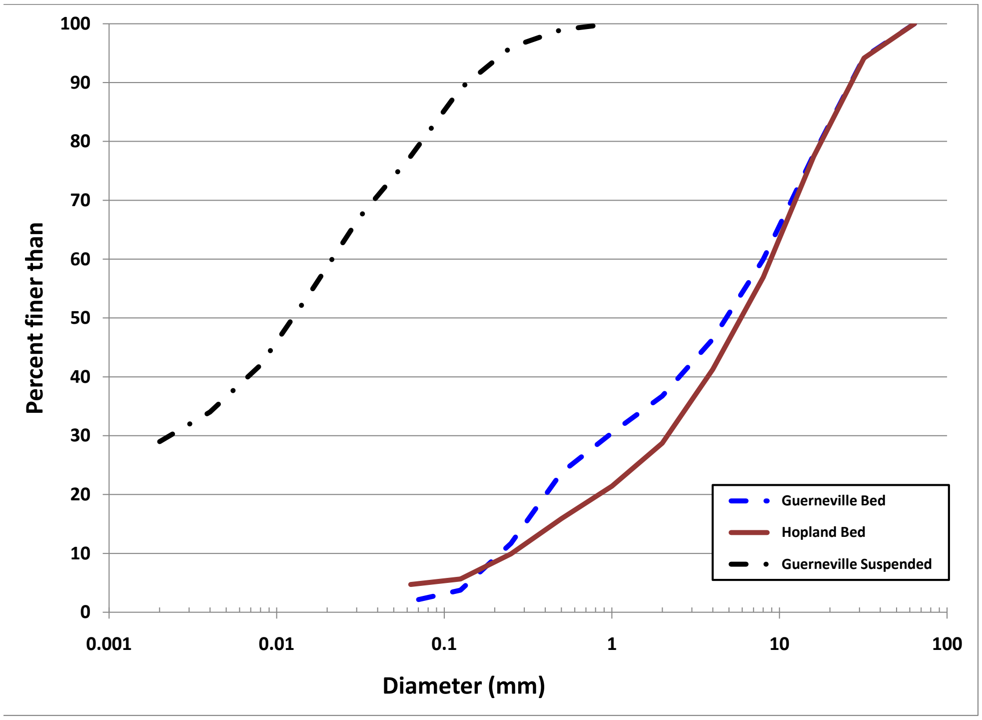

Figure 4.3: Grain size distribution of bed and suspended sediment samples collected by the USGS. The suspended sediment distribution is the average of 88 samples with grain size analyzed down to 2 microns.

4.3 Methods and Data

The main variables in this chapter center are turbidity, suspended sediment concentration, water discharge, suspended sediment discharge, and entrainment rates. Notation is summarized in Table 4.8 at the end of the chapter.

4.3.1 Measurements

The U.S. Geological Survey (USGS) has been monitoring discharge on the Russian River since 1909 and sediment since 1939. The majority of the data used in this study were collected by the USGS at Hopland (USGS site id 11462500) and Guerneville (11467000). These sites are on the mainstem of the river, 79 river kilometers apart (Figure 4.1). The entrainment study and total sediment load calculations use turbidity and discharge data collected at 15-minute intervals since 2002 at both sites. Some analyses also use daily measurements. Discharge is calculated by the USGS using a stage-discharge relationship from depth measurements collected with pressure sensors. The USGS updates the stage-discharge relationship several times a year.

Turbidity is monitored with optical backscatter probes. Modern measurements are reported in Nephelometric Turbidity Units (NTU) or Formazin Turbidity Units (FTU or FNU), which are roughly equivalent. Periodic field measurements made by the USGS are used to calibrate the turbidity data and enhance the analysis. These measurements include suspended sediment concentrations; bedload transport rate; and grain size distributions of the bed, bedload, and suspended sediment.

Precipitation data from NOAA rain gauges at Sebastopol, Ukiah, Cloverdale, and Healdsburg are used (yellow stars in Figure 4.1). These sites were chosen because they are spread throughout the basin and because of the completeness of the datasets.

Reservoir outflow data obtained from the California Data Exchange Center were used to identify dam releases from Coyote Dam and Warm Springs Dam. The data were originally collected by the United States Army Corps of Engineers.

I collected several suspended sediment samples at Hopland and at the base of Coyote Dam on the East Fork (Figure 4.1). Six samples were collected at Hopland during a short dam release at moderate discharge. These samples were collected using a US D-74 depth-integrating sampler that was lowered from a cart suspended on a cable over the river. The other samples were collected at low flow using a US DH-48 hand-held depth-integrating suspended sediment sampler. Access to sampling equipment and gauging stations was granted by the Ukiah office of the USGS.

Suspended sediment samples collected at Hopland and Coyote dam were analyzed to determine SSC. Sediment was collected by passing the samples through 0.45 micron filters using a weak vacuum and dried at 105°C. The filters were weighed before and after to determine SSC. Turbidity measurements made at the sampling times by the nearby turbidity probes were used to obtain the Turbidity-SSC relationship. All but two of the samples were passed through 0.22 micron filters following the 0.45 micron filter in order to capture more sediment. This extra step added about 20% to measured SSC in samples at low-flow at Coyote Dam, about 10% to SSC at low-flow at Hopland, and a negligible amount to SSC at Hopland at moderate flow. Samples that did not include sediment between 0.22 and 0.45 microns are noted.

An additional turbidity probe was installed at the USGS stream gauge at the base of Coyote Dam on the East Fork at Ukiah (site 11462000). This probe is a DTS-12 optical backscatter unit from Forest Technology Systems. This unit was installed from the fall of 2008 and operated until the fall of 2010. A large percentage of the unit's measurements are unusable due to fouling and other instrument issues. The turbidity probe at Coyote Dam was calibrated at low flow by comparison with a hand-held turbidity probe used by the USACE; the hand-held unit measured 19NTU and the probe measured 22NTU. The probe was also calibrated using turbidity standards that ranged from 20 to 1000 NTU. All measurements were 20-25% lower than the turbidity standards. The less turbid standards were created by mixing water with the 1000 NTU standard, so this bias may be caused by error in the initial standard mixture rather than a problem with the probe.

4.3.2 Calibrations

Turbidity is used as a proxy for suspended sediment concentration. The T-SSC relationship is a function of organic content and sediment particle size and color, and must be calibrated for each site. The USGS has collected over a thousand concurrent turbidity and suspended sediment measurements at Guerneville. At discharges of 10 m^3/s or less, the T-SSC relationship is fairly weak ($R^2 = 0.50$). This is probably due to algae, which have widely-varying light-scattering effects. In contrast, mineral particles from a given geological source have a small range of shape and color. The T-SSC relationship at Guerneville during higher flows is very good ($R^2 = 0.94$) with a standard error of 4% for a given turbidity value. It is based on turbidity data ranging from 1-1000 NTU (Figure 4.4):

$$SSC = 3.0T^{0.96} \qquad \text{(at Guerneville,)} \tag{4.5}$$

where SSC is in mg/l.

The suspended sediment samples from Hopland and Coyote Dam do not fall on the T-SSC relationship for Guerneville (Figure 4.4.) At a given turbidity, the SSC is lower at these two upstream sites, suggesting that sediment flux calculations for Hopland and Coyote Dam using equations (4.5) will be overestimated. Regression through the seven Hopland measurements yield the following T-SSC relationship for Hopland:

$$SSC = 0.6T^{1.14} \qquad \text{(at Hopland.)} \tag{4.6}$$

Equation 4.6 is uncertain because there are so few points and all are at moderate turbidities. In addition, (4.6) is weighted by the sample denoted by a black triangle with SSC at 9

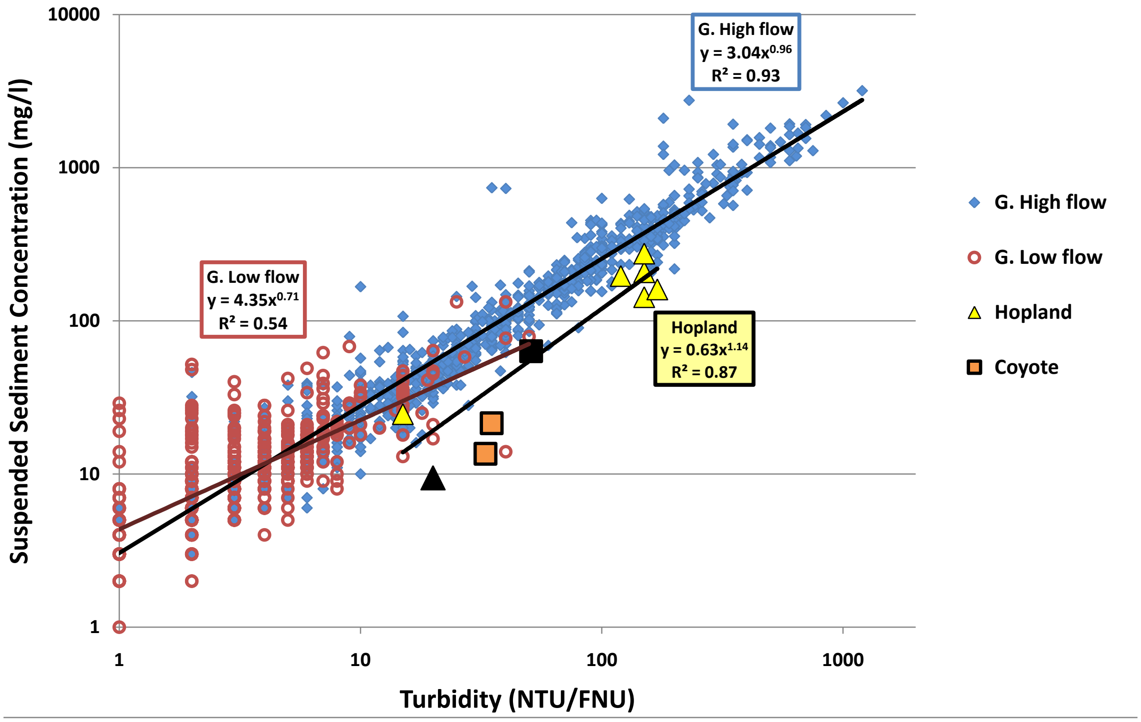

Figure 4.4: The relationship between turbidity and suspended sediment concentration (SSC) on the Russian River. All data from Guerneville and turbidity data at Hopland were collected by the USGS. Low-flow at Guerneville is defined as Q<= $10m^3/s$ for this figure. SSC measurements for Hopland and Coyote Dam and turbidity data from Coyote Dam were collected in this study.

mg/l. For all of the other samples at Hopland, the suspended sediment was passed through a 0.45 micron filter and the filtrate was then passed through a 0.22 micron filter. The second filtration was not performed for one of the subsamples of the point in question. SSC for this subsample was adjusted by 17% to correspond to the sediment between 0.22 and 0.45 microns found in the second subsample. This adjustment increases the SSC at this point by 5% and alters the leading coefficient and the exponent in equation 4.6 by 7% and 1%, respectively. The sample point denoted with a black square is from Coyote Dam. It was collected on a 1.0 micron filter with no subsequent filtration. It is not adjusted in this figure.

Suspended sediment flux at Hopland will be calculated using both equations (4.5) and (4.6) for the entrainment analysis. Neither estimate is ideal. Entrainment between Hopland and Guerneville calculated using (4.5) is underestimated because sediment transport at Hopland is overestimated. Entrainment calculated using (4.6) is uncertain at high T because the relationship is not well-constrained at the upper end.

Ritter and Brown [67] developed T-SSC relationships for a number of sites closer to Hopland than Guerneville and it would be useful to use these measurements to improve or verify the T-SSC relationship for Hopland. Unfortunately, the USGS has only continued to monitor suspended sediment at one of these sites. This site is on Dry Creek downstream of Warm Springs Dam; this drainage has the highest sediment yield in the Russian River basin Ritter and Brown [67]. Considering the difference between this location and Hopland, the T-SSC relationship from Dry Creek is not applicable to Hopland.

The six suspended samples collected at Hopland during a short dam release were analyzed for particle size distribution by a Coulter LS laser diffraction size analyzer. The analyzer takes a subsample of less than 100 milliliters and stirs the fluid fast enough to break up flocs into their consituent particles. This would result in a calculated GSD with less coarse material and more fine material than the same sample analyzed by the USGS, which determines grain diameter using a sedigraph to measure fall velocity at Guerneville. The Coulter analyzer reports sizes between 0.4 and 1000 microns (1mm).

4.3.3 Digital Watershed

The calculations in this chapter rely on a digital watershed that ties together USGS daily and 15-minute monitoring data, USGS field samples, NOAA atmospheric data, and reservoir flow and storage. Snapshots of data were accessed using a data cube with a pivot table in Excel. The data cube yields simple and fast summaries of data availability by site and time period as well as cross-referencing between datasets. Once datasets were identified using the data cube, they were downloaded and analyzed in SQL, Matlab, and Excel. The data cube includes the majority of USGS monitoring data for California and is accessible at http://bwc.berkeley.edu/DataServerdefault.htm with permission from the Berkeley Water Center.

4.3.4 Data-filling and smoothing

The USGS 15-minute discharge and turbidity data are prone to noise from turbulence, other transient conditions, and instrumental error. To deal with this, discharge was smoothed using a running average window of seven 15-minute points, representing 105 minutes. The seven-point window was chosen because it was large enough to smooth out most noise but small enough to be able to pinpoint hydrograph peaks. The turbidity data are much noisier than discharge and a larger smoothing window is required in order to see patterns over the course of storms or at low flow. Turbidity data were smoothed by averaging over a triangular moving window with a width of 15 data points (225 minutes). This triangular window gives the most weight to the central points.

The turbidity record had many data gaps due to fouling or limitations of the probe. These gaps were filled through linear interpolation. Most data gaps were less than an hour (4 data points) but some lasted for over a day. Because the data gaps often occurred during large storms, this results in underestimates of peak suspended sediment transport. These large data gaps only affect the calculations of annual sediment load. Over 90% of the data points are available for most years. The exceptions were 2006 at Hopland and 2003 and 2005 at Guerneville, for which more than 80% of the data are available. Analysis of individual storms and dam releases was limited to periods with no data gaps longer than an hour.

4.3.5 Indentification of storms and dam releases

The dam releases through Coyote Dam (Lake Mendocino) offer a chance to view sediment exchange between the riverbed and the water column, as all of the suspended sediment is either from the reservoir or is entrained from the streambed or banks. The continuous turbidity records at Hopland and Guerneville, both downstream of Lake Mendocino, make it possible to estimate downstream differences in suspended sediment discharge. The difference in sediment flux is assumed to equal cumulative entrainment from the reach.

Reservoir outflow data were analyzed to identify large releases from Coyote Dam that were not concurrent with large releases from Warm Springs Dam. There were over 30 large releases from Coyote Dam during the period covered by the 15-minute USGS turbidity record. Of these, there are 4 releases that have turbidity records without gaps and where the dam release hydrograph can be distinguished from releases from Warm Springs Dam and from storm hydrographs at both Guerneville and Hopland. The four releases studied are summarized in Table 4.2; the other dam releases are summarized in Table 4.3.

4.3.6 Sediment flux

Suspended sediment flux on the Russian River is calculated by translating instantaneous turbidity (T) into suspended sediment concentration (SSC) and multiplying by with the water discharge (Q).

Number	Dates of release	Q_{Coy} (m^3/s)	Q_H (m^3/s)	u_* (m/s)
DR1	February 20-22 2003	57	66	0.088
DR2	December 26-28 2003	57	74	0.091
DR3	January 14-16 2004	52	63	0.086
DR4	January 12-13 2005	70	114	0.103

Table 4.2: Dates and average flow rates for the dam releases studied. Q_{Coy} is outflow from Coyote Dam and Q_H is discharge at Hopland. The shear velocity is calculated using the relation $u_* = (ghS)^{0.5}$ with reach-averaged bed slope S and water depth at Hopland h.

Dates	Reason
20-Feb-2002 – 22-Feb-2002	1
01-Jan-2003 – 03-Jan-2003	1,2
14-Jan-2003 – 15-Jan-2003	2
27-Jan-2003 – 29-Jan-2003	2
18-Feb-2003 – 19-Feb-2003	1
14-Apr-2003 – 15-Apr-2003	2
22-Dec-2003 – 23-Dec-2003	1
30-Dec-2003 – 31-Dec-2003	1
02-Jan-2004 – 04-Jan-2004	2
14-Jan-2004 – 16-Jan-2004	2
20-Jan-2004 – 22-Jan-2004	2
03-Feb-2004 – 06-Feb-2004	1,2
09-Feb-2004 – 12-Feb-2004	2
19-Feb-2004 – 22-Feb-2004	2
27-Feb-2004 – 29-Feb-2004	2
28-Jan-2005 – 04-Feb-2005	1
02-Mar-2005 – 03-Mar-2005	2
04-Apr-2005 – 06-Apr-2005	2
11-Apr-2005 – 15-Apr-2005	2
19-May-2005 – 20-May-2005	1,2
30-Jan-2006 – 04-Feb-2006	1,2
28-Feb-2006 – 03-Mar-2006	2
13-Apr-2006 – 15-Apr-2006	1,2

Table 4.3: Dam releases with good data coverage not used in this study. Dates are for flow at Hopland. Many dam releases without good data coverage are not included in this table. Reasons for not using this DR are: (1) hydrograph merged with another large flow, and (2) concurrent DR at Warm Springs Dam.

4.4 Results

4.4.1 Cumulative sediment discharge

Annual suspended sediment discharge is calculated for the water years 2003-2006 using 15-minute data. These values are compared with cumulative suspended flux calculated from mean daily suspended sediment discharge reported by the USGS between 1967 and 1986. This analysis is presented first because it is a useful demonstration of the power of the 15-minute data set and the error associated with not having a good T-SSC relationship for Hopland.

Cumulative suspended sediment yield is shown for 2003-2006 in Figure 4.5. The majority of sediment flux occurs during large storms, which appear as steps in Figure 4.5. In this period the average erosion rate in the watershed above Guerneville is $0.2mm/yr$.

The choice of the T-SSC relationship used at Hopland has a large impact sediment calculations, which can alter interpretation of basin dynamics. Sediment yield at Hopland in Figure 4.5 was calculated using the T-SSC relationship from Guerneville. In Figure 4.6, sediment yield from this T-SSC relationship is compared against sediment yield calculated using the relationship from Hopland. On average, the sediment flux is 51% lower using the Hopland relationship. Using the relationship from Guerneville, the total sediment yield is about the same in the two portions of the basin. Using the Hopland relationship it appears that the basin is much less erosive upstream of Hopland than downstream of Hopland. Also demonstrated in Figure 4.6 is the impact of using 15-minute vs. daily data to calculate sediment yield. Yield is 17% lower calculated using the daily data than using the 15-minute data. SSC is greatest during stormpeaks, and a disproportionately large portion of the sediment flux occurs near peak flow. Mean daily turbidity does not capture this behavior.

Annual sediment discharge calculated using daily average turbidity is an underestimate but it allows comparison with earlier USGS data. In Figure 4.7 annual sediment discharge past Guerneville is compared with annual water discharge for water years 1967-85 (blue squares) and 2003-06 (red stars). This figure suggests that sediment yield is mainly a function of discharge and that there is a threshold behavior, where suspended sediment flux is very low at total water discharge less than 1 km^3. Most of the discharge occurs in the largest stormflow, which is seen by comparing peak annual stormflow with annual sediment flux (Figure 4.8). We can assume that the sediment supply is unusually high if the marker for a given year is above the data cloud in both figures. This occurs for one of the recent years and 1966, which is marked by the heavily outlined square. Ritter and Brown [67] found that the sediment supply during 1966 was still elevated from the 1964 flood. The fact that the recent data are on the upper edge of the cloud suggests that the sediment supply may have increased recently.

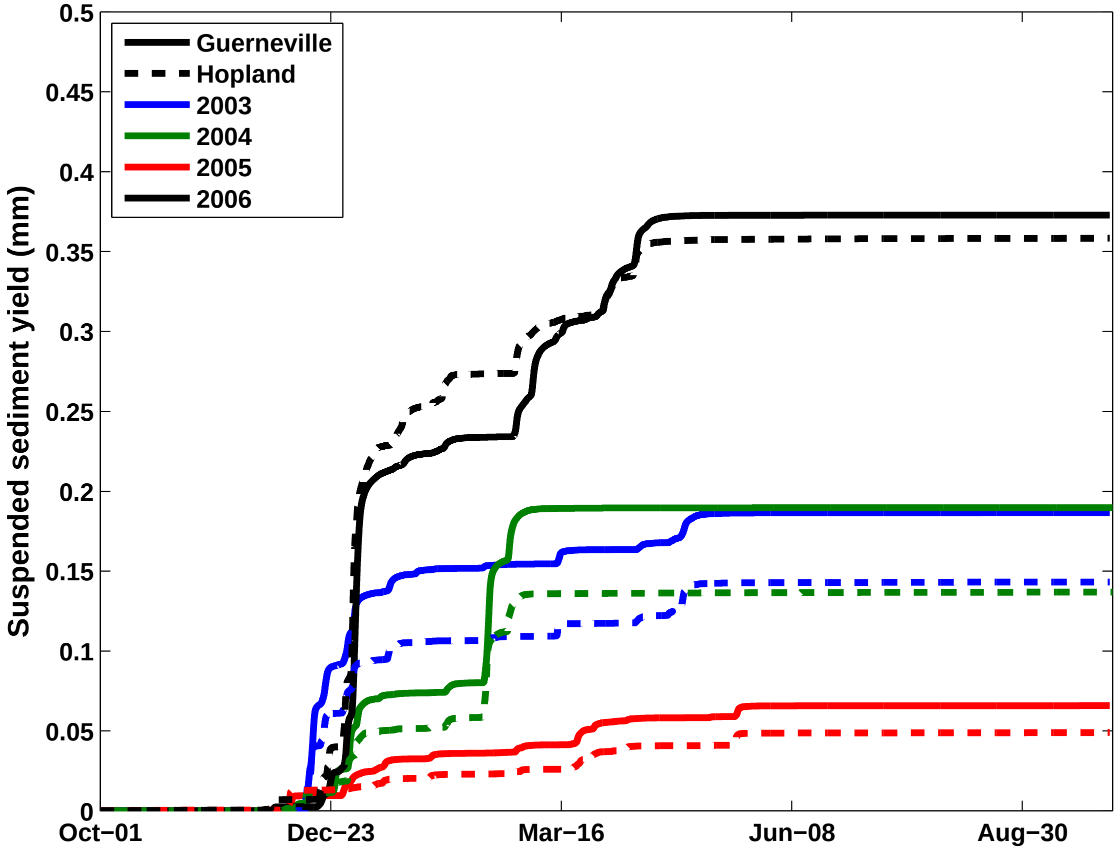

Figure 4.5: Cumulative suspended sediment yield. The solid lines represent the basin upstream of Guerneville and the dashed lines represent the Hopland watershed for the same years. Calculations of Hopland sediment yield use the T-SSC relationship from Guerneville data.

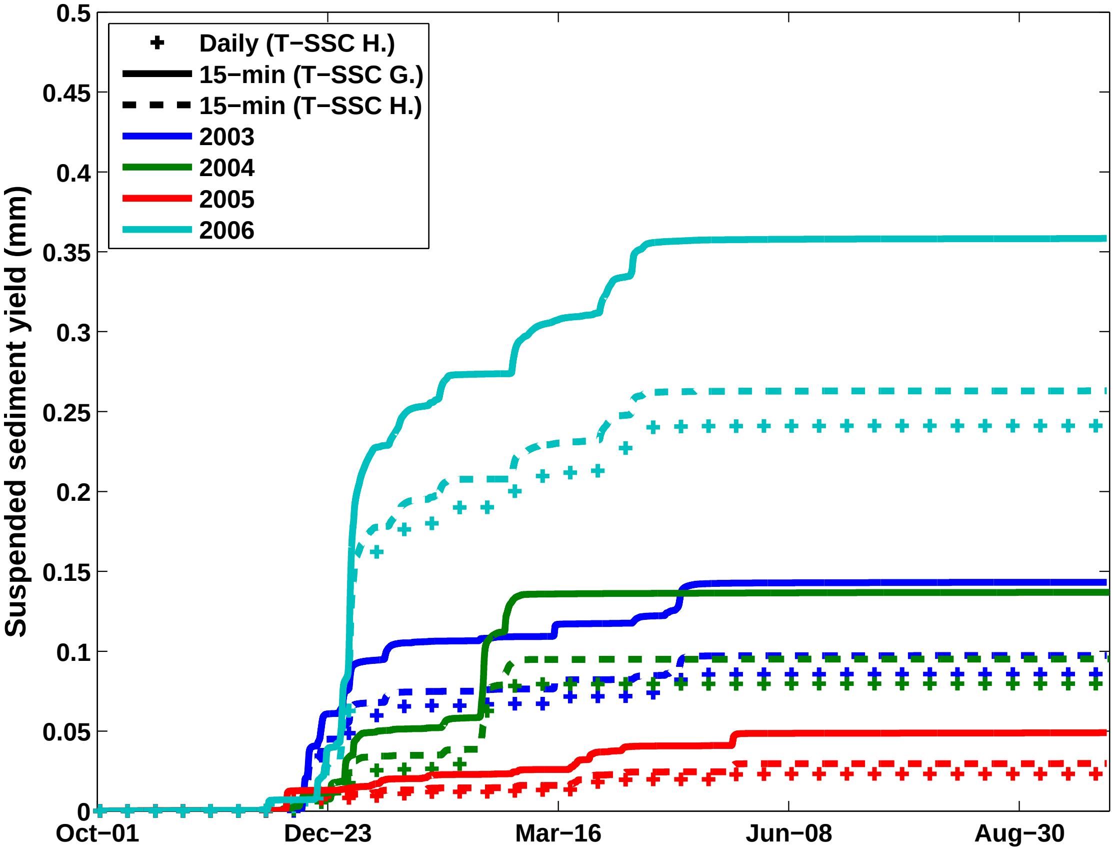

Figure 4.6: The effect of T-SSC relationship and time discretization on estimates of sediment yield at Hopland. The curves denoted with solid lines use the T-SSC relationship from Guerneville, while the other two sets of curves use the relationship built from samples at Hopland. The curves with dashed lines were calculated using 15-minute discharge and turbidity data, while the curves with '+' symbols were calculated using daily average data.

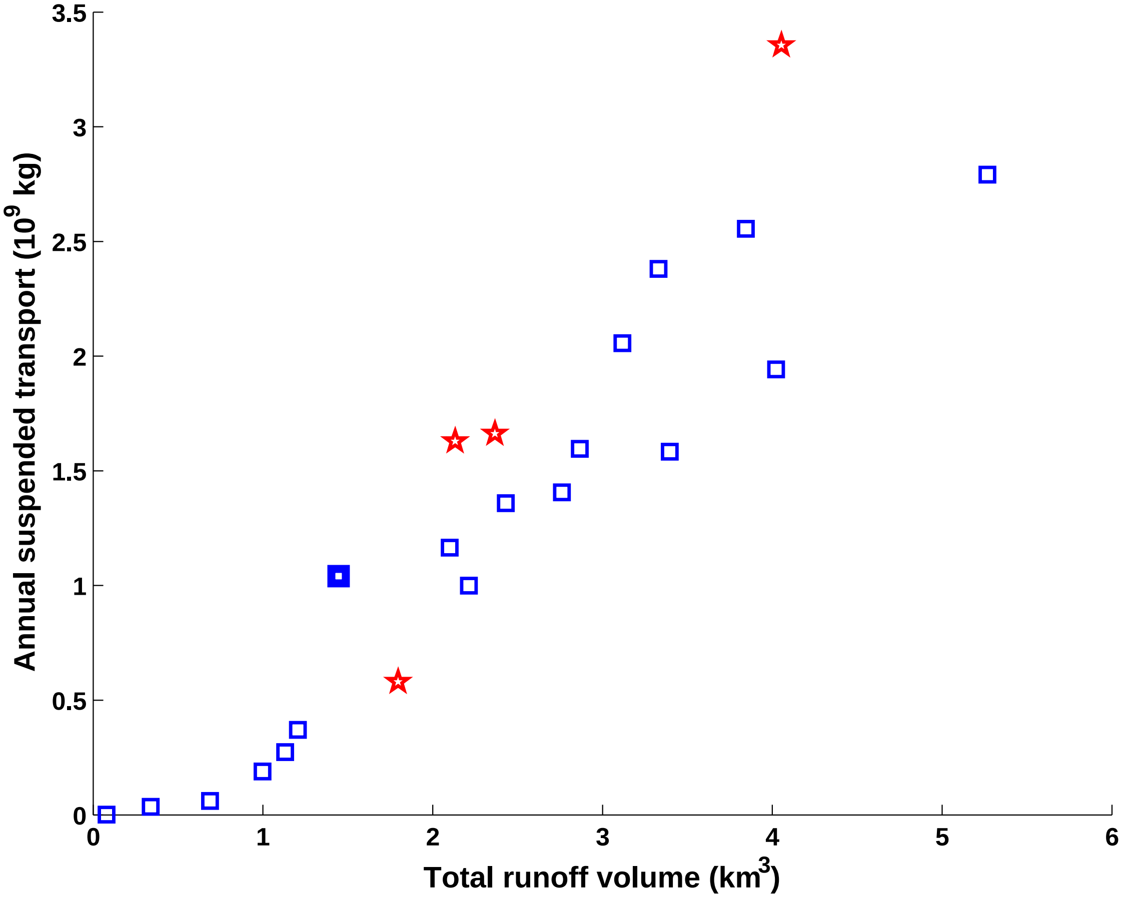

Figure 4.7: The longterm relationship between annual suspended sediment discharge and annual water discharge at Guerneville. The blue squares represent USGS calculations from 1967-85 and the red stars are estimates made in this paper from 2003-2006 daily averaged data. The heavily outlined square is from 1966.

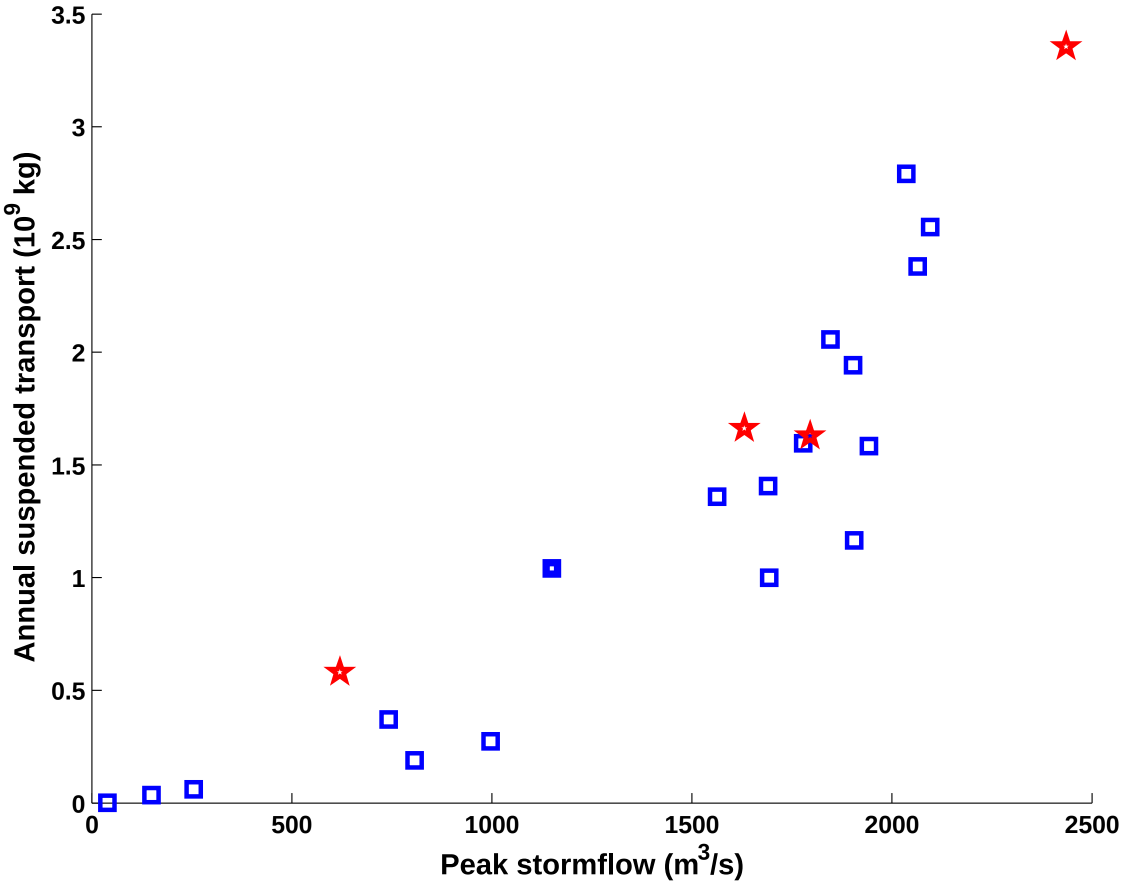

Figure 4.8: The longterm relationship between annual suspended sediment discharge and annual peak stormflow. The blue squares represent USGS calculations from 1967-85 and the red stars are estimates made in this paper from 2003-2006 daily averaged data.

Figure 4.9: The Russian River at Hopland at low discharge. The light-colored streak is a plume of fine sediment released when sampling the bed.

4.4.2 Entrainment calculation

In this section, entrainment of suspended sediment from the riverbed between Guerneville and Hopland is estimated. This analysis is performed to demonstrate that there is a measurable mass of suspended sediment entrained, to explore what variables determine entrainment rates, and to search for evidence that entrainment is from the surface or the subsurface

Disturbance of the gravel bed surface on the Russian River releases a plume of suspended sediment (Figure 4.9). This suggests that there is a high content of suspendable sediment in the upper layers of the riverbed that will be entrained if gravel is mobilized. Cumulative entrainment of subsurface fines into suspension will depend on the areal fraction of the streambed that is mobilized during these flows. Once cumulative entrainment from the reach is calculated, this is transformed into a timeseries of local entrainment by estimating bed mobility from USGS bedload data. The timescale t_{ex} and total mass of suspended sediment M_o are then compared with forcing factors such as discharge.

Entrainment during the four DRs is calculated by comparing sediment flux at the two sites. Cumulative entrainment is denoted $\rho_s EA$, where ρ_s is the density of sediment (m/l^3), E is entrainment (l/t), and A is the total area of the bed from which entrainment occurs (l^2). The timeseries of cumulative entrainment $(\rho_s EA)(t)$ is transformed into a timeseries of local entrainment $E(t)$ (l/t). Example time-series for each step of the calculation are given in figures, and each DR is shown once. Entrainment estimates are made using both the T-SSC relationships from Hopland and Guerneville to calculate sediment flux at Hopland. Figures are made using the T-SSC relationship from Hopland (equation 4.6) to calculate sediment transport at Hopland.

The term total entrainment should be distinguished from cumulative entrainment; total entrainment refers to the sum of entrainment over the duration of the DR.

Background sediment flux

In order to obtain a time-series of sediment transport that is only related to entrainment, the background sediment flux needs to be subtracted from the sediment transport record at both sites. The background flux is defined as the suspended sediment that would pass each station if the dam release hadn't been made. The hydrograph, total sediment flux, and background sediment flux at both Hopland and Guerneville are shown for DR1 in Figure 4.10. Only the portion between the two black asterisks is considered for this analysis; the earlier portion is excluded because it overlaps a small rainstorm and the late portion is excluded because the discharge is too small to be distinguished at Guerneville. The background sediment flux is calculated by connecting sediment flux before and after the DR using an exponential decay function.

To determine how the background flux decays, the falling limbs of seven stormflows on the Russian River were studied at both sites. Stormflows were chosen for which there were complete data records and which were followed by at least one day without another storm (Table 4.4). Figure 4.11 is a plot of $Q_{sG}/Q_{sGo}(t)$ against time for all seven storms at Guerneville, where Q_{sG} is suspended sediment transport at Guerneville and Q_{sGo} is the peak sediment transport rate in the storm. The pattern is similar between storms, with Q_{sG} decaying exponentially at an average rate of 0.08 per hour. Background sediment transport is calculated for the DR's by connecting Q_{sG} before and after each DR background an exponential fit. This was not possible for DR2 because the end of the DR hydrograph overlapped a large storm. Instead, $Q_{sG,bk}(t)$ was calculated by extending the timeseries $Q_{sG}(t)$ leading up to DR2 forward in time at a decay rate of 0.08 per hour.

At Hopland the behavior is more complex. Figure 4.12 is a plot of suspended sediment flux at Hopland (Q_{sH}) on the falling limb of storm peaks. An exponential decay would appear as a straight line; post-storm suspended sediment transport at Hopland does not decay in a regular exponential pattern. The trends become exponential after 12-18 hours but there is no common decay coefficient between storms. The study DR's all occur more than four days after the previous storm, and so an exponential fit is used. For DR1, DR3, and DR4, $Q_{sH,bk}(t)$ is estimated by connecting $Q_{sH}(t)$ before and after the DR with an

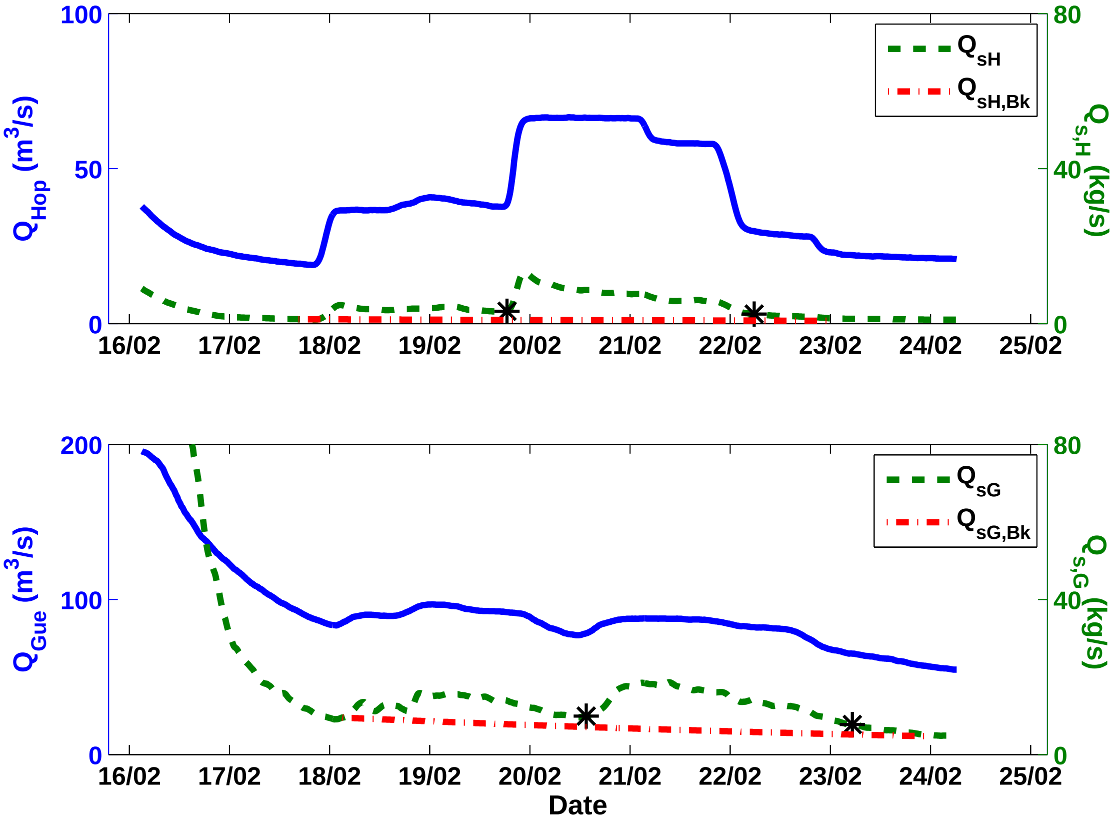

Figure 4.10: Background sediment transport over DR1. The solid blue line is a DR hydrograph, corresponding to the left y-axis. The dashed green line is the suspended sediment transport and the dash-dot red line is the background suspsended sediment transport (right y-axis). The top figure shows the DR at Hopland and the bottom figure shows the same DR at Guerneville. The black asterisks show the start and end points of the DR used in this analysis.

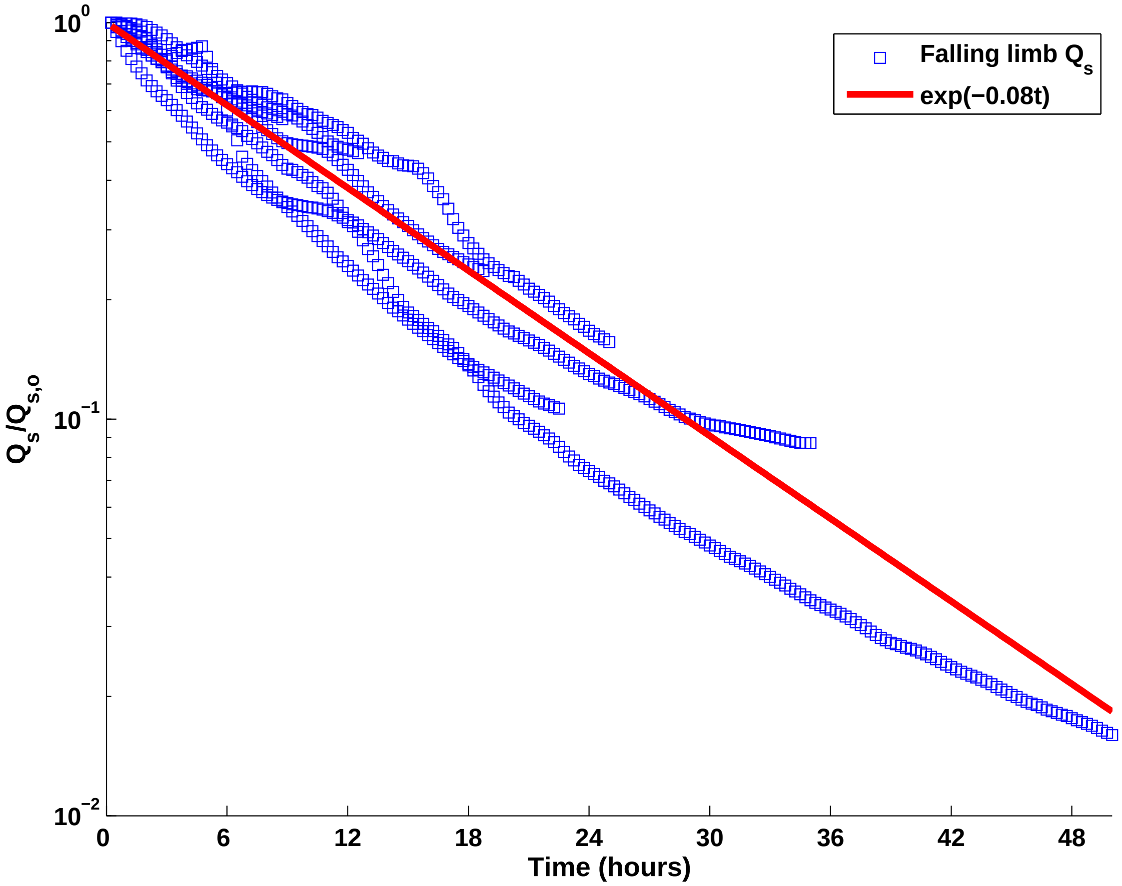

Figure 4.11: The decay in sediment transport at Guerneville on the falling limbs of seven storms (Table 4.4). The data for a given storm continue until the beginning of another storm or DR hydrograph interupts the falling limb. The red line represents the average exponential decay in this data.

Date	Peak discharge (m^3/s)	Peak turbidity (NTU)
14-Dec-03	222	769
28-Feb-05	108	371
26-Dec-05	152	518
29-Jan-06	109	633
12-Dec-06	79	1002
22-Dec-06	46	510
22-Feb-07	77	484

Table 4.4: Model stormflows used to study sediment transport decay rates. These stormflows have good data records for both turbidity and streamflow and are followed by at least a day without further storm activity. Date, peak flow, and peak turbidity values are given for Hopland.

exponential regression (Figure 4.10). For DR2, $Q_{sH,bk}(t)$ is estimated by extending forward the exponential decay seen before the DR; the decay coefficient is 0.1 per hour.

Travel time

To develop a record of cumulative entrainment, the sediment transport records at both sites need to be related with a travel time. There are two travel times that are used to calculate entrainment. These are the travel times of suspended sediment τ_s, which moves at the water velocity, and the travel time of the hydrograph τ_w, which moves at the wave speed. Wave speed is greater than the water velocity and so τ_w is less than τ_s [46].

Travel times are a function of discharge because deeper water is less affected by bed friction and thus moves faster. τ_s and τ_w are estimated as the difference in arrival times of the hydrograph peaks or sediment peaks at the two sites. τ_w can be estimated for DR's and for stormflows (summarized in Table 4.5). The scatter in storm data is caused by spatial variability in rainfall, which shifts the centroid of the hydrograph during transit. τ_s is shown only for DR's, because noise in the sediment signal during rainstorms makes it difficult to determine τ_s. Relationships between travel time and discharge are determined by linear regression through the storm and DR data (Figure 4.13):

$$\tau_s = 25.7 - 0.04Q_H, \qquad \text{and} \tag{4.7}$$

$$\tau_w = 21.3 - 0.04Q_H, \tag{4.8}$$

where Q_H is water discharge at Hopland in m^3/s and τ_s and τ_w are in hours.

It is possible to simply estimate entrainment by relating suspended transport records Q_{sG} and Q_{sH} on a point-by-point basis, using the sediment travel time and subtracting the

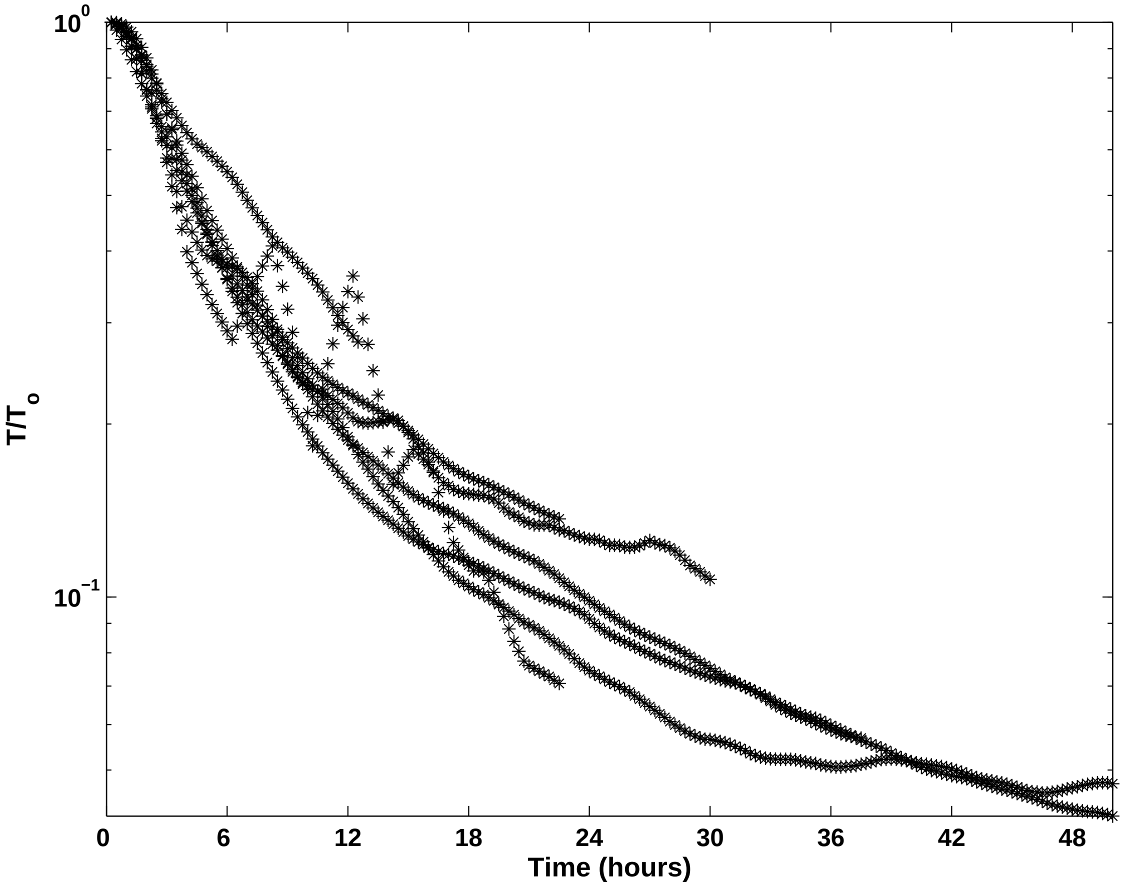

Figure 4.12: The decay in sediment transport at Hopland on the falling limbs of seven storms (Table 4.4). The trend for a given storm continues until the beginning of another storm or DR hydrograph interrupts the falling limb.

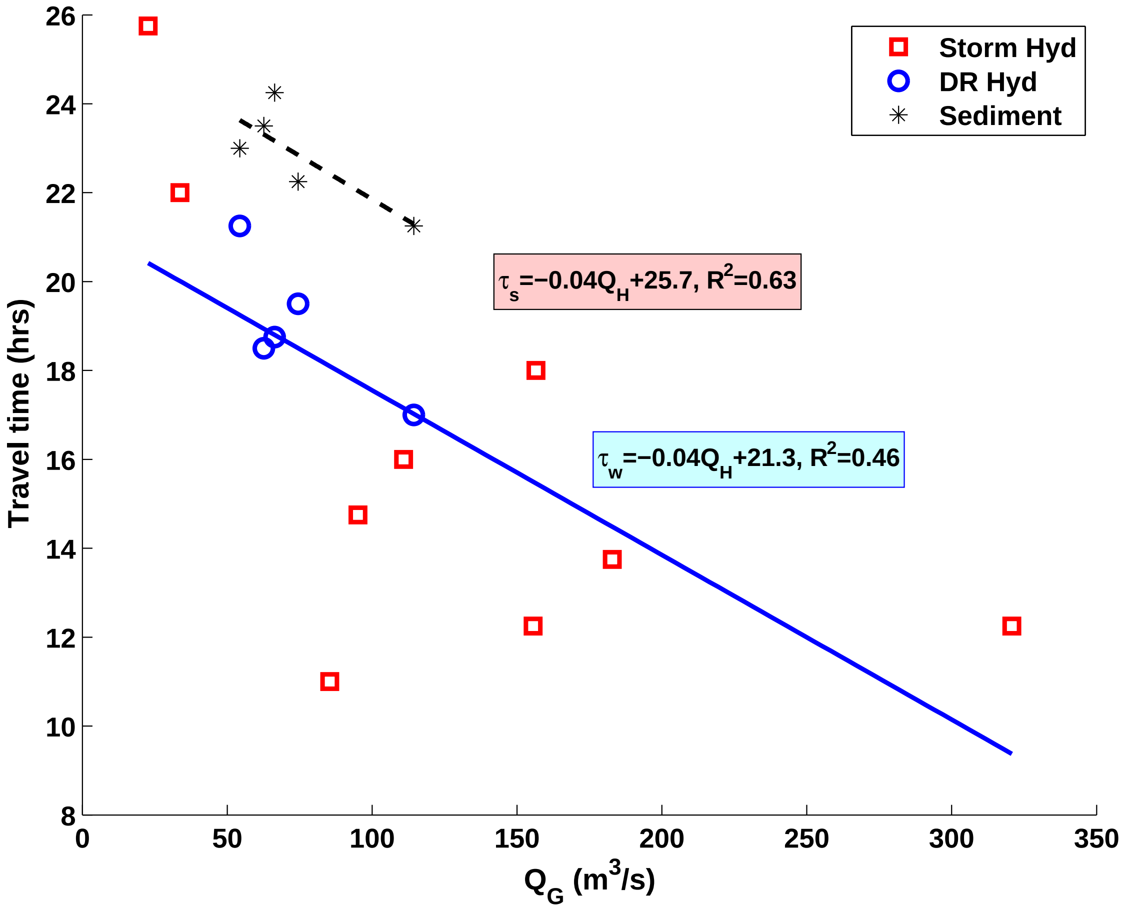

Figure 4.13: Travel times for sediment waves and hydrographs between Hopland and Guerneville. Storm hydrographs are represented with red squares. Dam release (DR) hydrographs are blue circles. Black asterisks are lags for sediment waves from dam releases.

Date	Peak discharge (m^3/s)
06-Dec-03	85
25-Feb-04	321
08-Jan-05	95
11-Jan-05	156
20-Feb-05	33
28-Mar-05	183
14-Jan-06	111
18-Jan-06	157
04-Jan-07	23

Table 4.5: Model stormflows used to study hydrograph travel times. These stormflows have good data records and are separated in time from other stormflows by enough time to clearly distinguish the hydrograph at Guerneville. Date and peak flow values are given for Hopland.

background fluxes. This is the naïve calculation for entrainment:

$$(\rho_s EA)(t) = \big(Q_{sG}(t) - Q_{sG,bk}(t) - Q_{sH}(t-\tau_s) + Q_{sH,bk}(t-\tau_s)\big). \tag{4.9}$$

An example timseries calculated using (4.9) is given for DR2 in Figure 4.14, along with discharge and excess sediment transport $Q_{sG} - Q_{sG,bk}$ at Guerneville. One problem with this simple entrainment calculation is the presence of a sharp drop in entrainment near the beginning of the DR (Figure 4.14). If the T-SSC relationship from Guerneville is used to calculate Q_{sH}, the sharp drop leads to negative values in entrainment. This drop is common to all four DR's and corresponds to the spike in Q_{sH} at the beginning of the DR at Hopland (Figure 4.3). There is a peak in Q_{sG} at Guerneville but it is much less pronounced, and the difference leads to an apparent drop in entrainment. Equation 4.9 ignores longitudinal shear dispersion, which would spread out the signal from Hopland.

In order to obtain a realistic timeseries of entrainment, shear dispersion must be addressed. The excess sediment transport signal from Hopland is transformed using a function that accounts for both dispersion and the relative travel times of the hydrograph and sediment. This transformation is easier if the frame of reference is changed to travel downstream with the hydrograph. This change allows downstream dispersion, so that some sediment arrives at Guerneville before the peak from Q_{sH}.

Dispersion

Shear dispersion will spread a pulse of suspended sediment into a normal curve distribution as it travels downstream. The standard deviation of this curve in space is $\sigma_{dp} = \sqrt{2K_x\tau_s}$, where K_x is the dispersion coefficient and the subscript dp is for dispersion [24]. The sediment

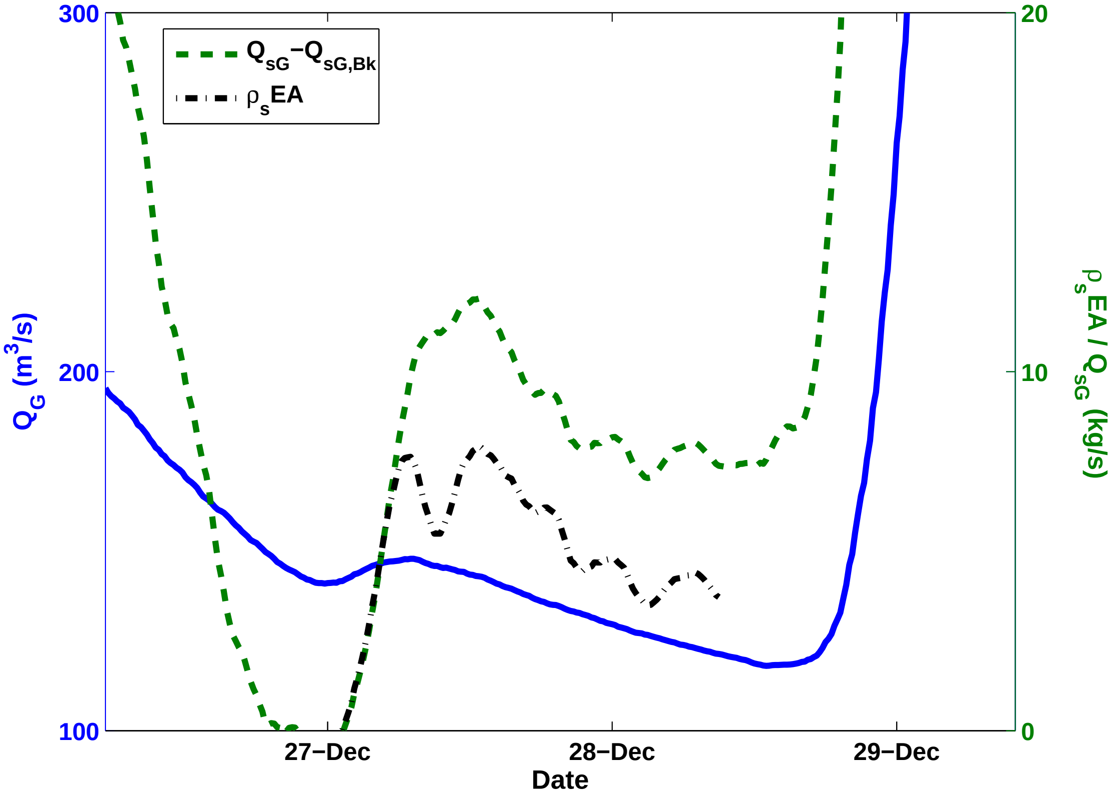

Figure 4.14: Naïve estimate of cumulative entrainment $\rho_s EA(t)$ for DR2, calculated by equation 4.9. The solid blue line is discharge at Guerneville (left y-axis). The entrainment and flux terms correspond to the right y-axis. The difference between $Q_{sG} - Q_{sG,bk}$ and $\rho_s EA$ is the excess suspended sediment flux from Hopland.

transport records are functions of time rather than functions of space, so the standard deviation in the record $Q_{sG}(t)$ will be $\sigma_{dpt} = \sigma_{dp}/U$, where U is the average water velocity, and σ_{dpt} has units of time. Seo and Cheong [73] developed an empirical prediction for K_x using 35 measurements in made in natural rivers.

$$\frac{K_x}{Hu_*} = 5.915 \left(\frac{W}{H}\right)^{0.620} \left(\frac{U}{u_*}\right)^{1.428}. \tag{4.10}$$

where W is channel width (l), H is water depth (l), and K_x has units (l^2/t). The river data used to develop this relationship ranged from $W = 10$ to 540 meters, $H = 0.2$ to 20 meters, $U = 0.1$ to 1.7 meters per second, $u_* = 0.02$ to $0.27\ m/s$, and $K_x = 1$ to $1500\ m^2/s$. K_x and σ_{dpt} can be estimated from hydraulic variables from the Russian River (Table 4.1). Equation 4.10 predicts that σ_{dp}/U is less than one hour for suspended sediment traveling between Guerneville and Hopland.

Excess sediment flux at Hopland $(Q_{sH} - Q_{sH,bk})$ is numerically dispersed into a timeseries of that sediment as it arrives at Guerneville:

$$(\widetilde{Q_{sH} - Q_{sH,bk}})(t) = \int\limits_{DR} \frac{Q_{sH}(t') - Q_{sH,bk}(t')}{(2\pi\sigma_{dpt}^2)^{0.5}} \exp\left[-\frac{(t - (t' + (\tau_s - \tau_w)))^2}{2\sigma_{dpt}^2}\right] dt', \tag{4.11}$$

where the tilde over the term on the left indicates dispersion, t' is the dummy variable for integration over time, and DR indicates integration over the time of the dam release at Hopland. The expression inside the integral is a normal distribution with the center of the distribution shifted from t' to $t' + \tau_s - \tau_w$. This time corresponds to the point in the hydrograph when the turbidity spike from Hopland would pass Guerneville.

This dispersed signal of $(\widetilde{Q_{sH} - Q_{sH,bk}})$ is subtracted from the sediment transport record at Guerneville to calculate $\rho_s EA$, where t is relative to the start of the hydrograph:

$$(\rho_s EA)(t) = Q_{sG}(t) - Q_{sG,bk}(t) - (\widetilde{Q_{sH} - Q_{sH,bk}})(t). \tag{4.12}$$

Figure 4.15 shows how dispersion effects the cumulative entrainment timeseries for DR4. This figure includes the DR hydrograph (solid blue line) and $(\rho_s EA)(t)$ calculated using two different values of K_x. The first value of K_x is from equation 4.10 (the solid black line), and the second value is ten times greater (the dashed red line). Dispersion using K_x from (4.10) is not sufficient to get rid of the sharp drop in entrainment at the beginning of the DR. The drop disappears when K_x is ten times greater. It is feasible that dispersion on the Russian River corresponds to a value of K_x 10 times greater than predicted by equation (4.10). Longitudinal dispersion varies widely on rivers, and there are many features on the Russian that could increase dispersion. This will be expanded upon in the Discussion section.

Cumulative entrainment is estimated using values of K_x ten times greater than predicted by (4.10). Total entrainment over the four DR's is given in Table 4.6.

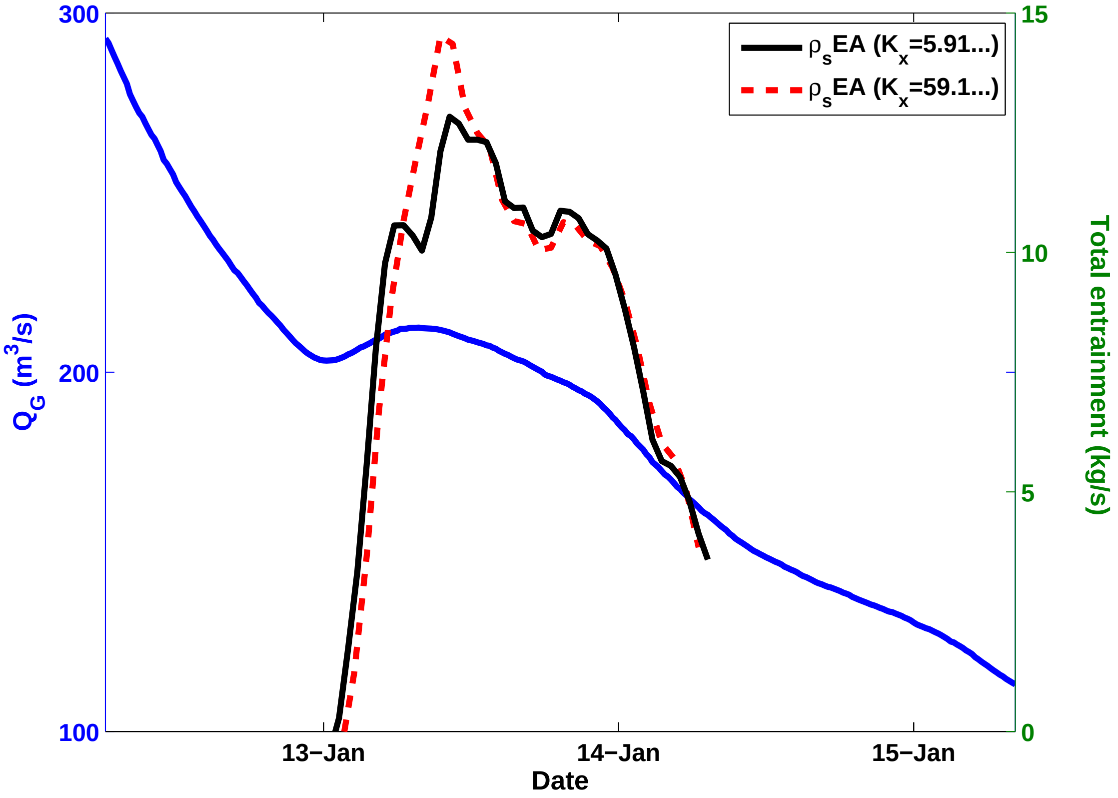

Figure 4.15: Cumulative entrainment $\rho_s EA(t)$ during DR4. The solid blue line is the DR hydrograph at Guerneville (left y-axis.) The entrainment timeseries correspond to the right y-axis. The solid black line corresponds to a dispersion coefficient predicted by equation 4.10, and for the dashed red dispersion is set ten times higher. The higher dispersion coefficient is used in the final entrainment calculations.

	Total (m^3)	t_{ex} (hr)	$\rho_s E_o A$ (kg/s)
DR 1	470 (164)	38.3 (28.1)	9.26 (4.79)
DR 2	227 (55)	15.9 (5.2)	8.04 (9.34)
DR 3	728 (340)	70.5 (34.7)	14.11 (10.92)
DR 4	369 (145)	20.6 (19.7)	13.18 (7.75)

Table 4.6: Summary of cumulative entrainment for the four DR's. Values in parentheses are calculated using the T-SSC relationship from Guerneville at Hopland; values not parenthesized use the T-SSC relationship from Hopland. 'Total' is the sum of cumulative entrainment over the DR. t_{ex} is the timescale of decay of entrainment, and $\rho_s E_o A$ is the peak entrainment rate for the entire reach calculated from equation 4.15.

Local entrainment

In order to estimate a timeseries of local entrainment $E(t)$, $(\rho_s EA)(t)$ needs to be transformed to account for dispersion of sediment between the location where it is entrained and Guerneville and the variable velocity of the hydrograph and the sediment wave. To do so, the form of the mathematical function $E(t)$ must be assumed. In the introduction of this chapter, assumptions from Wu and Chou [89] were used to demonstrate that if deposition is negligible compared to entrainment, then entrainment should decay exponentially with time. This form will be assumed for now and tested later using estimated entrainment and deposition rates:

$$E(t, x) = E_o e^{-(t)/t_{ex}}, \tag{4.13}$$

where E_o is the initial entrainment rate (l/t) and t is the time relative to when the DR first reaches x. The timescale t_{ex} is estimated from regression on the decaying part of the cumulative entrainment timeseries $(\rho_s EA)(t)$ (Table 4.6.)

In the frame of reference moving with the hydrograph, the velocity of water and thus suspended sediment is negative $U_r = (\tau_w - \tau_s)/L$. $\rho_s EA$ is the integral of local entrainment from throughout the reach:

$$(\rho_s EA)(t) = \frac{\rho_s A}{L} \int_0^L \widetilde{E}(t + x/U_r) dx, \tag{4.14}$$

where the tilde indicates dispersion. Explicitly accounting for diffusion, the relationship between cumulative and local entrainment is

$$(\rho_s EA)(t) = \frac{\rho_s A}{L} \int_{x=0}^{x=L} \int\limits_{DR} \left(E_o e^{-t'/t_{ex}} \right) \left(2\pi\sigma_x^2 \right)^{-0.5} \exp\left[-\frac{(t - (t' - \frac{x}{U_r}))^2}{2(\sigma_x^2)} \right] dt' dx, \tag{4.15}$$

where $\sigma_x = (2K_x x/U_s)^{0.5}/U_s$ is the standard deviation in time from shear dispersion between x and Guerneville, t' is a dummy variable for time, and entrainment has units (l/t). For any combination of x and t', the product inside the integrals is the contribution to sediment transport at Guerneville at time t resulting from entrainment at location x at time t'. The middle and far-right terms inside the integral are the probability distribution associated with a normal curve. The centroid of the distribution is shifted in time by x/U_r to account for the variable travel times of sediment and water.

$\rho_s E_o A$ is estimated by pulling E_o out of the integral in equation 4.15, numerically integrating over both x and t', and dividing $\rho_s EA$ point-by-point by the integral. The mean value of this ratio during the middle 2/3 of the DR is taken for $\rho_s E_o A$. In order to validate the exponential model (4.13), the integral in (4.15) is evaluated using the calculated value for $\rho_s E_o A$. This yields a timeseries of predicted cumulative entrainment; this timeseries is compared with calculated cumulative entrainment $(\rho_s EA)(t)$ for DR3 in Figure 4.16. These timeseries have very similar shape, demonstrating that excess sediment transport is consistent with an exponential model.

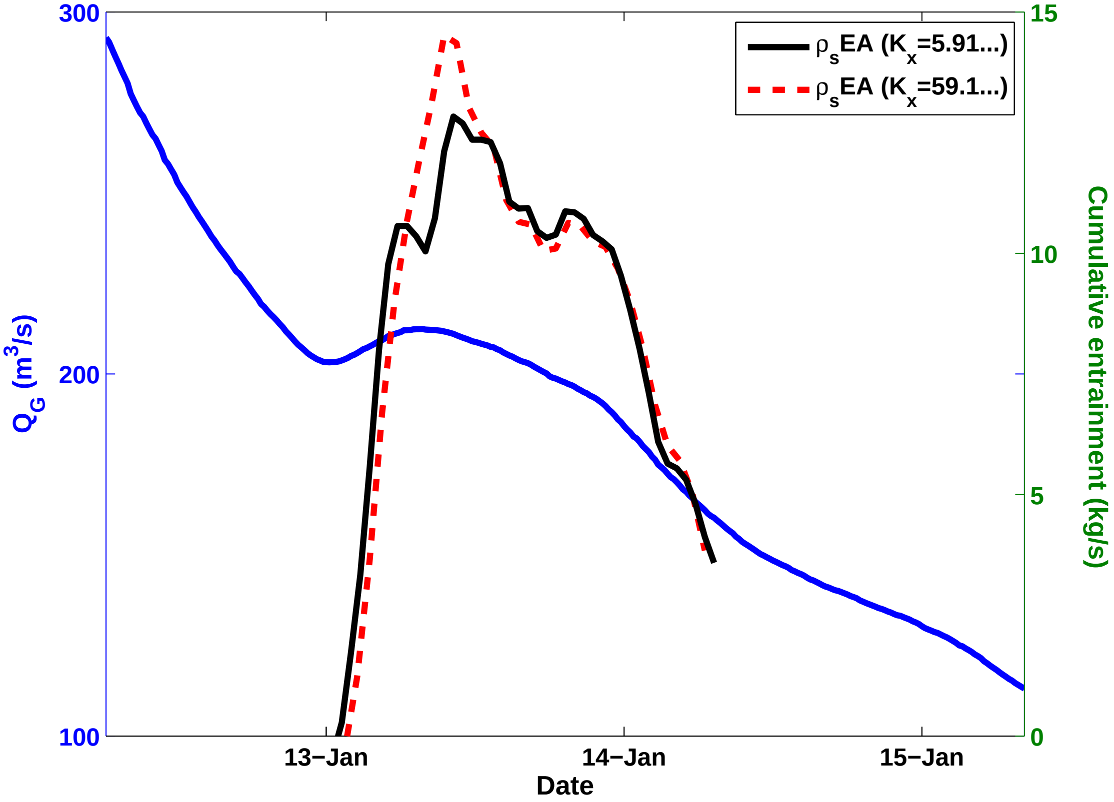

Figure 4.16: Cumulative entrainment during DR3. The blue line is taken from the sediment transport record. The red line is calculated by numerically dispersing local entrainment $E_o e^{-t/t_{ex}}$ and integrating over the reach.

Bed mobility and local entrainment

The final step in estimating local entrainment is to calculate the area from which material is entrained, A. If the entrained material is from the subsurface, it can only be from portions of the bed where the bed was mobile. Full mobility across an entire riverbed may occur only during very large flows. The recurrence interval of the largest DR ($Q_H = 114m^3/s$) is less than one year [26], and so it is likely that much of the bed was immobile. The mobile bed area $A = WL$, is assumed to extend the length of the reach, so length $L = 97$ kilometers and W is the width of the mobile corridor. USGS bedload samples can be used to estimate W and thus $E(t)$. Calculating W involves making large assumptions about bed mobility, and there are no data to verify the calculated values, and so these calculations should be taken as suggestive, order-of-magnitude estimates.

USGS bedload samples from Hopland suggests that bedload transport begins at approximately $50m^3/s$ (Figure 4.17), and so it is reasonable to assume that portions of the bed become partially mobile starting at $50m^3/s$. Full bed mobility is the condition in which the grain size distribution of sediment in transport is equal to the grain size distribution of surface bed material. At partial mobility, the coarsest sediment is less mobile than fine bed material. Figure 4.18 shows that the D_{50} and D_{84} in bedload samples continue to increase up to discharges of $300m^3/s$. This indicates that bed mobility is increasing. Many studies have found that the bed is at least partially mobile throughout the channel at bankfull flow e.g. [35, 11]. Goodwin et al. [33] estimated bankfull flow on the Russian River at Hopland to be between 450 and 570 m^3/s; I take the mean value of $510m^3/s$ as bankfull flow. Since 1940, flow has exceeded $510m^3/s$ on 14 days, giving it a recurrence interval of approximately 5 years. There are no bedload samples from discharges above 300 m^3/s, so it is hard to quantify bed mobility. However, some information can be taken from changes in the USGS stage-discharge relationship.

Figure 4.19 shows how the size of a stormflow at Hopland affects the likelihood that the USGS will need to change the stage-discharge relationship. The data are taken from 548 field measurements from 1958 to the present day and are binned in increments of 10 m^3/s. The peak discharge is the maximum discharge between two site visits. The USGS changes these relationships when field visits indicate that enough morphological change has occured that the old stage-discharge relationship does not represent current conditions. The fraction of stormflows that cause resetting of the relationship approaches 100% as stormflow increases to 500 m^3/s. I take this as an indication that the bed is fully mobile at 500 m^3/s, and assume that the fraction of the bed that is mobile increases linearly from 0% at 50 m^3/s to 100% at 510 m^3/s:

$$A(Q) = A_{tot}\frac{Q_H - 51}{510 - 51} \tag{4.16}$$

where A_{tot} is the total bed area. Equation (4.16) predicts that the mobile fraction of the bed during DR1-DR4 is 4%, 4%, 3%, and 14%, respectively. The corresponding values of W are 2, 2, 1, and 6m.

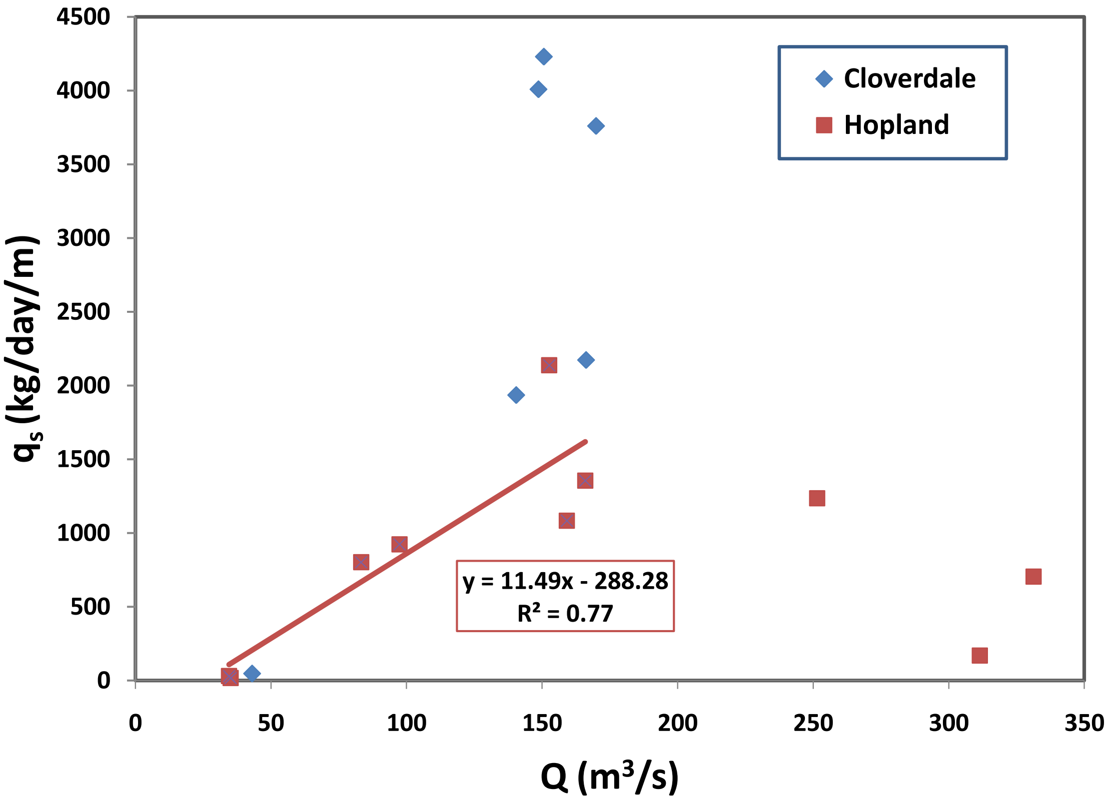

Figure 4.17: Bedload transport normalized by channel width vs. the local water discharge. Cloverdale is between Hopland and Guerneville. The trendline is for measurements at Hopland with discharge less than 200 m^3/s. Data were collected by the USGS between 1992 and 1996.

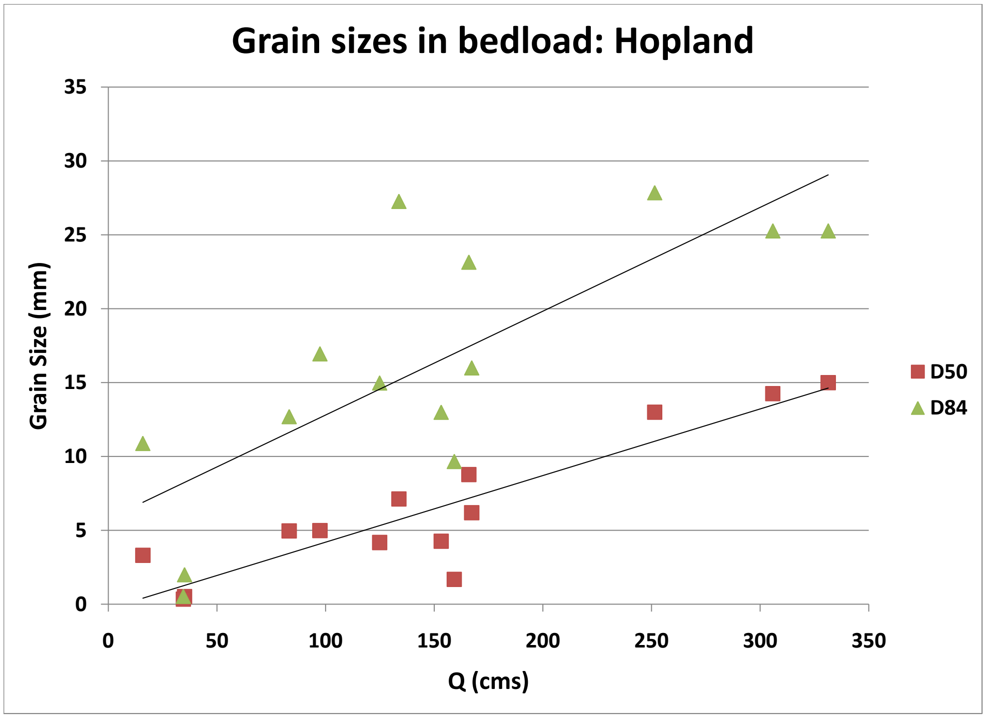

Figure 4.18: Median grain size and D_{84} of bedload samples collected at Hopland under a range of flows. The bedload D_{50} is greater than typical bed sediment D_{50} at flows above $Q = 150m^3/s$, indicating full bed mobility.

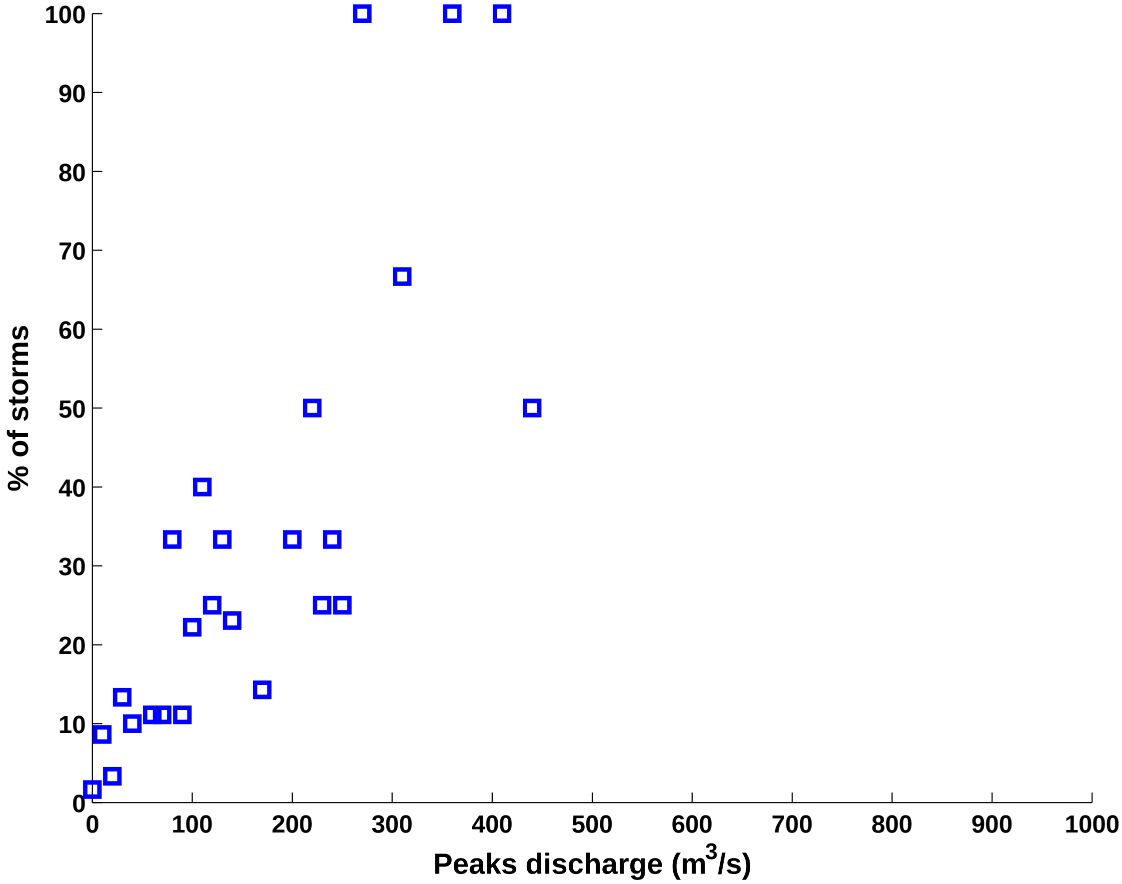

Figure 4.19: The fraction of stormflows that result in the USGS resetting the stage-discharge relationship at Hopland. Data are from 548 field mmeasurements between 1958-2010 and are binned in increments of 10 m^3/s.

	E_o (mm/hr)	M_o kg/m^2
DR 1	0.1	10
DR 2	0.1	3
DR 3	0.2	35
DR 4	0.04	2

Table 4.7: Initial local entrainment rate and suspended sediment supply in the bed, based on order of magnitude estimates of bed mobility. Calculations are based on use of the T-SSC relationship from Hopland to calculate suspended sediment flux at Hopland.

E_o is calculated assuming these values of W (Table 4.7). Estimates of E_o are between 0.03 and 0.22 mm/hr. This value sheds some insight on the source of sediment. If material is being entrained from the surface, the rate should be comparable to $E_{GP}f$, where E_{GP} the Garcia-Parker model for entrainment and f is the fraction of suspendable sediment on the bed. For the flow conditions in the DR's (Table 4.2), $E_{GP} = 0.3w_s$. The d_{50} from USGS suspended sediment samples at Guerneville is about 5 microns, which has a settling velocity of $0.02mm/s$ [16]. USGS bed samples suggest that $f = 0.05$, so $E_{GP}f = 1mm/hr$. The maximum calculated values of local entrainment E_o was one to two orders of magnitude smaller than $E_{GP}f$, suggesting that most of the entrainment was not directly from the riverbed surface.

Development of the exponential model for $E(t)$ assumed that entrainment far outstripped deposition. This can be tested using the estimates of E_o, which ranged from 0.03 and 0.22 mm/hr. The maximum SSC at Hopland during the four DR's is 57 $mg/liter$, and the settling velocity of the suspended d_{50} is $0.02mm/s$ [16]. Using a sediment density of $\rho_s = 2650kg/m^3$, the gravitational settling flux is $1.5x10^{-3}mm/hr$, one to two orders of magnitude smaller than entrainment.

By assuming that the entrainment rate decays exponentially over time, we can estimate the total mass of suspendable sediment that would be entrained during an infinitely long flushing flow, $M_o = E_o t_{ex} \rho_s$. Using this definition, M_o is the total supply of suspendable sediment in the bed. Calculated values are given in Table 4.7. M_o ranges from 2 to 35 kg/m^2 per bed area. These values of M_o are close to $4.0kg/m^2$, the subsurface supply of suspended sediment estimated from USGS bed samples.

What determines M_o and t_{ex}?

The ability to predict the timescale, peak entrainment rate, and supply of suspendable sediment in the bed would be very useful in designing flushing flows. In this section, the estimates of t_{ex} and M_o are compared with controlling factors.

Wu and Chou [89] successfully modeled flushing of sand from the subsurface by assuming that the flushing rate is inversely proportional to the timescale, which is itself a function

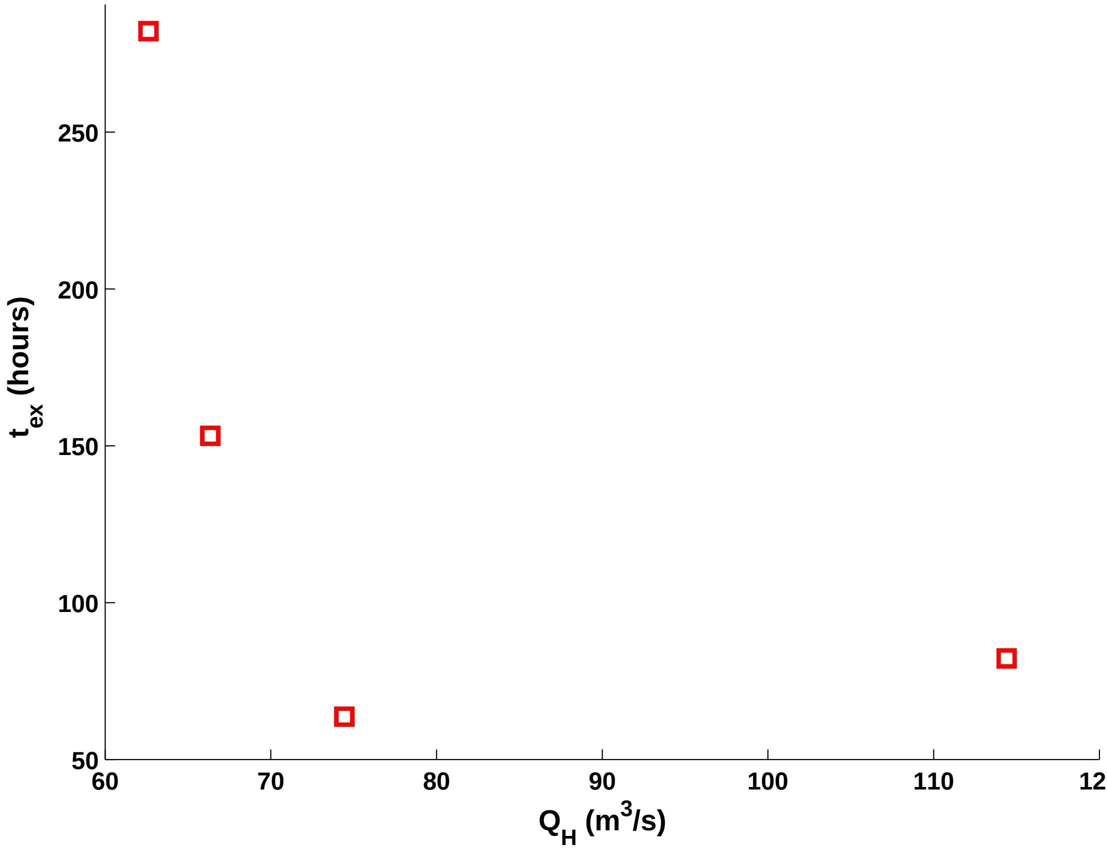

Figure 4.20: The exchange timescale vs. water discharge at Hopland. The point near $Q_H = 74m^3/s$ is DR2.

of bed material transport. USGS samples show that bedload transport increases linearly at Hopland for flows between 50 and 150 m^3/s (Figure 4.17):

$$Q_{bl} = 11.5Q_H - 288 \qquad \text{(bedload)}, \tag{4.17}$$

where Q_{bl} is bedload transport in kg/day/meter width. Above $Q_H = 150m^3/s$, total transport appears to decrease Figure 4.17). The measurement at $250m^3/s$ is on the falling limb of a storm, and so may indicate sediment exhaustion. The two measurements above 300 m^3/s are unlikely to represent an actual drop in bedload transport, but rather indicate difficulty measuring sediment trasnsport at high discharge. Nevertheless, this portion of the figure is not important for determining Q_{bl} for the DR's, which were at discharge less than $150m^3/s$. Since bedload transport is linearly proportional to discharge, estimated values of t_{ex} can be compared directly with Q_H. As suggested by Wu and Chou [89], t_{ex} is inversely tied to Q_H (Figure 4.20). The value for DR2 does not follow this trend. This may suggest that the estimate of the background suspended transport was wrong.

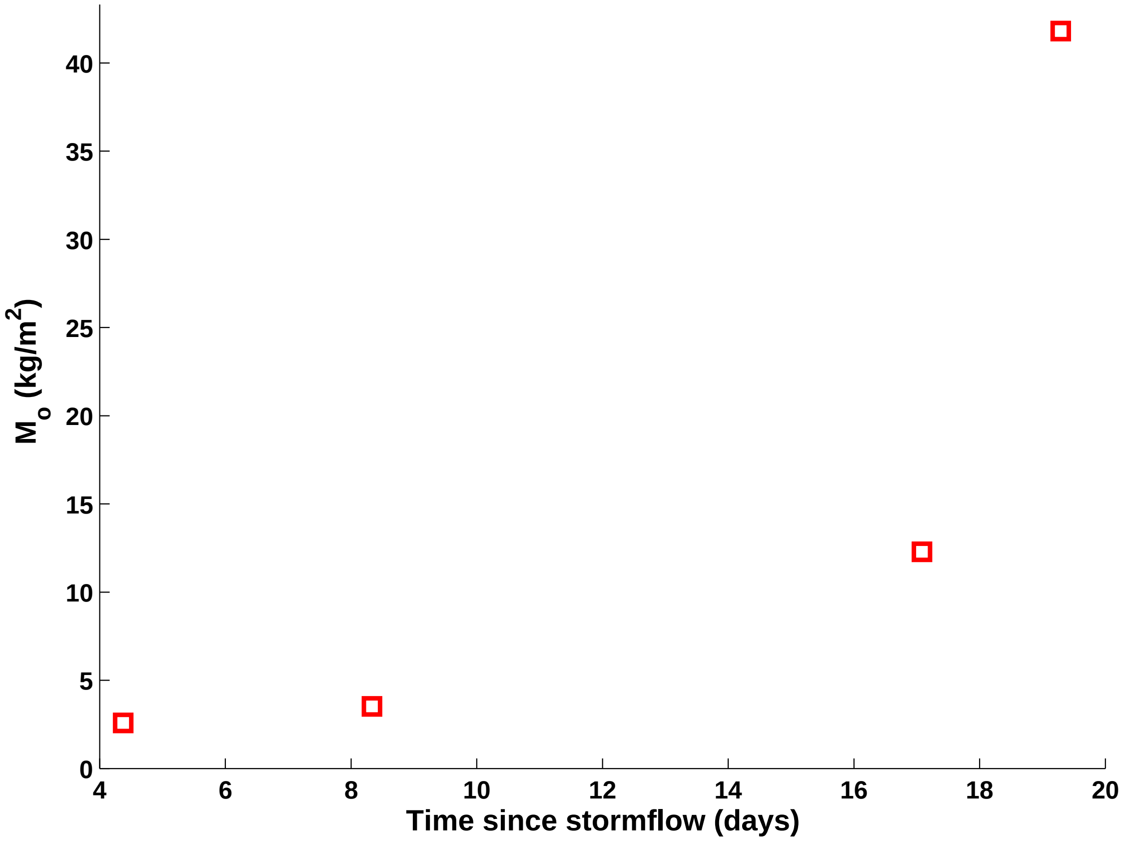

Figure 4.21: Total supply of suspendable sediment available for entrainment, M_o, as a function of the time that passed between the last large stormflow prior to the DR and the DR.

Zimmerman and LaPointe [92] found that bed permeability in a redd decreases over time at low to moderate flow, presumably due to continuous infiltration. For each DR, suspended sediment can deposit during the period of time between the peak of the last storm large enough to mobilize the bed prior to the DR and the beginning of that DR. This period is referred to as the build-up time. The total supply of fine sediment M_o should increase with the build-up time; the relationship between them is shown in Figure 4.21. The relationship is strictly positive, indicating that suspended sediment continues to deposit in or on the riverbed over weeks.

It is possible that the build-up time affects t_{ex}, as the bed becomes more armored over time and thus mobility is reduced. It is also possible that Q_H affects the total available mass of entrainable sediment M_o, because the scouring depth will be deeper at greater flows. Unfortunately, there is a covariance in the dataset that prevents exploration of these relationships. The largest DR's occur very soon after stormflows because there are flooding concerns and the storage space is being freed as fast as possible. Listing the four DR's in this study in order of decreasing Q_H is equivalent to listing them in order of increasing build-up

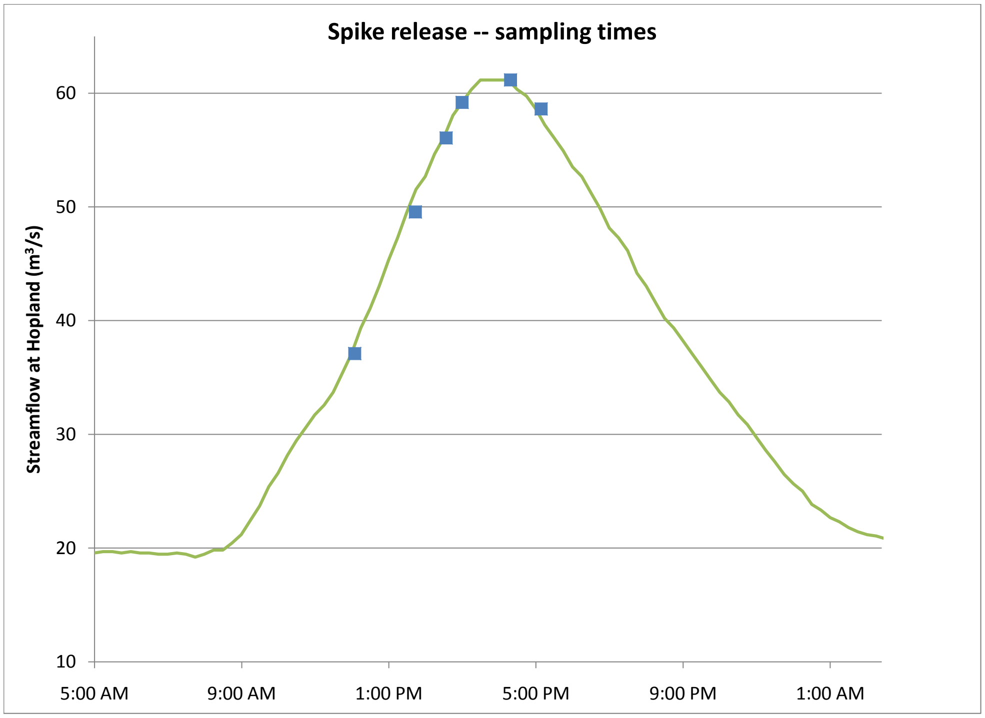

Figure 4.22: Dam release hydrograph from 14-Feb-2008. Blue squares indicate sampling times.

time. This limitation in the data makes it impossible to definitively state what controls M_o and t_{ex}. Because $E_o = M_o/(t_{ex}\rho_s)$, it is also not possible to make a prediction of E_o.

4.4.3 Suspended sediment sampling during a dam release

Four short dam releases with moderate peak flow were made from Coyote Dam between February 12 and February 15, 2008. These releases were made to calibrate hydropower equipment on the dam; flows were increased and decreased quickly to minimize outflow. Suspended sediment samples were collected at Hopland during the largest of these releases, on February 14. Maximum discharge was 61 m^3/s. The hydrograph and sampling times are given in Figure 4.22.

The suspended sediment samples were analyzed for concentration and grain size distribution. Grain size distributions for these samples were obtained using the Coulter LS laser particle size analyzer (Figure 4.23). The GSD was uniform throughout the DR except just before peak flow and at peak flow. Fines found in the riverbed are coarser than fines in

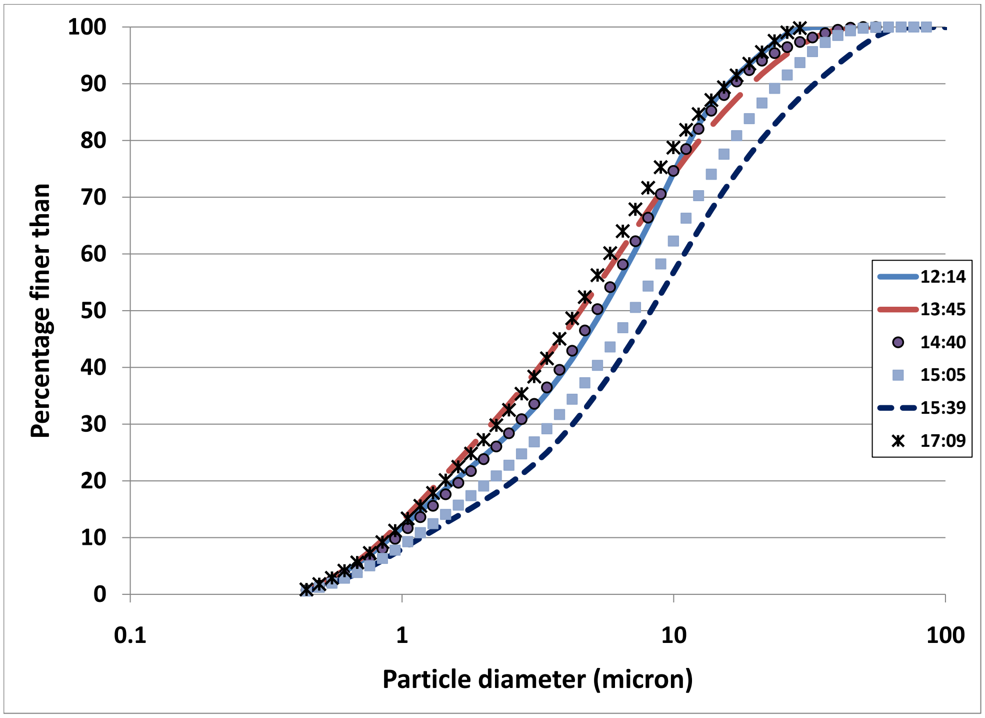

Figure 4.23: Grain size distributions from suspended sediment samples collected during the dam release on 14-Feb-2008.

transport due to selective deposition. Thus, the coarser GSD's at peak flow suggests that suspended sediment was being entrained from the riverbed.

4.5 Discussion

In this chapter, the sediment dynamics of the Russian River were analyzed using a digital watershed of USGS discharge and sediment data and NOAA precipitation data. The aims were to estimate entrainment from the riverbed, present evidence that this entrainment can be from the bed subsurface, demonstrate the utility of this dataset in exploring sediment dynamics on multiple time-scales, and determine its utility as a predictor of salmon spawning habitat quality.

There were three large assumptions in the entrainment analysis that add uncertainty to the calculations: the turbidity-suspended sediment concentration (T-SSC) relationship used at Hopland, the dispersion coefficient, and the bed mobility estimate.

USGS field data provide a well-defined T-SSC relationship for Guerneville. Suspended sediment samples indicate that this relationship overestimates SSC at Hopland, and so a new T-SSC relationship was built. This relationship is not constrained at high T because there are no data; the data that are used may not be representative of typical conditions at Hopland. The five samples at moderate discharge were all taken during a DR, when entrainment from the riverbed may have skewed the GSD towards coarser material. The other two measurements were at low flow, and low-flow measurements at Guerneville were discarded because they did not correspond to the moderate and high-flow data. These unknowns make the relationship at Hopland uncertain. However, the Hopland data are far from the cloud of Guerneville data. If the sediment was unusually coarse during the DR when samples were collected at Hopland, then typical measurements would be even further from the Guerneville data. It's clear that the Guerneville relationship shouldn't be used for Hopland. It would be helpful if some more suspended sediment samples were taken at Hopland.

Cumulative entrainment was first estimated by comparing excess sediment flux at the two sites point-by-point. This led to a physically unrealistic sharp drop in entrainment near the beginning of the dam release, corresponding to a spike in flux at Hopland. Longitudinal dispersion could explain the decrease in this spike by Guerneville, but only when the dispersion coefficient was set to ten times the value predicted by the empirical relationship from Seo and Cheong [73]. Such dispersion coefficients are not extraordinary. The Seo and Cheong [73] relationship was validated on 24 data points with a similar range. 21% of the predictions did not match the data well according to Seo and Cheong [73], including one point that was off by an order of magnitude. There are several features that would increase dispersion between Hopland and Guerneville, including slow-moving secondary channels, large boulders and woody debris that induce dead zones, backwaters in former channels, and a check dam at Healdsburg. Several creeks enter the mainstem between Hopland and Guerneville; these cause cross-channel currents that can increase dispersion [38]. Finally, the measured values of K_x used to develop equation 4.10 were from dye dispersion studies, but dispersion of suspended sediment is often be greater than dispersion of dye e.g. [23].

Calculation of local entrainment required estimating the mobile fraction of the riverbed. The mobile fraction was estimated by linear interpolation between a reasonable estimate for the onset of mobility and a speculative value for full mobility. There is no way to directly verify these estimates. This uncertainty affects the estimates of E_o and M_o, which is used to conclude that much of the sediment is entrained from the riverbed surface rather than the subsurface. The inability to demonstrate that material is coming from the surface or the subsurface is a major drawback to this study.

The entrainment analysis demonstrated that sediment transport during the DR's is consistent with an entrainment rate that decays exponentially with time. This is useful for determining the duration of flushing flows. The parameterized time scale of entrainment was calculated for four dam release events. The timescale of entrainment was above 150 hours at discharges less than $70m^3/s$ and 80 hours at $114m^3/s$. The timescale estimated for DR2 was anomolously low in this pattern. This discrepancy may indicate error in the estimate of background sediment, which was difficult to estimate for this dam release. Calculated values of t_{ex} are more certain that the estimates of E_o and M_o, which relied on the bed mobility assumption.

Using a DR discharge of $100m^3/s$ and $t_{ex} = 100hr$, it would require about $0.1km^3$ of water to flush 90% of the fine sediment out of the bed would require. This is on the order of 5% of total annual runoff, as estimated in the annual sediment yield analysis. Flushing flows would generally be made during dry years, when 5% of total annual runoff is needed for other uses. In order to make a flushing flow feasible, flushing would have to be performed in conjunction with some other water use such as water delivery.

Several factors from the calculated entrainment timeseries support the hypothesis that the turbidity record during the DR's is a record of entrainment. These factors are: 1) the large positive difference in total suspended transport between Hopland and Guerneville during all DR's; 2) the consistently positive entrainment estimates throughout all of the DR's; and 3) the consistent exponentially-decaying pattern in entrainment which corresponds to exhaustion of supply.

There are several reasons to believe that the entrainment timeseries are at least partly composed of sediment from the subsurface. Entrainment rates were far slower than the Garcia-Parker relationship for entrainment from the bed surface. Disturbance of the riverbed releases a plume of suspended sediment, and USGS bedload samples suggest bed gravel would be in transport during the DR's. The GSD of suspended sediment samples grew suddenly coarser when flow surpassed $60m^3/s$, which would be expected if fines from the bed were being suspended from the bed.

The calculated values of M_o increase with time between the last large storm prior to the DR and the beginning of the DR. This suggests that, unlike sand infiltration which stops as soon as the sand seal is built, infiltration of silt and clay continues over time. If so, then chronic sources of suspended sediment pose a problem for bed permeability, especially if natural flushing flows are cut off by dams.

Annual suspended sediment flux was estimated for the years 1966-83 and 2003-2006. Cumulative sediment discharge is highly tied to both annual water discharge and peak stormflow, with low sediment yield at annual discharge below $1km^3$ of peak stormflow below $500m^3/s$. For a given peak stormflow or annual discharge, there is a range in annual sediment discharge. This variability is probably a function of supply. Ritter and Brown [67] showed that the highest sediment yield in the Russian River basin was in Dry Creek, which had high slopes and over 40% deforestation. The effect of supply on annual sediment discharge in the basin was seen in 1966, which had excess sediment supply leftover from the large storm in December 1964. This excess sediment was apparently gone by 1967. Annual sediment yield for 2002-2006 was slightly higher for the same peak discharges than in the period 1967-1983, indicating that land use intensification in the basin is increasing fine sediment supply. If the hydrology of the Russian River basin becomes flashier with climate change, very large storms will occur more often and total sediment flux may go up.

The time discretization of the data has an impact on the total sediment flux calculation. Because the suspended sediment concentration is greatest at large discharge, a disproportionate fraction of total suspended flux occurs at the largest flows relative to discharge. Estimates of sediment yield are 17% lower when calculated using daily data than using 15-minute data. This effect should be considered when studying old suspended sediment yield calculations.

4.5.1 Conclusions

In this chapter, sediment dynamics on the Russian River were analyzed on several time scales to demonstrate how real-time turbidity monitoring can be used to study the fine sediment content in a riverbed. This has potential uses by river managers for determining the timing and design of flushing flows.

Analyses in this chapter included calculations of entrainment of suspended sediment from the riverbed during four large flood-control releases from Coyote Dam, patterns in annual suspended sediment discharge, and supporting analyses needed to complete these studies.

The main contribution of this chapter is a set of estimates of entrainment of suspended sediment from the riverbed during four flood-control dam releases. The results are consistent with a local entrainment function that decays exponentially with time. By making large assumptions about bed mobility, rough estimates of were made of peak local entrainment rates and total local sediment supply. The magnitude of these values gives an indication of the source of the sediment. Local peak entrainment rates are estimated to be on the order of 0.1 mm/hr (in volume per bed area per time), the exponential decay timescale on the order of days, and total local suspended sediment supply is on the order of 10 kg/m^2. This mass is similar to the expected mass of suspendable sediment in the subsurface. Some of the sediment probably came from the surface, but comparisons with the Garcia-Parker model as well as bedload and suspended sediment samples suggest that subsurface fines are being entrained.

Design of flushing flows requires understanding of what sets the peak entrainment rate and the timescale of its decay. The timescale of entrainment t_{ex} is inversely related to streamflow at Hopland. The total mass suspended M_o appears to be tied to the total suspended flux between the dam release and the last stormflow large enough to flush the bed that occured before the dam release. This indicates that deposition of suspended sediment into the riverbed continues over time at moderate and low flows.

There is a well-defined relationship developed between turbidity and suspended sediment concentration at Guerneville. Suspended sediment concentrations in samples collected for this study suggest that this relationship does not work for Hopland. The suspended sediment samples were used to develop a new T-SSC relationship for Hopland, but this relationship is uncertain and not constrained at high turbidity.

Annual suspended mass flux past Hopland and Guerneville was calculated for the years 1966-1983 and 2002-2006. There is a strong relationship between annual suspended sediment flux and cumulative discharge. If long-term changes in land use have affected annual sediment flux, this effect is much less significant than the relationship with discharge in most years. Land use intensification probably increases erosion during extremely large storms, increasing the sediment supply for at least a year afterwards. The choice of whether to use the T-SSC relationship from Guerneville or the T-SSC relationship from the 7 suspended sediment samples from Hopland had a large impact on these totals. Using the relationship from Guerneville, the total flux is 51% greater than calculated using the relationship from Hopland. The choice of time discretization also affected the totals, with daily values of turbidity and discharge decreasing the total flux calculation by 17% below the value calculated using 15-minute data.

Several supporting analyses were performed in order to accomplish the entrainment estimates; these can be used to support other hydrological and sediment studies. The supporting analyses include 1) collection of suspended sediment samples at Hopland and analsis of these samples for concentration and grain size distribution, 2) calculation of turbidity - suspended sediment concentration relationships, 3) calculation of travel times of hydrographs and sediment waves between Hopland and Guerneville, 4) calculation of the decay rate of suspended sediment flux on the falling limb of storms, 5) estimate of a longitudinal dispersion coefficient for suspended sediment transport between Hopland and Guerneville, 6) estimates of the areal fraction of the bed that is mobile during different flows, and 7) identification of dam releases and stormflows with good data records for study.

Variable	Description	Units
d	Particle diameter of fine sediment	l
f	Volume of suspendable sediment as a fraction of total bed sediment	$-$
g	Gravitational acceleration	l/t^2
t_{ex}	Timescale of entrainment (exchange timescale)	t
u_*	Shear velocity	l/t
w_s	Particle settling velocity	l/t
x	Downstream distance	l
A	Bed area from which entrainment occurs	l^2
A_{tot}	Bed area from which entrainment occurs	l^2
D	Gravel diameter	l
E	Entrainment rate	l/t
E_o	Peak entrainment rate	l/t
H	Water depth	l
K_x	Longitudinal dispersion coefficient	l^2/t
M	Mass per bed area of suspendable sediment	m/l^2
M_o	Initial mass per bed area of suspendable sediment	m/l^2
$Q(Q_G, Q_H)$	Water discharge (at Guerneville and Hopland)	l^3/t
$Q_{sG}(Q_{sH})$	Suspended sediment discharge at Guerneville (Hopland)	m/t
$Q_{sGo}(Q_{sHo})$	Initial SS discharge	m/t
$Q_{sG,bk}(Q_{sH,bk})$	Background SS discharge	m/t
Re_p	Particle Reynolds number	-
S	Slope	-
SSC	Suspended sediment concentration	m/l^3
T	Turbidity	NTU/FNU
W	Channel width	l
Z	Term in the Garcia-Parker entrainment relation	-
ν	Water viscosity (kinematic)	l^2/t
ρ_w	Density of water	m/l^3
ρ_s	Density of sediment	m/l^3
σ_{dp}	Standard deviation of a dispersed distribution in space	l
σ_{dpt}	Standard deviation of a dispersed distribution in time	l
$\tau(\tau_s, \tau_w)$	Travel time (of sediment, water)	t
$\widetilde{f(t)}$	Dispersed signal of a function $f(t)$	

Table 4.8: Variables for suspended sediment dynamics on the Russian River

Bibliography

[1] R. M. Acornley and D. A. Sear. Sediment transport and siltation of brown trout (salmo trutta l.) spawning gravels in chalk streams. *Hydrological Processes*, 13(3):447–458, 1999. Times Cited: 45.

[2] J.N. Adams and R.L. Beschta. Gravel bed composition in oregon coastal streams. *Canadian Journal of Fisheries and Aquatic Sciences*, 37(10):1514–1521, 1980.

[3] J. M. H. Barton and S. G. Buchberger. Geometrical analysis of sand piles on small platforms. *Physical Review E*, 68(1):011303, 2003.

[4] J. Bear. *Dynamics of fluids in porous media*. Environmental Science Series. American Elsevier, Ottawa, 1972.

[5] R. L. Beschta and W. L. Jackson. Intrusion of fine sediments into a stable gravel bed. *Journal of the Fisheries Research Board of Canada*, 36(2):204–210, 1979.

[6] M. Brunke and T. Gonser. The ecological significance of exchange processes between rivers and groundwater. *Freshwater Biology*, 37(1):1–33, 1997.

[7] Kristin Bunte and Steven R. Abt. Sampling surface and subsurface particle-size distributions in wadable gravel- and cobble-bed streams for analyses in sediment transport, hydraulics, and streambed monitoring. Technical Report Gen. Tech. Rep. RMRS-GTR-74, U.S. Department of Agriculture, Forest Service, Rocky Mountain Research Station, 2001.

[8] P.A. Carling and C.P. McCahon. Natural siltation of brown trout (salmo trutta l.) spawning gravels during low flow conditions. In Craig J.F and Kemper J.B, editors, *Regulated Streams*, pages 229–244. Plenum Publishing Corporation, New York, 1989.

[9] CDFA. Grape crush report, final 2009 crop, 2010.

[10] D.W. Chapman. Critical review of variables used to define effects of fines in redds of large salmonids. *Transactions of the American Fisheries Society*, 117(1):1–21, 1988.

[11] J. A. Clayton and J. Pitlick. Spatial and temporal variations in bed load transport intensity in a gravel bed river bend. *Water Resources Research*, 43(2):13, 2007.

[12] Cook. Chinook salmon spawning study russian river fall 2005. Technical report, Sonoma County Water Agency, 2006.

[13] M. R. Cover, C. L. May, W. E. Dietrich, and V. H. Resh. Quantitative linkages among sediment supply, streambed fine sediment, and benthic macroinvertebrates in northern california streams. *Journal of the North American Benthological Society*, 27(1):135–149, 2008.

[14] Y. Cui, J. K. Wooster, P. F. Baker, S. R. Dusterhoff, L. S. Sklar, and W. E. Dietrich. Theory of fine sediment infiltration into immobile gravel bed. *Journal of Hydraulic Engineering-Asce*, 134(10):1421–1429, 2008.

[15] R. J. Davies-Colley and D. G. Smith. Turbidity, suspended sediment, and water clarity: A review. *Journal of the American Water Resources Association*, 37(5):1085–1101, 2001.

[16] W. E. Dietrich. Settling velocity of natural particles. *Water Resources Research*, 18(6):1615–1626, 1982.

[17] P. Diplas and G. Parker. Pollution of gravel spawning grounds due to fine sediment. St. Anthony Falls Hydraul. Lab. Prof. Rep. 240, University of Minnesota, 1985.

[18] P. Diplas and G. Parker. Deposition and removal of fines in gravel-bed streams. In P. Billi, R. D. Hey, C. R. Thorne, and P. Tacconi, editors, *Dynamics of Gravel-bed Rivers*, pages 313–329. John Wiley & Sons Ltd., 1992.

[19] H.A. Einstein. Deposition of suspended particles in a gravel bed. *J. Hydraul. Div. Am. Soc. Civ. Eng.*, 94(5):1197–1205, 1968.

[20] A. H. Elliott and N. H. Brooks. Transfer of nonsorbing solutes to a streambed with bed forms: Theory. *Water Resources Research*, 33(1):123–136, 1997.

[21] S. Ergun. Fluid flow through packed columns. *Chemical Engineering Progress*, 48:89–94, 1952.

[22] R. I. Ferguson. Accuracy and precision of methods for estimating river loads. *Earth Surface Processes and Landforms*, 12(1):95–104, 1987.

[23] A. Filip. Investigation of dispersion and dilution of suspended species in river flow by radio-tracer techniques. *The International Journal of Applied Radiation and Isotopes*, 22(6):331 – 337, 1971.

[24] Hugo B. Fischer, John E. List, C. Robert Koh, Jorg Imberger, and Norman H. Brooks. *Mixing in Inland and Coastal Waters.* Academic Press, 1979.

[25] Joan Florsheim, Karen Gaffney, Alice Rich, Leonard Charles, Lori Brooke, Theresa Hughes, and Damen Sakai. Upper russian river aggregate resources management plan mendocino county. Technical report, Philip Williams & Associates, Ltd., 1997.

[26] Joan L. Florsheim and Peter Goodwin. Geomorphic and hydrologic conditions in the russian river, california: Historic trends and existing conditions. Technical report, Philip Williams & Associates, Ltd., 1993.

[27] J. S. Fries. Predicting interfacial diffusion coefficients for fluxes across the sediment-water interface. *Journal of Hydraulic Engineering-Asce*, 133(3):267–272, 2007.

[28] L. E. Frostick, P. M. Lucas, and I. Reid. The infiltration of fine matrices into coarse-grained alluvial sediments and its implications for stratigraphical interpretation. *Journal of the Geological Society*, 141(NOV):955–965, 1984.

[29] M. Garcia and G. Parker. Entrainment of bed sediment into suspension. *Journal of Hydraulic Engineering-Asce*, 117(4):414–435, 1991.

[30] D. R. Geist and D. D. Dauble. Redd site selection and spawning habitat use by fall chinook salmon: The importance of geomorphic features in large rivers. *Environmental Management*, 22(5):655–669, 1998.

[31] S. Gibson, D. Abraham, R. Heath, and D. Schoellhamer. Vertical gradational variability of fines deposited in a gravel framework. *Sedimentology*, 56(3):661–676, 2009.

[32] S. Gibson, D. Abraham, R. Heath, and D. Schoellhamer. Bridging process threshold for sediment infiltrating into a coarse substrate. *Journal of Geotechnical and Geoenvironmental Engineering*, 136(2):402–406, 2010. Gibson, Stanford Abraham, David Heath, Ronald Schoellhamer, David.

[33] T. H. Goodwin, A. R. Young, M. G. R. Holmes, G. H. Old, N. Hewitt, G. J. L. Leeks, J. C. Packman, and B. P. G. Smith. The temporal and spatial variability of sediment transport and yields within the bradford beck catchment, west yorkshire. *Science of the Total Environment*, 314:475–494, 2003.

[34] P. E. Grams and P. R. Wilcock. Equilibrium entrainment of fine sediment over a coarse immobile bed. *Water Resources Research*, 43(10), 2007.

[35] J. K. Haschenburger and P. R. Wilcock. Partial transport in a natural gravel bed channel. *Water Resources Research*, 39(1):9, 2003.

[36] John N. Holeman. The sediment yield of major rivers of the world. *Water Resources Research*, 4, 1968.

[37] P.Y. Julien. *Erosion and Sedimentation.* Cambridge University Press, New York, 1998.

[38] Stephen T. Kenworthy and Bruce L. Rhoads. Hydrologic control of spatial patterns of suspended sediment concentration at a stream confluence. *Journal of Hydrology*, 168(1-4):251 – 263, 1995.

[39] G. M. Kondolf. Lessons learned from river restoration projects in california. *Aquatic Conservation-Marine and Freshwater Ecosystems*, 8(1):39–52, 1998.

[40] G. M. Kondolf. Assessing salmonid spawning gravel quality. *Transactions of the American Fisheries Society*, 129(1):262–281, 2000.

[41] G. M. Kondolf, M. J. Sale, and M. G. Wolman. Modification of fluvial gravel size by spawning salmonids. *Water Resources Research*, 29(7):2265–2274, 1993.

[42] G. M. Kondolf and P. R. Wilcock. The flushing flow problem: Defining and evaluating objectives. *Water Resources Research*, 32(8):2589–2599, 1996.

[43] K.V. Koski. *The survival of Coho salmon (Oncorhynchus kisutch) from egg deposition to emergence in three Oregon streams.* PhD thesis, Oregon State University, 1966.

[44] M. Lapointe, B. Eaton, S. Driscoll, and C. Latulippe. Modelling the probability of salmonid egg pocket scour due to floods. *Canadian Journal of Fisheries and Aquatic Sciences*, 57(6):1120–1130, 2000.

[45] T. E. Lisle. Sediment transport and resulting deposition in spawning gravels, north coastal California. *Water Resources Research*, 25(6):1303–1319, 1989.

[46] W. A. Marcus. Lag-time routing of suspended sediment concentrations during unsteady-flow. *Geological Society of America Bulletin*, 101(5):644–651, 1989.

[47] R.R. McDonald, J.M. Nelson, and J.P. Bennett. Multi-dimensional surface-water modeling system user's guide. Technical Report Techniques and Methods, 6-B2, U.S. Geological Survey, 2005.

[48] C. B. Meyer, M. D. Sparkman, and B. A. Klatte. Sand seals in coho salmon redds: Do they improve egg survival? *North American Journal of Fisheries Management*, 25(1):105–121, 2005.

[49] E. I. Meyer, O. Niepagenkemper, F. Molls, and B. Spanhoff. An experimental assessment of the effectiveness of gravel cleaning operations in improving hyporheic water quality in potential salmonid spawning areas. *River Research and Applications*, 24(2):119–131, 2008.

[50] MKF. Economic impact of wine and vineyards in sonoma county. Technical report, MKF Research Publications, 2005.

[51] H. J. Moir and G. B. Pasternack. Relationships between mesoscale morphological units, stream hydraulics and chinook salmon (oncorhynchus tshawytscha) spawning habitat on the lower yuba river, california. *Geomorphology*, 100(3-4):527–548, 2008. Moir, Hamish J. Pasternack, Gregory B.

[52] H. Nagaoka and S. Ohgaki. Mass-transfer mechanism in a porous riverbed. *Water Research*, 24(4):417–425, 1990.

[53] William W. Nazaroff and Lisa Alvarez-Cohen. *Environmental Engineering Science.* John Wiley & Sons, Inc., New York, 2001.

[54] Dietrich W.E. Nelson, P.A. and J.G. Venditti. Bed topography and the development of forces bed surface patches. *Journal of Geophysical Research - Earth Surface*, 2010.

[55] R. W. Nelson, J. R. Dwyer, and W. E. Greenberg. Regulated flushing in a gravel-bed river for channel habitat maintenance - a trinity river fisheries case-study. *Environmental Management*, 11(4):479–493, 1987.

[56] K.M. Nolan, T.E. Lisle, and H.M. Kelsey. Bankfull discharge and sediment transport in northwester california. In *Erosion and Sedimentation in the Pacific Rim,Corvallis Symposium*, 1987.

[57] Jeff J. Opperman, Kathleen A. Lhse, Colin Brooks, N.M. Kelly, and Adina M. Merenlender. Influence of land use on fine sediment in salmonid spawning gravels within the russian river basin, california. *Canadian Journal of Fisheries and Aquatic Sciences*, 62(12):2740–2751, 2005.

[58] J. Ortlepp and U. Murle. Effects of experimental flooding on brown trout (salmo trutta fario l.): The river spol, swiss national park. *Aquatic Sciences*, 65(3):232–238, 2003.

[59] David Owen. The efficiency dilemma. *The New Yorker*, 2010.

[60] A. Packman, M. Salehin, and M. Zaramella. Hyporheic exchange with gravel beds: Basic hydrodynamic interactions and bedform-induced advective flows. *Journal of Hydraulic Engineering-Asce*, 130(7):647–656, 2004.

[61] A. I. Packman and N. H. Brooks. Hyporheic exchange of solutes and colloids with moving bed forms. *Water Resources Research*, 37(10):2591–2605, 2001.

[62] A. I. Packman and J. S. MacKay. Interplay of stream-subsurface exchange, clay particle deposition, and streambed evolution. *Water Resources Research*, 39(4), 2003.

[63] C. Paola, G. Parker, R. Seal, S. K. Sinha, J. B. Southard, and P. R. Wilcock. Downstream fining by selective deposition in a laboratory flume. *Science*, 258(5089):1757–1760, 1992.

[64] K. J. Rehg, A. I. Packman, and J. H. Ren. Effects of suspended sediment characteristics and bed sediment transport on streambed clogging. *Hydrological Processes*, 19(2):413–427, 2005.

[65] K. Ridgway and K. J. Tarbuck. Particulate mixture bulk densities. *Chemical and Process Engineering*, 49(2), 1968.

[66] John J. Risley, J. Rose Wallick, Ian Waite, and Adam Stonewall. Development of an environmental flow framework for the mckenzie river basin, oregon. Technical report, USGS, 2010.

[67] John R. Ritter and III Brown, William H. Turbidity and suspended-sediment transport in the russian river basin, california, 1971.

[68] RMA. Hec-5q simulation of water quality in the russian river basin. Technical report, Resource Management Associates Inc. for Sonoma County Water Agency, 2001.

[69] J.F. Ruff and L.W. Gelhar. Turbulent shear flow in porous boundary. *J. Engrg. Mech. Div.*, 98(4):975–991, 1972.

[70] Ramaswamy Sakthivadivel and Hans Albert Einstein. Clogging of porous column of spheres by sediment. *Journal of the Hydraulics Division*, 96(2):461–472, 1970.

[71] U. Schälchli. Basic equations for siltation of riverbeds. *Journal of Hydraulic Engineering-Asce*, 121(3):274–287, 1995.

[72] D. A. Sear. Fine sediment infiltration into gravel spawning beds within a regulated river experiencing floods - ecological implications for salmonids. *Regulated Rivers-Research & Management*, 8(4):373–390, 1993. ISI Document Delivery No.: MM654 Times Cited: 48 Cited Reference Count: 0.

[73] Il Won Seo and Tae Sung Cheong. Predicting longitudinal dispersion coefficient in natural streams. *Journal of Hydraulic Engineering*, 124(1):25–32, 1998.

[74] J.J. Sherard, L.P. Dunnigan, and J.R. Talbot. Basic properties of sand and gravel filters. *Journal of Geotechnical Engineering*, 110(6):684–700, 1984.

[75] Y. Shimizu, T. Tsujimoto, and H. Nakagawa. Experiment and macroscoping modelling of flow in highly permeable porous medium under free-surface flow. *Journal of Hydroscience and Hydraulic Engineering*, 8(1):69–78, 1990.

[76] M. G. Sidiropoulou, K. N. Moutsopoulos, and V. A. Tsihrintzis. Determination of forchheimer equation coefficients a and b. *Hydrological Processes*, 21(4):534–554, 2007.

[77] A. St-Hilaire, D. Caissie, R. A. Cunjak, and G. Bourgeois. Streambed sediment composition and deposition in a forested stream: Spatial and temporal analysis. *River Research and Applications*, 21(8):883–898, 2005.

[78] Environmental Consulting Steiner. A history of the salmonid decline in the russian river. Technical report, Sonoma County Water Agency, California State Coastal Conservancy, 1996.

[79] D. Tonina and J. M. Buffington. A three-dimensional model for analyzing the effects of salmon redds on hyporheic exchange and egg pocket habitat. *Canadian Journal of Fisheries and Aquatic Sciences*, 66(12):2157–2173, 2009.

[80] USEPA. Developing water quality criteria for suspended and bedded sediments (sabs): Potential approaches. 2003. http://water.epa.gov/scitech/datait/tools/warsss/sabs.cfm.

[81] USEPA. Section 303(d) list fact sheet for watershed, russian, 2006.

[82] USFWS. Pacific salmon, (oncorhynchus spp.), 2000. http://www.fws.gov/species/species/accounts/bio/salm.html.

[83] L. van Rijn. Sediment transport, part ii: Suspended load transport. *Journal of Hydraulic Engineering*, 110:1613–1641, 1984.

[84] J.G. Venditti, A. Nelson, P, J.T. Minear, J. Wooster, and W. E. Dietrich. Response of alternate bar topography to variation in sediment supply in gravel-bedded rivers. *Water Resources Research*, 2010.

[85] S. Vollmer and M. G. Kleinhans. Predicting incipient motion, including the effect of turbulent pressure fluctuations in the bed. *Water Resources Research*, 43(5), 2007.

[86] P. R. Wilcock, A. F. Barta, C. C. Shea, G. M. Kondolf, W. V. G. Matthews, and J. Pitlick. Observations of flow and sediment entrainment on a large gravel-bed river. *Water Resources Research*, 32(9):2897–2909, 1996. Times Cited: 55.

[87] P. R. Wilcock, G. M. Kondolf, W. V. G. Matthews, and A. F. Barta. Specification of sediment maintenance flows for a large gravel-bed river. *Water Resources Research*, 32(9):2911–2921, 1996.

[88] J. Wooster, S. Dusterhoff, Y. Cui, L. Sklar, W. E. Dietrich, and M. Malko. Sediment supply and relative size distribution effects on fine sediment infiltration into immobile gravels. *Water Resources Research*, 44, 2008.

[89] F. C. Wu and Y. J. Chou. Simulation of gravel-sand bed response to flushing flows using a two-fraction entrainment approach: Model development and flume experiment. *Water Resources Research*, 39(8), 2003.

[90] T. Yamada and N. Kawabata. A theoretical study on the resistance law of the flow over porous layer. *Proc. Jap. Soc. civ. Engrs*, 325:69–90 (in Japanese), 1982.

[91] Fu-Ling Yang. *Interaction Law for a Collision Between Two Solid Particles in a Viscous Liquid*. PhD thesis, 2006.

[92] A. E. Zimmermann and M. Lapointe. Intergranular flow velocity through salmonid redds: Sensitivity to fines infiltration from low intensity sediment transport events. *River Research and Applications*, 21(8):865–881, 2005.